FABRICATION OF SUPERPARAMAGNETIC AND FERROMAGNETIC NANOPARTICLES

by

NARAYAN POUDYAL

Presented to the Faculty of the Graduate School of

The University of Texas at Arlington in Partial Fulfillment

of the Requirements

for the Degree of

DOCTOR OF PHILOSOPHY

THE UNIVERSITY OF TEXAS AT ARLINGTON

December 2008

DEDICATED TO

My parents and daughter Priyanka

ACKNOWLEDGEMENTS

I would like to express my deepest appreciation and gratitude to my advisor, Professor J. Ping Liu, for providing invaluable guidance for my research and for constantly supporting me over the past five years. I especially thank him for introducing me to scientific research and providing me with challenges. His expertise in nanostructured magnetism, along with his vision of nanotechnology, has been a source of inspiration for me to pursue further research in this exciting field. The present research could not have been completed without his expert guidance, constant supervision, and onging encouragement.

I would also like to express my appreciation to Professors John L. Fry, Truman Black, Ali R. Koymen, and Qiming Zhang for serving on my dissertation supervisory committee. I am grateful to them for their support of my research and for their careful and critical reading of my dissertation.

I am indebted to past and present colleagues for their important suggestions, assistance, encouragement of my studies and research, and wonderful friendship during our time together. Among them are Dr. Chuan-bing Rong, Dr. Girija Chaubey, Vikas Nandwana, Dr. Kevin Elkins, Dr. Yiping Wang, Dr. Zhiqiang Jin, Dr. Yang Li, Dr. Ming Yue, Dr. Baki Altuncevahir, Dr. Shirly Machluf, Dr. Kendra Wallis, Dr. Nguyen Van Vuong, Yunpeng Zhang, Kazuaki Yano, Daren Li, Vamsi Chakka, Tejaswi Vedantam, Kung-Te Chu, Hamed Arami, John Griffis and Chengyang Liu.

I am thankful to our collaborator, Dr. Z. L. Wang at The Georgia Institute of Technology for providing assistance with the HRTEM analysis. I am also grateful to Dr. Shishou S. Kang for his help with the HRTEM analysis at The University of Alabama. I am thankful to Dr. Jiechao

Jiang in the Department of Materials Science and Engineering at UTA for the technical support he provided with for operating the TEM and SEM.

I would like to thank all the faculty and staff members in the Department of Physics at UTA. My studies and research experiences have been so memorable because of their diligent effort to create a great environment for all students. I am grateful to The University of Texas at Arlington for providing me such a wonderful environment for my studies. I also express my indebtedness to all of my friends for their encouragement to complete this study, particually I am grateful to Yogendra, Prakash, Puspa, and Meena.

There can be no adequate acknowledgement for the loving encouragement I have received from my parents, brothers, sisters and all family members. Without their constant support and inspiration all this would never have been possible.

My final thanks go to my wife Sita, who has continuously supported me throughout the process of my pursuing this PhD. The daily encouragement she provided makes this dissertation as much hers as it is mine.

This work was supported by US DoD/MURI grant N00014-05-1-0497 and DARPA through ARO under Grant No DAAD 19-03-1-0038. This work was also supported by The Center of Nanostructured Materials and Characterization Center for Materials and Biology at The University of Texas at Arlington.

November 24, 2008

ABSTRACT

FABRICATION OF SUPERPARAMAGNETIC AND FERROMAGNETIC NANOPARTICLES

Narayan Poudyal, PhD.

The University of Texas at Arlington, 2008

Supervising Professor: J. Ping Liu

Monodisperse magnetic nanoparticles with controlled size and geometry have drawn great attention in the last decade for fundamental scientific studies and for their potential applications in advanced materials and devices such as ultra-high-density magnetic recording media, exchange-coupled nanocomposite magnets, biomedicines and nanodevices. This dissertation focuses on the fabrication and characterization of superparamagnetic and ferromagnetic nanoparticles of hard magnetic materials (FePt, $SmCo_5$, Sm_2Co_{17}, and $Nd_2Fe_{14}B$) and soft magnetic materials ($CoFe_2O_4$, $NiFe_2O_4$, and FeCo). Novel preparation techniques, including salt-matrix annealing, surfactant-assisted ball milling and magnetic field milling have been adopted in this study.

The FePt nanocrystals, with a variety of morphologies, including nanowires, nanorods, spherical nanoparticles, nanocubes, and nanosized multi-pods, were synthesized by a polyol reduction process. The size and shape control was achieved by adjusting synthesis parameters. The as-synthesized FePt nanocrystals have chemically disordered fcc structure and are superparamagnetic at room temperature. Upon heat treatment, the nanoparticles were

transformed into hard magnetic films with ordered fct structure, and high coercivity up to 25 kOe was achieved. Monodisperse $L1_0$ FePt nanoparticles from 3 to 15 nm were prepared by a salt-matrix annealing technique. Size dependent phase transition and chemical ordering of FePt nanoparticles were also systematically investigated. Magnetic properties of $L1_0$ FePt nanoparticles including magnetization and coercivity are strongly dependent on both the particle size and the chemical ordering and increase with particle diameter. The giant coercivity up to 35 kOe was achieved for 8 nm $L1_0$ FePt nanoparticles with faceted shape.

Monodisperse $CoFe_2O_4$ and $NiFe_2O_4$ nanoparticles of different sizes ranging from 3 to 20 nm were also synthesized by a polyol reduction process. Air-stable FeCo nanoparticles with controllable particle size and narrow size distribution were prepared by reductive salt-matrix annealing of $CoFe_2O_4$ nanoparticles. Size and temperature dependent magnetic properties of $CoFe_2O_4$, $NiFe_2O_4$, and FeCo have been reported.

Sm_2Co_{17}, $SmCo_5$, and $Nd_2Fe_{14}B$ nanoparticles with narrow size distribution were fabricated by high energy ball milling in the presence of surfactants and followed by subsequent size selection process. Significant room-temperature coercivity up to 3.2 kOe was achieved with the Sm_2Co_{17} nanoparticles of an average size of $\sim$ 20 nm. $Nd_2Fe_{14}B$ and Sm_2Co_{17} sub-micron particles were also prepared by ball milling in a magnetic field. Particles milled in a magnetic field, consisting of nano-sized grains, exhibit strong magnetic anisotropy compared with the particles milled without a magnetic field.

TABLE OF CONTENTS

LIST OF ILLUSTRATIONS

LIST OF TABLES

CHAPTER 1

FUNDAMENTALS OF MAGNETISM AND MAGNETIC MATERIALS

1.1 Introduction

All materials exhibit magnetic properties regardless of their phase and composition. Magnetic properties in materials arise from the motion of electrons within their atoms and from the way they interact with their surrounding environment. All materials are influenced to one degree or another by the presence of magnetic field, depending on how materials respond to the magnetic field. In general, magnetic effects on materials can be classified into three groups according to the interaction and configuration of their electrons. These three types of magnetism are diamagnetism, paramagnetism, and ferromagnetism; in addition, antiferromagnetism and ferrimagnetism are considered to be subclasses of ferromagnetism.[1-3] These three types of magnetism will be discussed in Section 1.2.

Atomic Origins of Magnetism: Viewed from the atomic level of matter, the origin of magnetism can be said to lie in the orbital and spin motion of electrons and in how electrons interact with each other. Except for some nucleic magnetic effects, which are much smaller, these two types of electron motion are the source of the macroscopic magnetic phenomena in materials. Each electron may also be thought of as spinning around its own axis, which brings about spin moment. Another magnetic moment originates from this electron spin, which is directed along the orbit around the nucleus of the atom. The net magnetic moment of an atom is just the sum of the magnetic moments of each of the constituent electrons, including both orbital and spin contributions. All materials exhibit at least one of these types of magnetism, and the behavior of the material depends on the response of electron and atomic magnetic dipoles to the application of an externally applied magnetic field.

Magnetic Fields and Variables: The magnetic field strength (or intensity) is usually represented by *H*. The magnetic moment per unit volume of a magnetic material is measured by *M,* the magnetization (or

polarization). *M* results from two atomic motions: the orbital and spin motions of electrons as mentioned above. Magnetic induction, *B,* is defined as: [2, 3, 8]

$$B = H + 4\pi M. \text{[CGS]} \tag{1.1}$$

The nature of *H, M,* and *B* is fundamentally the same, as implied by equation (1.1). The units of these three parameters are also similar and depend on the system of units being used. There are currently three systems of units that are widely used, including CGS or Gaussian system and SI system (see Appendix A).

Magnetic Susceptibility and Magnetic Permeability: The magnetic properties of a material are characterized not only by the magnitude of *M* but also by the way in which *M* varies with *H*. The ratio of these two quantities is called susceptibility (*k*):[2, 8]

$$k = \frac{M}{H}. \tag{1.2}$$

This susceptibility is unitless, as seen by equation (1.2). A quantity closely related to the susceptibility is the permeability (μ) which is defined by:

$$\mu = \frac{B}{H}. \tag{1.3}$$

The physical meaning of equation (1.3), especially if it is written as $B = \mu H$, is that a current generated magnetic field *H*, when applied to a material of large permeability is enhanced by the factor of μ to create a large field *B*. From equations (1.1), (1.2), and (1.3) one can obtain that:

$$\mu = 1 + 4\pi k. \tag{1.4}$$

1.2 Types of Magnetism in Materials

The origin of magnetism lies in the orbital and spin motions of electrons. Electron interactions also have strong effect in magnetism. In some materials, there is no collective interaction of atomic magnetic moments, whereas in other materials there are very strong interactions among atomic moments. The way to classify the different types of magnetism depends on how materials respond to magnetic fields. The magnetic behavior of materials can be classified into diamagnetism, paramagnetism,

and ferromagnetism in which anitferromagnetism and ferrimagnetism are considered to be its subclasses.[3, 8]

1.2.1 Diamagnetism

Diamagnetism is a fundamental property of all matter, although it is usually very weak. It is due to the non-cooperative behavior of orbiting electrons when exposed to an applied magnetic field. Diamagnetic substances are composed of atoms which have no net magnetic moments (i.e., all the orbitals are filled and there are no unpaired electrons). However, when exposed to a field *H*, the orbiting electrons either accelerate or decelerate so that their magnetic moments are in the opposite direction from the external field. Once the external field is removed, the diamagnetic material loses its magnetization, and a negative magnetization is produced and thus the susceptibility χ_m is < 0 (order of 10^{-5}) for a diamagnetic material, resulting in very low moments.[1-6, 8]

1.2.2 Paramagnetism

For this class of materials, some of the atoms or ions in the material have a net magnetic moment due to unpaired electrons in partially filled orbitals. However, the individual magnetic moments do not interact magnetically, and as with diamagnetism, the net magnetization is zero when the field is removed. In the presence of a field, there is a partial alignment of the atomic magnetic moments in the direction of the field, resulting in a net positive magnetization such that the susceptibility χ_m is > 0 (order of 10^{-5} to 10^{-2}) for paramagnetic materials.[1-3] In addition, the efficiency of the field in aligning the moments is opposed by randomizing effects of temperature. This results in a temperature dependent susceptibility known as the Curie Law.

1.2.3 Ferromagnetism

Ferromagnetic materials exhibit parallel alignment of permanent magnetic moments, resulting in a large net magnetization even in the absence of a magnetic field. These moments originate from the overall contribution of electron spin and orbital magnetic moments.[4] The elements Fe, Ni, and Co and many of their alloys are typical ferromagnetic materials. Magnetic susceptibility as high as 10^6 is possible for ferromagnetic materials. Two distinct characteristics of ferromagnetic materials are their spontaneous magnetization and the existence of magnetic ordering temperature. The spontaneous magnetization is

the net magnetization that exists inside a uniformly magnetized microscopic volume in the absence of a field. As the temperature increases, the arrangement of atomic moments is disturbed by the thermal agitation, thus resulting in temperature dependence of spontaneous magnetization. In spite of the presence of spontaneous magnetization, a block of ferromagnetic or ferromagnetic substance is usually not spontaneously magnetized but exists rather in a demagnetized state. This is because the interior of the block is divided into many magnetic domains, each of which is spontaneously magnetized. Since the direction of domain magnetization varies from domain to domain, the resultant magnetization can be changed from zero to the value of spontaneous magnetization.[1, 8] The saturation magnetization (M_{sat}) is the maximum induced magnetic moment that can be obtained in a magnetic field beyond this field; no further increase in magnetization occurs. Saturation magnetization is an intrinsic property, independent of particle size but dependent on temperature.

1.2.3.1 Antiferromagnetism

In some other types of materials, the magnetic moment coupling between adjacent atoms or ions results in the antiparallel alignment of the magnetic dipoles. This phenomenon of the alignment of spin moments of neighboring atoms or ions in exactly opposite directions is termed antiferromagnetism. The opposing magnetic moments cancel one another, resulting in zero net magnetization of the material.[2, 4, 8] For example, in manganese oxide (MnO), the A and B sub-lattice moments are exactly equal but opposite, and thus the net moment is zero.

1.2.3.2 Ferrimagnetism

Ferrimagnetism is another type of magnetic ordering. In ferrimagnets, the moments of adjacent atoms or ions are in an antiparallel alignment, but they do not cancel out each other. The best example of a ferromagnetic mineral is magnetite (Fe_3O_4), in which two iron ions are trivalent while another is divalent. The two trivalent ions align with opposite moments and cancel out one another, so the net moment arises from the divalent. The structural formula for magnetite is $[Fe^{3+}]A\ [Fe^{3+},Fe^{2+}]BO_4$. This particular arrangement of cations on the A and B sublattices is called an inverse spinel structure. With negative AB exchange interactions, the net magnetic moment of magnetite is due to the B-site Fe^{2+}. Ferrimagnetism is therefore similar to ferromagnetism. Ferrimagnetism exhibits all the hallmarks of ferromagnetic behavior-

spontaneous: magnetization, Curie temperatures, hysteresis, and remanence. However, ferro and ferrimagnets have very different magnetic ordering.[8]

1.3 Ferromagnetic Materials[1-5, 8]

Curie temperature: Even though electronic exchange forces in ferromagnets are very large, thermal energy eventually overcomes the exchange interaction and produces a randomizing effect. This occurs at a particular temperature called the Curie temperature (T_c). Below the Curie temperature, the ferromagnet is ordered, and above the Curie temperature the ferromangnet is disordered. The saturation magnetization goes to zero at the Curie temperature. The Curie temperature is an intrinsic property of materials and is a diagnostic parameter that can be used for mineral identification. However, it is not fullproof because different magnetic minerals, in principle, can have the same Curie temperature.

Magnetic domains: Any ferromagnetic material at a temperature below Curie temperature (T_c) is composed of small-volume regions known as domains, in which there is the mutual alignment of the magnetic moments in the same direction, as illustrated in Figure 1.1(A). Each domain is magnetized to its saturation magnetization, and adjacent domains are separated by domain walls, across which the direction of magnetization gradually changes (see Figure 1.1(B)).

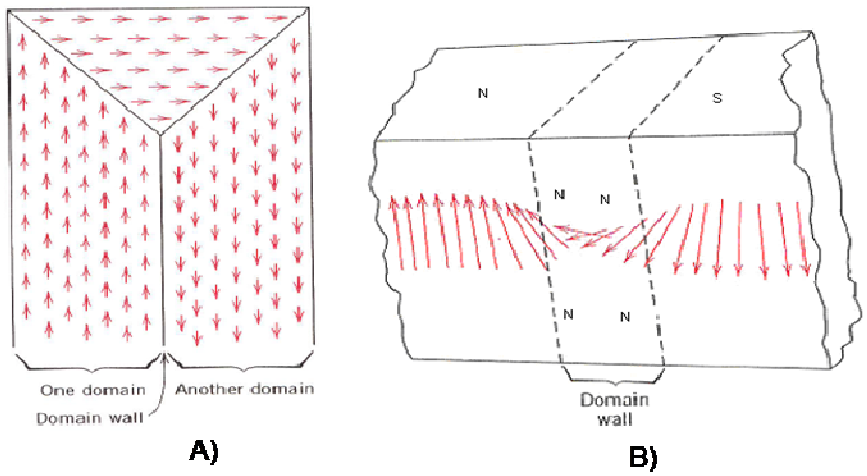

Figure 1.1 (A) Creation of domain and domain wall and (B) spin orientation rotation through domain (Bloch) wall.[4, 8]

Hysteresis: Ferromagnets can retain the memory of an applied field even after the field is removed. This behavior is called hysteresis, and a plot of the variation of magnetization with magnetic field is called a hysteresis loop. The hysteresis loop is a means of characterizing magnetic materials, and various parameters can be determined from it. Initially, the moments of the constituent domains are randomly oriented in such a way that there is no net *B (or M)* field. As shown in Figure 1.2, on the application of a field to an unmagnetized sample, the polarization increases initially by the growth of favorably oriented domains, which will be magnetized in the easy direction of the crystal. When the polarization can increase no further by the growth of domains, the direction of magnetization of the domains then rotates away from the easy axis to align with the field. When all of the domains have fully aligned with the applied field, saturation is reached, and the polarization can increase no further. The maximum value of *M* is called the saturation magnetization M_s, and the resultant *M*-*H* curve is called the initial magnetization curve. Starting from the saturation point (see Figure 1.2), when the *H* field is reduced, the curve does not retrace its original path. A hysteresis effect is produced in which the *M* field lags behind the applied *H* field or decreases at a lower rate. At zero *H* field, a residual *M* that is called the remanence or remanent magnetization M_r is retained, indicating that the material remains magnetized even in the absence of an external *H* field. The polarization will only decrease after a sufficiently high field is applied to: (1) nucleate and grow domains favorably oriented with respect to the applied field or (2) rotate the direction of magnetization of the domains towards the applied field. After applying a high enough reversal field, saturation polarization will be achieved in the negative direction. If the applied field is then decreased and again applied in the positive direction then the full hysteresis loop is plotted (Figure 1.2). The area contained within the loop indicates the amount of energy absorbed by the material during each cycle of the hysteresis loop. The reverse field required to bring the magnetic induction B of a specimen to zero is called the inductive coercivity (H_b) whereas the reverse field required to bring the magnetization M to zero is called the intrinsic coercivity (H_c). The remanence ratio M_r/M_s is generally used as measure of squareness of the *M*-*H* loop.

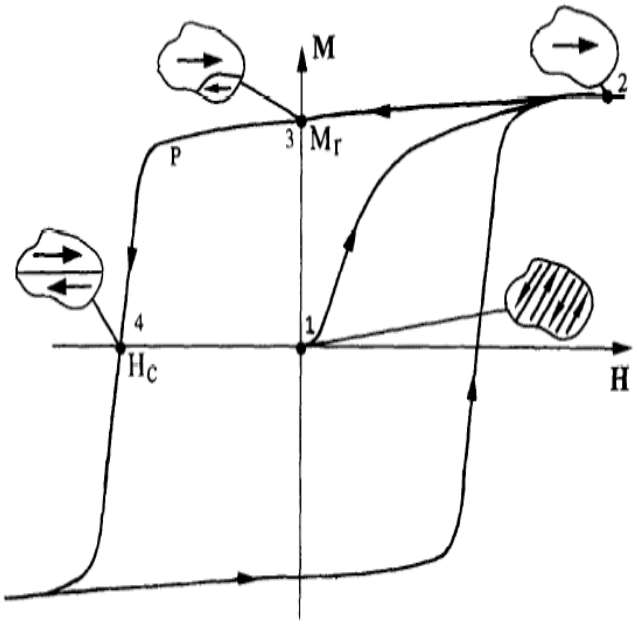

Figure 1.2 The magnetization curve and hysteresis loop of a permanent magnet showing the magnetic domain structure in the virgin state (1), at saturation (2), at remanence (3), and at the coercive field (4).[9]

1.3.1 Magnetic Anisotropy

In many situations, the susceptibility of a ferromagnetic material will depend on the direction in which it is measured. Such a situation is called magnetic anisotropy. When magnetic anisotropy exists, the total magnetization of a ferromagnetic M_s will prefer to lie along a special direction called the easy axis or crystal axis. In case of hexagonal close packed (HCP) or tetragonal crystal, the easy axis is usually the c-axis. Under an applied field, the magnetic moment deviates from the easy direction and returns to its original alignment with the removal of the field. The energy associated with this alignment is called the anisotropy energy and in its lowest order form is given by:[2, 8]

$$E_a = K\sin^2\theta, \tag{1.5}$$

where θ is the angle between M_s and the easy axis, and K is the anisotropy constant (units is ergs/cm^3). There are several causes of anisotropy, including those induced by stress and prior mechanical handling of materials. Two important and common sources of anisotropy, which are magneto crystalline anisotropy and shape anisotropy, are discussed next.

1.3.1.1 Magnetocrystalline Anisotropy

Only magnetocrystalline anisotropy, or simply crystal anisotropy, is intrinsic to the materials; all other anisotropies are induced. In crystal anisotropy, the ease of obtaining saturation magnetization is different for different crystallographic directions. The direction of easy magnetization of crystal is the direction of spontaneous domain magnetization in the demagnetized state. An example is a single crystal of cobalt as shown Figure 1.3.

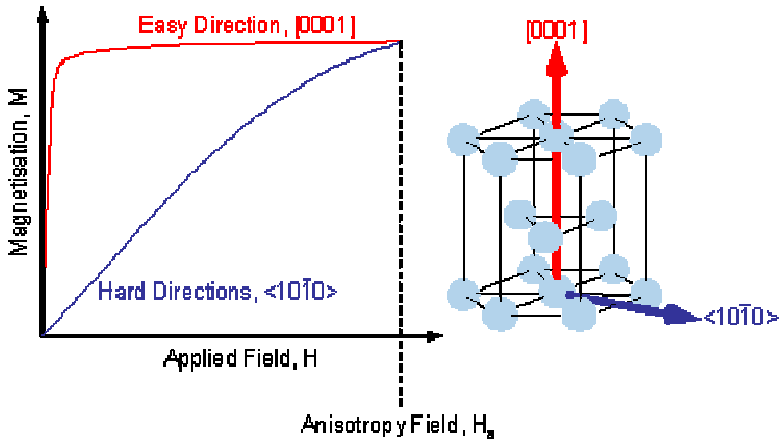

Figure 1.3 Directional dependence of saturation magnetization in Cobalt metal.[21]

1.3.1.2 Shape Anisotropy

It is easier to induce a magnetization along the long direction of a nonspherical piece of material than along a short direction. This is so because the demagnetizing field is less in the long direction, for the reason that the induced poles at the surface are farther apart. Thus, a smaller applied field will negate the internal, demagnetizing field. The shape anisotropy can be very important for nonspherical materials. The long axis of a specimen plays the same role as the easy axis of the crystal, and the shape anisotropy constant K_s is given by:

$$K_s = \tfrac{1}{2}(N_a - N_c)M^2. \qquad (1.6)$$

Magnetization is easy along the c-axis and equally hard along any axis normal to *c*. If *c* decreases until it equals *a*, the specimen becomes spherical ($N_a = N_c$, $K_s = 0$) and shape anisotropy disappears.[2, 8]

1.3.2 Coercivity Mechanism

There are various methods of increasing or decreasing the coercivity of magnetic materials, all of which involve controlling the magnetic domains within the material. For hard magnetic materials it is desirable that the domains cannot easily rotate their direction of magnetization and that the domain walls do not move easily and/or nucleation of reversal domains is difficult. To prevent the easy rotation of domains, the material could have strong uniaxial magnetocrystalline anisotropy. Alternately, shape anisotropy can occur in needle-like particles or grains, leading to magnetic hardening. In case of shape anisotropy, the magnetostatic energy is less when the magnetization is in the long axis of the needle compared to the short axis. If the size of a magnetic particle or grain decreases, then there is a critical size below which the decrease in magnetostatic energy splitting into two domains is less than the increase in energy due to the introduction of the domain wall. Particles that are below this critical size are known as single domain particles. If they have sufficiently high anisotropy to prevent the easy rotation of the direction of magnetization, then the particles will be permanently magnetic and it will be difficult to demagnetize them. Permanent magnets can also achieve their resistance to demagnetization by pinning of the domain walls and by making the new domain nucleation difficult. Nucleation controlled permanent magnets are easily magnetized, as the initial state has several domains in each crystal, but it is difficult to demagnetize such magnets because this would require the nucleation of new reversal domains. Magnetic materials are broadly classified into two main groups: soft and hard, depending on their hysteresis characteristics.[1-5, 8]

1.3.3 Soft Magnetic Materials and Their Applications[8]

Soft magnetic materials can be easily magnetized and demagnetized by low-strength magnetic field. When an applied field is removed, soft magnetic materials will return to a state of relatively low residual magnetization. Soft magnetic materials are used primarily to enhance or channel the flux produced by an electric current. The main parameter, which is often used as a figure of merit for soft magnetic materials, is the relative permeability, which is a measure of how readily the material responds to the applied magnetic field. The other main parameters of interest are the coercivity, the saturation

magnetization, and the electrical conductivity. As shown in Figure 1.4, typical soft materials have an intrinsic coercivity of less than 100 Oe and high saturation magnetization M_s but low M_r.

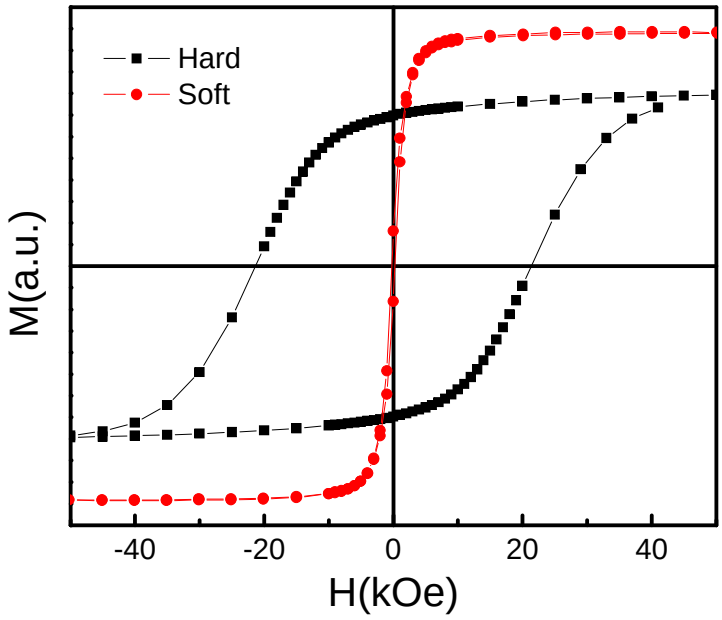

Figure 1.4 Typical *M-H* curves for soft and hard magnets.

The types of applications for soft magnetic materials fall into two main categories: DC and AC. In DC applications, the material is magnetized in order to perform an operation and then demagnetized on completion of the operation, e.g., an electromagnet on a crane at a scrap yard will be switched on to attract the scrap steel and then switched off to drop the steel. In AC applications the material will be continuously cycled from being magnetized in one direction to the other throughout the period of operation, e.g., a power supply transformer.

1.3.4 Hard Magnetic Materials and Their Applications

Hard magnets, also referred to as permanent magnets, are magnetic materials that can retain their magnetism after being magnetized. The term “hard” is used to describe materials that have sufficiently high resistance to demagnetizing field. Coercivity is therefore the key to distinguishing

between hard and soft phase magnetic materials. As shown in Figure 1.5 materials that have an intrinsic coercivity of greater than 1000 Oe and typically high remanece M_r are hard magnetic materials. Such material have high energy product $(BH)_{max}$, which is the figure of merit of hard magnet. Hard magnets are indispensable in modern life and their role in today's technology is growing increasingly. Some of the fields of applications of permanent magnetic materials are: Automotive, Telecommunications, Data Processing, Consumer Electronics, Electronics and Instrumentation, Industry, Aeronautics and Aerospace and Biosurgery.[8, 20]

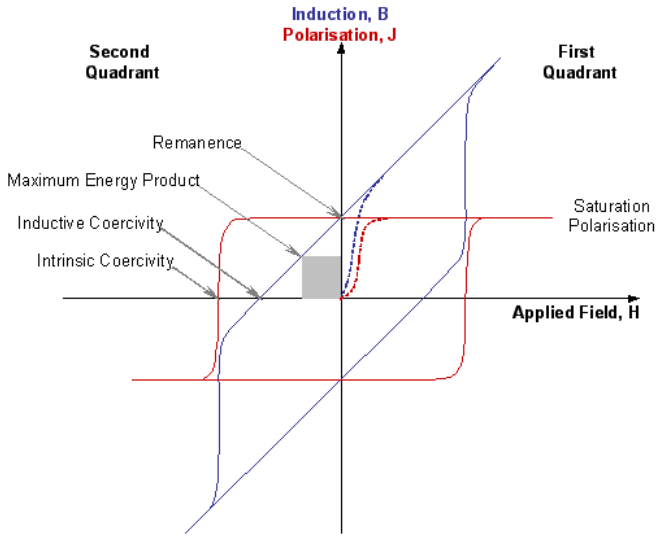

Figure 1.5 Typical *M-H* and *B-H* loops of ferromagnetic materials.[21]

Maximum Energy Product $(BH)_{max}$: In *B-H* loop, the maximum value of the product of *B* and *H* is called the maximum energy product, ($(BH)_{max}$) and is a measure of the maximum amount of useful work that can be performed by the magnet. $(BH)_{max}$ is used as a figure of merit for permanent magnet materials. Its unit is KJ/m^3 (MGOe). For a permanent magnetic material, the $(BH)_{max}$ is twice the maximum magnetostatic energy available from a magnet of optimal shape. The product tends to increase with both increasing coercive field H_c and saturation magnetization M_s. However, for materials with sufficiently high H_c values ($H_c > 2\pi M_s$), the theoretical limit for the energy product is limited only by M_s and is given by:[16]

$$(BH)_{max} \leq (2\pi M_s)^2. \quad (1.7)$$

The highest value of $(BH)_{max}$ of a material requires an ideal rectangular hysteresis loop. Several different types of permanent magnetic materials are now available including a variety of alloys, intermetallics, and ceramics. The most widely studied permanent magnetic materials are: Cobalt-rare earth alloys ($SmCo_5$, or Sm_2Co_{17}), neodymium-iron-boron ($Nd_2Fe_{14}B$), iron-platinum (FePt), cobalt-platinum (CoPt), hard ferrites ($SrO\text{-}Fe_2O_3$ or $BaO\text{-}6Fe_2O_3$), and Alnicos.

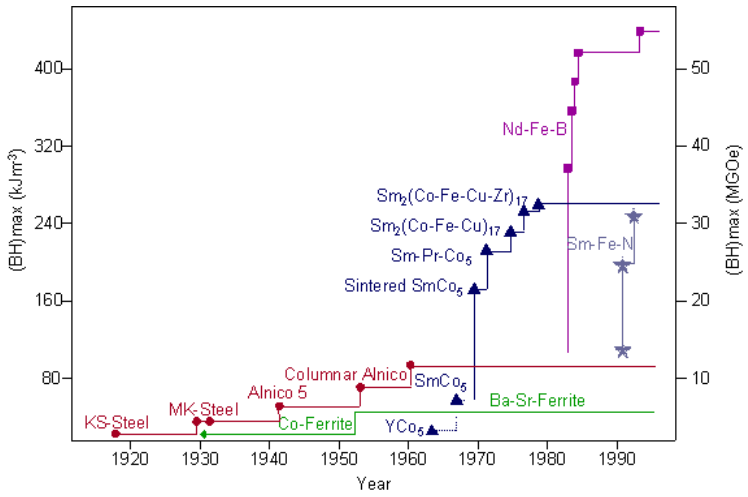

Figure 1.6 Progress in the energy product of permanent magnets in the 20th century.[21]

The 20th century has witnessed quite an extraordinary development in hard magnetic materials, where the coercivity and the maximum energy product have been significant enhanced in rare-earth-transition-metal permanent magnets. Figure 1.6 shows the development of energy products of these materials in the 20th century.[21]

1.3.5 Hard/Soft Nanocomposite Magnets

Driven by the limitation in equation (1.7)$(BH)_{max} \leq (2\pi M_s)^2$, research has focused on developing new high-anisotropy materials with high M_s and Curie temperature T_c. Thus, new hard-magnet compounds such as $SmCo_5$, Sm_2Co_{17}, and $Nd_2Fe_{14}B$ are made, increasing transition metal (TM) rich to enhance M_s. Unfortunately, these compounds still have magnetization values significantly lower than that

of Co, Fe, or $Fe_{65}Co_{35}$, which have $4\pi M_s$ values of 18, 21, and 24 kG, respectively.[16] In 1991, Kneller and Hawig[10] proposed an alternative approach to enhance the TM content to increase M_s by making a nanocomposite of exchange-coupled hard and soft magnetic phases. Such magnets are referred to as "exchange-spring" magnets and provide a new approach to increased $(BH)_{max}$. The hard phase provides the requisite magnetic anisotropy and stabilizes the exchange-coupled soft phase against demagnetization, and the soft phase provides the high magnetization (as shown in Figure 1.7).[13, 15, 19]

First, exchange-coupled nanocomposite was observed by Coehoorn *et al.*[14] in a melt-spun $Nd_{4.5}Fe_{77}B_{18.5}$ sample that, when annealed, consisted of a mixture of $Nd_2Fe_{14}B$, Fe_3B, and Fe phases. Skomski and Coey explored the theory of exchange-coupled films and predicted that a giant energy product of 120 MGOe might be attainable by exploiting the exchange-spring mechanism in oriented nanostructured magnets.[11, 17, 18] It has also been predicted that, for effective exchange coupling, the grain size of soft phase should not be larger than twice the domain-wall thickness of hard phase. Future applications of exchange-spring magnets will likely be based on a nanodispersed composite geometry obtained in bulk processing.[7, 12, 18]

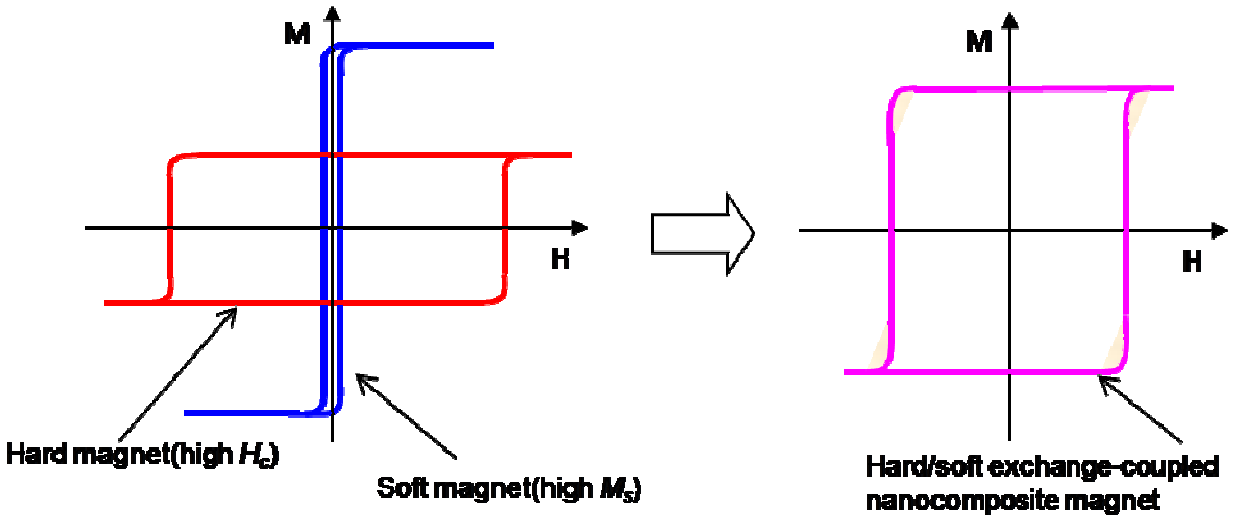

Figure 1.7 Hysteresis loops of soft, hard, and hard/soft nanocomposite magnets.

CHAPTER 2

SMALL PARTICLE MAGNETISM AND FABRICATION

2.1 Small Particle Magnetism

Magnetic nanoparticles exhibit a variety of unique magnetic phenomena that are drastically different from those of their bulk counterparts because of the high surface to volume ratio of the particle at nanometer scale. Magnetic properties of small ferromagnetic particles, such as coercivity and saturation magnetization, are mainly dominated by two key features: (1) a size limit below which the specimen cannot be broken into domains, and so it remains with single domain; and (2) the thermal energy in small particles, which decouples the magnetization from the particle itself to give rise to the phenomenon of superparamagnetism. These two key features are represented by two key sizes (on the length scale): the single domain size and the superparamagnetic size.[2, 8, 9]

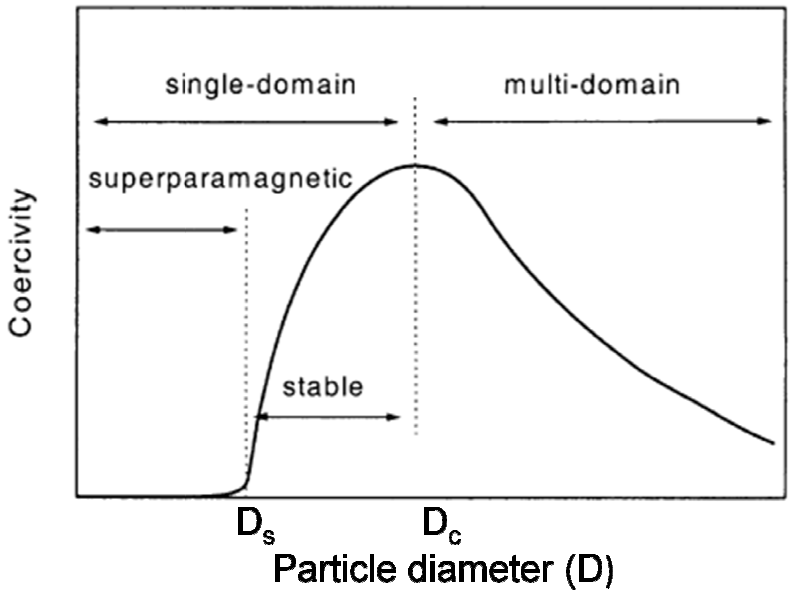

Figure 2.1 Variation of coercivity with particle diameter.[8]

2.1.1 Single-Domain Particles

The magnetostatic energy of a ferromagnet could be decreased by restructuring the material into domains. There is a limit to this because the formation of domains costs energy as a result of domain wall formation. Thus, in a large body there could be minimum domain size below which the energy cost of domain formation exceeds the benefits of decreasing the magnetostatic energy. When the size of the particles decreases to a critical particle diameter, the formation of domain walls is energetically less favorable, and the particles have only a single domain. Magnetization reversal in single-domain particle occurs via spin rotation, since there are no domain walls to move. Single-domain particles consequently have a larger coercivity compared to multidomain system as it is harder to rotate the magnetization than to move a domain wall.[2, 8, 9]

In this single-domain regime, the magnetic coercivity increases as the size of the nanoparticle increases with the relationship:

$$Hc = 2K/m_s[1- 5(kT/KV)^{1/2}], \quad (2.1)$$

where m_s is the saturation magnetization[33] Above the critical size ($D > D_c$), multidomain magnetism begins in which a smaller reversal magnetic field is required to make the net magnetization zero. Saturation magnetization of nanoparticles is also strongly dependent on their size. Magnetic materials intrinsically possess magnetically disordered spin glass like layers near the surface due to the reduced spin–spin exchange coupling energy at the surface.[34,35] In bulk cases, since the disordered surface layer is minimal compared to the total volume of the magnet, such surface spin canting effects are negligible. Upon reduction of the size of magnetic materials to the nanoscale regime, however, the surface canting effects are dramatically pronounced in the saturation magnetization value (m_s), described as:

$$m_s = M_S[(r - d)/r]^3, \quad (2.2)$$

where r is the size, M_S is the saturation magnetization of bulk materials, and d is the thickness of disordered surface layer.[34] For very small nanoparticles (less than ~5 nm) such size effect on m_s is more noticeable, since internal spins of the nanoparticle also start to be canted as do the surface spins because of increased interactions between the surface and internal spins.[34]

2.2.2 Superparamagnetism

Superparamagnetism is a phenomenon where magnetic materials exhibit a behavior similar to paramagnetism at temperatures below the Curie or the Neel temperature. Superparamagnetism occurs when the material is composed of very small crystallites (1-20 nm). In this case even though the temperature is below the Curie or Neel temperature, the thermal energy is sufficient to overcome the coupling forces between neighboring atoms, and to change the direction of magnetization of the entire crystallite. The resulting fluctuations in the direction of magnetization cause the magnetic field to have an average of zero. The material behaves in a manner similar to paramagnetism, except that instead of each individual atom being independently influenced by an external magnetic field, the magnetic moment of the entire crystallite tends to align with the magnetic field. The energy required to change the direction of magnetization of a crystallite is called the crystalline anisotropy energy (*KV*) and depends both on the materials properties and the crystallite size. As the crystallite size decreases, so does the crystalline anisotropy energy, resulting in a decrease in the temperature at which the material becomes superparamagnetic.[2,8,9] A typical hysteresis loop of superparamgnetic nanoparticles is shown in Figure 2.2 with H_c =0 and M_r/M_s =0.

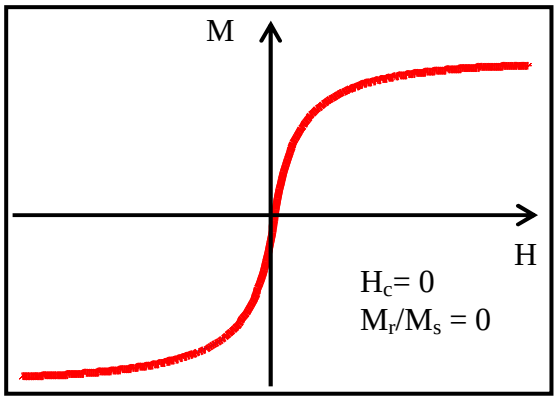

Figure 2.2 A typical hysteresis loop for superparamagnetic particles.

The phenomenon of superparamagnetism is timescale-dependent due to the stochastic (random variable) nature of the thermal energy. The time scale for a successful jump can be calculated by:[2]

$$\tau = \tau_o \, e^{-KV/kBT}, \tag{2.3}$$

where the attempt timescale (τ_o) is about 10^{-9} s, and V is the volume of particle. This equation (2.3) describes the time scale over which the moment of particles ($\mu_p = M_s V$) attampts to jump the anisotropy energy (KV) barrier.

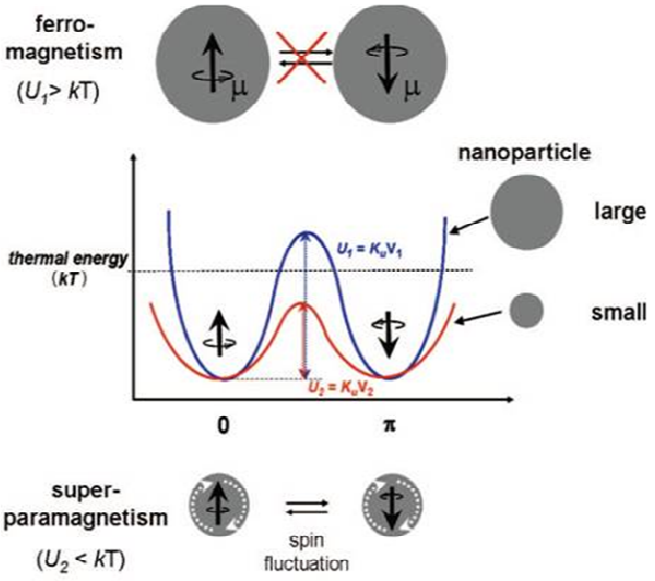

Figure 2.3 Energy diagram of magnetic nanoparticles with different magnetic spin alignment, showing ferromagnetism in a large particle (top) and superparamagentism in a small nanoparticle (bottom).[32]

Typical experiments with a magnetometer take 10 to 100 s; if M_s reversed at times shorter than the experimental time scale, the system appears superparamagnetic. Using τ = 100 s and $\tau_o = 10^{-9}$ s, we can obtain the critical volume from equation (2.4): [2]

$$V_{sp} = \frac{25 k_B T}{K} \, . \tag{2.4}$$

A particle with a volume smaller than this quantity acts superparamagnetically on the 100 s experimental timescale. Equation (2.4) can be rearranged to yield:

$$T_B = \frac{KV}{25k_B} \ . \tag{2.5}$$

T_B is called the blocking temperature; below T_B, the free movement of the moment of particles ($\mu_p = M_s V$) is blocked by the anisotropy; above T_B, $k_B T$ kicks the moment loose so that the system appears superparamagnetic.

Blocking temperature (T_B) which is characteristic for ferromagnetic to superparamagnetic transition can be ascertained in nanoparticles by measuring the zero field cooling (ZFC) and field cooling (FC) magnetization temperature as shown in Figure 2.4. As the particles cool in a zero applied field, they will tend to magnetize along preferred crystal directions in the lattice, thus minimizing the magneto-crystalline energy. Since the orientation of each crystallite varies, the net moment of the system will be zero. Even when a small external field is applied, the moments will remain locked in the preferred crystal directions, as is seen in the low temperature portion of the ZFC curve. As temperature increases, more thermal energy is available to disturb the system. Therefore, more moments will align with the external field direction in order to minimize the Zeeman energy term. In other words, thermal vibration is providing the activation energy required for the Zeeman interaction. Eventually, the net moment of the system reaches a maximum where the greatest population of moments has aligned with the external field. The peak temperature is called the blocking temperature (T_B) which depends on particle volume. As temperature rises above T_B, thermal vibrations become strong enough to overcome the Zeeman interaction and thus randomize the moments.

Field cooled (FC) measurements proceed in a similar manner to ZFC, except that the constant external field is applied while cooling and heating. The net moment is usually measured while heating, however. The FC curve will diverge from the ZFC curve at a point near the blocking temperature as seen in Figure 2.4. This divergence occurs because the spins from each particle will tend to align with the easy crystalline axis that is closest to the applied field direction, and will remain frozen in that direction at low temperature.

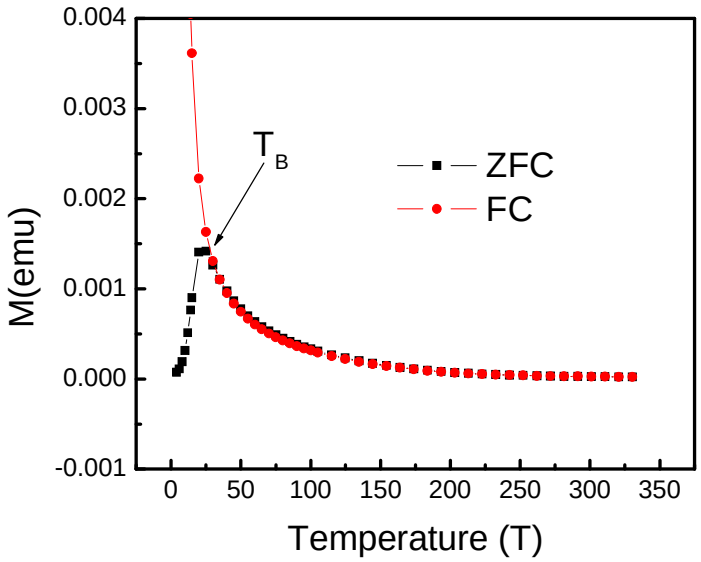

Figure 2.4 Typical ZFC and FC curves showing the blocking temperature of nanoparticles.

In the case of high-K_μ magnetic materials such as FePt, $SmCo_5$, and CoPt, etc., in order to maintain the thermal stability of the sigle-domain nanoparticles, this ratio should satisfy:[22-24]

$$\frac{K_\mu V}{k_B T} \geq 60 . \tag{2.6}$$

We can estimate therefore, the superparamagnetic size limit D_s by assuming the cubic shape of grains:[25]

$$D_s = \left(\frac{60 \cdot k_B T}{K_\mu} \right)^{\frac{1}{3}} . \tag{2.7}$$

As for FePt nanoparticles, taking K_μ = 6.6~10×10^7 erg/cm^3, T = 300 K and k_BT = 3.77×10^{-14} erg, the superparamagnetic size limit D_s is 2.8~3 nm at room temperature.[25-27] This theoretical superparamagnetic size limit also predicts that FePt nanoparticles below a critical size limit cannot convert to hard magnetic phase.[25] This transition size limit has been proved theoretically and experimentally to be well matched with the range of the superparamagnetic size limit.[28-31]

2.1.3 Magnetic Viscosity

The thermal activation leads to time and temperature dependent coercivity and magnetization that is known as magnetic viscosity. Magnetic viscosity of particles is determined by keeping the external field *H* constant and monitoring the magnetization as a function of time. It is caused by the thermal activation of magnetization reversals over activation energy barriers ΔE. For an ensemble of magnetizations in metastable states with identical ΔE, the relaxation time τ is related to an absolute temperature *T* by the Arrhenius-Neel law:[36]

$$\tau = \tau_o \, e^{\Delta E / K_B T}, \tag{2.8}$$

where τ_0 is a characteristic time constant, which is of the order of $10^{-10} \sim 10^{-12}$. However, for most materials with a broad and slowly varying distribution of ΔE, the time dependence of magnetization is well described by the relation:[37]

$$M(H; t) = M_0(H) - S(H) \ln(t + t_0), \tag{2.9}$$

where *S* is the magnetic viscosity coefficient, and M_0 and t_0 are fitting constants. According to Equation (2.9), the magnetic viscosity coefficient $S(H)$ can be obtained by fitting the time dependence of magnetization.

2.2 Applications of Magnetic Nanoparticles[8]

Nanoparticles exhibit unique mechanical, optical, electronic, magnetic and chemical properties that are drastically different from those of their bulk counterparts.[24, 25, 38] These novel properties arise from the large fraction of atoms that lies on the surface of the particles and from the finite number of the atoms within each particle. Magnetic nanoparticles are of special interest, owing to their unique magnetic properties as a result of their reduced size (< 100 nm). There are a number of potential technological applications form magnetic nanoparticles. We will discuss here some of the differerent forms of the potential applications of nanoparticles, such as surface functionalized particles in biomedical applications, as particle arrays in magnetic storage media, as compacted powders in permanent magnets and in solutions as ferrofluids. [39-52]

2.2.1 Magnetic Recording Media

Synthesis and assembly of magnetic nanoparticles have attracted great attention because of their potential application in ultra-high-density magnetic recording.[45] Continued increases in the areal density of hard disk drives will be limited by thin-film media in which each bit of information is stored over hundreds of grains. Self-assembled nanoparticle media and patterned media in which data are stored in an array of single-domain magnetic particle have been suggested as a means to overcome this limitation and to enable recording density up to 1 Tbit inch^{-2}.[46] In such ultra-high-density media, small material grain and a narrow size distribution are required because of high recording density. To obtain both a high signal-to-noise ratio and thermal stability of the media, isolated, noninteracting, or very weekly interacting nanoparticles with very high magnetic anisotropy energy K_u are required.[47] Extensive researche is being done on $CoFe_2O_4$ and FePt nanoparticles for high-density recording media.[47,49] $CoFe_2O_4$ nanoparticle is a well-known material with a very high cubic magnetocrystalline anisotropy, good coercivity, and moderate saturation magnetization.[49-51] These properties make $CoFe_2O_4$ nanoparticles a promising material for high-density magnetic recording devices. FePt $L1_0$ nanoparticles are one of the best candidates for ultra-high-density recording media because of their very high magnetocrystalline anisotropy (K_u is 10^8 erg/cm^3), which is much higher than those of the currently used CoCr-based alloys.[47] This large crystalline anisotropy allows for thermally stable grain diameters down to 2.8 nm.[53] However, the as-synthesized FePt nanoparticles are superparamagnetic and have the face-centered cubic (fcc) structure. These particles have to be annealed at temperature as high as 580 ^oC in ordere to produce face-centered tetragonal (fct) structure and retain magnetic orientation to be useful for recording. The post-annealing leads to poor control over the arrangement of nanoparticles due to extensive particle aggregation, which also makes magnetic easy axes alignment difficult, limiting their technological applications.[45] Recently, our group, Liu et al.[54] have made a break-through by successfully preparing monodisperse FePt fct nanoparticles with high coercivity, which make possible the direct application of fully converted fct FePt nanoparticles in high density magnetic media.

2.2.2 Exchange-Coupled Nanocomposite Magnets

Exchange-coupled nanocomposite magnets consist of a uniform mixture of exchange coupled magnetically hard and soft phases.[12,17-19] This type of magnet is promising for advanced permanent magnetic applications, as high energy products $(BH)_{max}$ and relatively high coercivities can be developed in these nanocomposite magnets. A small grain size (less than 20 nm) and a uniform mixture of the hard and soft phases are required for effective exchange coupling between the hard and the soft phases. Zeng *et al.* demonstrated in 2002 that exchange-coupled nanocomposite magnet such as FePt-Fe_3Pt can be made using monodisperse nanoparticles of FePt and Fe_3O_4 as precursors by self assembly technique.[12] In the exchange-coupled isotropic FePt-Fe_3Pt nanocomposite, the energy product of 20.1 MGOe was achieved, which is 50% higher than that expected theoretically from a single phase, nonexchange-coupled isotropic FePt.

Recently, the same group prepared an exchange-coupled bimagnetic core/shell nanoparticles system with a ferromagnetic FePt core and a ferrimagnetic MFe_2O_4 (M=Fe, Co) shell.[55] The advantage of this system is that the magnetic properties such as magnetization and coercivity can be controlled by tuning the core/shell dimensions and by tuning the material parameters of both core and shell. This system shows great promise for achieving potential high-energy products in exchange-coupled nanocomposite magnets. An anisotropic nanocomposite magnet with both the hard and soft phases aligned is expected to show a much higher energy product than the isotropic one.[10, 13] However, controlling the morphology including grain size and grain alignment, in nanocomposite magnet remains a great challenge.[42]

2.2.3 Biomedical Applications

Magnetic nanoparticles have been proposed for biomedical applications for several years.[40, 52] In recent years, nanotechnology has developed to a stage that makes it possible to produce, characterize, and specifically tailor the functional properties of nanoparticles to applications. This shows considerable promise for applications in biomedical and diagnostic fields, such as targeted drug delivery, hyperthermic treatment for malignant cells, and magnetic resonance imaging (MRI).[38, 40-42, 52] There are three reasons why magnetic nanoparticles are useful in biomedical applications. First, the size of magnetic

nanoparticles can be controlled, ranging from a few nanometers up to tens of nanometers and are thus smaller in size than a cell (10-100µm), a virus (20-450 nm), a protein (5 -50 nm) or a gene (2nm wide and 10 - 100 nm long). Magnetic nanoparticles can get close to cells and genes, and they can be coated with biomoleclues to make them interact or bind with biological entities. Second, magnetic nanoparticles can be manipulated by an external magnetic field gradient. Magnetic nanoparticles can be used to deliver a package, such as an anticancer drug, to a targeted region of the body such as a tumor. Third, magnetic nanoparticles can also be made to respond resonantly to a time-varying magnetic field, with an associated transfer of energy from the field to the nanoparticles. Magnetic nanoparticles can be made to heat up, which leads to their use as hyperthermia agents, delivering toxic amounts of thermal energy to targeted bodies such as tumors or as chemotherapy.[40-42,52] For biomedical applications, magnetic nanoparticles must (1) have a good thermal stability; (2) have a larger magnetic moment; (3) be biocompatible; (4) be able to form stable dispersion so the particles could be transported in living system; and (5) response well to AC magnetic fields. Furthermore, better control of particle size and properties will be necessary to use these particles in biomedical applications, in which uniformity of the properties will ensure accurate doses and delivery.[52] The widely used magnetic nanoparticles for biomedical applications are magnetite (Fe_3O_4) and related oxides, which are chemically stable, nontoxic, non-carcinogenic, and have attractive magnetic properties.[44]

2.2.4 Ferrofluids

A ferrofluid is a special solution of magnetic nanoparticles in a colloidal suspension whose flow can be controlled by magnets or magnetic fields.[56] Particles are coated with a surfactant that disperses the particles and prevents agglomeration by overcoming the van der Waals forces that exist between the particles.[44] As a result, when such a fluid is not in the presence of external magnetic field, it has zero net magnetization. When a strong magnet is brought close to the ferrofluid, several spikes will appear as the fluid arranges itself along the magnetic field lines of the magnet. When the field is removed, the particles again disperse, randomizing their orientation and establishing no net magnetization.[45, 57] These unique properties allow ferrofluids to have applications in numerous fields of technology. The most common application of ferrofluids is the cooling of loudspeakers. The ohmic heat produced in the voice coil can be

transmitted to the outer structure by the fluid which increases the cooling by a factor 3 approximately. In sealing technology, a drop of ferrofluid is put into the gap between a magnet and a highly permeable rotating shaft. In the small gap, a strong magnetic field fixes the ferrofluid, and pressure differences about 1 bar can be sealed without serious difficulties.[57] Some of the other technological applications of ferrofluids includes their being used as bearings, dampers, stepping motors, and sensors.[31, 38, 56, 57]

2.3 Fabrication Techniques of Nanoparticles

The fabrication of discrete nanoparticles can be accomplished through “bottom-up” or “top-down” methods. In a bottom-up approach, small building blocks such as atoms and clusters are assembled into nanoparticles; examples of this approach include chemical synthesis, laser-induced assembly, and colloidal aggregation.[58-70] In the top-down approach, large objects are broken down to finer particles, e.g., mechanical milling.[71, 72]

Various synthesis strategies for the preparation of magnetic nanoparticles have been investigated, including chemical co-precipitation,[50, 61] sonochemical reactions,[68, 73] sol-gel, [64, 65] micelle microemulsion,[66] hydrothermal[74] and ball milling.[71, 72] Compared to other methods, chemical routes have often been found to be the better methods for the production of high-quality nanoparticles for chemically stable materials. Here we discuss two fabrication techniques, i.e., chemical methods and ball milling both of which have been employed for the preparation of nanoparticles in this study.

2.3.1 Chemical Synthesis: Concepts and Mechanism [38]

The synthesis of nanoparticles in a solution occurs, which chemical reactions form stable nuclei with subsequent particle growth. Upon the addition of precipitating, reducing, or oxidizing reagents to the solution containing the reactants, chemical reactions occur, and the solution becomes supersaturated with products. The thermodynamic equilibrium state of the system is restored by the condensation of the nuclei of the reaction product. Kinetic factors compete with the thermodynamics of the system in a growth process. Such kinetic factors as the reaction rates, the transport rates of reactants, accommodation, removal, and redistribution of matter compete with the influence of the thermodynamic process in the particles growth. Particle morphology is influenced by factors such as supersaturation, nucleation and growth rate, colloidal stability, recrystalization, and the aging process. When the nuclei are formed nearly

at the same time in a supersaturated solution, subsequent growth of these nuclei results in the formation of particles with a very narrow size distribution. To maintain a narrow size distribution, it is very important to prevent agglomeration, Ostwald ripening, and continued nuclei formation.

Nanoparticles possess large surface areas and often form agglomerates as a result of attractive van der Waals forces and the tendency of the system to minimize the total surface or interfacial energy. Agglomeration of particles can occur during any of the following stages: synthesis, drying, handling, and processing. In many applications and processes where dispersed particles or stabilized dispersions are required, undesirable agglomeration in each step of synthesis and processing must be prevented. Surfactant is any substance that lowers the surface or interfacial tension of the medium in which it is dissolved. Surfactants are used during the synthesis of the nanoparticles in order to reduce interparticle interaction through an increase in repulsive forces. Surfactants are also used to control particle size and distribution in most chemical synthesis routes.

2.3.2 Ball Milling Techniques and Mechanisms

Ball milling has been successful to produce a large range of nanoscaled materials, including nanocrystaline structure, nanoparticles, and nanocomposites.[75] Ball milling techniques use mechanical energy to crush powder or to activate chemical reaction and structural changes, which includes disordering, amorphization and compositional changes. Whenever two balls collide with or a ball collides with a wall of vial, some amount of powder is trapped in between them. The force of the impact plastically deforms the powder particles, leading to work hardening and facture. Typically, in dry ball-milling the new surface created enables the particles to weld together, and this leads to an increase in particle size. The process involves repeated flattening, cold welding, fracturing, and the re-welding of powder particles in a controlled atmosphere (usually an inert medium). In wet-milling, cold welding and the re-welding of particles can be prevented by using surfactants along with milling media during milling. During the milling process, as soon as fresh surfaces or particles are formed, surfactants are absorbed on to the surface of the particles by the formation of the chemical bonds, which prevents agglomeration of the nanoparticles. This greatly reduces cold welding and the re-welding of crushed particles, which finally leads to finer particle sizes.

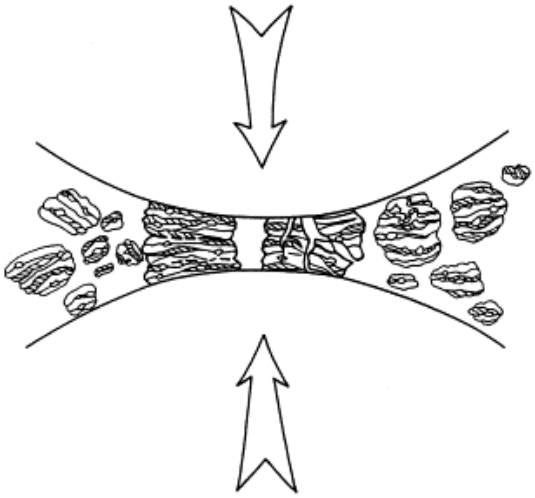

Figure 2.5 Ball-powder-ball collision of powder during milling.[75]

Ball milling is a complex process that involves the optimization of a number of variables to achieve the desired product phase or structure.[75] Some of the important parameters that have an effect on the final constitution of the powder are: (1) the type of mill, (2) the milling container, (3) milling speed, (4) milling time, (5) the type, size, and size distribution of the grinding medium (balls), (6) the ball to powder ratio, (7) the extent to which the vial is filled, (8) the milling atmosphere (9) the process control agent (milling media) and (10) the temperature of milling.

Two different types of milling equipment were used for preparing the nanoparticles in this study: i) Spex 8000M Shaker Mill (High-energy mill): The milling container containing the sample and the balls is secured in the clamp of the miller and is swung energetically back and forth several thousand times a minute. The back and forth shaking action is combined with lateral movements of the ends of the vial, and the vial appears to be describing a figure 8 as it moves. Because of the amplitude (about 5 cm) and speed (about 1200 rpm) of the clamp motion, the ball velocities are high (on the order of 5 m/s) and consequently the force of the balls impact is unusually great. These mills are therefore classified as high-energy mills.[75]

Figure 2.6 Spex 8000M Shaker mill and milling container along with balls.

ii) Roll mill (Low energy mill): The container is typically rotated at low speeds of 70 to 300 rpm. In this horizontal rotation type mill, the milling action results from : (1) the grinding balls runing down the inside wall of the vial which leads to friction effects, and (2) balls lifting off and traveling freely through the inner chamber of the vial and then falling on to the powder which leads to impact effects. The rotating speed of the vial must be just below the critical speed that would pin the balls to the internal wall of the mill, and thus the impact frequency is generally low.

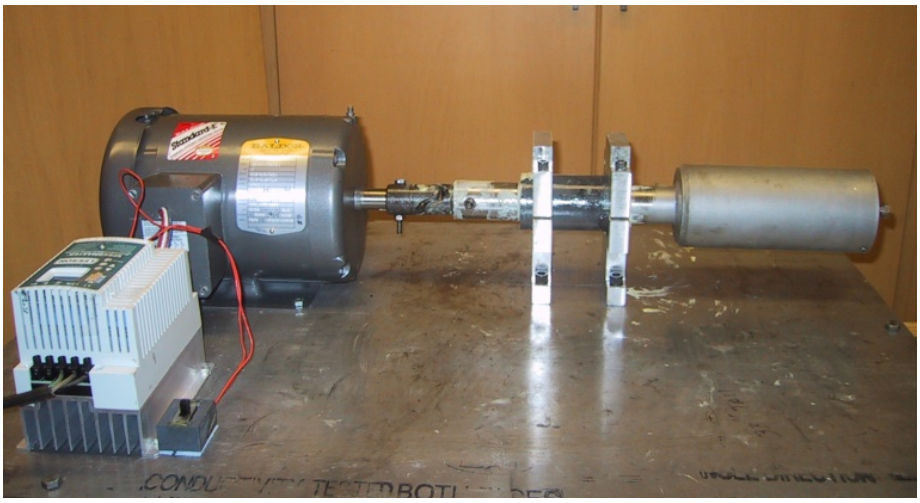

Figure 2.7 Roll-milling set up with milling container.

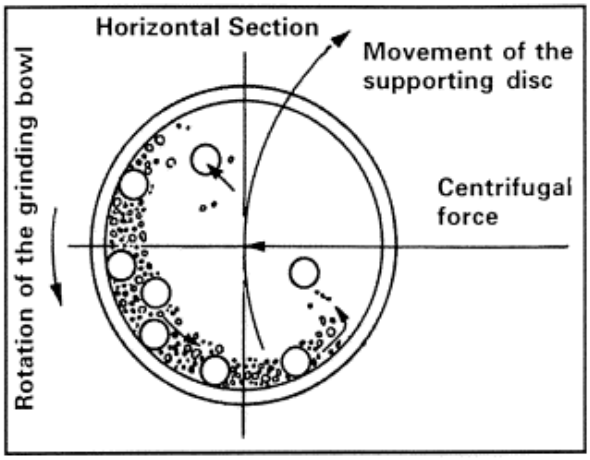

Figure 2.8 Schematic showing the motion of the balls.[75]

CHAPTER 3

FABRICATION OF MAGNETIC NANOPARTICLES

This chapter explains the experimental techniques that have been used and developed based on knowledge and the experience gained from our experiments. Fabrication of magnetic nanoparticles was accomplished through both bottom-up and top-down methods. FePt, $CoFe_2O_4$, $NiFe_2O_4$ and FeCo nanoparticles were synthesized by chemical solution phase (bottom-up), while Sm-Co and Nd-Fe-B based particles were synthesized by ball milling techniques (top-down approach).

3.1 Chemical Synthesis of Nanoparticles

Solution phase chemistry synthesis has been seen as one of the most promising approaches for the preparation of monodisperse magnetic nanoparticles. Magnetic nanoparticles with various sizes and shapes can be prepared by this technique as it can offer an important homogeneous nucleation and facilitates the controlled growth of the nuclei in the solution. In this study, chemical synthesis of nanoparticles was done by standard airless technique in a nitrogen or argon atmosphere. FePt, $CoFe_2O_4$, and $NiFe_2O_4$ nanoparticles with different size and shapes were synthesized by solution phase chemistry.

All the chemicals and reagents used in the experiments are commercially available. Phenyl ether (99%), benzyl ether (99%), octyl ether (99%) 1,2-hexadecanediol (97%), oleic acid (90%), oleylamine (>70%), cobalt(II)acetylacetonate ($Co(acac)_2$), iron(III) acetylacetonate ($Fe(acac)_3$), platinum acetylacetonate (II) ($Pt(acac)_2$), nickel acetylacetonate(II) ($Ni(acac)_2$), and iron pentacarbonyl ($Fe(CO)_5$) were purchased from Sigma-Aldrich Chemical Corporation. The ethanol 200% proof, and heptane, hexane, octane, and acetone used were of 99.8% purity. The reagents obtained from commercial sources were used without further purification.

3.1.1 Synthesis of FePt Nanoparticles

Synthesis of FePt nanoparticles was done by standard airless technique in a nitrogen or argon atmosphere. FePt nanoparticles of size 2 nm were synthesized by chemical reduction of $Pt(acac)_2$ and $Fe(acac)_3$ by 1,2-hexadecanediol at high temperature in solution phase.[76,77] FePt nanoparticles bigger than 3 nm were synthesized by simultaneous chemical reduction of $Pt(acac)_2$ and decomposition of $Fe(CO)_5$ at high temperature in solution phase.[77-80] Particle diameter was tuned from 2 nm to 15 nm by varying reaction parameters.

Synthesis of 2 nm FePt Nanoparticles: The synthesis process of 2 nm FePt nanoparticles involves the simultaneous chemical reduction of $Pt(acac)_2$ and $Fe(acac)_3$ by 1,2-hexadecanediol at high temperature in solution phase. A mixture of 0.5 mmol of $Pt(acac)_2$, 0.5 mmol to 2 mmol of $Fe(acac)_3$, and a corresponding amount of 1,2-hexadecanediol was added to a 125 mL European flask containing magnetic stir bar. 30 mL of Octyl ether was then transferred into the flask and the contents stirred while purging with Ar for 20 minutes at room temperature. The flask was then heated to 100^oC and held at 100^oC for 20 minutes. During this hold, 0.05 mmol (0.17 mL) of oleyl amine and 0.05 mmol (0.16 mL) of oleic acid were injected into the flask while continuing the Ar purge. After that hold, the mixture was maintained under an Ar blanket and heated to 295^oC at a rate of approximately 7^oC per minutes. The mixture was maintained at the refluxing temperature of 295^oC for 30 minutes before cooling down to room temperature under the Ar blanket. Afterward, all handling was performed in air.

Synthesis of 3 ≥ nm FePt Nanoparticles: The FePt nanoparticles bigger than 3 nm were synthesized by the simultaneous chemical reduction of $Pt(acac)_2$ and decomposition of $Fe(CO)_5$ at high temperature in solution phase.[77-80] In a typical procedure, 0.5 mmol of $Pt(acac)_2$ and 10 ml of octyl ether were added to a 125 ml flask with a magnetic stir bar. After purging argon gas for 20 minutes, the flask was heated up to 110 ºC for 10 minutes. After the Pt precursor dissolved completely at 110ºC, 0.5 mmol of oleic acid and oleylamine were added into the flask followed by 0.5 mmol of $Fe(CO)_5$. The flask was then heated up to 300ºC and refluxed for 1 hour. After $Fe(CO)_5$ was added, the color of the solution changed from transparent yellow to black, which suggests the formation of FePt nanoparticles. After the reflux, the flask was cooled down to room temperature under flow of Argon gas. Afterwards, all handling

was performed in air. The as-synthesized black product was washed using a mixture of ethanol and hexane and was separated by centrifugation.

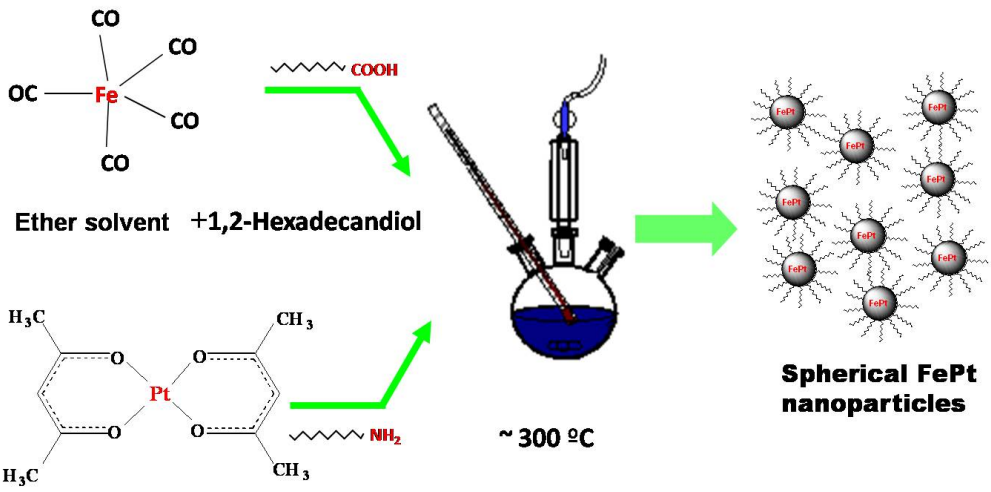

Figure 3.1 Typical polyol synthesis route for FePt nanoparticles.

Size and Composition Control of FePt Nanoparticles: The size of FePt nanoparticles was controlled by varying the surfactant/Pt precursor molar ratio. Surfactants typically play an important role in tuning the particle size.[76-82] Increasing the surfactants to $Pt(acac)_2$ molar ratio from 1.0 to 8.0, the particle size increased from 3 to 9 nm. Particle size can be changed with 1 nm accuracy by controlling the amount of surfactants. The change in size of nanoparticles can be expressed by the number of nuclei at the first step of particle formation. The increase of amount of surfactants results in the formation of stable nuclei, which suppresses the nucleation rate but increases the growth rate.[77-79] To make 15 nm Pt@Fe3O4 core-shell particles, 10 nm Pt cores were first synthesized by the addition of a Pt precursor at 290℃ in a mixture of octyl ether and surfactants and then they were coated with iron.[80] Final composition of FePt nanoparticles can be tuned by adjusting the initial precursor ratio of Fe and Pt in the synthesis.

3.1.2 Synthesis of FePt Nanorods and Nanowires

FePt nanorods and nanowires were synthesized by the simultaneous reduction of $Pt(acac)_2$ and $Fe(CO)_5$ in the presence of 1,2-hexadecanediol, oleyl amine, and oleic acid in a high-boiling ether solvent.[81] In a typical synthesis of FePt nanowires, a mixture of 0.25 mmol of $Pt(acac)_2$ and 100 mg of

1,2- hexadecanediol was added to a 125 mL European flask containing a magnetic stir bar. 2 mL of dioctyl ether and 6 mL of oleyl amine were then transferred into the flask, and the contents were stirred while purging with N_2 for 20 minutes at room temperature. The flask was then heated to 100 ^oC and the temperature was held for 20 min. During this time, 0.05 mmol of $Fe(CO)_5$ was injected into the flask while the N_2 purging continued. After 20 minutes, 3 mL of oleic acid was injected, and the mixture was maintained under N_2 blanket and heated to 295 ^oC at a rate of 1.5^oC per minute. The flask was maintained at the refluxing temperature of 295^oC for 30 minutes before cooling down to room temperature under the N_2 blanket. The FePt nanowires of length 150 nm were re-dispersed in hexane and stored under refrigeration. The length of FePt nanorods/nanowires can be controlled from 15 nm to over 150 nm by varying the molar concentration of 1,2- hexadecondiol(HDD) and oleic acid while keeping other parameters constant. For example, FePt nanowires with lengths of over 150 nm were formed when 100 mg of HDD and 3 mL of oleic acid were used. When 200 and 400 mg of HDD was taken with 6 mL of oleic acid, the length of the wires were reduced to 50 nm and 15 nm, respectively. A further increase of HDD and oleic acid led to the formation of spherical particles of diameter of 3 nm.

3.1.3 Shape Control Synthesis of FePt Nanocrystals

The synthesis was carried out using standard airless techniques in a nitrogen atmosphere. FePt nanocrystals were grown by the simultaneous reduction of $Pt(acac)_2$ and the thermal decomposition of $Fe(CO)_5$ in the presence of 1,2-hexadecanediol, oleyl amine, and oleic acid. The reaction was carried out using oleylamine and oleic acid as both the solvents and the surfactants. We have established a new method for controlling the shape of FePt nanocrystals by controlling the reaction kinetics, the molar ratio of the surfactants, the addition sequence of surfactants, and the reaction temperatures.[82]

A typical recipe for the synthesis of FePt nanowires involves a mixture of 0.25 mmol $Pt(acac)_2$ and 100 mg of 1,2- hexadecanediol was added to a 125 mL European flask containing a magnetic stir bar. 10 mL of oleylamine was then injected into the flask, and the contents were stirred while purging with N_2 for 20 minutes at room temperature. The flask was then heated to 100 ^oC and the temperature was held for 20 minutes. During this time, 0.05 mmol of $Fe(CO)_5$ was injected into the flask while N_2 purging continued. Next, 2 mL of oleic acid was injected and the mixture was maintained under N_2 blanket and

heated to 300 ^{o}C at a rate of 1.5 ^{o}C per minute. The mixture was maintained at the refluxing temperature of 300 ^{o}C for 30 min before cooling down to room temperature under the N_2 blanket. Afterwards, all handling was performed in air. The as-synthesized black product was washed using a mixture of ethanol and hexane and was separated by centrifugation. The length of FePt nanorods/nanowires can be controlled from 20 nm to over 150 nm by varying the molar concentration of 1, 2- hexadecondiol (HDD) and oleic acid while keeping other parameters constant. For example, FePt nanowires with lengths over 150 nm were formed when 100 mg of HDD and 2 mL of oleic acid were used. While 300 mg of HDD was taken with 2 mL of oleic acid, the length of the wires was reduced to 20 nm. The diameter of the FePt nanorods can also be tuned from 3 nm to 5 nm by altering the molar ratio of oleylamine and oleic acid from 2:1 to 2:1.5. Further increases of HDD and oleic acid led to the formation of oval-shaped nanoparticles. When both the surfactants were added at the beginning of the reaction and the molar ratios of oleylamine to oleic acid were varied between 3:1 to 1:1, spherical nanoparticles, nanocubes, and multi-pods were formed

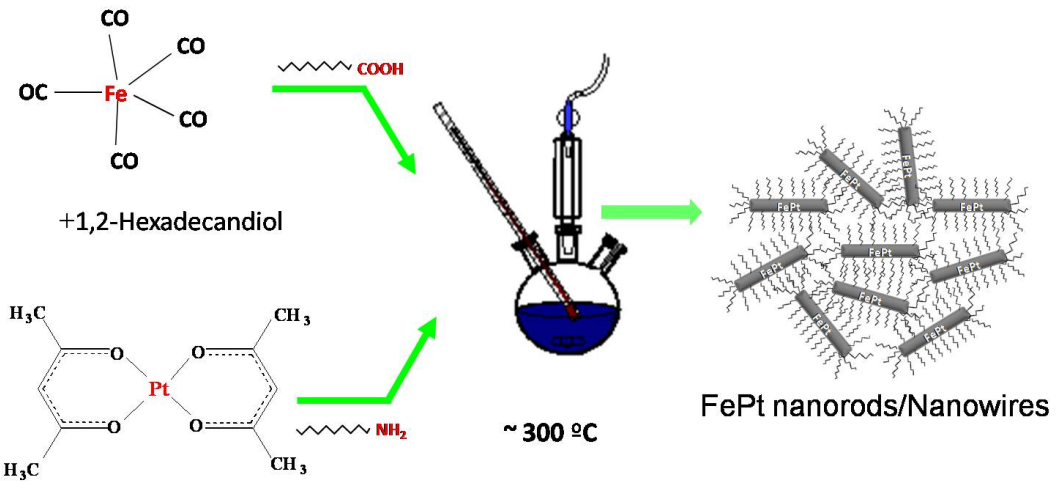

Figure 3.2 Typical polyol synthesis route for FePt nanorods/nanowires.

3.1.4 Purification and Deposition of Nanoparticles

The chemically synthesized nanoparticles in the ether solvents and surfactants were first precipitated from the solvents by the addition of excess anhydrous ethyl alcohol (200 % proof) in a typical volume ratio of 1 part reaction fluid to 4 parts anhydrous ethyl alcohol. The samples were centrifuged for 15 minutes at 6000 rpm, after which the supernatant was removed from the centrifuge tube, leaving the precipitated particles distributed inside. Generally, 5-10 mL of hexane was added to the centrifuge to re-disperse the particles. Occasionally, a minimal amount of oleic acid or oleyl amine can be added to the hexane along with sonication of the centrifuge tube to assist with the re-dispersion of the particles. This centrifugation process can be repeated up to three times to remove the ether solvent and other impurities from the final product after the synthesis to obtain a good dispersion of the particles in solvent such as hexane or octane.

As-synthesized nanoparticles can be stored up to 6 months or longer as required for validation of the original results or stability assessments of the nanoparticles. It was found that particles stored in under refrigeration in the ether solvent provided good long-term stability. Therefore, upon completion of the reaction, the final product was cooled to room temperature, the liquid was transferred to a 50 mL polyethylene conical bottom centrifuge tube, capped, and then placed in a refrigerator. Nanoparticles stored under refrigeration can be re-dispersed by the purification process as needed for thin film deposition on silicon substrates or on TEM grids.

The dispersion of nanoparticle in hexane was deposited on silicon or glass substrates after the purification process for magnetic, structural, and morphological characterizations. For AGM, SQUID, and VSM, nanoparticle samples were prepared for magnetic measurement by deposition of the dispersion on an approximately 3×3 mm silicon substrate at room temperature. Controlled evaporation of the solvents allows the particles to self-assemble on the substrate in a monolayer or in multilayers. The samples were then dried in air or in a vacuum to evaporate volatile organics from the assemblies. Epoxy was used as the binder to prevent movement of the nanoparticles during magnetic measurements. For TEM analysis, a 300-mesh copper grid with a carbon film deposited on a formvar backing, purchased from Ted Pella, was used. A diluted drop of the nanoparticle dispersion solution in octane was put on the formvar side of

the TEM grid, and the solvents were allowed to evaporate in air. The surface energy of the formvar is apparently higher than the solvent, and hence the solvent can spread out easily on the grid instead of beading in the form of a small drop which it does when deposited on the carbon film. Nanoparticles coated with surfactants can assemble into arrays on the grid under proper conditions. For powder XRD analysis, dispersions of nanoparticles were deposited on approximately 1 cm^2 silicon or glass substrate at room temperature. The samples were then dried in air or in a vacuum to evaporate the volatile organics from the assemblies.

3.2 Preparation of $L1_0$ FePt Thin Films and Nanoparticles

The as-synthesized fcc FePt nanoparticles have disordered *A*1 phase, which has low magnetocrystalline anisotropy. Post annealing above 600 ^oC is required to transform *A*1 phase of FePt to $L1_0$ ordered phase, which has the high magnetocrystalline anisotropy essential for many applications. Annealing experiments of fcc FePt nanoparticles were carried out in a Lindberg Blue-M tube furnace on silicon or glass substrates and in salt-matrix. The maximum temperature that can be reached in this furnace was 1100 ^oC.

3.2.1 Annealing of fcc FePt Nanoparticles on Substrates

In order to transfer the disordered face-centered cubic (fcc) structure of the as-synthesized FePt nanoparticles to $L1_0$ ordered phase, the deposited thin film samples were placed in a ceramic annealing boat and annealed either in Argon or forming gas (Ar 93% + H_2 7%) atmosphere at temperatures between 550 ^oC and 900 ^oC in a Lindberg split top furnace. Samples, once inserted in the quartz tube, were purged in argon or forming gas for 30 minutes and then ramped to the desired annealing temperature over 30 minutes. Annealing times at the desired temperature ranged from 1 to 4 hours. Once the annealing time was completed, the furnace was opened, and the quartz tube was air-cooled while purging with Ar. Annealing experiments on selected fcc FePt nanoparticles were performed on substrates to determine the change in structural and magnetic properties due to phase transformation.

Figure 3.3 Lindberg Blue-M tube furnace.

3.2.2 Salt-Matrix Annealing of fcc FePt Nanoparticles

The as-synthesized fcc FePt nanoparticles were annealed, mixing in ball-milled salt powder, in order to prepare isolated $L1_0$ ordered phase FePt nanoparticles. The fine salt powder works as a separating media between the FePt nanoparticles, which keeps the particles dispersed in matrix during high temperature (> 700 ^{o}C) annealing, and prevents sintering and growth of the nanoparticles. Sodium chloride (NaCl) was chosen as the separating media due to its chemical stability to the FePt nanoparticles, melting point of 801^{o}C and high solubility in water. The NaCl powder with particle size less than 7 μm was prepared by ball milling with a surfactant (oleyl amine) in heptane for 24 hours. The milling was carried out in a 500 ml Nalgene high-density polyethylene plastic container inserted into a stainless steel container in a roll mill as shown in Figure 3.4. The plastic container was loaded with mixture of (1) 100 grams of salt (NaCl) powder, (2)10 mm diameter 316 stainless steel balls, total weight = 500 grams, (3) heptane = 250 mL, and (4) oleyl amine = 20 mL. The mixture was then milled for 24 hours at 70 RPM.

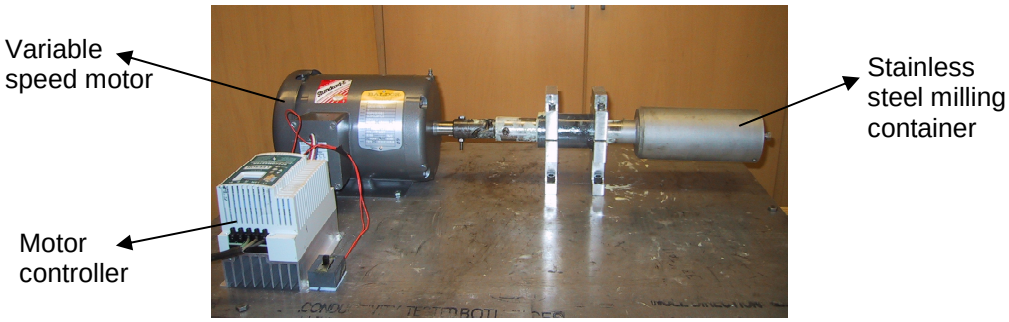

Figure 3.4 The ball milling set up used for milling of NaCl powders.

The ball-milled NaCl salt powder (~ 7 µm) and fcc FePt nanoparticles (2 to 15 nm) in mass ratio of larger then 400:1 was mixed. The mixture of fcc FePt nanoparticles and ball-milled salt was then dispersed in hexane and stirred by magnetic stir bar to mix homogeneously and was continued stirring until mixture dried. The mixture was then annealed at temperatures from 600-700^{o}C for 2-8 hours in forming gas (93% Ar + 7% H_2) in quartz boats. After annealing, the salt was completely washed out from the samples by washing the mixtures in water and ethanol, followed by a series of centrifugation as shown in Figure 3.5.

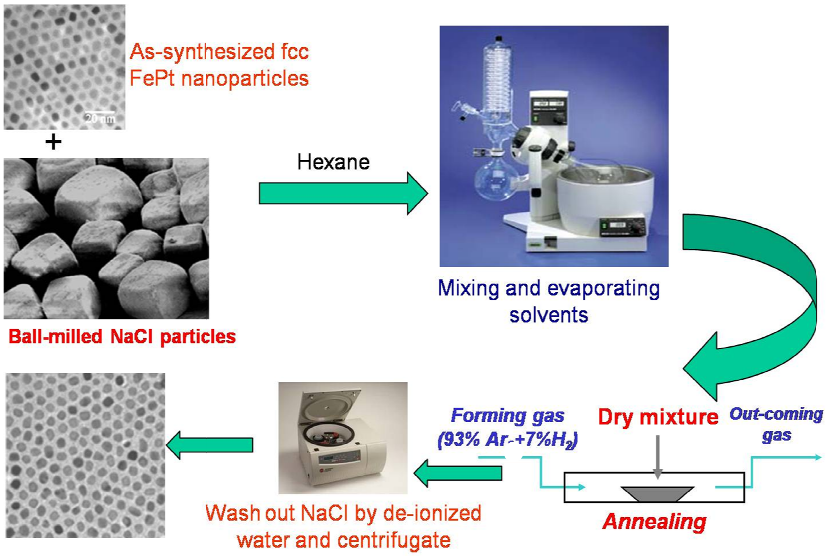

Figure 3.5 Schematic showing salt-matrix annealing technique.

The remaining particles were then rinsed with ethanol only and were centrifuged again to remove water. Dispersions of the $L1_0$ FePt nanoparticles were eventually obtained in an organic solvent such as ethanol or cyclohexane. Salt-matrix annealing experiments on 2 to 15 nm fcc FePt nanoparticles were performed to determine the change in structural and magnetic properties due to phase transformation.[83-86]

3.3 Synthesis of $CoFe_2O_4$ and $NiFe_2O_4$ Nanoparticles

3.3.1 Size Control of $CoFe_2O_4$ Nanoparticles

$CoFe_2O_4$ nanoparticles were synthesized by simultaneous chemical reduction of $Fe(acac)_3$, and $Co(acac)_2$, by 1, 2-hexadecanediol at high temperature in solution phase. Particle diameter was tuned from 3 nm to 20 nm by varying reaction conditions or by seed-mediated growth methods.[58,59]

Synthesis of 3 nm $CoFe_2O_4$ Nanoparticles: The synthesis was performed by standard airless chemical synthesis technique in a nitrogen atmosphere. In a typical synthesis, $Fe(acac)_3$ (1.5 mmol), $Co(acac)_2$ (1 mmol), 1, 2-hexadecanediol (10 mmol), oleic acid (5 mmol), oleyl amine (5 mmol), and phenyl ether (20 mL) were mixed and magnetically stirred under a flow of Ar for 30 minutes. The flask was then heated to 100 ^oC and held for 20 minutes. During this hold, 5 mmol (1.7 mL) of oleylamine and 5 mmol (1.6 mL) of oleic acid were injected into the flask while continuing the Ar purge. After the 20 minutes hold, the mixture was maintained under an Ar blanket and heated to 200 ^oC and held for 20 minutes and then heated to 265 ^oC at a rate of approximately 10 ^oC per minute. The flask was maintained at the refluxing temperature of 265 ^oC for 30 minutes before it was cooled down to room temperature under the Ar blanket. Following a similar purification process, 3 nm $CoFe_2O_4$ nanoparticles were obtained from the final product after a series of centrifugation. 6 nm $CoFe_2O_4$ particles were obtained in one-pot synthesis by replacing phenyl ether with benzyl ether and holding the mixture at 200 $^\circ C$ for 120 minutes and refluxing for 60 minutes at 300 $^\circ C$ before the mixture was cooled down to room temperature under the Ar blanket.

Larger (> 6 nm) $CoFe_2O_4$ Nanoparticles: Particles size bigger than 6 nm were prepared by seed-mediated growth method using the 3 nm and 6 nm as seeds. In this process, the smaller $CoFe_2O_4$ nanoparticles (as seeds) were mixed with more precursor materials, and the mixture was heated in the synthesis of 3 nm or 6 nm particles. By controlling the quantity of nanoparticle seed, $CoFe_2O_4$

nanoparticles with various sizes can be synthesized. For example, mixing and heating 60 mg of 3 nm $CoFe_2O_4$ particles with 1.5 mmol of $Fe(acac)_3$, 1 mmol of $Co(acac)_2$, 8 mmol of 1, 2 -hexadecanediol, 2 mmol of oleic acid, and 2 mmol of oleylamine formed 8 nm $CoFe_2O_4$ particles. Similarly, mixing and heating 50 mg of 8 nm $CoFe_2O_4$ seed particles with 2 mmol of $Fe(acac)_3$, $Co(acac)_2$, 8 mmol of 1, 2-hexadecanediol, 2 mmol of oleic acid, and 2 mmol of oleylamine formed 12 nm $CoFe_2O_4$ particles, while changing the mass of seeds to 20 mg and 15 mg formed 15 and 20 nm $CoFe_2O_4$ nanoparticles, respectively.

3.3.2 Size Control of $NiFe_2O_4$ Nanoparticles

The synthesis was performed by standard airless chemical synthesis technique in a nitrogen atmosphere. In a typical synthesis of 18 nm $NiFe_2O_4$ nanoparticles, a mixture of 257 mg of $Ni(acac)_2$, and 500 mg of 1, 2- hexadecanediol was added to a 125 mL European flask containing a magnetic stir bar. 20 mL benzyl ether was then transferred into the flask and the contents were stirred while purging with N_2 for 20 minutes at room temperature. The flask was then heated to 120 ^oC and the temperature was held for 20 minutes. During this time, 0.2 ml of $Fe(CO)_5$ was injected into the flask while the N_2 purge continued. After 3 minutes, 1 mL of oleic acid and 1 mL of oleyl amine were injected, and the mixture was maintained under N_2 blanket and heated to 160 ^oC at a rate of 5 ^oC per minute and then held for 10 minutes. The flask was maintained at the refluxing temperature of 295 ^oC for 30 minutes before cooling down to room temperature under the N_2 blanket. Afterwards, all handling was performed open in air. The size of the $NiFe_2O_4$ nanoparticles was controlled well by varying the solvents, amount of surfactants and heating rates. For example, when benzyl ether was replaced by phenyl ether, particle size was reduced from 18 nm to 6 nm, keeping other reaction parameters the same. Yet when benzyl ether was used as a solvent and the amount of both the surfactants as increased from 1 mL to 2 mL, the size of the particles was increased from 18 nm to 22 nm.

3.4 Reductive Salt-Matrix Annealing of $CoFe_2O_4$ Nanoparticles

Monodispese FeCo nanoparticles were prepared by extending the salt-matrix annealing technique discussed above for preparation of $L1_0$ FePt nanoparticles. $CoFe_2O_4$ nanoparticles were first synthesized by chemical reduction of $Fe(acac)_3$ and $Co(acac)_2$ by 1, 2- hexadecanediol at high

temperature solution phase. Particle diameter was tuned from 8 to 20 nm by seed-mediated growth method.[58, 59] The as-synthesized $CoFe_2O_4$ nanoparticles were then mixed with ball-milled NaCl powder in hexane with different weight ratios of salt to $CoFe_2O_4$ nanoparticles. The mixture was dispersed in hexane and stirred with a magnetic stir bar to mix homogeneously until the mixture was dry. The mixtures were then annealed in a forming gas (93% Ar + 7% H_2) atmosphere at temperatures between 400 ^oC to 500 ^oC for different annealing times in a quartz boat. After the annealing, the salt powder was first washed out by deionized water and then recovered FeCo nanoparticles were immediately rinsed by ethanol and acetone. The details of salt-matrix annealing technique have been reported in our earlier studies of FePt nanoparticles.[83-86]

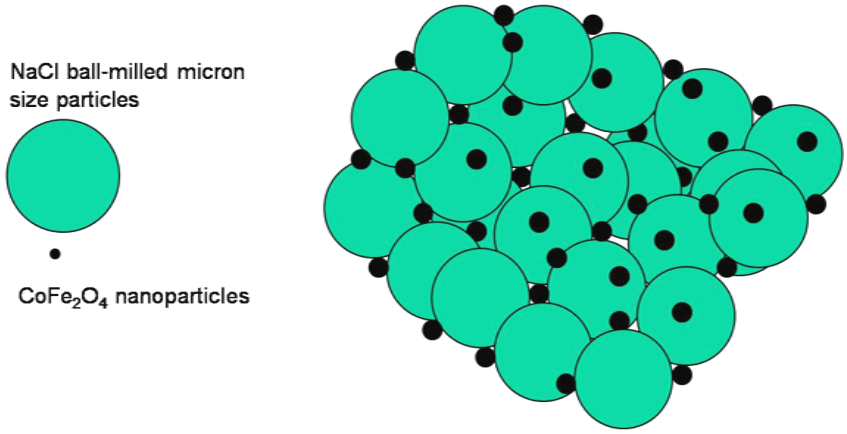

Figure 3.6 Salt-matrix works as a separating media.

3.5 Ball Milling of Sm-Co and Nd-Fe-B Powders

Ball milling is a versatile technique and has been successful in producing a large range of nanoscaled materials, including nanocrystalline structures, nanoparticles, and nanocomposites.[75] Ball milling techniques use mechanical energy to grind/crush raw powder into smaller particles. In this study, Sm-Co and Nd-Fe-B base particles were prepared by ball milling techniques.

Sm_2Co_{17}, $SmCo_5$, and $Nd_2Fe_{14}B$ alloy powders used for the experiments had a purity higher than 98% and particle sizes < 45 µm (-325 mesh) were obtained from Electron Energy Corporation and Alfa Aesar. These alloy powders were handled and stored in an oxygen-free inert (Argon) environment inside

a glove box (Innovative Technology's System One glove box) to prevent oxidation. The oxygen levels inside the glove box were maintained at 0.0 to 2.0 ppm for most of the experiments. The solvents (heptane, hexane) used had a purity of 99.8%. The surfactants, oleic acid (90%), oleyl amine (>98%) and ethanol (200% proof), were purchased from Sigma-Aldrich corporation.

3.5.1 Surfactants-Assisted Ball Milling[87, 89]

The Sm–Co and Nd-Fe-B based powders, which are both commercially available, were studied in our experiments. The raw materials have particle sizes from ~10 to 45 μm. The organic solvent heptane (99.8% purity) was used as the milling medium, and oleic acid (90%) and oleylamine (98%) were used as the surfactants during milling. The powders were ground in a milling vial with balls made of 440C hardened steel by using a Spex 8000M high-energy ball milling machine. The milling process and the handling of both the starting materials and the milled products were carried out in an Argon gas environment inside a glove box to protect the particles from oxidation. A typical milling load consists of:

(1) 5 grams of starting powder

(2) 15 – 10 mm 440C hardened steel balls, total weight = 50 grams

(3) Ball to powder weight ratio = 10:1

(4) 5 ml heptane

(5) 1.5 ml surfactant, ~ 10 to 15 % by weight of starting powder

When surfactants were added, along with heptane solvent, during milling a black-colored liquid containing a dispersion of nanoparticles was obtained along with coarse particles (slurry particles) which quickly settled down at the bottom of the milling vial. The black liquid contained a dispersion of different size nanoparticles ranging from 3 to 50 nm. But when surfactants were not added to heptane during ball milling, the heptane color did not change, indicating that there was no dispersion of particles in the heptane (as shown in Figure 3.7).

Figure 3.7 Particles in heptane solvent after milling.

Figure 3.8 Glove box maintained in Ar gas environment to protect samples from oxidation during process and storage.

3.5.1.1 Size Selection Process [87, 89]

The surfactants absorbed by particles during the ball milling process greatly enhance the dispersion of nanoparticles in a solvent. It was found that the suspending time of particles milled without surfactants in heptane was less than 1 minute, while particles milled with surfactants remained floating in

heptane anywhere from several seconds to even many days, depending on the particle size. Based on the above observations, different sizes of the nanoparticles were separated by using centrifugal separation and controlling the “settling-down” time of the nanoparticle solutions. Slurry particles settled down in 5 minutes at the bottom of the vial from heptane dispersion of powder ground for 20 hours. Different sizes of the nanoparticles were separated using centrifugal separation and controlling the settling-down time of the nanoparticle solutions. It was found that the small-size nanoparticles are floated in the heptane solvent even after a centrifugation of 3000 rotations per minute (rpm) (relative centrifugal force: 1600 *g*) for 25 minutes. Therefore, the small nanoparticles can be separated simply by applying a centrifugation procedure to remove large particles from the solution. To obtain larger nanoparticles, the slurry particles were washed once by heptane to remove the smallest floating nanoparticles. Then, the remaining part was transferred into a surfactant-coated centrifugal tube and dispersed in heptane again by ultrasonic vibration; the particles dispersed in solution were then settled down statically for anywhere from 20 minutes to over 24 hours. Once the particles were collected using this settling-down time, a low-speed centrifugal separation of 500 rpm (45 *g* relative centrifugal force) was carried out to remove the largest particles. Different sizes particles were separated by centrifugation process at 6000 RPM over 30 minutes by mixing 20 mL of ethanol with 30 mL of dispersion particles in heptane.

3.5.1.2 High Vacuum Annealing

Annealing experiments of ball-milled particles were carried out in a Lindberg Blue-M tube furnace. The maximum temperature that can be reached in this furnace was 1100 ^{o}C. The furnace uses a quartz tube that is connected to the glove box using vacuum fittings (as shown in Figure 3.9). The sample to be annealed can be transferred directly from the glove box to the pre-vacuumed and purged quartz tube, thus preventing any exposure of the sample to air. Annealing was done either in inert (Ar) or reducing-forming gas (93% Ar + 7% H_2) atmospheres. The samples for annealing were prepared by depositing the nanoparticle dispersion liquids on silicon or glass substrate. After annealing, the sample was coated with epoxy to prevent oxidation.

Figure 3.9 High vacuum set up connected with inert medium glove box.

3.5.2 Magnetic Field-Ball Milling[90]

The balls and vial were made of non-magnetic stainless steel. The balls were about 1 cm in diameter. The ball-to powder weight ratio was 30. The milling was carried out for up to 100 hours in Vertrel XF solvent or mineral oil, and the powders were sampled every 25 hours. $Nd_2Fe_{14}B$ and Sm_2Co_{17} based coarse powders (~ mesh 325) were obtained by pulverizing ingots. The grain size in the ingot is of the order of tens of micrometers. The powders were then ball milled in a magnetic field (>3 kOe) using a low-energy roll mill. The milling container in this case was a 316 stainless steel container with an internal volume of about 500 ml. A typical milling load consists of:

(1) 20 grams of starting powder

(2) 10 mm diameter 316 stainless steel balls, total weight = 500 grams

(3) Ball to powder weight ratio = 25:1

(4) Rotation speed of 150 to 210 rpm

(5) 150 mL Vertrel XF.

The milling was performed outside the glove box, but the milling container was loaded inside the glove box and tight-sealed before taking it out of the glove box in order to provide an inert environment during the milling process. A viton o-ring compressed between the cap and the container body prevented any

leakage of gases and/or liquids in and out of the container. Thus the atmosphere inside the milling container was the same as that of the glove box, which was oxygen-free. At the end of the milling, the milling container was re-inserted into the glove box, and the milled mixture was recovered. First, the balls were separated out from the mixture. Then, the liquid was allowed to stand for several minutes to sediment particles. The top liquid was then removed, and particles were stored in a closed container inside the glove box. The sampled powders were aligned in a magnetic field of 6–7 kOe in hardening epoxy ball milled with field and without field for comparison.

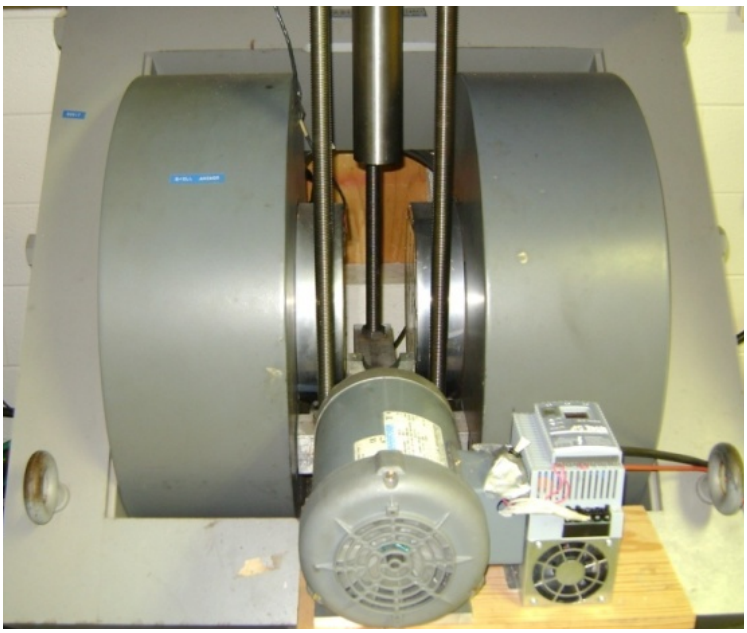

Figure 3.10 Roll-milling set up for magnetic fieldmilling.

CHAPTER 4

CHARACTERIZATION OF MAGNETIC NANOPARTICLES

Transmission electron microscopy (TEM), high resolution TEM (HRTEM), scanning electron microscopy (SEM), and powder and X-ray diffraction (XRD) were used for morphological, structural and characterization of FePt, $CoFe_2O_4$, $NiFe_2O_4$, FeCo, Sm-Co and Nd-Fe-B nanoparticles. Small angle X-ray scattering (SAXS) and a laser particle size analyzer (LPSA) were also used to measure the particle size and size distribution of some of the selected samples. Inductively coupled plasma-optical emission spectroscopy (ICP-OES), energy dispersive X-ray (EDX), and nano-EDS were used for compositional characterization of nanoparticles before and after annealing. Atomic absorption spectroscopy (AAS) was used to determine quantitatively the content of metal in some of the selected samples. Mössbauer Spectroscopy was used to characterize the magnetic property of $CoFe_2O_4$ at room temperature and low temperature. Raman spectroscopy was used to investigate the presence of carbon in some selected samples prepared by salt matrix annealing. An Alternating gradient magnetometer (AGM), a superconducting quantum interference device (SQUID) magnetometer, and a vibrating sample magnetometer (VSM) were used for magnetic property measurements. In this chapter, a brief description of these equipments and characterization techniques and the techniques used to prepare samples will be presented.

4.1 Morphological Characterization

4.1.1 Transmission Electron Microscopy (TEM)

TEM uses electromagnetic lenses to focus the electrons into a very thin beam. In TEM, a beam of electrons is transmitted though a thin specimen, interacting with the specimen as it passes. At the bottom of the microscope, the transmitted electrons hit a fluorescent screen, which makes a shadow image of the specimen with its different parts displayed in varying shades of darkness according to the density of the parts. The image can be studied directly by the operator or photographed with a camera. Contrast formation in the TEM depends on the mode of operation. The most common mode of operation for a TEM

is the bright field (BF) imaging mode. In the BF mode of the TEM, an aperture is placed in the back focal plane of the objective lens that allows only the direct beam to pass. Thicker regions of the sample, or regions with a higher atomic number will appear dark, while regions with no sample in the beam path will appear bright, therefore is termed as bright field.

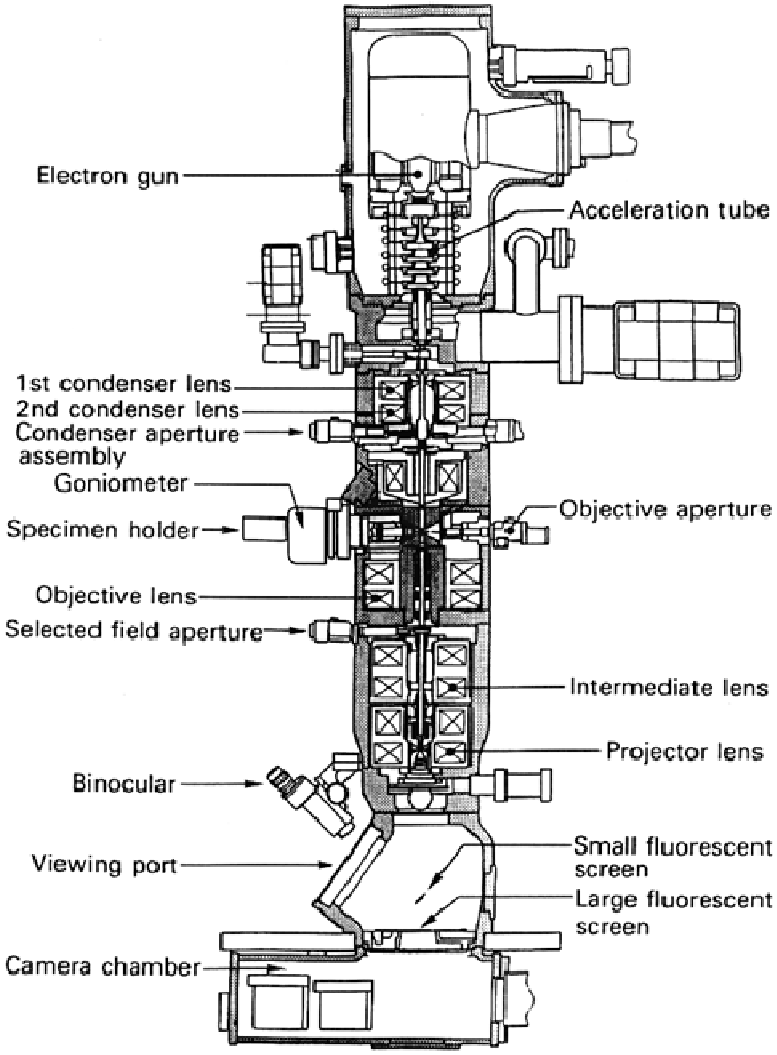

Figure 4.1 A typical structure and optics of TEM.[91]

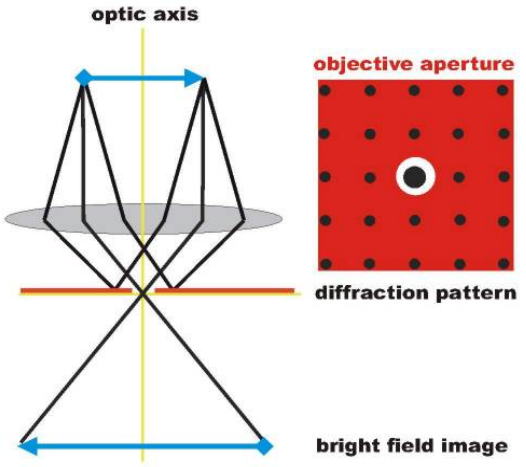

Figure 4.2 Optic of TEM in bright field mode.[92]

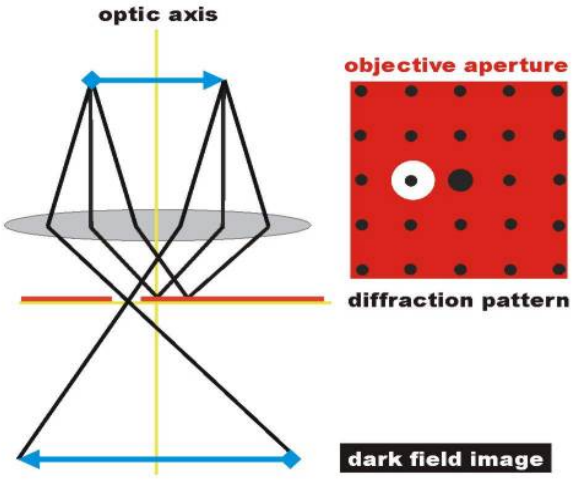

Figure 4.3 Optic of TEM in dark field mode.[92]

On the other hand, in dark field (DF) images, the direct beam is blocked by the aperture while one or more diffracted beams are allowed to pass the objective aperture. Since diffracted beams have strongly interacted with the specimen, very useful information can be obtained from DF images, such as planar defects, stacking faults, or particle size. A diffraction pattern can be obtained by adjusting the magnetic lenses placed on the imaging apparatus. For thin crystalline samples, this produces an image

that consists of a series of dots in the case of a single crystal or a series of rings in the case of a polycrystalline material. For the single crystal case, the diffraction pattern is dependent upon the orientation of the specimen. From diffraction patterns, information about the crystal and the crystal's orientation to the beam path and crystal structure can be obtained.

In our study, JEOL's 1200EX TEM was used for observing the nanoparticles' morphologies and crystal structure information. It uses an acceleration voltage of 120 kV and can be used for magnification up to 500 K times. Bright field images as well as the selected area diffraction patterns (SADP) were captured on negatives, which were then developed and later scanned to produce digital copies. A 300 mesh copper grid with a carbon film deposited on a formvar backing, which was purchased from Ted Pella, was used for preparing the TEM samples. A drop of the nanoparticle dispersion liquid was put on the formvar side of the TEM grid, and the solvent (octane/ hexane) was allowed to dry in air. Formvar is more hydrophobic than carbon, and hence the solvent (which is also hydrophobic) can spread out more easily on the grid instead of staying agglomerated in the form of a small drop. Nanoparticles coated with surfactants assemble on the grid. For TEM imaging of the nanoparticles, it is important that there is no excessive surfactant surrounding the nanoparticles. Excessive surfactant causes difficulties in the the transmission of the electron beam through the sample, reducing the contrast and hence hindering clear observation of the nanoparticles.

4.1.2 High Resolution TEM (HRTEM)

HRTEM is an imaging mode of the transmission electron microscope (TEM) that allows the imaging of the crystallographic structure of a sample at an atomic scale. Because of its high resolution, is an valuable tool to study nanoscale properties of crystalline material. HRTEM contrast arises from the interference in the image plane of the electron wave with itself. To obtain lattice images, a larger objective aperture has to be selected that allows many beams, including the direct beam, to pass. The image is formed by the interference of the diffracted beams with the direct beam (phase contrast). If the point resolution of the microscope is sufficiently high and a suitable sample is oriented along a zone axis, then high-resolution TEM (HRTEM) images are obtained. In many cases, the atomic structure of a specimen can be investigated directly by HRTEM.

In this study, HRTEM imaging and EDX analysis on some selected samples were carried out with at The Georgia Institute of Technology and The University of Alabama and at Ames Lab, Iowa State University. Sample preparation for HRTEM analysis was the same as that for TEM.

4.1.3 Scanning Electron Microscope (SEM)

A scanning electron microscope uses a tiny electron beam to scan across the sample. In SEM, the signals are observed on the same specimen site as the incoming electron beam. As mentioned above, very thin samples are required for TEM methods, where as compact samples or bulk samples can be investigated by SEM. Valuable information about morphology, surface topology, and composition can be obtained.

For conventional imaging in the SEM, specimens must be electrically conductive, at least at the surface, and electrically grounded to prevent the accumulation of electrostatic charge at the surface. Nonconductive specimens tend to charge when scanned by the electron beam, and (especially in secondary electron imaging mode) this causes scanning faults and other image artifacts. Samples are usually coated therefore with an ultrathin coating of electrically-conducting material such as gold or gold/palladium alloy deposited on the sample either by low-vacuum sputter coating or by high vacuum evaporation. Coating prevents the accumulation of static electric charge on the specimen during electron irradiation.

Grisham's EDX (Energy Dispersive X-ray) detector connected to the SEM was used for studying the elemental composition of samples. The samples were mounted on an Aluminum sample stub or Si substrates using double-sided carbon stick tabs. A thin layer of Au-Pd was also deposited on the samples to make them conductive.

4.1.4 Small Angle X-ray Scattering (SAXS)

Selected samples' morphology and size distribution were studied by SAXS measurement in Regaku, Ultima IV, XRD machine. Samples were prepared by depositing a thin layer of nanoparticles on miler film. Samples were then mounted on a specially designed SAXS sample holder.

SAXS is an analytical X-ray application technique used to study the structural characterization of solid and fluid materials in the nanometer range. In SAXS experiments, the sample is irradiated by a well-

defined, monochromatic X-ray beam. When a non-homogeneous medium is irradiated, structural information about the scattering particles can be derived from the intensity distribution of the scattered beam at very low scattering angles. With SAXS, it is possible to study both monodisperse and polydisperse systems. In the case of monodisperse systems, one can determine size, shape, and internal structure of the particles. For polydisperse systems, a size distribution can be calculated under the assumption that all particles have the same shape. SAXS is used to investigate structural details in the 0.5 to 65 nm size range in materials by using the XRD Machine (Ultima IV).

4.1.5 Laser Particle-Size Analyzer (LPSA)

LPSA was used to analyze the particles' size and size distribution of as-synthesis nanoparticles with Nanotrac, from Microtrac Inc. Samples for particle size analysis were prepared by dispersing as-synthesized nanoparticles in hexane or heptane solvent.

Particles suspended in a dispersing fluid are subject to random collisions with the thermally excited molecules of the dispersing fluid, resulting in Brownian motion. The Nanotrac uses an advanced power spectrum analysis of Doppler shifts to produce a full volume distribution of particle sizes. Scattered light caused by interaction with randomly moving particles is mixed with a portion of the original laser after being reflected back into the probe at 180 degrees. The combined light passes through a fiber-optic cable to a single detector, and advanced electronics and software analyze the signals to calculate the Doppler shifts corresponding to particle size.[93]

4.2 Structural Characterization by X-ray Diffraction (XRD)

Regaku Ultima IV and Philips PW 1710 diffractometers with Cu-Kα radiation (wavelength λ=1.54056 A^{o}) were used to study the structure and crystallinity of the samples. The samples were prepared by depositing them on glass or Si substrates.

XRD is a versatile, non-destructive technique that reveals detailed information about the chemical composition and crystallographic structure of natural and manufactured materials. X-ray is based on the diffraction of monochromatic X-ray light by crystal lattices. This phenomenon involves the occurrence of interference of the waves scattered at the successive planes (as shown in Figure 4.4), which is described by Bragg's equation:[97]

$$n\lambda = 2d \sin\theta \ (n = 1, 2, 3, ...), \quad (4.1)$$

where λ is the wavelength, d is the lattice plane distance and θ is half the diffraction angle. This relation is used for the structure analysis of crystals. By varying the angle θ, the condition of Bragg's Law are satisfied by different *d*-spacings in materials. Plotting the angular positions and intensities of the resultant diffracted peaks of radiation produces a pattern that is characteristic of the sample. Usually 2θ is used instead of θ.

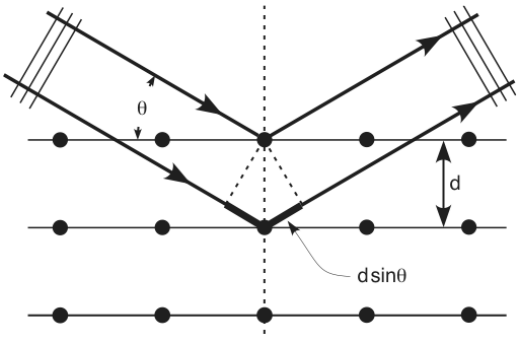

Figure 4.4 Bragg's law.[94]

Using the Scherrer's equation the grain size of sample can be calculated from the XRD patten:[97]

$$L = \frac{0.94\lambda}{B(2\theta)\cos\theta}, \quad (4.2)$$

where *L* is the crystal dimension, *λ* = 0.154056 nm is the wavelength of the X-ray, and *B(2θ)* is the full width in radians subtended by the half-maximum intensity width of the peak at angle *θ*.

4.3 Compositional Characterization

4.3.1 Inductively coupled plasma-optical emission spectroscopy (ICP-OES)

ICP-OES analyses of the composition of selected powder samples were processed by Galbraith Research Labs. This technique uses argon plasma that contains a large amount of cations and electrons. Temperatures within the plasma can reach up to 10,000 K, allowing the sample to ionize fully, whether injected into the plasma as an aerosol, thermally generated vapor, or fine powder. Recombination with electrons within the plasma generates characteristic x-rays associated with the ions present. A

spectrophotometer can then detect the wavelength and intensity of the emission, allowing the determination of multiple elements and relative quantities within the sample.

4.3.2 Atomic Absorption Spectroscopy (AAS)

Atomic absorption spectroscopy (AAS) is a technique for determining the concentration of a particular metal element in a sample. Atomic absorption spectroscopy can be used to analyze the concentration of over 62 different metals in a solution. AAS uses the absorption of light to measure the concentration of gas-phase atoms. Concentration of metals in nanoparticles of the selected samples was characterized by AAS at The University of Texas Southwestern in Dallas.

4.4.3 Raman Spectroscopy

All substances have characteristic spectroscopic features, fingerprints that allow them to be uniquely identified. Raman spectroscopy is a light-scattering technique, in its simplest form, it is a process wherein a photon of light interacts with a sample to produce scattered radiation of different wavelengths. It therefore provides a fingerprint by which the molecule can be identified. The fingerprint region of organic molecules is in the (wavenumber) range 500-2000 cm^{-1}. For selected samples, the presence of carbon in nanoparticles obtained by salt-matrix annealing was investigated by Raman Spectroscopy at The University of Texas at Dallas and at UTA. Samples were prepared by depositing the nanoparticle dispersion on (1x1) inch glass substrates and drying the organic solvent in air.

4.4 Magnetic Property Measurement

4.4.1 Alternating Gradient Magnetometer (AGM)

In an AGM measurement, the sample is mounted on an extended rod attached to a piezoelectric element and then placed at the center of the poles that generates a magnetic field. An alternating gradient magnetic field is generated that produces an alternating force on the sample. This force (*F*) is proportional to the magnitude of the alternating magnetic field (*B*) and the magnetic moment (*m*) of the sample. Thus,

$$E = - m. B \tag{4.3}$$

$$Fx = -dE/dx = mdB/dx. \tag{4.4}$$

This force is converted into a proportional voltage by a piezoelectric element, and hence the moment of the sample can be measured. The applied field is measured by a Hall probe sensor and the sensitivity of the AGM can reach up to 10 nemu. Samples with dimensions up to 5 mm x 5 mm can be measured in AGM. The maximum magnetic field that can be applied by AGM is limited to 14 kOe, and can only be operated at room temperature. Therefore, samples that have high anisotropy or require low or high temperature measurements will need magnetometers that can provide a much higher saturation field in order to get accurate magnetic measurements and that can have the capability of operating different at temperatures.

Figure 4.5 Princeton measurements corporation alternating gradient magnetometer.

4.4.2 Superconducting Quantum Interference Device (SQUID)

SQUID uses a superconducting magnet, through which large amounts of current can flow so that large magnetic field can be generated. The magnetic measuring mechanism of SQUID belongs to an inductive technique. During magnetic moment measurement, the sample moves through a system of superconducting detecting coils, and the magnetic moment of the sample causes changes in magnetic flux associated with the detecting coils, resulting in electric current being produced in the detecting coils. The detecting coils are connected to the SQUID sensor, which functions as a highly linear current-to voltage converter, producing very accurate variations in the output voltage that is proportional to the moment of the sample. The SQUID can generate a magnetic field as high as 70 kOe and can be

operated in temperatures from 2 K to 400 K. The sensitivity of SQUID is 10 nemu up to applied field of 2.5 kOe and 0.6 μemu above that. Liquid helium is required to operate SQUID, which makes the use of SQUID expensive. Sample dimension requirements of SQUID are almost the same as AGM, but the sample for SQUID can be longer in one of its dimensions. AGM is much easier, faster, and less expensive to operate compared to SQUID. Hence, room-temperature measurements of all samples that can be saturated below 14 kOe should be measured by AGM.

Figure 4.6 Quantum design SQUID magnetometer.

4.4.3 Vibrating Sample Magnetometer (VSM)

VSM is an integrated magnetometer in a Physical Property Measurement System (PPMS). VSM can generate a magnetic field as high as 140 kOe and can provide magnetic moment sensitivity up to 1 μemu. The magnetic measuring mechanism is a VSM, which belongs to an inductive technique similar to the SQUID, except that the motion of a sample in the detecting coils for the VSM is much faster than in the SQUID. The normal operating temperature of VSM is between 1.9 K and 400 K, however, a VSM with an oven option can be operated from room temperature and 1000 K. The measurement of VSM is faster than SQUID but has lower sensitivity. Measurements that require a saturation field higher than 70 kOe and temperatures higher than 400 K are performed by VSM instead of SQUID.

Figure 4.7 Quantum design PPMS with VSM insert.

Samples for magnetic characterization were prepared by depositing a few drops of the final dispersion on a 3 mm × 3 mm silicon substrate and evaporating the solvent (hexane/ethanol) at room temperature, which led to the formation of the nanoparticle assemblies on the substrate. The samples were then dried in a vacuum to remove volatile organics from the assemblies. The samples were measured before and after annealing in forming gas (93% Ar + 7% H_2) for different temperatures and annealing times. In case of fct FePt nanoparticles produced by salt-assisted annealing, samples were prepared by dropping the nanoparticle dispersion in ethanol and were coated with epoxy when solvent was evaporated to prevent nanoparticles being flown. FePt fct nanoparticles samples were prepared by putting drops of a mixture of nanoparticles with epoxy binder on Si substrates.

4.4.4 Mössbauer Spectroscopy

Characterizations of magnetic properties of some of the selected samples were done by ^{57}Fe Mössbauer Spectroscopy at different temperatures at Western Washington University. Samples for Mössbauer characterization were prepared by drying the nanoparticle evaporating organic solvent. Mössbauer spectroscopy is a versatile technique that can give very precise information about the chemical, structural, magnetic, and time-dependent properties of a material. The Mössbauer effect, a physical phenomenon, refers to the resonant and recoil-free emission and absorption of gamma rays by atoms bound in a solid form. In general, gamma rays are produced by nuclear transitions: from an unstable high-energy state to a stable low-energy state. The energy of the emitted gamma ray

corresponds to the energy of the nuclear transition, minus an amount of energy that is lost as recoil to the emitting atom. If the lost recoil energy is small compared with the energy-line width of the nuclear transition, then the gamma ray energy still corresponds to the energy of the nuclear transition, and the gamma ray can be absorbed by a second atom of the same type as the first.

CHAPTER 5

FCC FePt NANOCRYSTALS

FePt nanocrystals were prepared by the simultaneous reduction of platinum acetylacetonate and the thermal decomposition of iron pentacarbonyl or the reduction of iron acetylacetonate in the presence of solvents/surfactants. A variety of FePt nanocrystals, including nanowires, nanorods, spherical nanoparticles, nanocubes, and nanosized multi-pods, were successfully obtained. The shape control was realized by simply varying synthesis parameters, such as the molar ratio of surfactants to metal precursors, addition sequence of the surfactants and metal precursors, as well as the heating rate and reflux temperature. This chapter is divided into three sections (1) size control synthesis of spherical FePt nanoparticles and the study of their size dependent properties, (2) a facial synthesis route of one-dimensional FePt nanoparticles, including nanorods and nanowires and their characterization, (3) a novel shape control synthesis of FePt nanocrystals in one-pot reactions and the study of their size related properties.

5.1 Synthesis of FePt Nanoparticles

5.1.1 Introduction

The synthesis of monodisperse magnetic nanoparticles has been intensively pursued over the last decade due to their potential applications, such as ultra-high-density magnetic storage media [25,78, 84] advanced nanocomposite magnets,[12, 95, 98] biomedicines,[52, 95] and nanodevices.[25, 95] The interest in FePt is primarily because of its high magneto crystalline anisotropy and high saturation magnetization ($K_u \sim 7 \times 10^7$ erg/cm^3, M_s ~1100 emu/cm^3) in ordered $L1_0$ phase in near-equi-atomic percentage of Fe and Pt ratio. FePt alloys are chemically stable owing to the spin-orbit coupling and the hybridization between Fe *3d* and Pt *5d* as compared to other well-known hard magnetic materials such as Sm-Co and Nd-Fe-B.[25, 95] The magnetic properties of FePt alloys can be tuned by simply controlling the atomic ratio of Fe and Pt in the alloy structure. FePt nanoparticles ~ 3 nm can be ferromagnetic at ambient temperature.[25] The hard magnetic FePt nanoparticles are excellent candidates for these particle based applications.

Since the report in 2002 by Sun *et al*. on the synthesis of FePt nanoparticles, considerable work has been done to develop different methods for synthesizing FePt nanoparticles.[78] There are several physical and chemical methods used to fabricate FePt nanoparticles, such as gas-phase deposition,[100] mechanical ball milling,[99] and chemical synthesis.[76, 77] Among the various techniques used, experimental results have shown that chemical method is a versatile way of preparing of monodisperse FePt nanoparticles. Most of the previous works on the synthesis of FePt nanoparticles involved the reduction of $Pt(acac)_2$ and decomposition of $Fe(CO)_5$.[95] Other works include, synthesis of FePt nanoparticles via the simultaneous reduction of $FeCl_2$ and $Pt(acac)_2$[101] or by the simultaneous reduction of $Fe(acac)_3$ and $Pt(acac)_2$.[76] Hard magnetic FePt nanoparticles are promising building blocks for the fabrication of nanocomposite exchange-coupled permanent magnets.[12, 95, 98] Recently, the synthesis of bimagnetic $FePt/Fe_3O_4$ and $FePt/CoFe_2O_4$ core/shell structure particles and $FePt/CoFe_2O_4$ bricklike structure particles has been reported.[102, 103] Much attention has been given to the potential application of chemically synthesized FePt in ultra-high recording media because the size distribution of chemically synthesized nanoparticles can be controlled better than grains in sputtered film.[95] Therefore, the preparation of high-quality nanoparticles with desired size, size distribution, and composition is a prerequisite for investigating and utilizing their properties for many technological applications. Relatively simple and reproducible approaches for the synthesis of crystalline nanoparticles of controllable dimension and geometry are of great fundamental and technological interest.

In this section, we discuss the morphological control of spherical FePt nanoparticles, their structural characterization, and their size dependent magnetic properties at room temperature and low temperatures. Magnetic hardening of annealed $L1_0$ FePt thin film on substrates will also be discussed.

5.1.2 Size Control of FePt Nanoparticles

FePt nanoparticles were synthesized as described in Chapter 3 (Section 3.1.1). The FePt nanoparticles of size 2 nm were synthesized by the simultaneous chemical reduction of $Pt(acac)_2$ and $Fe(acac)_3$ by 1, 2-hexadecanediol at high temperature in solution phase.[76] The FePt nanoparticles bigger than 3 nm were synthesized by the simultaneous chemical reduction of $Pt(acac)_2$ and the thermal decomposition of $Fe(CO)_5$ at high temperature in solution phase. The size of the FePt nanoparticles was

controlled by varying the surfactant to Pt precursor molar ratio. Surfactants typically play an important role in tuning the particle size. [77, 78] By increasing the surfactants to $Pt(acac)_2$ molar ratio from 1.0 to 8.0, the particle size increased from 3 to 9 nm. The particle size can be changed with 1 nm accuracy by controlling the amont of surfactants amount. The change in size of nanoparticles can be expressed by the number of nuclei at the first step of particle formation. The increase of amount of surfactants results in the formation of stable nuclei, which suppresses the nucleation rate but increases the growth rate. [77] 15 nm $Pt@Fe_3O_4$ core-shell particles were prepared by first synthesizing 10 nm Pt cores through the addition of the Pt precursor at 290℃ in a mixture of octyl ether and surfactants, and then they were coated with iron.[80]

5.1.3 Structure and Morphology

Figure 5.1 shows the XRD patterns of the as-synthesized FePt nanoparticles size ranging from 2 nm to 9 nm with 1 nm difference and 15 nm $Pt@Fe_3O_4$ core-shell particles. The as-synthesized FePt nanoparticles are highly crystalline position relative intensity of peaks match well with standard disordered fcc structure of FePt phase. The strongest (111) peak at 40.3 ° corresponds to fcc structure obtained from the randomly oriented particles. It can be seen that the full width at half maximum (FWHM) of (111) peak increases with particle size. Figure 5.2 shows TEM images of monolayer assemblies of 2, 4, 6 and 8 nm as-synthesized FePt nanoparticles, deposited on TEM carbon-coated copper grid from their octane dispersion and dried at room temperature. TEM analysis shows that particles are monodisperse and have narrow size distribution (standard deviation < 10 %). Figure 5.3 shows a close-packed monolayer assembly of 8 nm FePt nanoparticles. A monolayer or multilayer self-assembly of FePt nanoparticles on a TEM grid or a substrate can be obtained by controlling the evaporation of the carrier solvent and the concentration of particle dispersion. The grain sizes of the particles were calculated using the Scherrer equation (5.1).[97]

$$L = \frac{0.94\lambda}{B(2\theta)\cos\theta}, \qquad (5.1)$$

where L is the crystal dimension, λ = 0.154056 nm is the wavelength of the X-ray, and $B(2\theta)$ is the full width in radians subtended by the half-maximum intensity width of the peak at angle θ. The (111) peaks

were chosen to calculate the grain sizes (Figure 5.1). These grain sizes also represent the particle sizes because all of the particles are single crystalline except the 15 nm particles which have a Pt@Fe_3O_4 core@shell structure. The average grain sizes of as-synthesized particles matches well with the direct observation of particle size from TEM micrograph images.

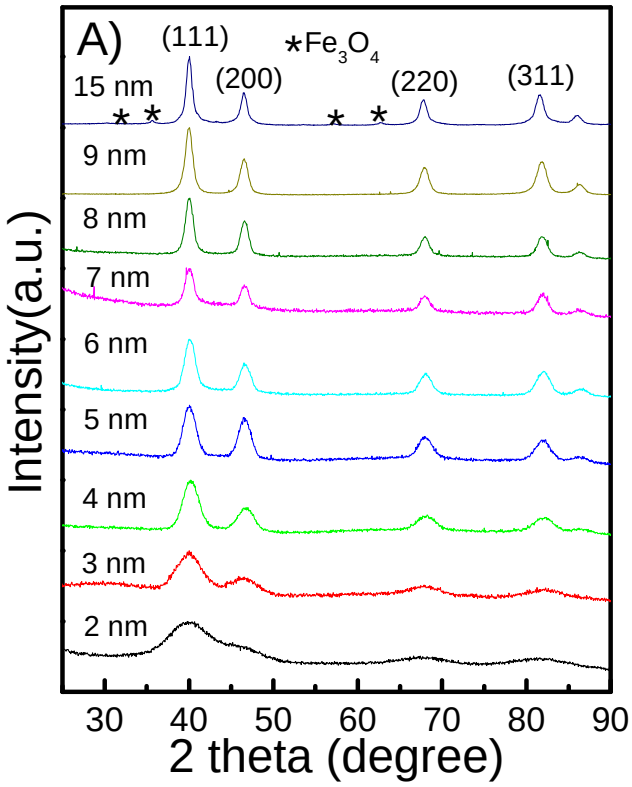

Figure 5.1 XRD patterns of the as-synthesized 2, 3, 4, 5, 6, 7, 8, and 9 nm fcc FePt nanoparticles, and 15 nm Pt@Fe_3O_4 nanoparticle assemblies.

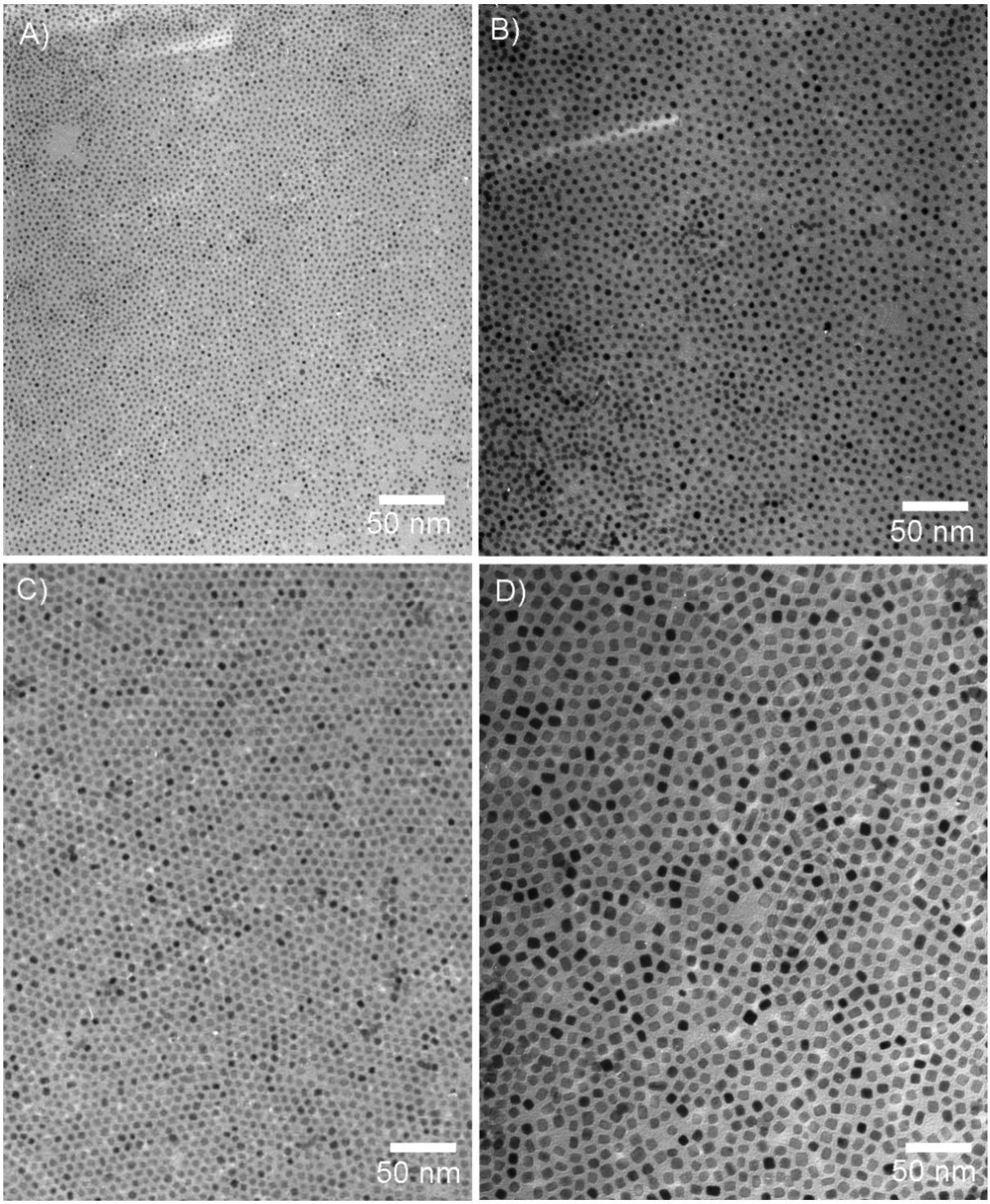

Figure 5.2 TEM images of monolayer assemblies of the as-synthesized FePt nanoparticles: A) 2 nm, B) 4 nm, C) 6 nm, and D) 8 nm.

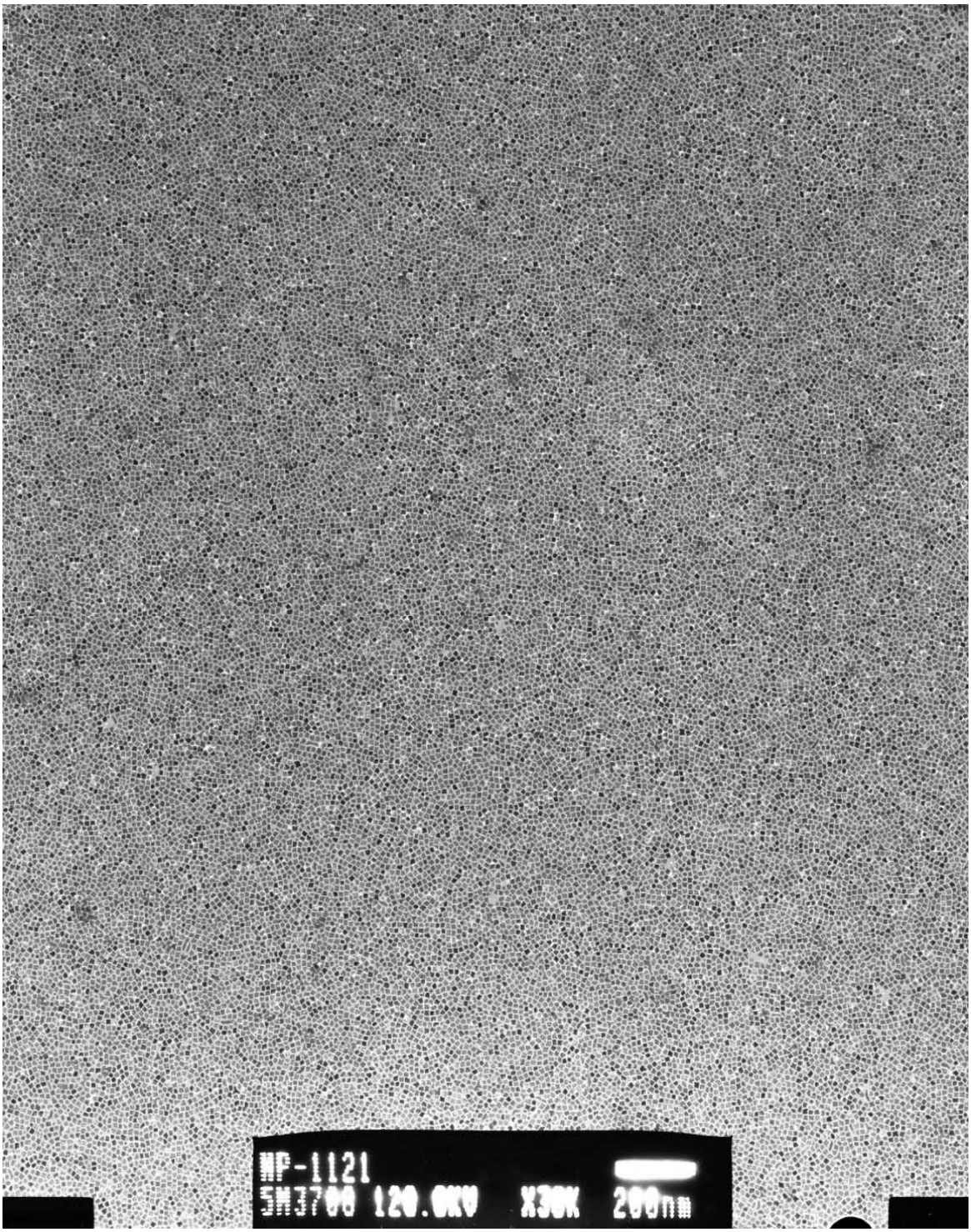

Figure 5.3 TEM image of the as-synthesized 8 nm FePt nanoparticles with a large area close packed monolayer self-assembly.

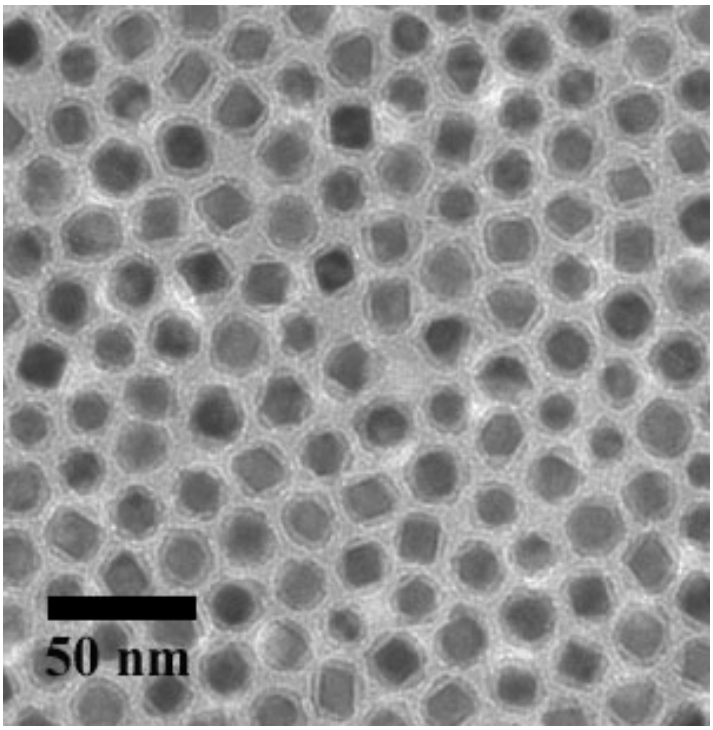

Figure 5.4 TEM image of a monolayer assembly of the as-synthesized 15 nm Pt@Fe_3O_4 nanoparticles.

Small Angle X-ray Scattering (SAXS): Analysis of particle size and size distribution of some of the selected samples of as-synthesized FePt nanoparticles was carried out using SAXS in the transmission geometry as described in Chapter 4 (Section 4.1.4). The experimental scattering curves measured by SAXS give no direct information about the size of the nanoparticles. A reasonable method for size determination is the direct fitting of model curves to experimental scattering curves. All the samples were fitted with a spherical model for experimentally measured scattering curves. Figure 5.5 shows the experimentally measured scattering curves and particles size and size distribution obtained by fitting scattering curves for 4 nm and 8 nm particles. Figure 5.5 (A) and 5.5 (C) show the typical SAXS patterns (scattering curves) measured in red colored lines for 4 nm and 8 nm particles. The blue-colored lines represent the simulated data. The size distributions of the particles were obtained by fitting the scattering profiles as seen Figure 5.5(B) and 5.5(D). It can be seen that the particles have narrow size distribution. The average particle diameter calculated from SAXS measurement is consistent with that observed by

TEM micrograph images and estimated from XRD patterns using the Scherrer equation. The average diameters were estimated to be 4.3 nm for 4 nm particles and 8.4 nm for 8 nm particles, which agrees well with the TEM images.

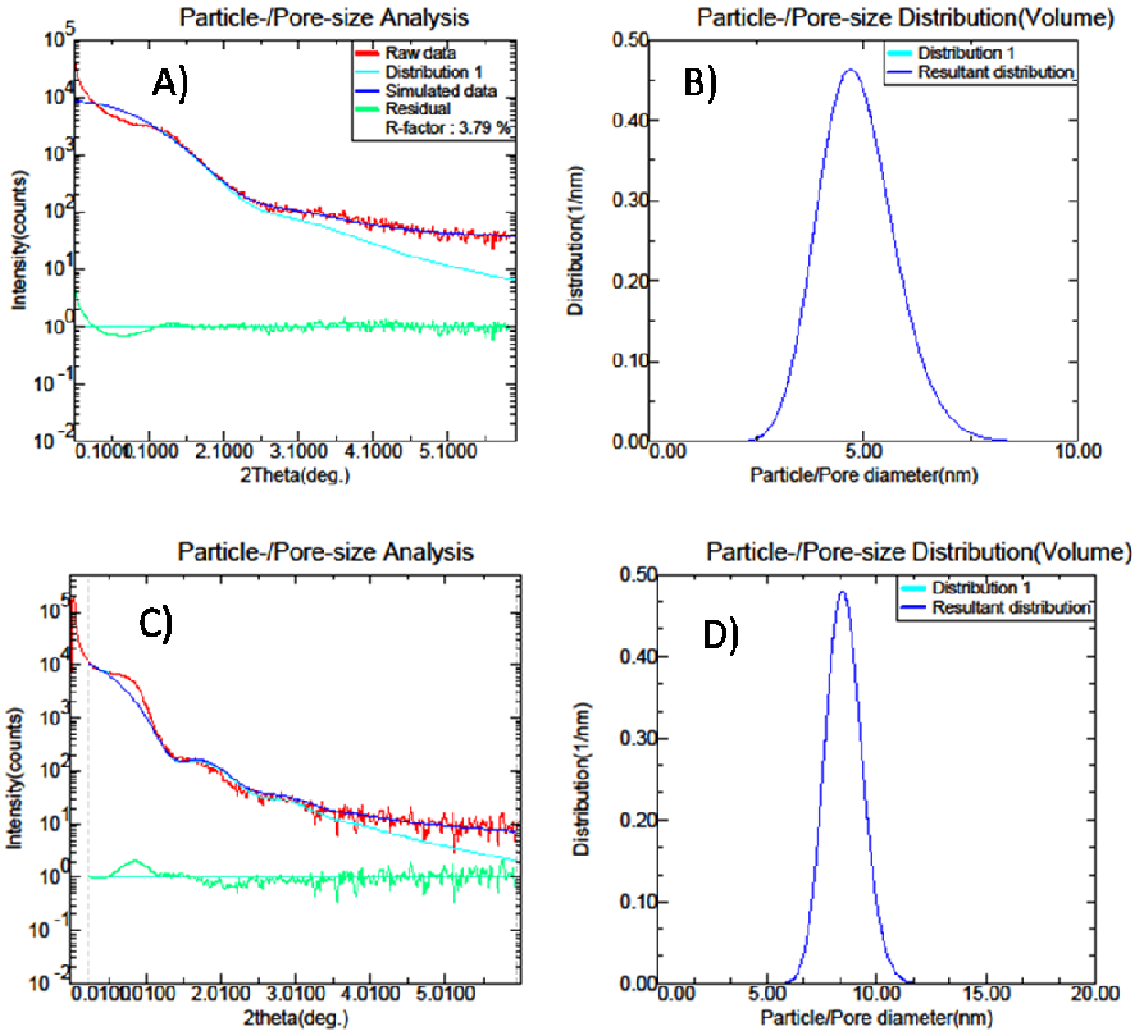

Figure 5.5 4 nm FePt nanoparticles A) SAXS patterns and B) size distribution, and 8 nm FePt nanoparticles C) SAXS patterns and D) size distribution.

5.1.4 Magnetic Properties

Room-temperature and low-temperature magnetic properties of the as-synthesized FePt nanoparticles were measured by SQUID. Figure 5.6 shows the hysteresis loops of as-synthesized FePt particles of 2, 4, and 8 nm measure at 5 K and 300 K. The as-synthesized FePt nanoparticles have chemically disordered fcc structure with very low magnetic anisotropy. It has been found that the as-synthesized 2, 4 and 8 nm nanoparticles are superparamagnetic at 300 K. This indicates that the thermal energy can overcome the anisotropy energy barrier of the individual nanoparticles, and the net magnetization of these nanoparticle assemblies is zero in the absence of an external field. However, all the particles are ferromagnetic at 5 K and the relative saturation magnetization at 5 K is much higher compared to 300 K (Figure 5.6). It was also observed that the saturation magnetization values of the particles are size dependent and increase with particle diameter.

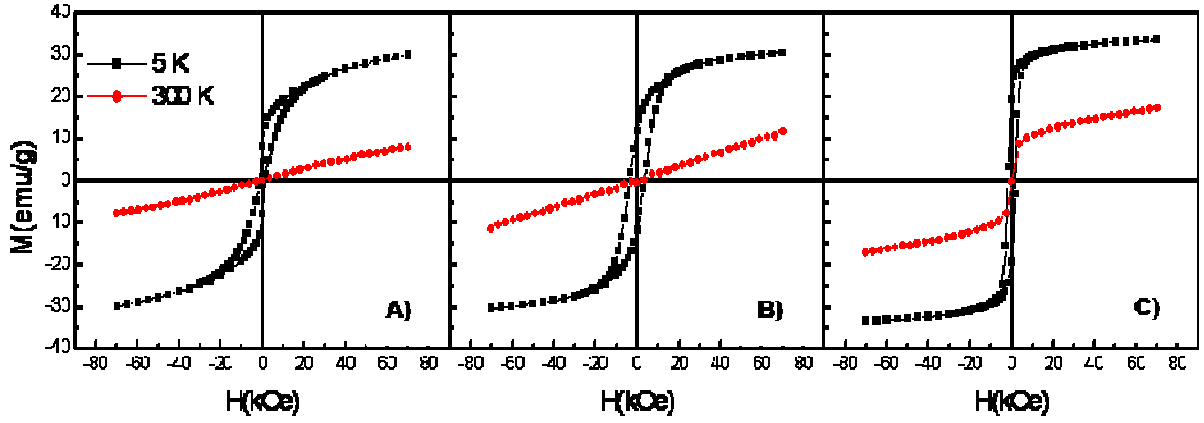

Figure 5.6 Hysteresis loops of the A) 2 nm, B) 4 nm, and C) 8 nm FePt nanoparticle assemblies measured at 5 and 300 K.

The temperature dependence of the magnetization of different size particles was measured using zero-field-cooling (ZFC) and field-cooling (FC) procedures. On cooling, the zero-field-cooled magnetization begins to drop and deviate from field-cooled magnetization at the blocking temperature (T_B) as shown in Figure 5.7. Figure 5.8 shows the plot of magnetization (M) versus temperature (T) for 2, 3, 4, 5, 6, 7 and 8 nm FePt nanoparticles with a measuring field of 100 Oe between 5 K and 250 K. The M

vs. T (measured in ZFC) curves show peaks characteristic of superparamagnetic transitions. The peak temperature in the M vs. T curve (blocking temperature), increases continuously with the increasing particle size (as shown in set in Figure 5. 8)

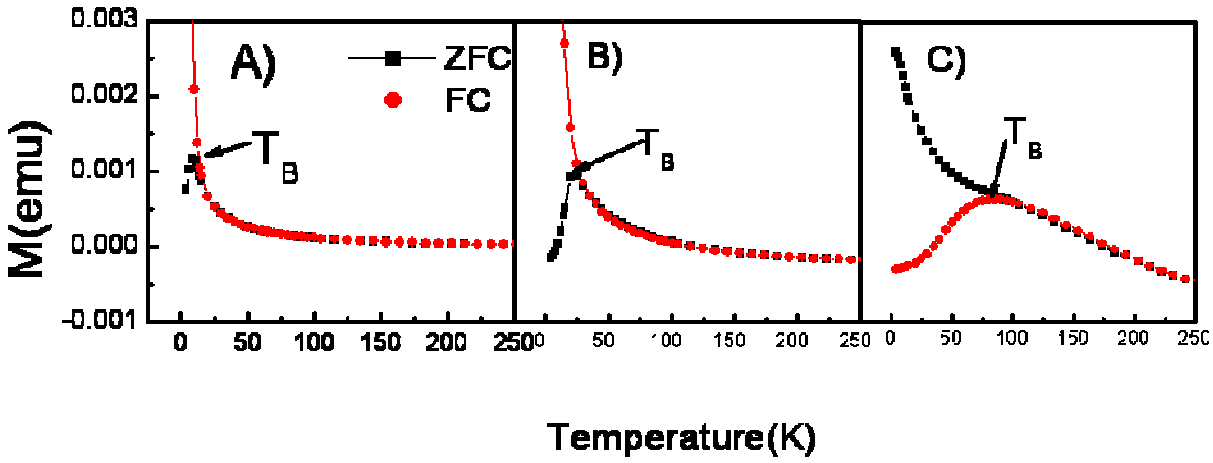

Figure 5.7 ZFC and FC curves measured for 2, 4 and 8 nm nanoparticles between 5 K and 250 K.

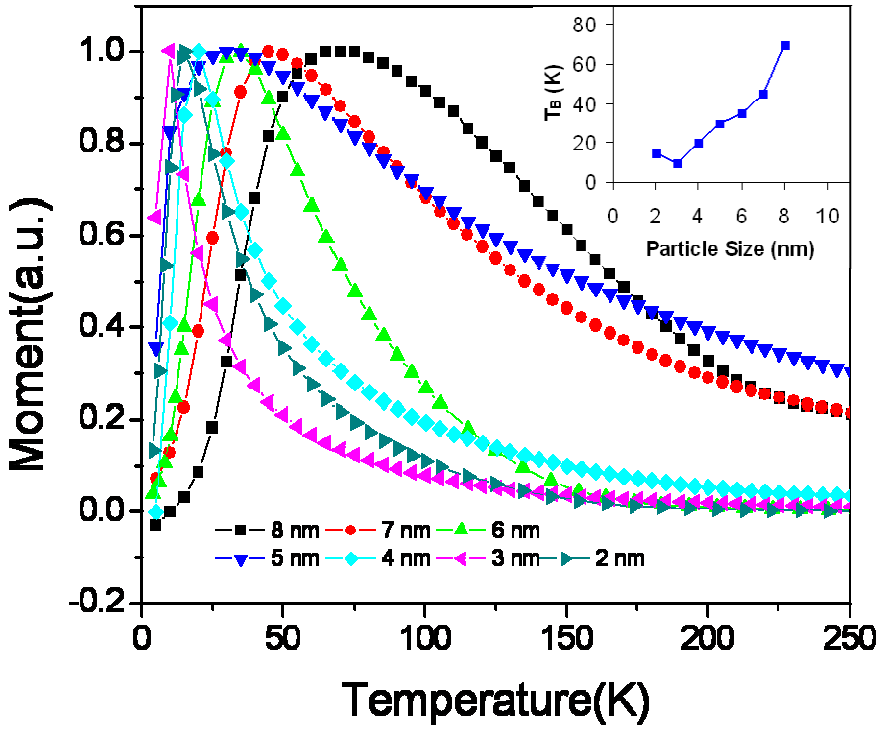

Figure 5.8 Magnetization verses temperature for 2, 3, 4, 5, 6, 7, and 8 nm FePt nanoparticles measured at 100 Oe field and blocking temperature of different size particles in set.

The magnetic properties of FePt nanoparticles strongly depend on their composition. The composition of the as-synthesized FePt nanoparticles was determined by energy dispersive X-ray spectroscopy (EDX) and inductively coupled plasma (ICP). The composition of these FePt nanoparticles can be readily controlled. The final composition can be adjusted by controlling the molar ratio of iron pentacarbonyl to platinum salt. As discussed above, the XRD patterns (Figure 2) show that the as-synthesized FePt nanoparticles possess a chemically disordered fcc crystal structure. The as-synthesized fcc structure FePt nanoparticles with low magnetic anisotropy can be transformed into fct structure with very high magnetic anisotropy through thermal annealing. In equi-atomic FePt phase, magnetic hardening shown by the coercivity is based on the fcc-fct phase transition. The as-synthesized fcc FePt particles were deposited on Si substrates and annealed in forming gas (Ar 93% + H_2 7%) from 500 ^oC – 700 ^oC annealing time was varied from 30 minutes to 4 hours. It was found from experimental observations that the annealed samples had good magnetic properties (i.e., comparatively high coercivity) when annealing was carried out between 650 ^oC to 700 ^oC for 1 hour. After the annealing, all the nanoparticles gave coercivity larger than (> 15 kOe) and coercivity as high as 25 kOe was achieved. Figure 5.9 shows a typical hysteresis loop of 4 nm FePt particles annealed at 700 ^oC for 1 hour in forming gas. The very high coercivity indicates the complete phase transformation of these nanoparticles and also shows that the particles are a single phase material.

Figure 5.10 shows the XRD patterns for the as-synthesized 4 nm FePt nanoparticles annealed in forming gas at 700 ^oC for 1 hour. It can be clearly seen from this figure that both the peak position and intensity for the annealed samples match perfectly with the standard $L1_0$ ordered phase of FePt. The (001) and (110) peaks characteristic of the $L1_0$ FePt phase developed fully when samples were annealed at 700 ^oC for 1 hour. The position of the peaks shifts to the high-angle direction as the transition is fully developed (obvious for the (111) peak), which is due to the lattice length change when atomic structure changes from fcc to fct.

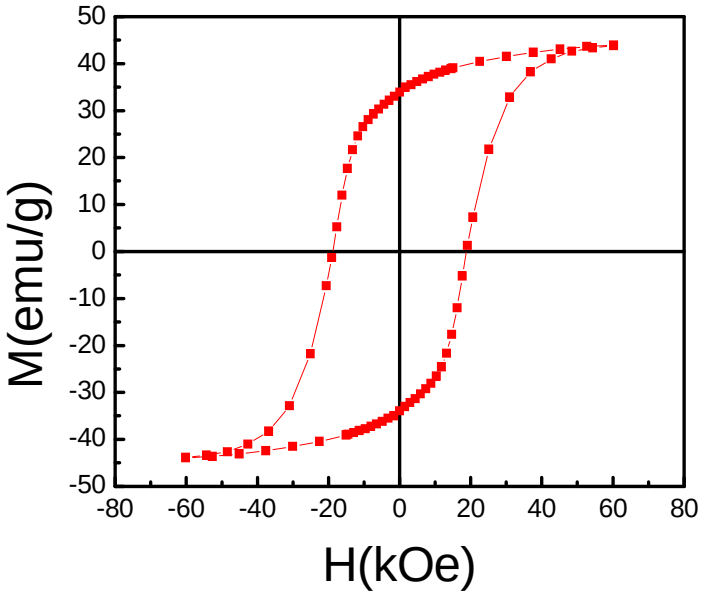

Figure 5.9 Room temperature hysteresis loop of 4 nm FePt nanoparticles annealed at 700^{o} C for 1 hour in forming gas (Ar 93% + H_2 7%).

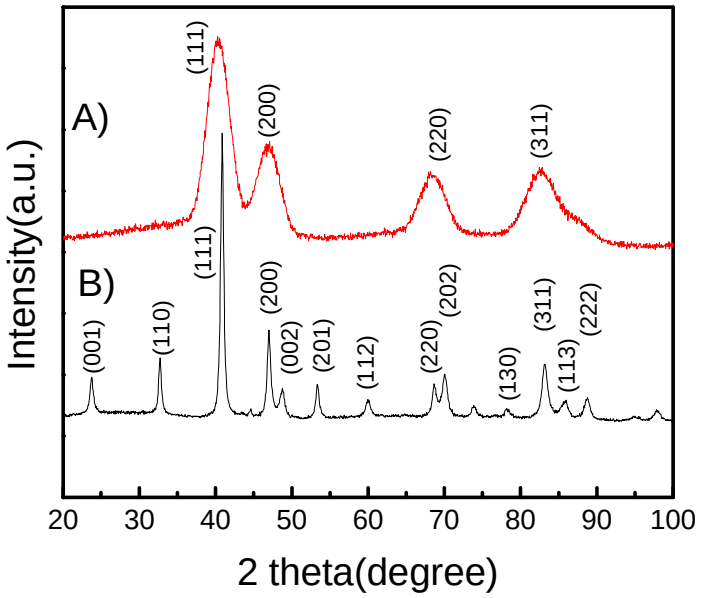

Figure 5.10 XRD patterns of A) as-synthesized 4 nm FePt nanoparticles, and B) annealed under forming gas (Ar 93% + H_2 7%) at 700^{o} C for 1 hour.

The heat treatment of FePt nanoparticle assemblies deposited on a Si substrate at 700 ^{o}C promotes sintering of FePt particles, resulting in grain growth and drastic change in morphology from discrete particles to a continuous thin film. By using Scherrer formula, the grain size calculated from XRD patters after annealing, was 29 nm. We also used salt-matrix as a separating media during heat treatment to prevent sintering and the grain growth of FePt nanoparticles. Preparation of monodisperse $L1_0$ FePt nanoparticles by using salt-matrix annealing techniques will be discussed in the next chapter in detail.

5.1.5 Conclusion

FePt nanoparticles of 2 to 15 nm in size with narrow size distribution have been prepared in a predictable and reproducible manner via chemical solution methods. The size and shape of these particles can be controlled in a systematic manner. The FePt nanoparticle size increases with increasing concentration of surfactants (oleic acid, oleyl amine). This effect is attributed to the slow rate of nucleation when there is a high concentration of stabilizer. In addition, the average size of the nanoparticle changes when the heating rate changes. The as-synthesized nanoparticles were found to be superparamagnetic at room temperature, and their blocking temperature which increases with particle is size dependent. After annealing in a reducing environment, thin film assemblies of these nanoparticles give coercivity up to 25 kOe, which indicates their complete transformation from the disordered fcc to the ordered fct structure.

5.2 FePt Nanorods and Nanowires

5.2.1 Overview of the Issue

In recent years, great progress has been made in the synthesis of various nanostuctures with controllable morphology and properties, including one-dimensional structures such as nanorods and nanowires.[77, 78, 104, 105] These nanorods and nanowires can also be used as building blocks for anisotropic nanostructured materials and devices such as high-density data storage devices based on domain wall motion.[110, 111] Morphological control has also been reported for nanorods and nanowires of semiconductors,[112] metals,[113, 114] and metal oxides.[115, 116] However, synthesis of hard magnetic nanorods and nanowires with the required geometry and composition remains a challenge. Recently, magnetic FePt nanorods and nanowires have attracted a great deal of attention because of their potential

application for strong permanent magnets and ultra-high-density recording media.[12, 54, 78, 84, 95, 98,109-113,117,118] Different techniques such as electrodeposition,[119] pulsed laser deposition,[120] electron beam-induced deposition,[121] biotemplate deposition,[122] solvothermal processes,[123, 124] and wet chemistry methods[125] have been employed for the synthesis of FePt nanorods and nanowires.

In this study, we report a facile method for synthesizing FePt nanorods and nanowires with controlled diameter and length. This method is based on a chemical solution recipe with precursors similar to those were used for synthsizing FePt spherical nanoparticles.[78] By simply modifying the synthetic parameters such as the molar ratio of surfactants to metal precursors, addition sequence of the surfactants and metal precursors, heating rate and reflux temperature, we successfully obtained nanorods/nanowires with an average diameter of 3 nm and a length tunable from 15 nm to 150 nm. The as-synthesized particles with chemically disordered fcc structure transformed to the chemically ordered $L1_0$ structure upon heat treatments. The heat-treated assemblies exhibit hard magnetic properties with coercivity as high as 24 kOe.

5.2.2 Morphology and Structure

FePt nanorods and nanowires were grown as described in Chapter 3 (Section 3.3.2). Figure 5.11(A-C) shows TEM images of monolayer assemblies of as-synthesized nanorods and nanowires (deposited from their octane dispersion onto an amorphous carbon coated copper TEM grid) that have a diameter of 3 nm with a length of about 15, 50, and 150 nm, respectively. The length of these FePt nanorods/nanowires can be controlled from 15 nm to over 150 nm by varying the molar strength of 1,2-hexadecondiol (HDD) and oleic acid while keeping other parameters constant. For example, FePt nanowires with length of over 150 nm were formed when 100 mg of HDD and 3 mL of oleic acid were used. When 200 and 400 mg of HDD was taken with 6 mL of oleic acid, the length of the wires were reduced to 50 nm and 15 nm, respectively. Further increase in HDD and oleic acid led to the formation of spherical particles of diameter of 3 nm.

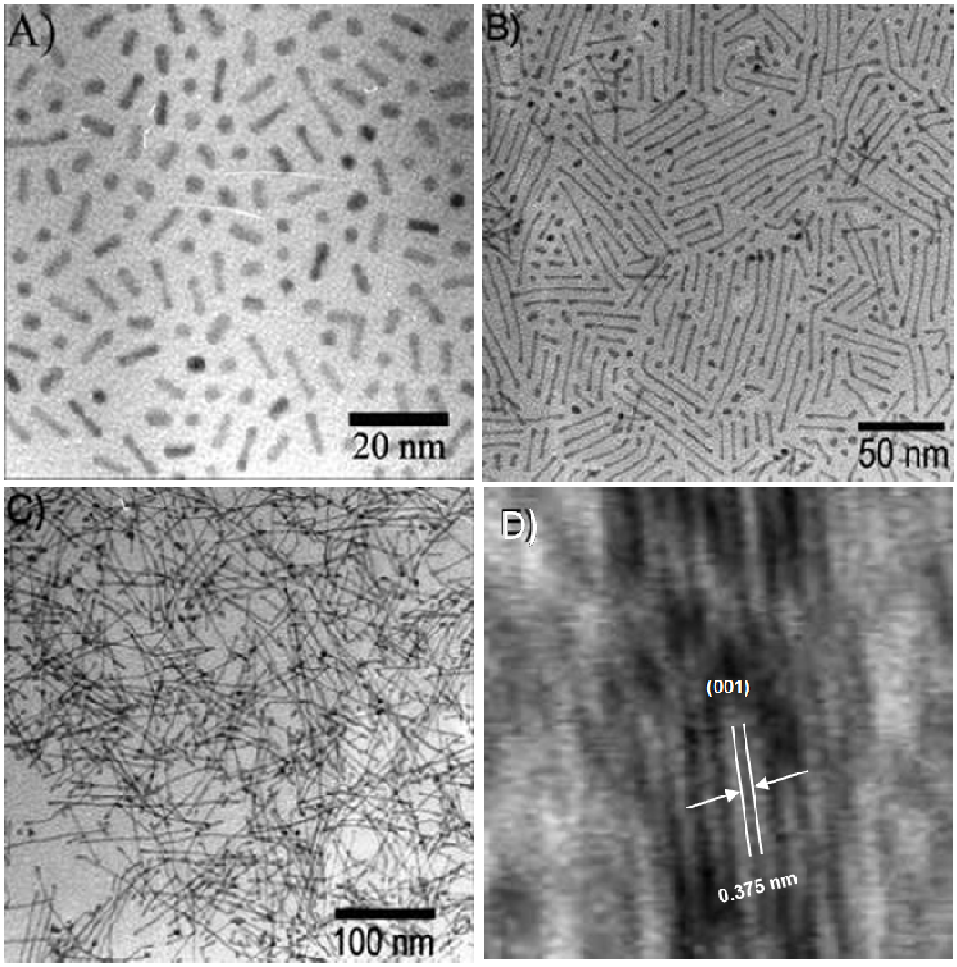

Figure 5.11 TEM images of monolayer assemblies of FePt nanorods/nanowires with average length of A) 15 nm, B) 50 nm, and C) 150 nm.

A high-resolution TEM (HRTEM) image of individual nanorods provides additional information about the structure of the wires. The HRTEM of a section of nanowire reveals good crystallinity and clear lattice fringes, as shown in Figure 11(D). The crystal structure of the rods is fcc and the (100) lattice spacing is about 3.75 Å, which is consistent with the known the chemically disordered fcc FePt structure. [126, 127] Figure 5.12, 5.13 and 5.14 show TEM images of the large area monolayer assemblies of FePt nanorods and nanowires deposited from their octane dispersion on a TEM grid.

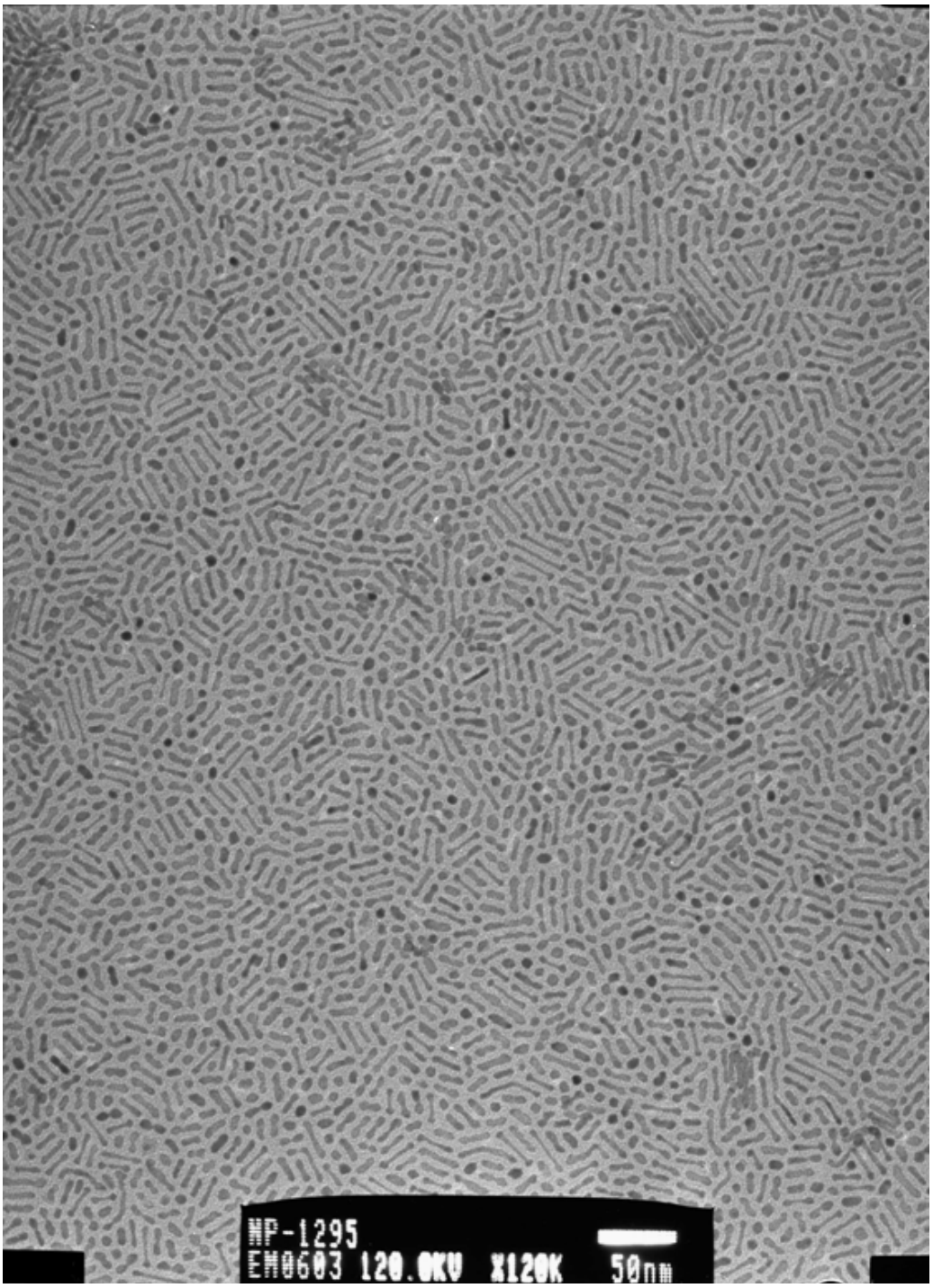

Figure 5.12 TEM image of a large area monolayer assembly of FePt nanorods with an average length of 20 nm.

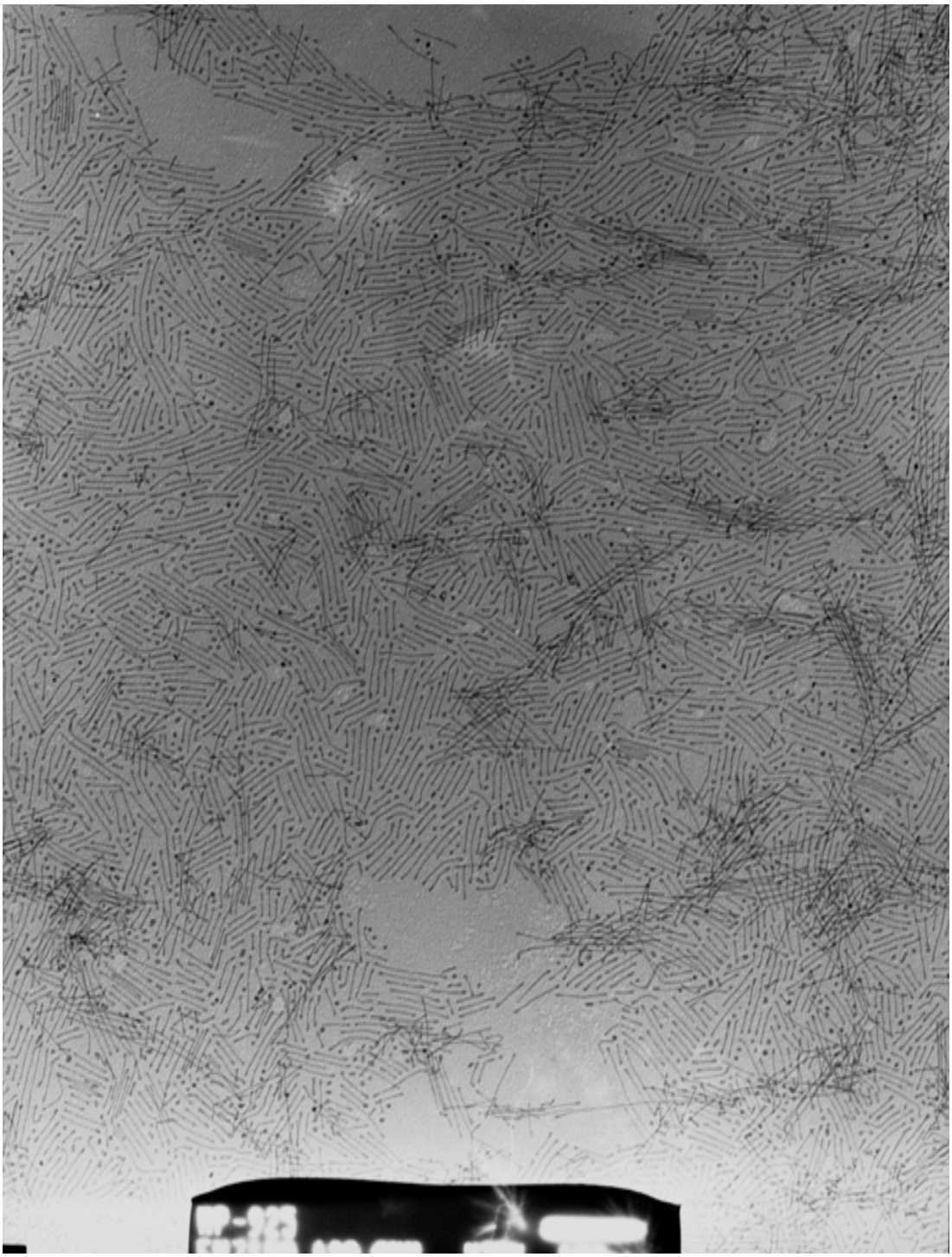

Figure 5.13 TEM image of a large area monolayer assembly of FePt nanorods with an average length of 50 nm.

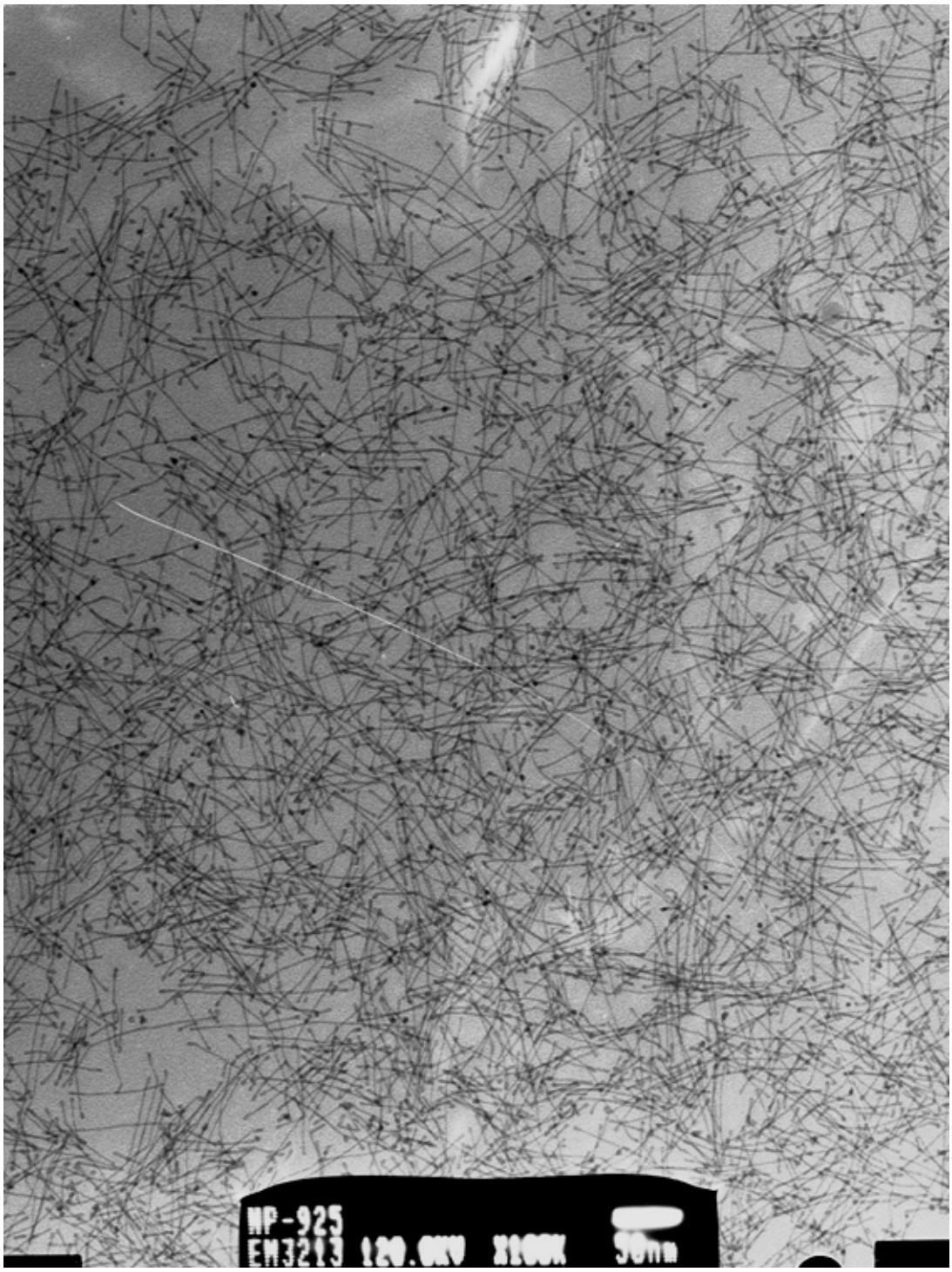

Figure 5.14 TEM image of a large area monolayer assembly of FePt nanowires with an average length of 150 nm.

5.2.3 Growth Mechanisms

Attempts were made to understand the formation mechanism of FePt nanorods/nanowires. Surfactants typically play a crucial role in controlling the size and shape of chemically synthesized nanocrystals.[77, 78, 118, 125] It has been believed that the formation of FePt nanorods/nanowires is related to the formation of cylindrical micelles that serve as templates. [114] Oleic acid and oleyl amine were chosen in our synthesis as they are the most common stabilizers used for synthesis of FePt nanoparticles.,[77, 78, 95] The anisotropic interaction between the capping agents and the different facets of Fe-Pt crystals should be the key for the formation of nanorods/nanowires.[128] For the typical synthesis of spherical FePt nanoparticles, surfactants are injected simultaneously after the addition of $Fe(CO)_5$. In our study, when oleylamine was added before the addition of $Fe(CO)_5$, the nanorods and nanowires were produced. To examine the effect of surfactants on the growth mechanism, we replaced oleylamine with hexadecylamine, which has an amine functional group. Similar morphological control over the Fe-Pt system was achieved, suggesting that the amine should be the crucial functional group in the anisotropic growth of Fe-Pt nanorods/nanowires.[114,123,125]

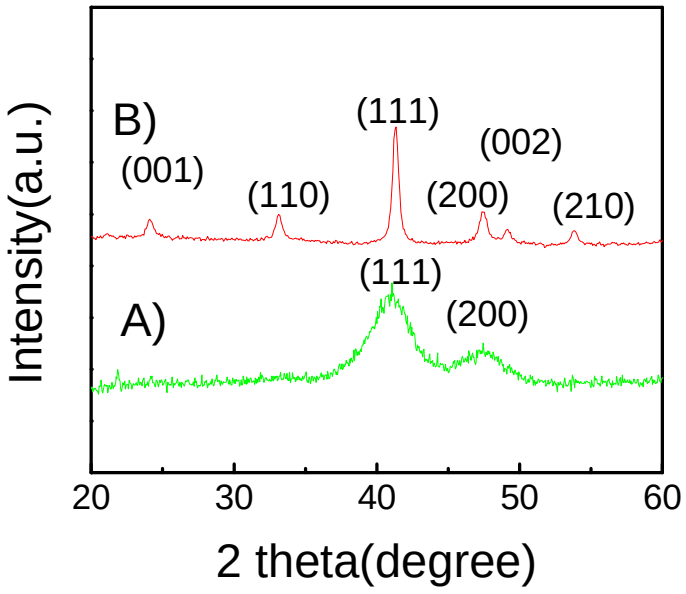

Figure 5.15 XRD patterns of A) as-synthesized FePt nanowires, and B) annealed under forming gas (Ar 93% + H_2 7%) at 650^o C for 1 hour.

In order to monitor the formation of FePt nanorods/nanowires we sampled the solution at different stages during synthesis and analyzed the morphology of samples by TEM. It was observed that thin necklace-like structures were initially formed before they grew up into nanorods/nanowires, similar to the process reported in previous references.[123, 125]

5.2.4 Magnetic Properties

The XRD pattern in Figure 5.15 (A) confirms that the as-synthesized FePt nanorods and nanowires possess a chemically disordered fcc crystal structure that has low magnetic anisotropy. The as-synthesized FePt nanorod and nanowire assemblies are superparamagnetic at room temperature.The temperature dependent magnetization was measured in a 100 Oe field between 5K and 300 K with the zero-field-cooling (ZFC) and field-cooling (FC) procedures for the 15 nm nanorods and the 150 nm nanowires (as shown in Figure 5.16). On cooling, the ZFC magnetization begins to drop and deviates from FC magnetization at blocking temperature (T_B). The M verses T curves show a peak characteristic of

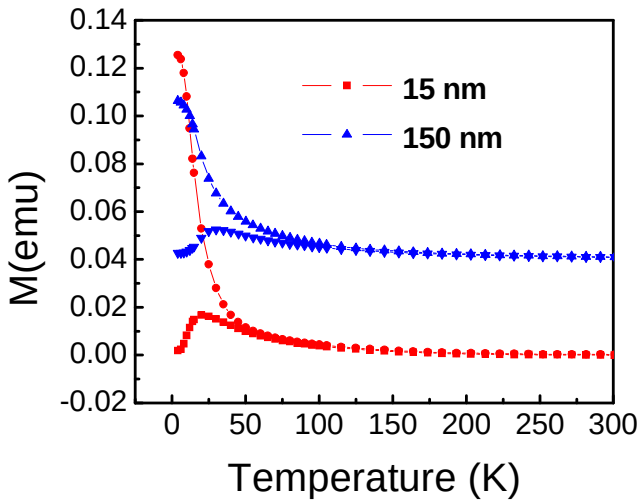

Figure 5.16.Zero-field-cooling and field-cooling curves measured at 100 Oe field between 5K to 300 K of the as-synthesized nanorods/nanowires of length 15 nm and 150 nm.

superparamagnetic transition. This study indicates that superparamagnetic behavior is blocked at 25 K and 40 K for 15 nm rods and 150 nm wires, respectively (Figure 5.16). These low blocking temperatures

are consistent with the low magnetocrystalline anisotropy of the fcc structure. Figure 5.17 shows hysteresis loops of as-synthesized 150 nm FePt nanowires at 5 K and 300 K. At 5 K FePt nanowires have coercivity of 4. 5 kOe and a saturation magnetization much higher than measured at 300 K.

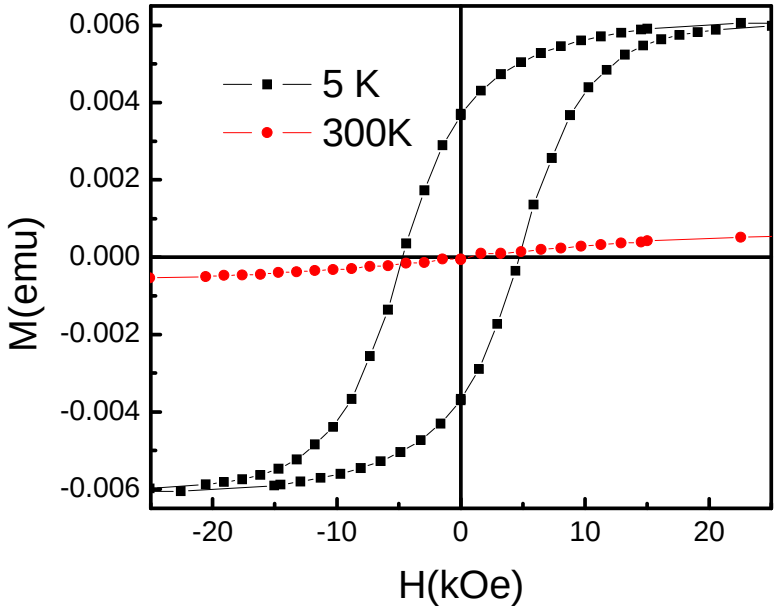

Figure 5.17Hysteresis loops of the as-synthesized 150 nm nanowires at 5 K and 300 K.

Heat treatment was applied to transform the disordered fcc FePt phase to the $L1_0$ phase, with high uniaxial magnetocrystalline anisotropy responsible for high coercivity.[127] Figure 5.15(B) shows the XRD pattern for the sample annealed in forming gas (Ar 93% + H_2 7%) at 650 ^oC for 1 hour. It can be clearly seen from this figure that both the peak position and intensity for the annealed sample match perfectly with the $L1_0$ structure, indicating that the tetragonal FePt phase was formed after the thermal annealing. The heat treatment on FePt nanorod/nanowire assemblies deposited on a Si substrate at 650 ^oC promotes sintering of FePt nanorods/nanowires, resulting in grain growth and drastic changes in morphology from rods/wires to continuous thin film. The grain size calculated from XRD patters after annealing by using the Scherrer formula was 25 nm. Preparation of $L1_0$ FePt nanorods/nanowires by using salt-matrix as a separating media[54, 84] to prevent sintering and grain growth during heat treatments

is underway. The hysteresis loops for the sample annealed in forming gas are shown in Figure 5.18. The coercivity value of the randomly oriented 150 nm nanowires annealed in forming gas at 650^{o} C for 1 hour is 24 kOe, indicating high magnetocrystalline anisotropy of the $L1_0$ FePt phase. The magnetic properties of nanoparticles/nanorods are related to their compositions. The EDX analysis of these samples revealed their final particle composition to be $Fe_{47}Pt_{53}$, $Fe_{48}Pt_{52}$, and $Fe_{47}Pt_{53}$, for 15, 50, and 150 nm rods/wires, respectively. The coercivity of these ferromagnetic assemblies is tunable by controlling the annealing temperature as well as the Fe/Pt initial molar ratio. The final composition was adjusted by changing the initial mole ratio of the metal precursors.

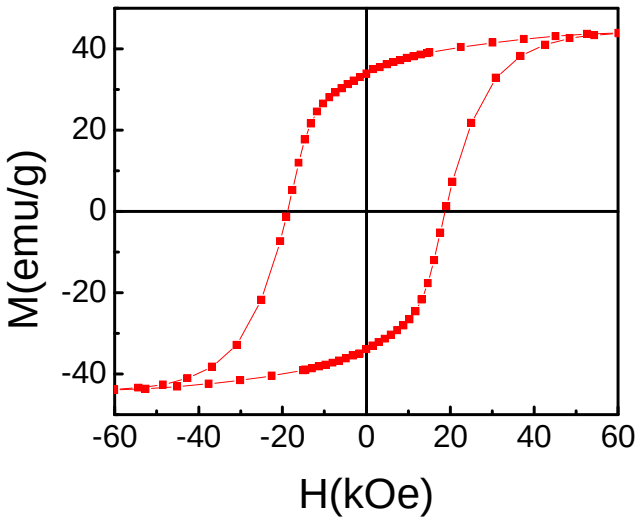

Figure 5.18. Room temperature hysteresis loop of the annealed FePt nanowires of length 150 nm at 650 ^{o}C for 1 hour in forming gas (Ar 93% + H_2 7%).

5.2.5 Conclusion

In summary, a simple procedure has been developed for the preparation of FePt nanorods/nanowires with uniform diameter of 3 nm and controllable length ranging from 15 to 150 nm. The sequence and the interval of injection of surfactants are the key to anisotropic growth of nanoparticle nuclei into nanorods/nanowires. The synthetic procedure reported here represents a substantial step in the controlled synthesis of uniform FePt nanorods/nanowires. The as-synthesized FePt nanorods/nanowires have chemically disordered fcc structure and are superparamagnetic at room

temperature. Their blocking temperature is size dependent, which increases with length of rods. After heat treatments, the fcc structured FePt nanorods/nanowires transformed into the $L1_0$ phase with coercivity up to 24 kOe. These nanorods/nanowires with controlled geometry and composition may be used as building blocks for future high-density recoding media, exchange-coupled nanocomposite permanent magnets and other nanodevices. Magnetic field alignment and consolidation experiments of FePt nanorods/nanowires are under process.

5.3 Shape Control of FePt Nanocrystals

5.3.1 Overview of the Issue

The synthesis of nanocrystals with different sizes and shapes has opened new technological horizons.[104, 128] Since it has been observed that the physical and chemical properties of nanoparticles are also related to their shape, the synthesis of nanocrystals with controllable shape has become a recent focus.[108, 110] Arranging nanocrystals into ordered patterns with a specific packing arrangement by self-assembly or other techniques is an important step toward the design of novel nanostructured materials and devices.[129, 130] In particular, FePt nanocrystals have been widely studied, because of their their uniaxial magnetocrystalline anisotropy promises great application potential in advanced magnetic materials such as ultra-high-density recording media and high-performance permanent magnets.[12, 78, 84, 95] Recent progress in chemical synthesis techniques for preparing FePt nanoparticles has shown a great deal of success in tuning particle size, while maintaining a narrow size distribution.[76, 77, 79] Progress has also been made in controlling the shape of FePt nanoparticles, including the preparation of one-dimensional structures such as nanorods and nanowires.[81, 123, 125] We described above that simultaneous reduction of $Pt(acac)_2$ and $Fe(CO)_5$ in the presence of 1,2-hexadecanediol, oleyl amine, and oleic acid in a high-boiling ether solvent leads to the formation of FePt nanorods and nanowires.[81]

Further experiments indicated that the shape of the FePt nanocrystals can be conveniently controlled through one-pot reactions without any ether solvent but just with surfactants. In this study, we give details of this novel facile method for synthesizing FePt nanocrystals with controlled shape and dimension, including nanowires, nanorods, spherical nanoparticles, nanocubes, and nanosized muti-

pods. Methods for controlling the diameter of nanorods will also be presented. In addition th magnetic properties of the nanocrystals and their changes upon heat treatments are studied.

5.3.2 Morphology and Structure

FePt nanocrystals were synthesized as described in Chapter 3 (Section 3.1.3). Figure 5.19 shows TEM images of monolayer assemblies of the as-synthesized FePt nanocrystals with different morphology, including nanowires, nanorods, oval-shaped particles, spherical particles, nanocubes, and multi-pods. It is known that surfactants play a vital role in the growth of nanocrystals.[76-78, 81, 95] The anisotropic interaction between the capping agents and the different facets of Fe-Pt crystals should be the key for the formation of differently shaped nanocrystals.[81] Typically, when a smaller amount of surfactants is injected simultaneously after the addition of $Fe(CO)_5$ in the ether solvent, spherical FePt nanoparticles are formed.[76-79] It has been found from our study that not only the molar ratio of surfactants but also the sequence in which surfactants and metal precusors are addded influence the shape of FePt nanoparticles. For example, nanorods and nanowires were obtained when oleyl amine was added before the addition of $Fe(CO)_{5,}$ followed by oleic acid at the molar ratio of oleylamine to oleic acid at 4:1(Figure 5.19(A) and 5.19(B)). Spherical particles were formed when both the surfactants were added simultaneously before the addition of $Fe(CO)_{5,}$ at the molar ratio of oleylamine to oleic acid at 4:1 (Figure 5.19(D)). Under the similar reaction conditions as the synthesis of spherical particles, the nanocubes and the multi-pods were obtained (Figure 5.19(E) and 5.19(F)), when the molar ratio of oleylamine to oleic acid was varied from 2:1 to 1:1. The as-synthesized FePt nanorods and nanowires (in Figure 5.19(A) and 5.19(B)) have a diameter of 3 nm with a length of about 20 and 150 nm, respectively. The diameter of the FePt nanorods can also be tuned from 3 nm to 5 nm (Figure 5.20(A) and 5.20(B)) by altering the molar ratio of oleylamine and oleic acid from 2:1 to 2:1.5 while other reaction parameters are kept unchanged. It can bee seen from Figure 5.22 (A) and 5.22(B) that the XRD patterns noticeably sharpening peaks with increaing the diamter of rods from increasing from 3 to 5 nm. A further increase of HDD and oleic acid led to the formation of oval-shaped nanoparticles (Figure 5.19(C)).

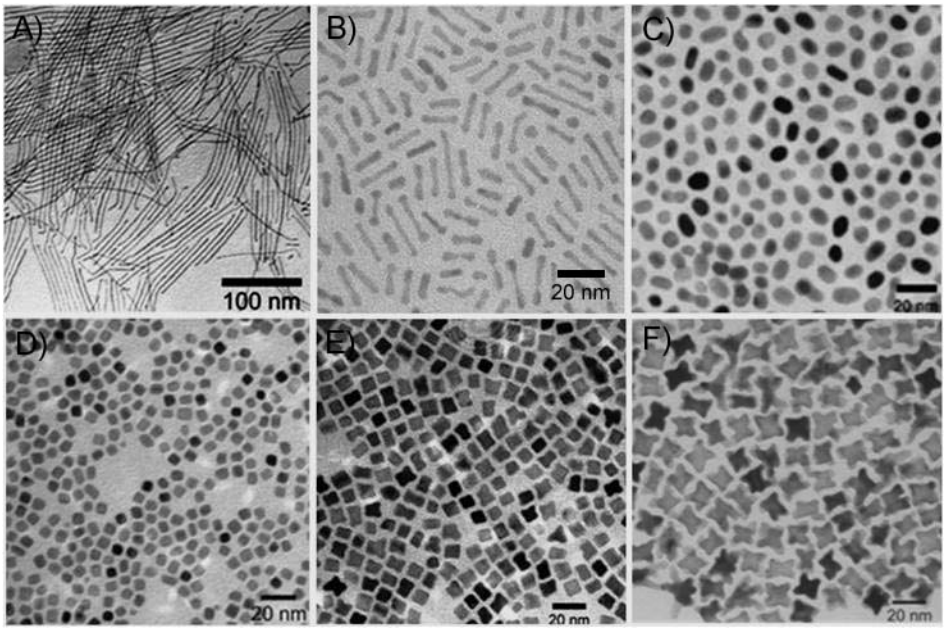

Figure 5.19 TEM images of monolayer assemblies of as-synthesized FePt A) nanowires, B) nanorods, C) oval-shape nanoparticles, D)spherical nanoparticles, D) nanocubes, and E) nanosized multi-pods.

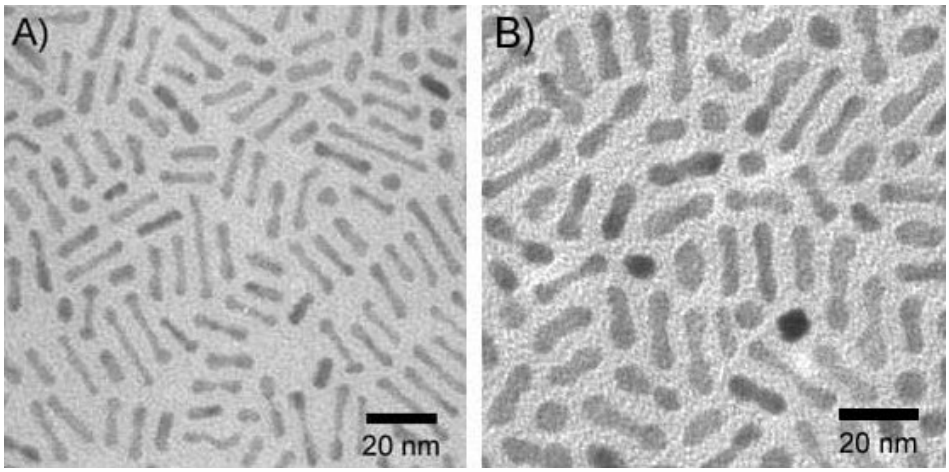

Figure 5.20 TEM images of monolayer assemblies of 20 nm long FePt nanorods with a diameter of A) 3 nm, and B) 5 nm.

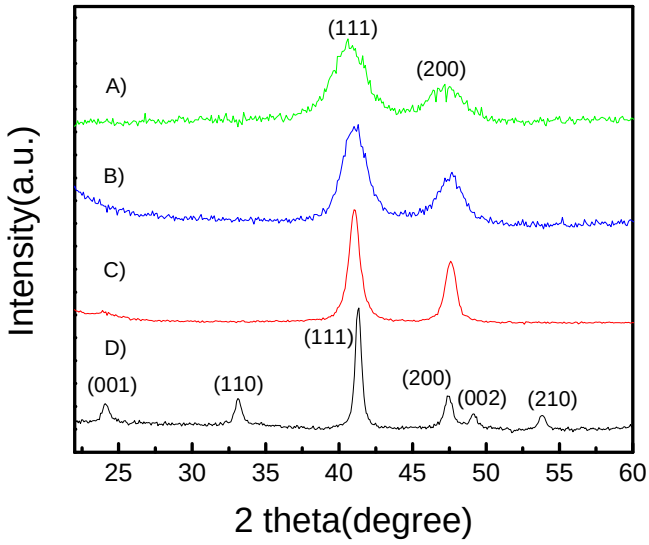

Figure 5.21 X-ray diffraction patterns of the as-synthesized FePt A) nanowires, B) spherical nanoparticles, C) multi-pods, and D) annealed FePt nanowires under forming gas (Ar 93% + H_2 7%) at 700 ^{o}C for 1 hour.

The XRD patterns in Figure 21.5 (A-C) confirm that the as-synthesized FePt nanocrystals possess a chemically disordered fcc crystal structure that has low magnetic anisotropy. The as-synthesized FePt nanocrystal assemblies are superparamagnetic at room temperature.

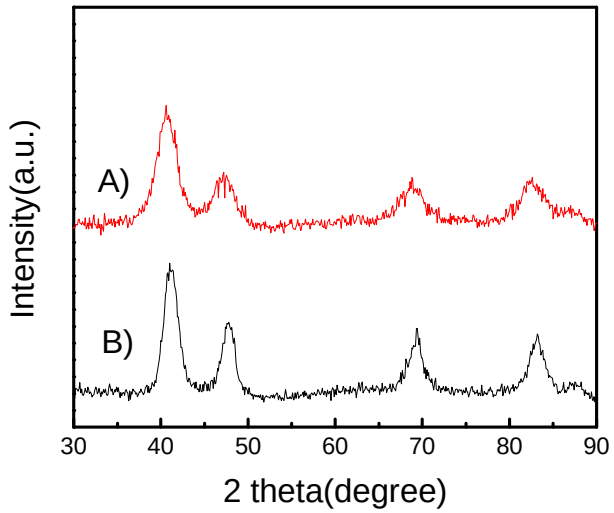

Figure 5.22 XRD patterns of the as-synthesized FePt nanorods of length 20 nm with a diameter of A) 3 nm, and B) 5 nm.

5.3.3 Magnetic Properties

Temperature dependent magnetization was measured for nanocrystals in a 100 Oe field between 5 and 300 K with the zero-field-cooling (ZFC) and field-cooling (FC) procedures. On cooling, the ZFC magnetization begins to drop and deviates from FC magnetization at the blocking temperature. The blocking temperature is defined as $T_B = KV/25K_B$, where K is the anisotropy energy constant, V is the volume of the particles, and K_B is the Boltzmann constant.[131] The M verses T curves show a peak characteristic of that for superparamagnetic transition. This observation indicates that superparamagnetic behavior is blocked at 20 K, 32 K, 85 K, and 134 K for 20 nm rods, 150 nm wires, 8 nm spherical particles, and 18 nm muti-pods, respectively (Figure 5.23). The change in T_B depends on the particle's volume, but the shape of the particles may also contribute to their anisotropy. The anisotropy constants of nanocrystals can be estimated from the measured T_B. In our study, differently shaped particles have different volumes. Therefore, it is hard to estimate exactly how much shape anisotropy contribute to the T_B of the nanocrystals.

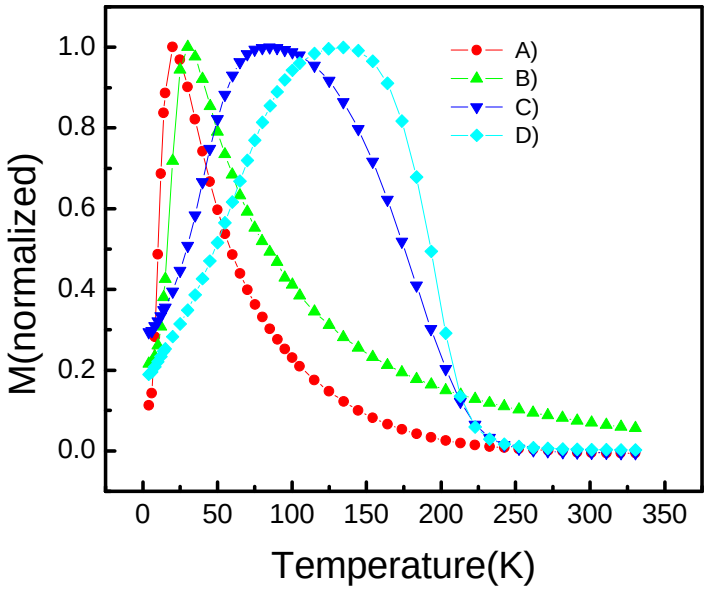

Figure 5.23 Magnetization versus temperature for as-synthesized FePt A) nanorods, B) nanowires, C) spherical nanoparticles, and D) multi-pods nanoparticles measured at 100 Oe field.

A heat treatment is needed to transform the disordered fcc FePt phase to the $L1_0$ phase with high uniaxial magnetocrystalline anisotropy, which is desirable for applications.[127] The as-synthesized FePt nanocrystal samples were annealed in forming gas (Ar 93% + H_2 7%) at 700 ^{o}C for 1 hour. It was found that both the peak positions and intensities of the annealed samples match perfectly with the $L1_0$ structure in XRD patterns. This indicates that the tetragonal FePt phase was formed after the thermal annealing at 700 ^{o}C. The heat treatments, however, also promote the sintering of FePt nanocrystals, which results in grain growth and a drastic change in morphology from discrete particles to continuous thin films. The average grain size calculated for annealed FePt nanowire assemblies, using the Scherrer formula, was 25 nm (Figure 5.22(D)).

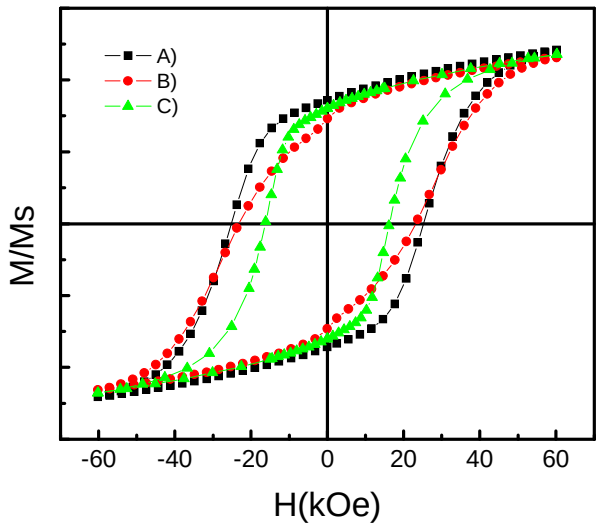

Figure 5.24 Hysteresis loops of FePt A) nanowires, B) multi-pods, and C) spherical particles annealed in forming gas (Ar 93% + H_2 7%) at 700 ^{o}C for 1 hour.

The hysteresis loops of randomly oriented nanowires, muti-pods, and spherical particles annealed in forming gas at 700 ^{o}C for 1 hour are shown in Figure 5.24 Differences in coercivity and the squareness of hysteresis loops are not completely known. These variations could be related to variation in the morphology and the microstructures of the annealed nanocrystal assemblies. Studies with high resolution TEM on the morphology and microstructure of annealed nanocrystal assemblies of different shapes on a

Si substrate of different shapes are under way. The high coercivity of up to 25 kOe of randomly oriented nanocrystals annealed in forming gas at 700 ^{o}C for 1 hour indicates high magnetocrystalline anisotropy of the $L1_0$ FePt phase. The compositions of the FePt nanocrystals were determined by EDX. Compositions of samples with high coercivity were found to be close to equi-atomic. The final composition was controlled by changing the initial molar ratio of the metal precursors. The coercivity of these ferromagnetic assemblies is tunable by controlling the initial molar ratio of Fe and Pt and the annealing temperature. Preparation of $L1_0$ FePt nanocrystals wtih different shapes by using salt-matrix as the separating media to prevent sintering and grain growth during heat treatment is underway.[54, 108]

5.3.4 Conclusion

In summary, a facile procedure has been developed for controlling the shape of FePt nanocrystals with a large variety of morphologies. The molar ratio of surfactants and the sequencing of the injection of the surfactants is the key to controlling the reaction kinetics and anisotropic growth of the nanocrystals. The as-synthesized FePt nanocrystals have chemically disordered fcc structure and are superparamagnetic at room temperature. Their blocking temperature is size dependent, which increases with particle size. After the heat treatment, the fcc structured FePt nanocrystals transformed into $L1_0$ phase with coercivity up to 25 kOe. These nanocrystals with controlled geometry and composition can be used as building blocks for future ultra-high-density recording media, exchange-coupled nanocomposite permanent magnets, and other nanodevices.

CHAPTER 6

$L1_0$ FePt NANOPARTICLES

6.1 $L1_0$ FePt Nanoparticles by Novel Annealing Technique

6.1.1 Introduction

Ferromagnetic nanoparticles with high magnetic anisotropy are essential for many advanced technological applications in order to overcome the superparamagnetic effect, which occurs because of thermal fluctuation when the size of particles reaches the nanoscale. Nanoparticles of FePt alloys are very attractive candidates for negating the superparamagnetic effect due to their high magnetocrystalline anisotropy ($K_u \sim 7 \times 10^7$ erg/cm^3), their high-saturation magnetization ($M_s \sim 1100$ emu/cm^3) in ordered $L1_0$ phase, and their superior chemical stability compared to other well-known hard magnetic materials such as Sm-Co and Nd-Fe-B.[25, 78, 132] Recently, $L1_0$ FePt nanoparticles have received tremendous attention as a result of their potential applications for ultra-high density magnetic recording media,[25, 78] nanocomposite permanent magnets, [12, 98] biomedical applications, [52] and nanodevices.[32]

Recent progress in chemical synthesis techniques for preparing FePt nanoparticles has shown a great deal of success in controlling particle size and shape while at the same time maintaining a narrow size distribution. [77-79, 80,133] Unfortunately, the chemically as-synthesized FePt nanoparticles have a disordered fcc structure with very low magnetocrystalline anisotropy, and such particles are therefore superparamagnetic at room temperature. High temperature annealing above 600 ^oC is necessary to realize phase transformation from $A1$ to $L1_0$ in FePt nanoparticles. The annealing, however, always leads to serious particle agglomeration and particle sintering, resulting in grain growth and destruction of nanoscale morphology, which are undesirable for many applications. Extensive efforts have been made since the year 2000 to obtain monodisperse $L1_0$ FePt nanoparticles after Sun et al. reported the chemical synthesis of fcc FePt nanoparticles at IBM. Elements such as Ag, Au, and Cu have been added to FePt

nanoparticles to lower the onset temperature for the A1 to the $L1_0$ phase transformation. Though the addition of elements in FePt nanoparticles has reduced the phase transition temperature, it has also resulted in enhanced grain growth.[134 -136] Direct chemical synthesis of $L1_0$ FePt nanoparticles has also been tried using high-boiling point solvents, but only partial magnetic hardening was achieved. [137-138] As an alternative, coating high-temperature material such as SiO_2, TiO_2 on FePt particles has been used to prevent particle sintering during the high-temperature magnetic hardening process.[139] Other approaches to obtaining monodisperse $L1_0$ nanoparticles include rapid thermal annealing, [140, 141] and pulse laser annealing. [142] Using most of these techniques resulted either in poor magnetic property and morphology or impurities on the particles. It is, therefore, highly desirable to find processing techniques to produce completely transformed $L1_0$ FePt monodisperse nanoparticles.

Recently, monodisperse $L1_0$ nanoparticles have been successfully prepared by a novel anealing technique developed in our lab, known as "salt-matrix annealing".[54, 84] In this chapter, our recent research results in producing monodisperse $L1_0$ FePt nanoparticles by salt-matrix annealing will be presented. Issues related to particle-size, such as morphology, chemical ordering, magnetic properties, phase transformation, and high-temperature stability of $L1_0$ FePt nanoparticles will be discussed in detail.

6.1.2 Structure and Chemical Ordering

$L1_0$ FePt nanoparticles were prepared by salt-matrix annealing technique as described in Chapter 3 (Section 3.2.2). As mentioned at the beginning of this chapter, the chemically synthesized FePt nanoparticles have a disordered fcc structure with very low magnetic anisotropy. Phase transformation from *A*1 to $L1_0$ ordered phase is required to develop magnetic hardening in FePt nanoparticles. The as-synthesized fcc FePt nanoparticles with different diameters (from 2 to 15 nm) embedded in salt-matrix were annealed in forming gas (Ar 93% + H_2 7%) under different annealing conditions in order to investigate A1 to $L1_0$ phase transformation. XRD patterns of FePt nanoparticles sufficiently annealed in salt-matrix show that annealed particles have the $L1_0$ phase. Figure 6.1 shows the XRD patterns of the 6 nm as-synthesized fcc FePt nanoparticles and the XRD patterns after these particles annealed under different conditions in salt-matrix. It was found that the (001) and (110) peaks characteristic for the $L1_0$ FePt phase started when a sample was annealed at 600^{o}C.

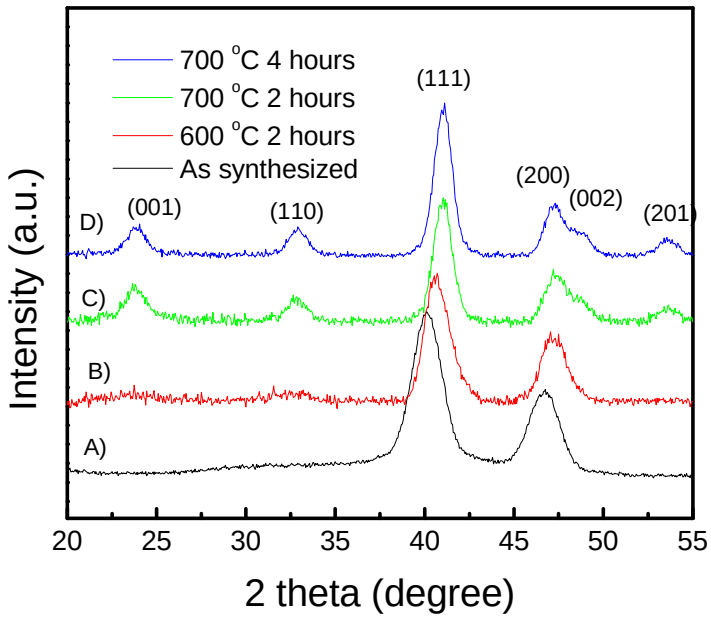

Figure 6.1 XRD patterns of 6 nm FePt nanoparticles: A) as-synthesized nanoparticles and annealed in salt-matrix; B) 600 °C for 2 hours; C) 700 °C 2 hours; D) 700 °C for 4 hours in forming gas (Ar 93% + H_2 7%) in the ratio of FePt nanoparticles to NaCl powder = 1:400 by weight.

With increasing annealing time and temperature, the A1 to $L1_0$ phase transition was fully developed as seen by the appearance of the more pronounced superlattice peaks (001) and (110). The position of the peaks shifts to the high-angle direction as the transition is fully developed (obvious for the (111) peak), which is due to the lattice length change when atomic structure changes from fcc to fct. It was also found that smaller particles need more time to complete the phase transition. In our experiments, after being annealed for 2 hours at 700°C, the fcc particles with 3 to 8 nm sizes were not transformed to $L1_0$ phase completely. Longer annealing time was required to complete the transformation from A1 to $L1_0$ phase for these particles as compared to 15 nm particles. Systematic annealing study of FePt nanoparticles (size ranging from 3 to 15 nm) in salt-matrix shows that the particles annealed at 700 °C for 4 hours complete the A1 to $L1_0$ phase transition. FePt nanoparticles were also annealed for extended time periods up to 16 hours at 700°C. No obvious evidence of further development of the transition was found from XRD patterns for particles annealed longer than 4 hours. From the XRD patterns, no peak of NaCl was found,

indicating that salt was not left after washing the mixture with water. ICP results also confirmed that the NaCl amount is negligible (only 0.099% in weight) and that the average composition of the annealed particles is close to equitomic.

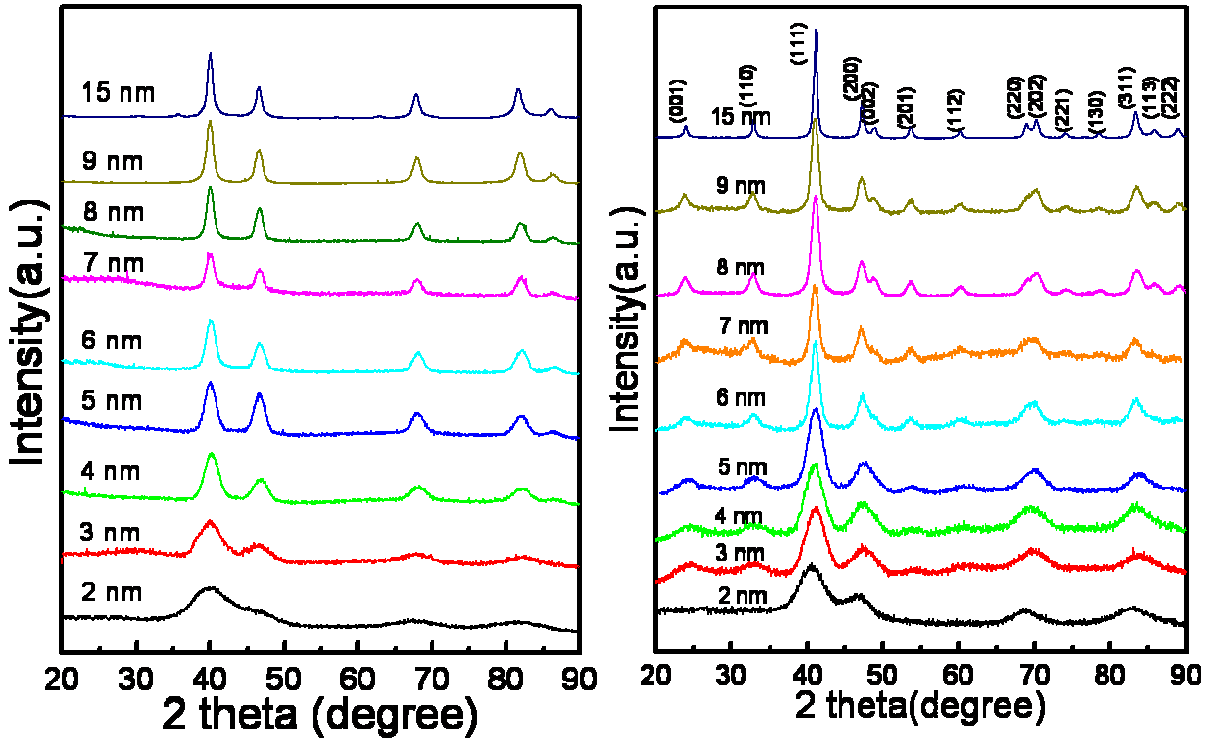

Figure 6.2 XRD patterns of the FePt nanoparticles: (Left) 2 to 15 nm as-synthesized fcc nanoparticles, and (Right) 2 to 15 nm nanoparticles obtained after salt-matrix annealing at 700 ^{o}C for 4 hours in forming gas (Ar 93% + H_2 7%) in the ratio of FePt to NaCl = 1:400 by weight.

Figure 6.2 (Left) shows the XRD patterns of the as-synthesized 2, 3, 4, 5, 6, 7, 8, 9 and 15 nm fcc FePt nanoparticles and Figure 6.2 (Right) shows XRD patterns of 2, 3, 4, 5, 6, 7, 8, 9 nm and 15 nm FePt nanoparticles annealed in salt-matrix at 700^{o}C for 4 hours in forming gas in the ratio of FePt nanoparticles to NaCl powder = 1:400 by weight. It is observed from the XRD patterns of annealed nanoparticles that A1 to $L1_0$ phase transition occurred upon annealing for nanoparticles whose size was larger than 3 nm. However, in the case of 2 nm FePt particles, even after being annealed at 700 ^{o}C for 8 hours, only (111) and (200) fundamental peaks were found and no superlattice peaks (001) and (110) developed, which

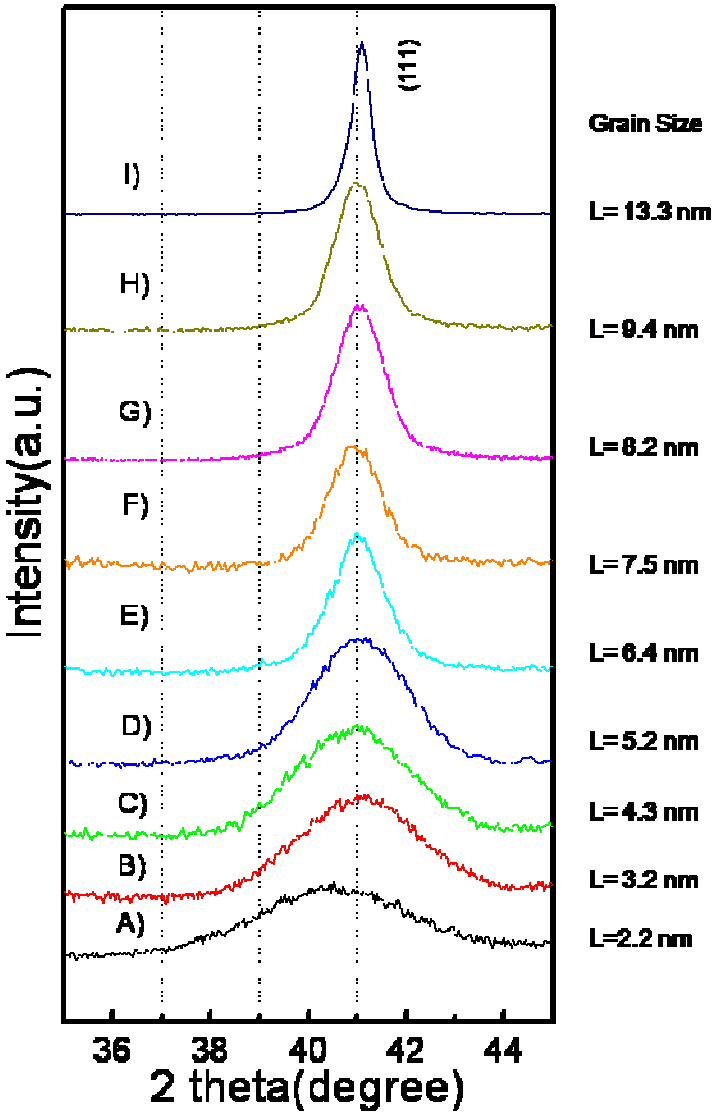

Figure 6.3 (111) XRD peaks of: A) 2 nm, B) 3 nm, C) 4 nm, D) 5 nm, E) 6 nm, F) 7 nm, G) 8 nm, H) 9 nm, and I) 15 nm. FePt nanoparticles were annealed at 700^{o}C for 4 hrs in forming gas (Ar 93% + H_2 7%) in the ratio of FePt to NaCl = 1:400 by weight.

indicates that the fcc to fct structure transition did not occur even when the nanoparticles were annealed for longer periods of time. It was also noticed that the position of the peaks does not shift to the high-angle direction that is caused by the lattice length change when atomic structure changes from fcc to fct. The grain sizes of the particles were calculated using the Scherrer equation:

$$L = \frac{0.94\lambda}{B(2\theta)\cos\theta} \tag{6.1}$$

where L is the crystal dimension; λ = 0.154056 nm is the wavelength of the X-ray; and $B(2\theta)$ is the full width in radians subtended by the half-maximum intensity width of the peak at angle θ. The (111) peaks were chosen to calculate the grain sizes as demonstrated in Figure 6.3. The average grain sizes of the $L1_0$ FePt nanoparticles annealed at 700 ^{o}C for 4 hrs were obtained at 2.2, 3.2, 4.3, 5.2, 6.4, 7.5 8.2, 9.4, and 13.3 nm for the 2, 3, 4, 5, 6, 7, 8, 9 and 15 nm particles, respectively, which matches the TEM observations. These grain sizes also represent the particle sizes because all of the particles are single crystalline except the 15 nm particles. The relatively smaller grain size for the 15 nm particles is obviously because of the polycrystalline structure of the 15 nm $L1_0$ FePt nanoparticles.[54, 84] Thus, it is also confirmed by XRD patterns that salt-matrix annealing completes the fcc to fct phase transition and prevents the grain growth during the heat treatments.

It has been observed in our experiments that smaller fcc nanoparticles need longer annealing time to complete the A1 to $L1_0$ phase transition. It has been reported that experimental and theoretical studies have shown that the degree of chemical ordering in FePt nanoparticles is related to the particle size. Ordering cannot be achieved when the particle size is below a critical size, which is approximately 2 to 4 nm as stated by previous studies.[31, 143-145] We carried out a systematic study on the size-dependent chemical ordering of FePt nanoparticles with the 2, 3, 4, 5, 6, 7, 8, 9 and 15 nm annealed in salt-matrix for 4 hours at 700^{o}C. The long-range order parameter is determined by the following formula:[146]

$$S \cong 0.85\left(\frac{I_{001}}{I_{002}}\right)^{\frac{1}{2}} \tag{6.2}$$

where I is the integrated intensity of the [001] and [002] peak from the XRD pattern, respectively.

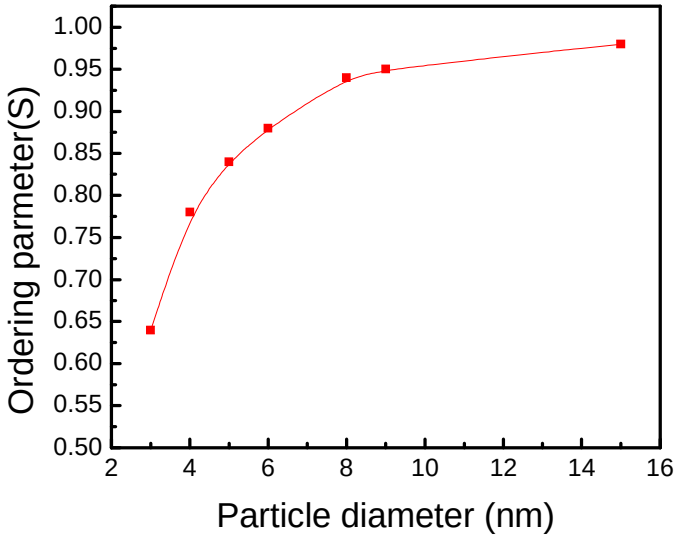

Figure 6.4 Long-range order parameter versus particle diameter of $L1_0$ FePt nanoparticles. 3 to 15 nm FePt nanoparticles were obtained after the salt-matrix annealing at 700 ^{o}C for 4 hours in forming gas (Ar 93% + H_2 7%) in the ratio of FePt to NaCl = 1:400 by weight.

As expected, S increases with increasing annealing temperature and time.[147] It reaches the highest value for different particle sizes when the annealing condition is 700^{o}C for 4 hours. In the case of 2 nm FePt particles, S vanishes because no [001] superlattice structure is found, even after being annealed at 700^{o}C for 8 hours, indicating that no A1 to $L1_0$ phase transition occurred in the 2 nm FePt particles. Figure 6.4 shows the relation between S and particle diameter for particles annealed at 700^{o}C for 4 hours. S increases as the particle diameter increases. When the annealing condition is 700^{o}C for 4 hours, S of 3, 4, 5, 6, 8, 9 and 15 nm FePt particles is 0.64, 0.78, 0.84, 0.88, 0.94, 0.95, and 0.98, respectively. This indicates that chemical ordering is more complete for FePt nanoparticles of larger size when the particles are annealed under the same conditions. This is obvious because most of the atoms are on the surface of the particles when particle size goes down to few nanometers. The ordering parameter of 15 nm FePt particles is very close to unity, indicating a nearly complete chemical ordering. As we see below in Figure 6.10, the coercivity follows the same trend as the ordering parameter. Higher coercivity corresponds to higher ordering parameter, except for 15 nm, which may be attributed to polycrystalline morphology (HRTEM shown in Figure 6.7(l)).

6.1.3 $L1_0$ Particles Morphology

The morphology of the $L1_0$ FePt nanoparticles obtained by salt-matrix annealing was closely monitored by TEM and HRTEM observations. It was found that the $L1_0$ FePt nanoparticles aggregate more easily than for the as-synthesized fcc FePt nanoparticles because of the magnetic attractive force between the particles with the force being a result of the strong dipolar interaction. The aggregations can be re-dispersed by ultra-sonication vibration in high-viscosity solvents, such as cyclohexanone, if diluted in solvent. Monodisperse nanoparticles can be observed with proper operations in TEM specimen preparations as seen in Figure 6.5. Figure 6.5 (A-I) shows the TEM images of the 2, 3, 4, 5, 6, 7, 8, 9 and 15 nm FePt particles annealed at 700 ^{o}C for 4 hours in forming gas (Ar 93% + H_2 7%) in the ratio of FePt to NaCl = 1:400 by weight. It is seen that the annealed particles are still monodisperse with a standard deviation of less than 10% in diameter with unchanged particle size and shape. It has been confirmed that the salt-matrix annealing technique has successfully prevented the particles with sizes from 2 to 15 nm from sintering and growth at 700 ^{o}C which is high enough for a complete phase transformation from the fcc to the fct structure except for 2 nm particles.[54, 84] It is also important to note that particle shape can also be retained by using this annealing method. The 8 nm fct particles have a cubic shape, as their precursors before the annealing had, indicating that the shape of the nanoparticles survived the heat treatment. Figure 6.6 shows TEM images of the 4 nm fcc FePt nanoparticles annealed using two different ratios of NaCl powder to FePt nanoparticles (20:1 and 400:1) by weight at 700 ^{o}C for 4 hours in forming gas (Ar 93% + H_2 7%). The particles annealed using lower salt ratio had significant particle sintering and grain growth (Figure 6.6(C)). It has been found in our experiments that the salt to FePt particle ratio has to be higher than 400:1 to prevent completely sintering and growth of particles when annealed at 700 ^{o}C for 4 hours or longer.[84]

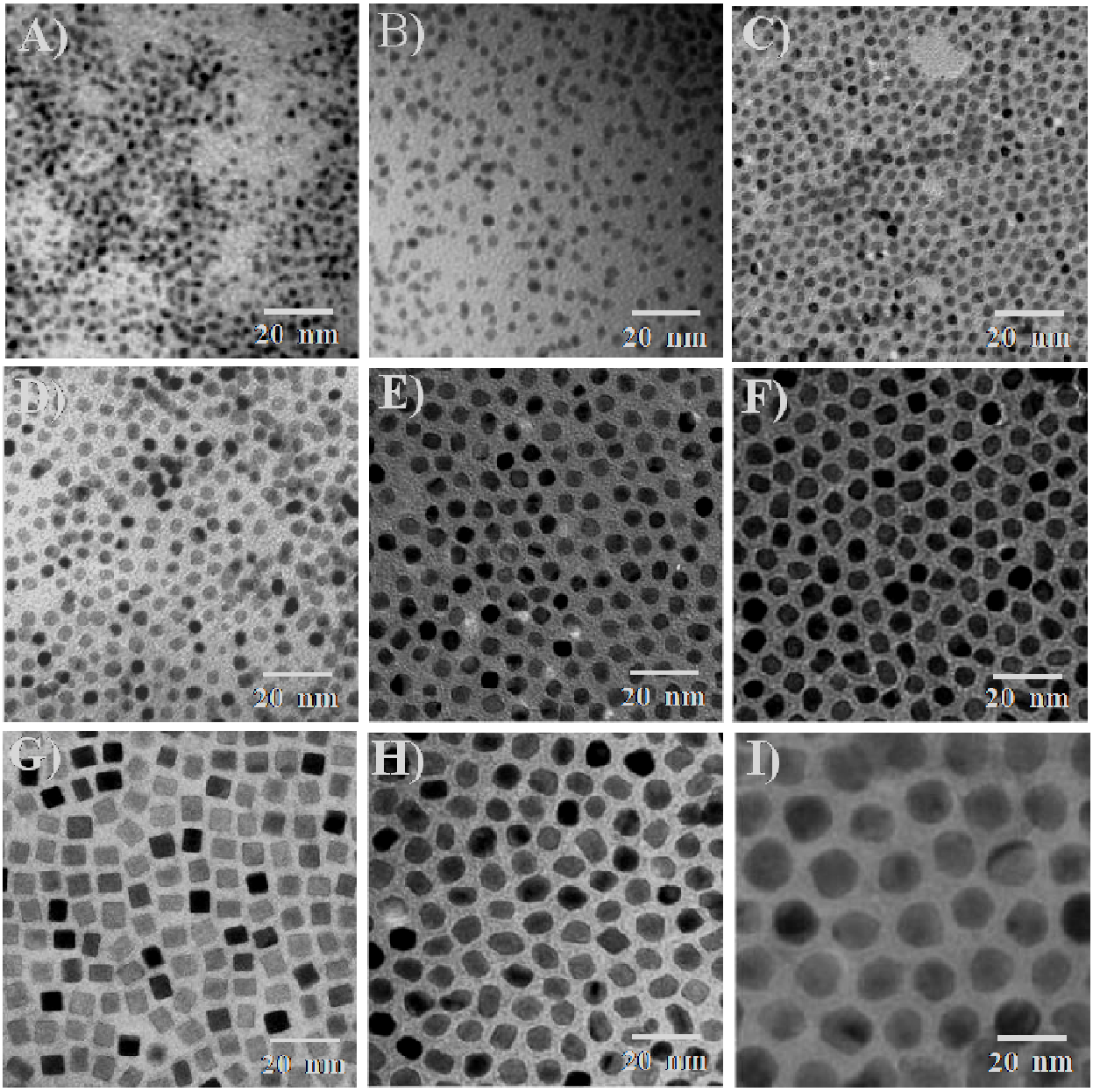

Figure 6.5 TEM images of 2, 3, 4, 5, 6, 7, 8, 9 and 15 nm FePt nanoparticles obtained after annealing at 700 ^{o}C for 4 hours in forming gas (Ar 93% + H_2 7%) in the ratio of FePt to NaCl = 1:400 by weight.

It has been found from our experimental observations that the salt particle size has no significant effect on the annealing, and the presence of salts has not altered the fcc to fct transition temperature. Annealing of larger FePt particles at higher temperatures and for extended time should be accompanied by higher salt to FePt ratio in order to avoid sintering. Figure 6.7(A-I) shows HRTEM images of single particles of 2, 3, 4, 5, 6, 7, 8, 9 and 15 nm FePt nanoparticles annealed at 700 ^{o}C for 4 hours. HRTEM observations have revealed that when the particle size is smaller than or equal to 9 nm, the $L1_0$ FePt nanoparticles are monocrystalline, whereas the 15 nm $L1_0$ FePt particles are polycrystalline.[54]

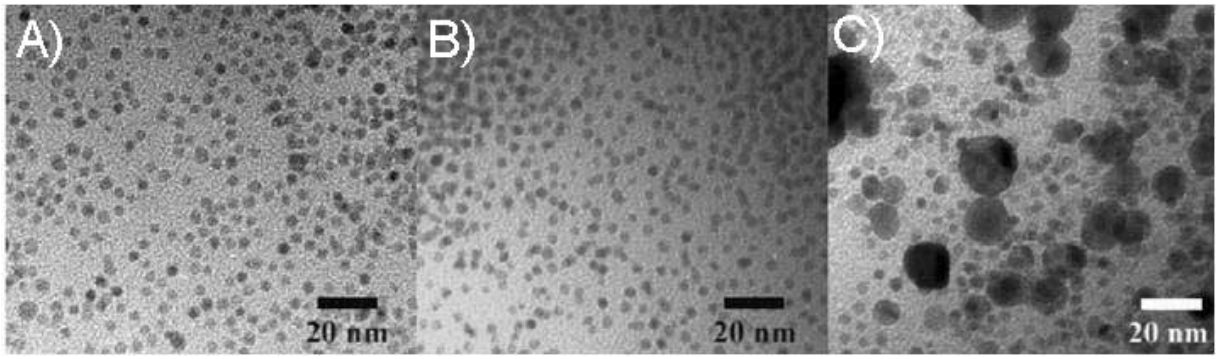

Figure 6.6 TEM images of A) 4 nm as-synthesized fcc FePt nanoparticles and 4 nm FePt nanoparticles annealed at 700 ^{o}C for 4 hours in forming gas (Ar 93% + H_2 7%) in the ratio of FePt to NaCl, and B) 1:400 and C) 1:20 by weight.

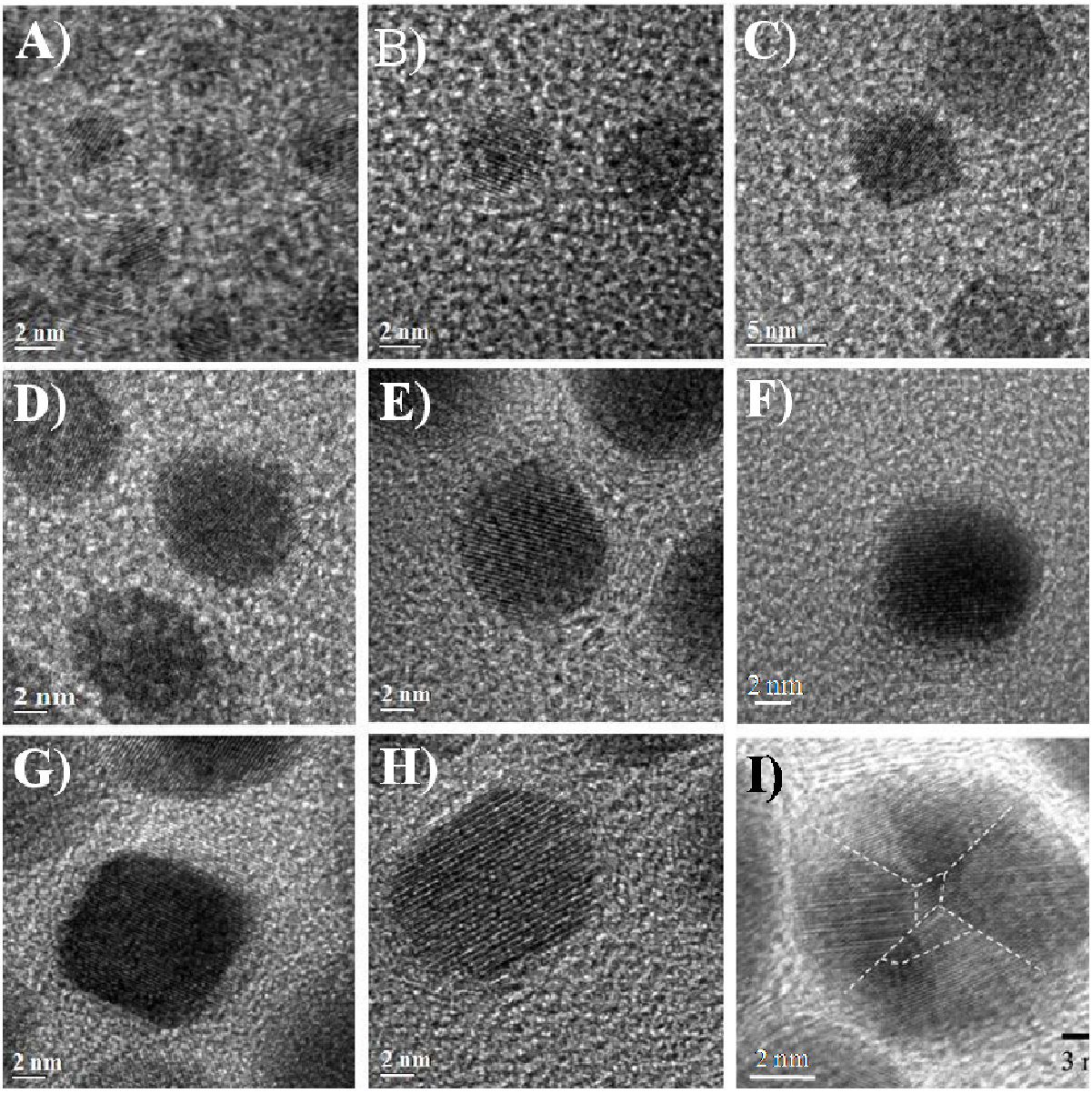

Figure 6.7 HRTEM images in inset of 2 nm to 15 nm FePt nanoparticles obtained after annealing at 700 ^{o}C for 4 hours in forming gas (Ar 93% + H_2 7%) in the ratio of FePt to NaCl = 1:400 by weight.

Analysis of particle size and size distribution of some of the selected samples of $L1_0$ FePt nanoparticles was carried out using SAXS in the transmission geometry as described in Chapter 4 (Section 4.4.1). The size of the nanoparticles was estimated by the direct fitting of model curves to experimental scattering curves. All the samples were fitted with a spherical model for experimentally

measured scattering curves. Figure 6.8 and Figure 6.9 show the experimentally measured scattering curves and particle size and size distribution obtained by fitting scattering curves for 4 nm and 8 nm $L1_0$ FePt nanoparticles. The blue-colored lines represent the simulated data (in Figure 6.8 and Figure 6.9 left side). The size distributions of the particles were obtained by fitting the scattering profiles (as seen in figure 6.8 and Figure 6.9 right side). It can be seen that the particles have a narrow size distribution with less than 10%. The average particle diameter calculated from SAXS measurements is consistent with that observed by TEM micrographs. The average diameters were estimated to be 4.8 nm for 4 nm and 8.6 nm for 8 nm, which agree well with the TEM images.

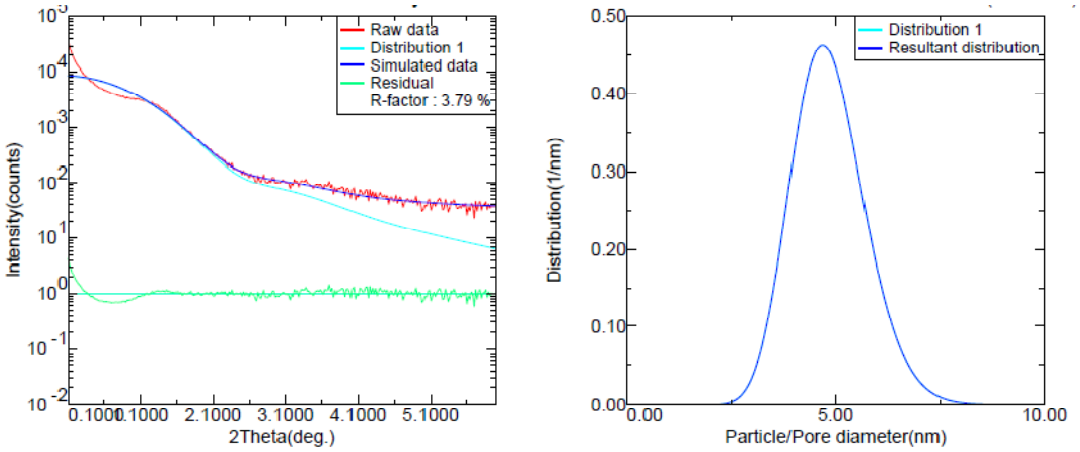

Figure 6.8 SAXS patterns (left), and size distribution of 4 nm FePt nanoparticles (right).

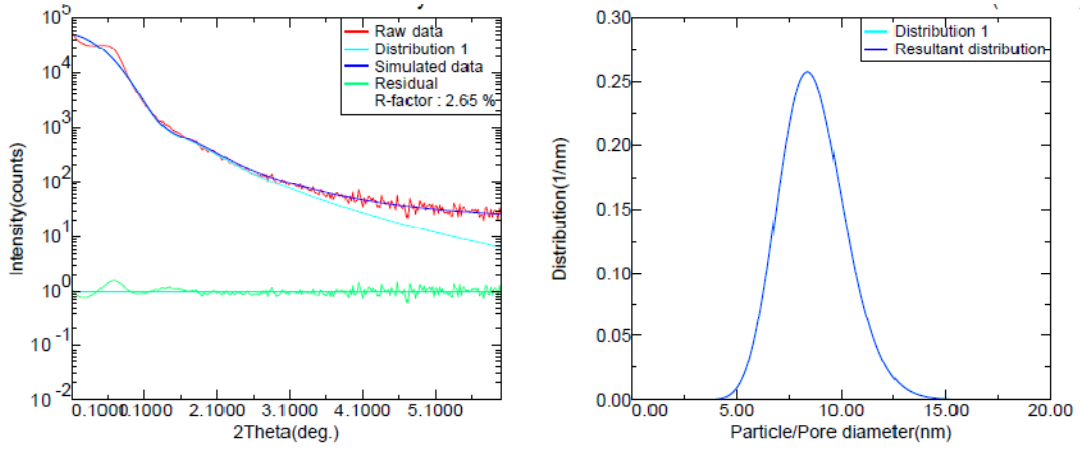

Figure 6.9 SAXS patterns (left), and size distribution of 8 nm FePt nanoparticles (right).

6.1.4 Magnetic Properties of $L1_0$ Nanoparticles

The $L1_0$ FePt nanoparticles obtained after salt-matrix annealing were mixed with epoxy to measure their magnetic properties. After the epoxy dried, the magnetization loops were measured with a SQUID magnetometer in different directions. Figure 6.10 shows the hysteresis loops of the 8 nm $L1_0$ FePt nanoparticles obtained after annealing in salt-matrix under different conditions. With increasing annealing temperature and time the hardening of the particles increases as that improves the chemical ordering of particles (as discussed above). Particles annealed at 700 ^{o}C for 4 hours exhibited very large coercivity up to 35 kOe at room temperature. Figure 6.11 shows the hysteresis loops at 300 K of the $L1_0$ FePt nanoparticles with different diameters. In the relatively small nanoparticles, the transition is not as complete as in large particles, which gives the two-phase behavior (as seen by the loops in Figure 6.11). The coercivity, *Hc*, increases with increasing particle size (*d*) when $d \leq 8$ nm. Giant coercivity values of up to 35 kOe have been obtained from the monodisperse 8 nm $L1_0$ nanoparticles, which may be related to their faceted shape.

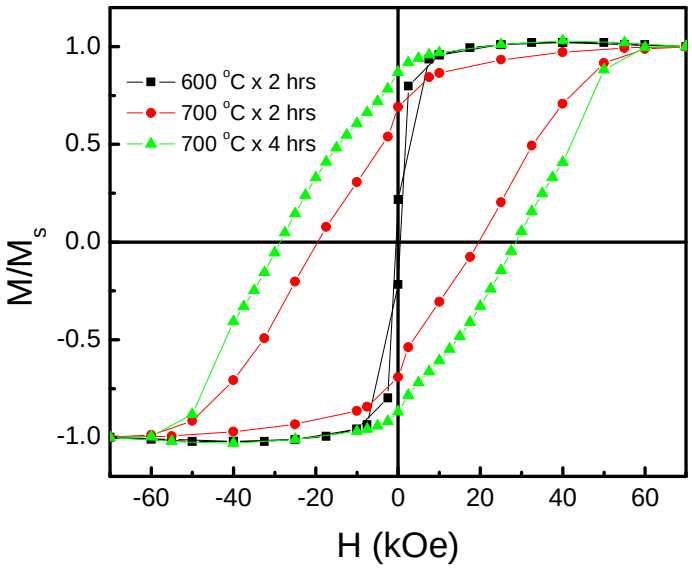

Figure 6.10 Hysteresis loops of 8 nm FePt nanoparticles annealed in salt-matrix under different annealing temperatures and annealing times in forming gas (Ar 93% + H_2 7%) in the ratio of FePt to NaCl = 1:400 by weight.

The enhancement of *H*c with increased particle size can be attributed partly to the size-dependent chemical ordering discussed above. However, larger particles of 15 nm have lower *H*c than the 8 nm particles. This may be caused by the polycrystalline structure, as intergranular exchange coupling leads to reduced magnetocrystalline anisotropy.[54] The exchange coupling can be further seen from the relatively high remanence ratio *M*r/*M*s > 0.5, where *M*r and *M*s are remanence and saturation magnetization, respectively. The reduced coercivity may also be attributed to multiple *c*-axes within a nanoparticle, which can lead to a significantly reduced effective anisotropy.[54] Figure 6.12 shows that the *M*s values decrease with decreasing particle size and are lower than the value for the bulk $L1_0$ phase at room temperature. The main reason for dependence of magnetization with particle size may be related to the reduced magnetization on the surfaces of the nanoparticles.[54, 84] Figure 6.13 shows temperature dependence of coercivity values of the 3, 4, 8, and 15 nm $L1_0$ FePt nanoparticles. It is interesting to see that the magnetic hardening of 4 nm particles was more temperature dependent than particles for large size. The reason for this requires further study.

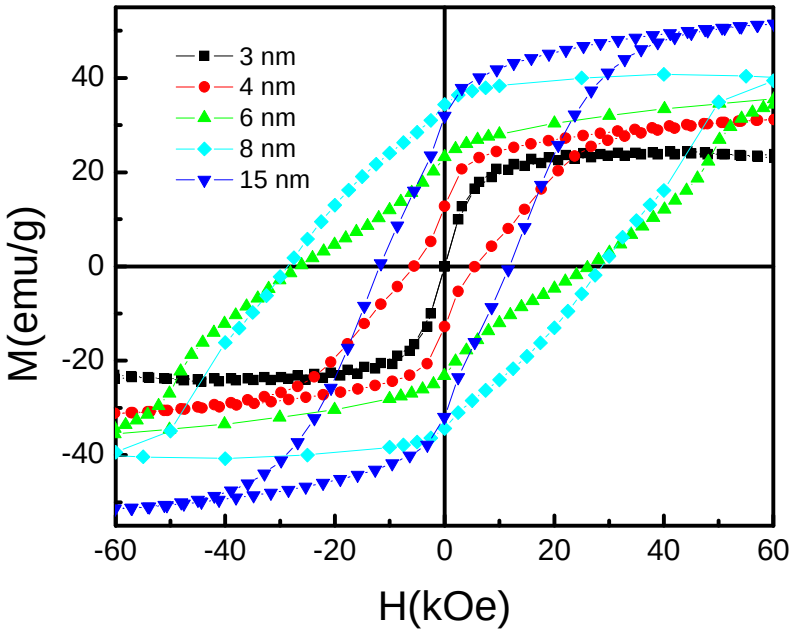

Figure 6.11 Hysteresis loops of 3, 4, 6, 8 and 15 nm $L1_0$ FePt nanoparticles obtained after salt-matrix annealing at 700 ^{o}C for 4 hours in forming gas (Ar 93% + H_2 7%) in the ratio of FePt to NaCl = 1:400 by weight.

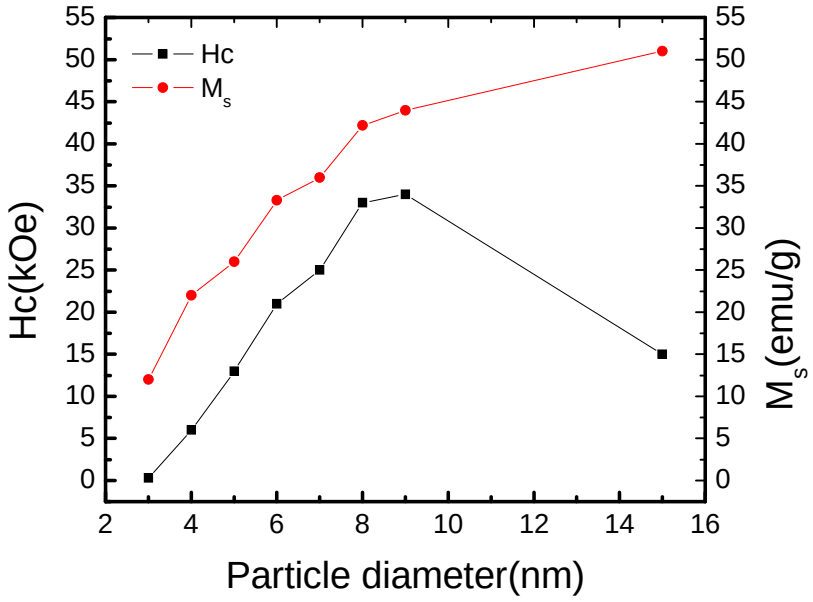

Figure 6.12 Size dependent coercivity and magnetization of $L1_0$ FePt nanoparticles.

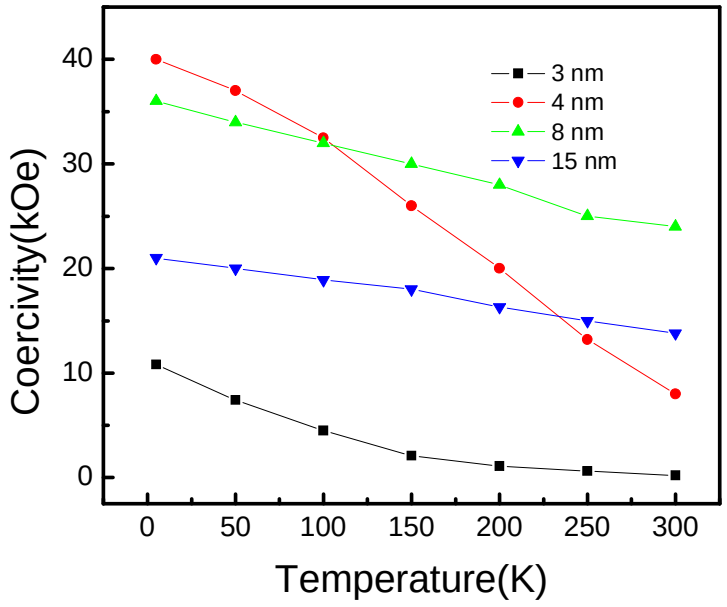

Figure 6.13 Coercivity versus temperature for different sizes of $L1_0$ FePt nanoparticles.

6.1.5 Nano-EDS Analysis on Single $L1_0$ FePt Nanoparticle

The $L1_0$ FePt nanoparticles were further characterized by HRTEM and Nano-Beam EDS to study the composition variation within a single nanoparticle. For comparison, two different batches of 8 nm FePt nanoparticles were chosen each having differently shaped hysteresis loops (smooth loop and loop with kink) and each annealed under same conditions (as shown in Figure 6.14). Both the samples were annealed for 4 hours at 700 ^{o}C under salt-matrix. The Nano-EDS spectrum of several individual particles gave a Fe/Pt atomic ratio very close to equi-atomic for the 8 nm FePt sample with a smooth hysteresis loop and fully transferred to fct structure as seen in Figure 6.16. However, it was found that the 8 nm FePt sample having a kink in the hysteresis loop consisted of large variations in the composition of particles even though the average composition of the sample by EDX was close to equi-atomic.

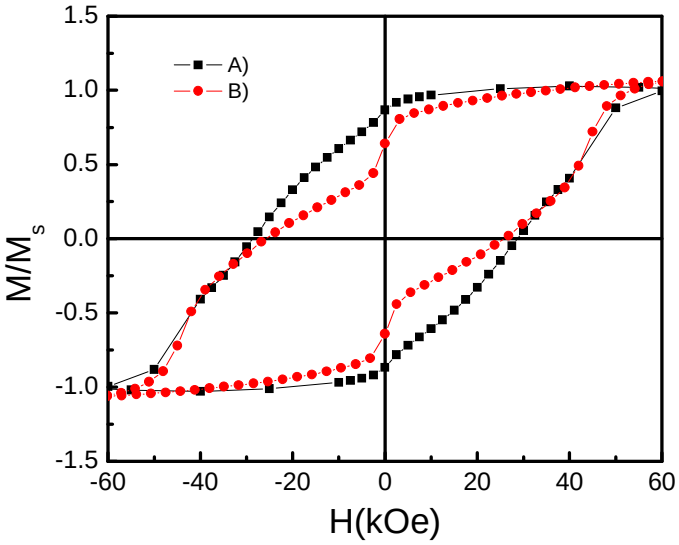

Figure 6.14 Hysteresis loops of 8 nm $L1_0$ nanoparticles obtained after salt-matrix annealing at 700 ^{o}C for 4 hours in forming gas (Ar 93% + H_2 7%) A) smooth loop, and B) loop with kink.

Interestingly, it was observed that even a single particle had variation in composition within the particle, suggesting that chemical ordering did not occur completely in some of the particles in the sample. HRTEM image analysis of individual particles also revealed that for some of the particles both the fcc and fct structure co-existent in a single particle (as shown in Figure 6.15(B)).

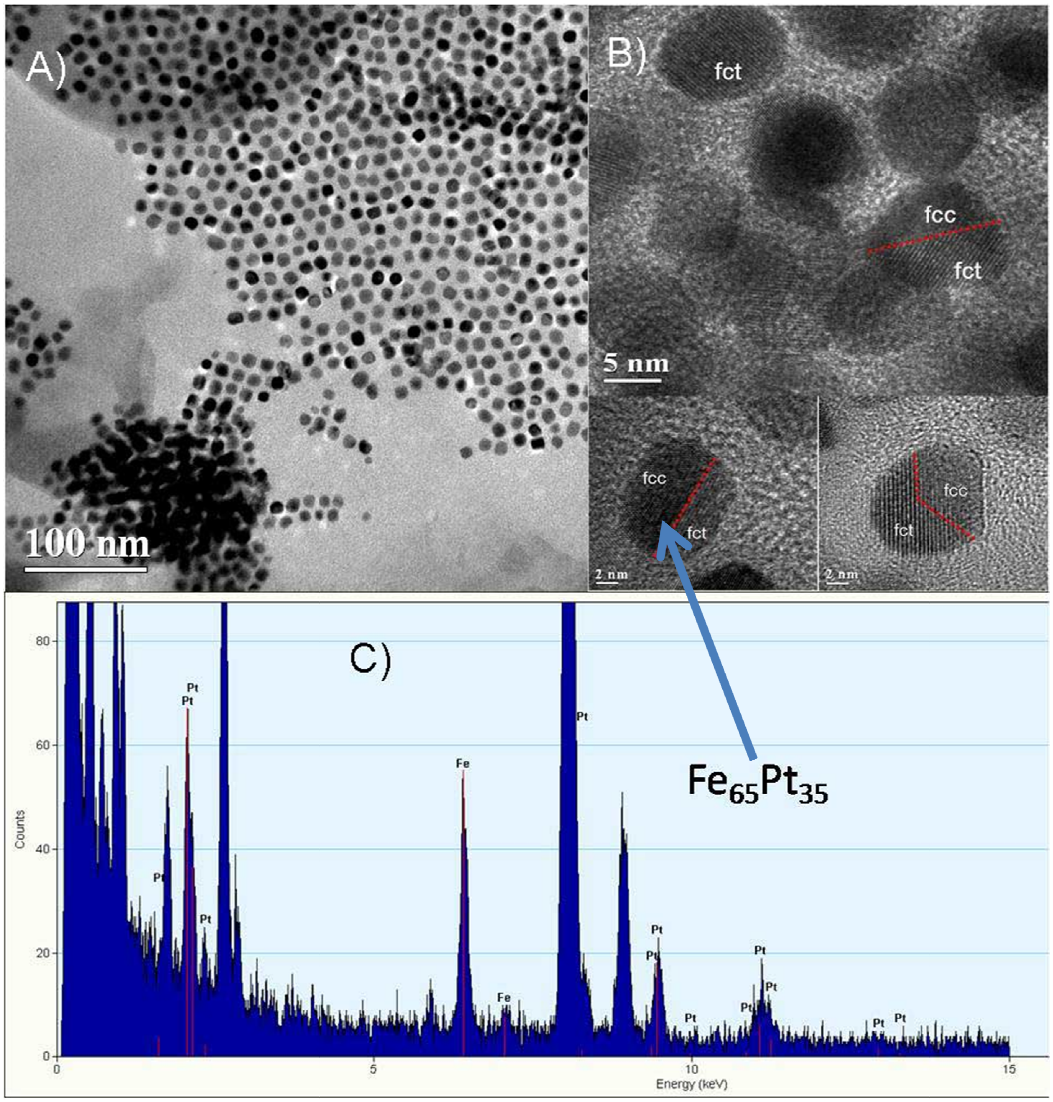

Figure 6.15 A) TEM image, B) HRTEM images and C) Nano-EDS spectrum of single 8 nm FePt nanoparticle showing compositional variation within the particles and the and the co-existence of both the fcc and fct structure in some of the particles (particles were annealed at 700 ^{o}C for 4 hours in forming gas(Ar 93% + H_2 7%)).

This suggests that the big kink in the hysteresis loop was due to the co-existence of both the fcc and fct structures. It should be noted from the phase diagram of FePt alloy that the thermodynamically stable $L1_0$ ordered FePt phase occurs only when the FePt alloy composition has between of approximately 35 and 65 atomic percent Fe. This suggests that the fcc to fct structure transformation did

not occurr or was not completed for fcc FePt nanoparticles whose composition range was not close to the equi- atomic percent of Fe and Pt.

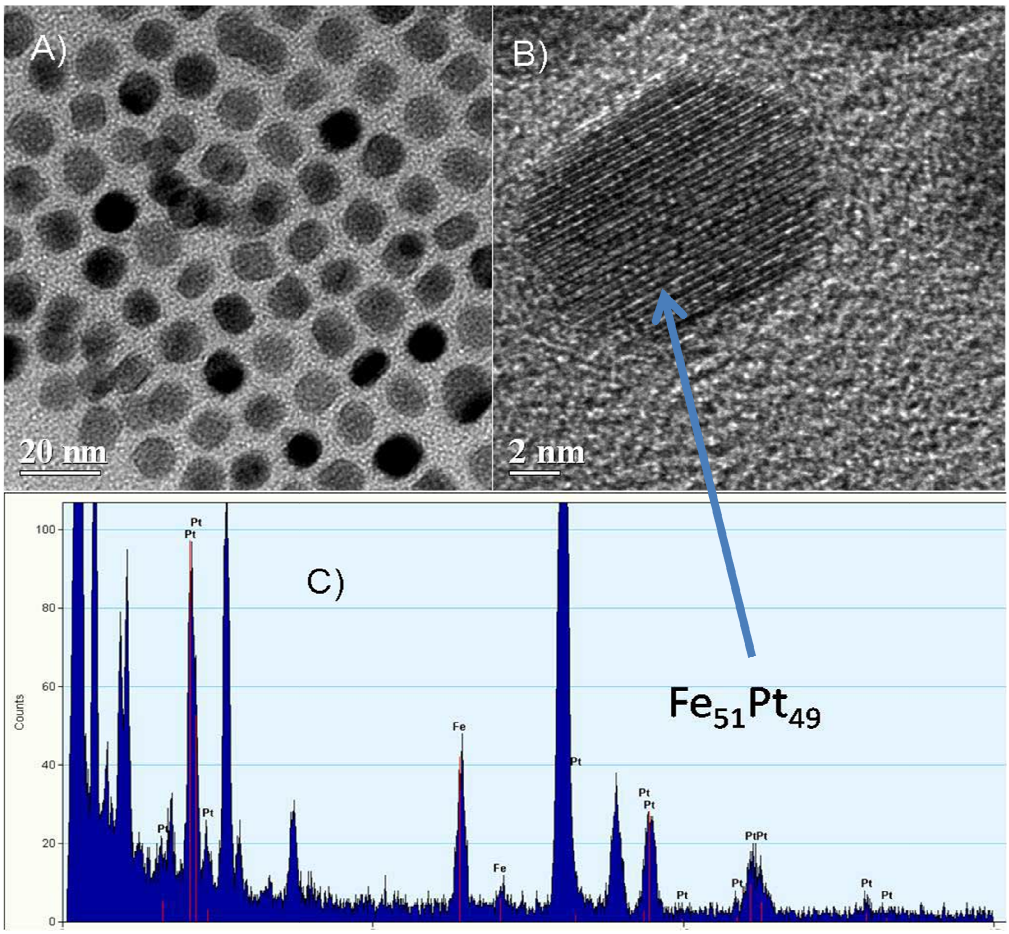

Figure 6.16 A) TEM image, B) HRTEM image and C) Nano-EDS spectrum of a single 8 nm FePt nanoparticles showing close to equi-atomic composition of Fe and Pt and fct structure (particles were annealed at 700 ^{o}C for 4 hours in forming gas(Ar 93% + H_2 7%)).

6.1.6 Phase Transition in 2 nm FePt Nanoparticles

For 2 nm FePt particles, even after being annealed at 700 ^{o}C for 8 hours, only (111) and (200) fundamental peaks were found, and no superlattice peaks (001) and (110) developed (as shown in Figure 6.17), which indicates that the fcc to fct structure transition did not occur even when the nanoparticles were annealed for longer than 8 hours. It has also been noticed that the position of the peaks does not

shift to the high-angle direction, which is caused by the lattice length change when atomic structure changes from fcc to fct.

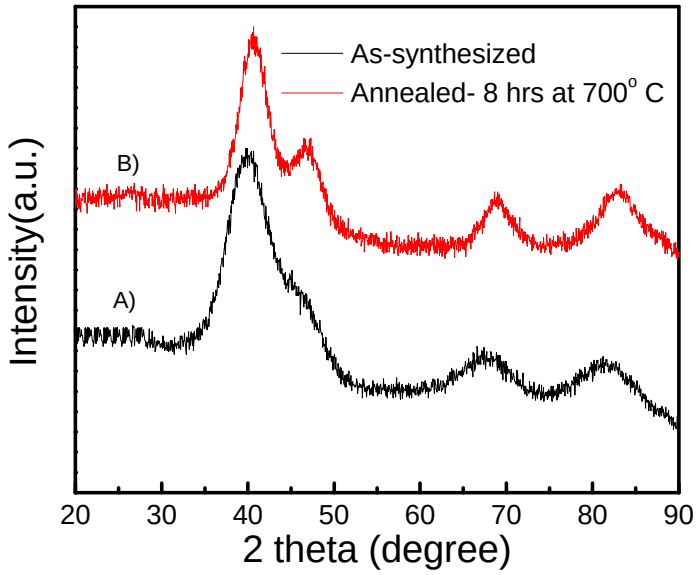

Figure 6.17 XRD patterns of A) as-synthesized 2 nm FePt nanoparticles, and B) 2 nm FePt nanoparticles annealed in salt-matrix at 700 ^{o}C for 8 hours in forming gas (Ar 93% + H_2 7%).

Figure 6.18 (A-B) shows the TEM images of as-synthesized 2 nm FePt nanoparticles and 2 nm FePt nanoparticles annealed in salt-matrix for 8 hours at 700 ^{o}C in forming gas. It can be seen from the TEM image that 2 nm FePt nanoparticles retained their size even when annealed at 700 ^{o}C for an extended period of time. Selected area electron diffraction (SAED) was therefore also used to identify the crystalline structure of the particles, especially for the smaller particles (Figure 6.18 (C)). The SAED patterns show that the annealed nanoparticles are $L1_0$ phase if the particle size is equal to or larger than 3 nm (Figure 6.18 C (i)). However, the SAED pattern of 2 nm particles in Figure 6.18 C (ii) does not show (001) and (110) rings (in contrast to the SAED pattern of the fct nanoparticles shown in Figure 6.18C (i). This indicates that the 2 nm FePt particles cannot be transformed to the fct structure under this annealing condition. We extended the annealing time to 8 hours, and the results remained the same. This direct experimental observation is consistent with theoretical predictions and is fundamentally important as well

as being significant for specific applications. It can be concluded that when the particle size is smaller than a critical value of around 3 nm, chemical ordering will not take place.

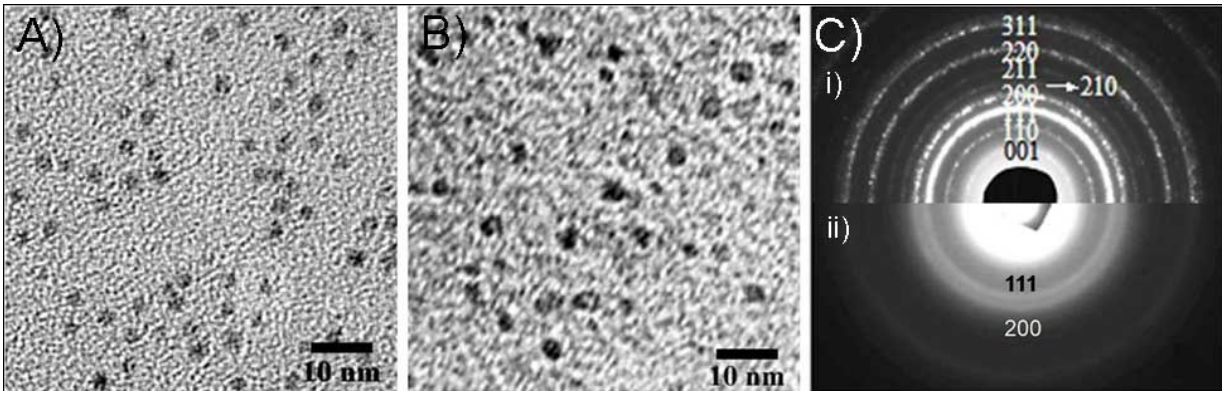

Figure 6.18 TEM images of A) as-synthesized 2 nm FePt nanoparticles, B) 2 nm FePt nanoparticles annealed in salt-matrix for 8 hours at 700 ^{o}C in forming gas (Ar 93% + H_2 7%), and C) SAED of i) 4 nm $L1_0$ FePt nanoparticles, and ii) 2 nm FePt nanoparticles annealed in salt-matrix for 8 hours at 700 ^{o}C.

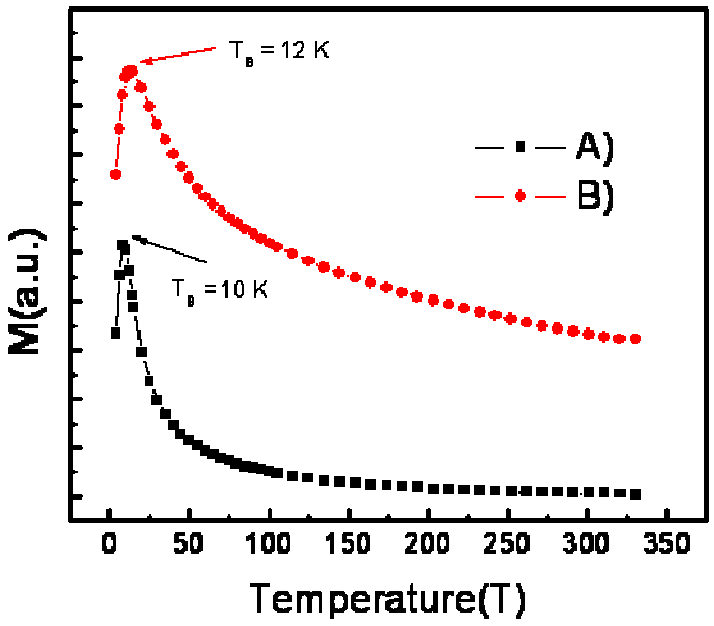

Figure 6.19 ZFC curves of A) as-synthesized 2 nm FePt nanoparticles, and B) 2nm FePt nanoparticles annealed in salt-matrix for 8 hours at 700 ^{o}C in forming gas(Ar 93% + H_2 7%).

Figure 6.19 (A-B) gives the ZFC curves of 2 nm FePt as-synthesized nanoparticles and 2 nm FePt nanoparticles annealed in salt-matrix for 8 hours at 700 ^{o}C in forming gas. It is interesting to see that the blocking temperatures (T_B) of 2 nm FePt nanoparticles before and after annealing are 10 K and 12 K respectively, suggesting that phase transformation did not occur when these particles were annealed for an extended time and at high temperature.Figure 6.20 (A-B) shows the hysteresis loops of 2 nm FePt nanoparticles before and after heat treatment for 8 hours at 700 ^{o}C at different temperature. The demagnetization curves have similar shapes before and after annealing, but annealed particles have slight higher coercivities in the corresponding temperatures.

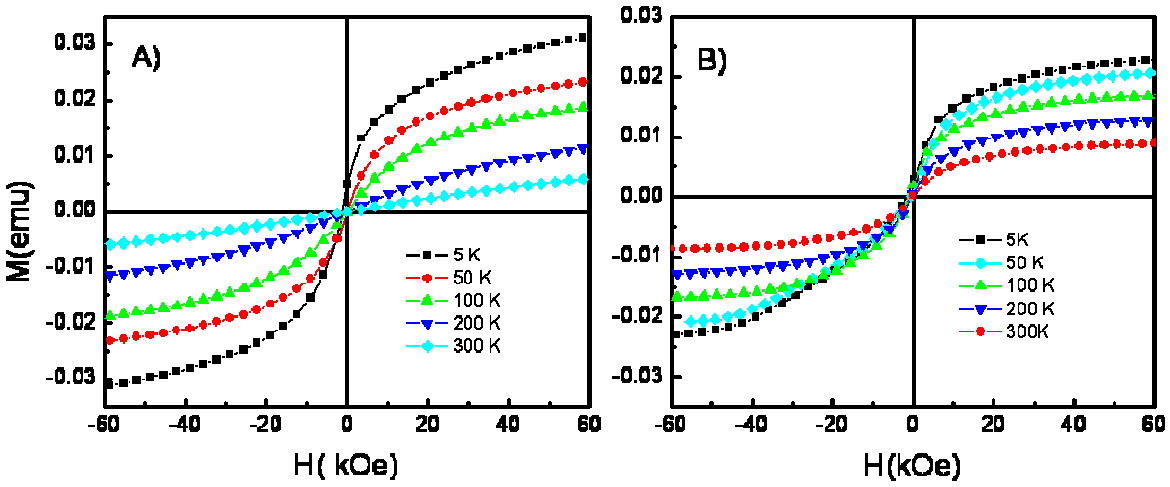

Figure 6.20 Hysteresis loops of 2 nm FePt nanoparticles measured at different temperatures A) as-synthesized nanoparticles, and B) nanoparticles annealed in salt-matrix for 8 hours at 700 ^{o}C in forming gas (Ar 93% + H_2 7%).

6.1.7 Phase Transition in 3 nm $L1_0$ Nanoparticles

As mentioned earlier, phase transformation of 2 nm FePt did not occur even after annealing for an extended period of time (> 8 hours). According to theoretical and experimental reports, the critical size for the phase transition from fcc to fct should be around 3 nm, [31, 143-145] which is attributed to the kinetics of atomic diffusion that is dependent on particle size. Therefore it is, interesting to look more closely at 3 nm FePt nanoparticles.

Figure 6.21 (a) and (b) shows the high-resolution TEM images of the 3nm FePt nanoparticles before and after annealing in salt-matrix at 700 ^{o}C for 4 hours, respectively. It can be seen that the particle sizes are retained after the annealing. Both the as-synthesized and annealed nanoparticles are monodisperse with a standard deviation of about 5-10 % in diameter, which is based on more than 100 particles from the high-resolution TEM images. A large region STEM high-angle annular dark field (HAADF) image (Figure 6.21(c)) also shows no sintering of the annealed particles. To check the phase transition by the salt-matrix annealing, the selected area electron diffraction (SAED) patterns was made for the particles before and after the annealing. The SAED patterns showed that the as-synthesized and annealed nanoparticles are fcc and fct phase, respectively.

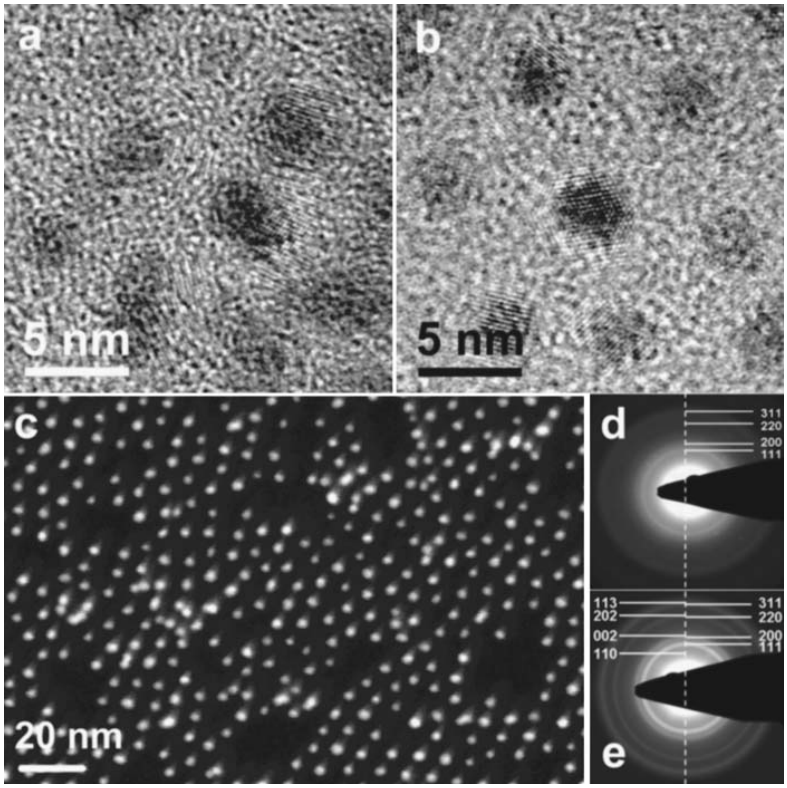

Figure 6.21 TEM analysis of the 3 nm FePt nanoparticle before and after salt-matrix annealing: (a) and (b) HRTEM images of the particles before and after salt-matrix annealing, respectively, (c) STEM HDAAF image of the annealed particles, (d) and (e) SAED patterns of the particle before, and after annealing, respectively.

The XRD patterns of the FePt nanoparticles (as shown in Figure 6.22) confirmed that the disorder structure was transferred to the ordered fct structure after the salt-matrix annealing. Figure 6.22 also gives the XRD pattern of the FePt film that was obtained by dropping the nanoparticles on a Si wafer and by traditional annealing at 700 ^{o}C for 1 hour without salt-matrix annealing. The grain size in this case was estimated around 30 nm.

To detect the degree of structural ordering of the $L1_0$ particles, the chemical ordering parameter S was calculated by using equation (6.2). It was found that S of the 3 nm annealed particles is 0.62. It is far lower than that of 4 nm $L1_0$ particles which is around 0.78.[84] The low observed S may be caused by the difficulties fo achieving an equilibrium state due to slow kinetic process for small particles, which agrees with theoretical works.[148] This result also shows that there may not be a “critical” and “onset” size for the transition, rather, there is a gradual correlation between particle size and chemical ordering.

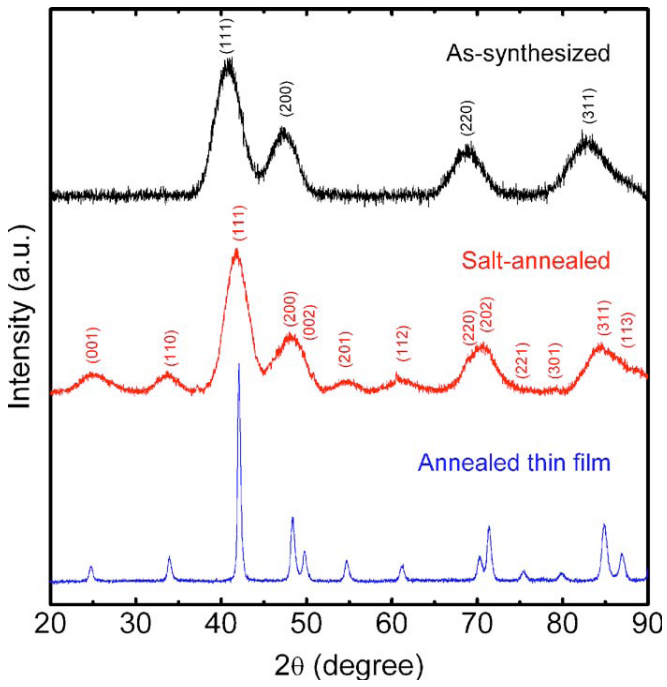

Figure 6.22 XRD patterns of the FePt nanoparticles before and after salt-matrix annealing. The pattern of the annealed film, which is made from the 3 nm nanoparticles, is also included for comparison.

Figure 6.23 gives the ZFC and FC curves of as-synthesized nanoparticles. The blocking temperature (T_B) of the fcc nanoparticles, which is determined from the maximum of the ZFC curve, is around 15 K. It is interesting to find that there is one peak and two inflexions in the ZFC curve (as shown in the inset of Figure 6.23). As reported in Reference,[149] some particles still have disordered fcc or partly ordered fct structure even after salt-matrix annealing. Therefore, the peak around 35 K should be the blocking temperature (T_{B1}) of the disordered (and/or partly ordered) nanoparticles, this blocking temperature is higher than that of totally disordered fcc nanoparticle before annealing. The two inflexions therefore are T_B of the ordered $L1_0$ FePt nanoparticles which are around T_{B2}=222, T_{B3}=368 K, respectively. Here, T_B was determined from the intersections of extrapolations of the greatest slope and flat region. By using the formula $K_u V/(k_B T_B) \approx 25$ for a random distribution of particles with a single magnetic domain,[150] the values of effective anisotropy K_u are estimated to be 4.5×10^5, 2.84×10^6, and 4.70×10^6 J/m^3 for the 3 nm particles with different T_B, respectively. Here V and k_B are the average particle volume and Boltzmann constant, respectively. On the other hand, if we establish that K_u of the particle with T_{B3} is fixed at 2.84×10^6 J/m^3, the particle size of T_{B3} is estimated around 3.5 nm. Therefore, it is reasonable that K_u is around 2.84×10^6 J/m^3 for the 3 nm $L1_0$ FePt nanoparticles, since it si enevitable that there will be very few relatively large particles.[151]

Figure 6.24 shows the hysteresis loops of the annealed nanoparticles at different temperatures. The demagnetization curves show big kinks, which means that the nanoparticles mainly consist of two types of phase, i.e., fcc and fct phases. It is interesting to find that the annealed nanoparticles show a ferromagnetic characteristic or property even at room temperature. However, the fcc nanoparticles show a coercivity of only 6 kOe at 5 K and then are superparamagnetic when the temperature is higher than 15 K (as shown in the inset of Figure 6.24). These results agree with the ZFC analysis. The structural and magnetic analyses show that after the annealing, the majority of the particles transformed to the ordered $L1_0$ phase, while a small portion of the particles remained disordered. The ordered particles have a relatively low chemical ordering parameter compared to large particles.[152]

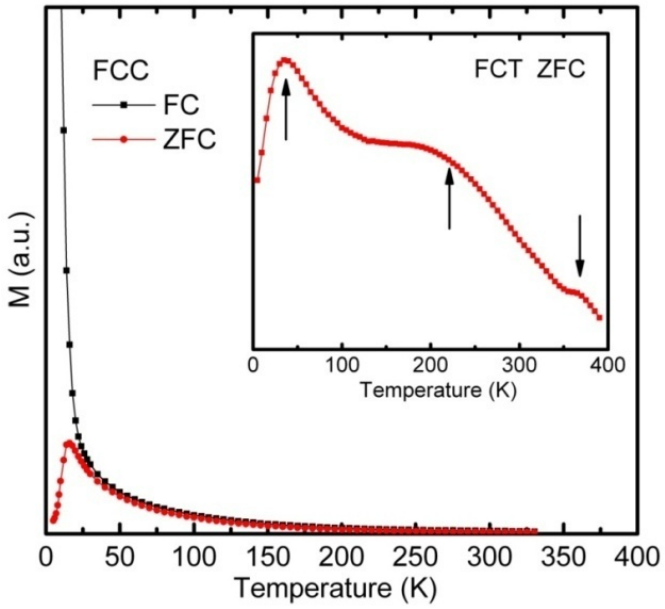

Figure 6.23 ZFC and FC curves of as-synthesized nanoparticles. The inset shows the ZFC curve of salt-annealed particles.

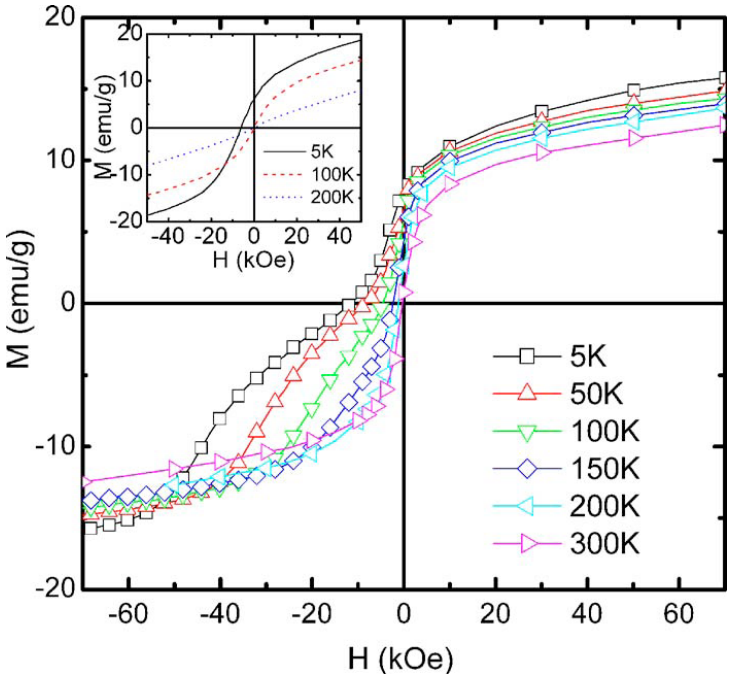

Figure 6.24 Hysteresis loops of the salt-annealed at 700 ^{o}C for 4 hours at different temperatures. The inset shows the hysteresis loops of the fcc nanoparticles before annealing.

6.2 High Thermal Stability of $L1_0$ FePt Nanoparticles

It is observed that salt-matrix annealed $L1_0$ FePt nanoparticles have high thermal stability and that no sintering occurred even when the particles were heated at 1100 ^{o}C for 1 hour. It was interesting and worthwhile to investigate what makes these tiny particles extremely super stable at such a high temperature. Figures 6.25 (a) and (b) show the morphology of the 8 nm FePt particles after annealing at 700 ℃ for 4 hours with a salt-to-FePt mass ratio of 20:1 and 400:1, respectively. It shows that the monodisperse $L1_0$ FePt nanoparticles were obtained with the ratio of 400:1. However, large particles of above 50 nm were observed for the ratio of 20:1 due to the particle sintering. This indicates the importance of the salt-to-FePt ratio. In other words, a continuous polycrystalline structure forms if there is no salt as the separating media. Even more interestingly, it was found that salt-matrix annealed monodisperse $L1_0$ FePt nanoparticles are very stable even after annealing at 1100 ℃ for 1 hour. As shown in Figure 6.25 (c), it is clear that there is no particle sintering and growth but only the formation of more regular shape after at high temperature annealing.

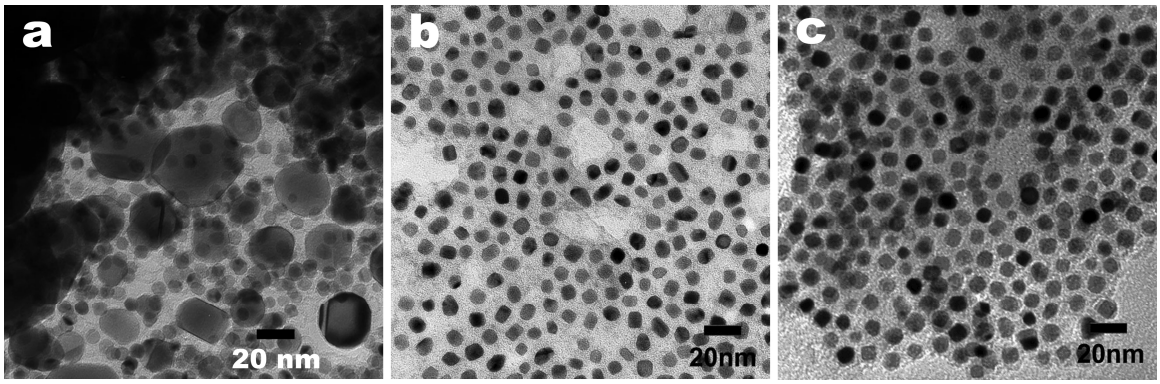

Figure 6.25 TEM images of the 8 nm nanoparticles annealed in salt-matrix at 700 ^{o}C for 4 hours with a salt-to-particle ratio of (a) 20:1 and (b) 400:1. (c) the $L1_0$ FePt nanoparticles after washing out the salt and annealing at 1100 ^{o}C for 1 hour.

Figure 6.26 shows the XRD patterns of the 3 nm and 8 nm salt-matrix annealed nanoparticles before and after annealing under forming gas at different temperatures. The grain size (determined by the Sherrer formula) of the salt-matrix annealed particles is around 3.0 ± 0.1 and 8.4 ± 0.2 nm, respectively. The equal grain size and particle size means both the 3 nm and 8 nm FePt particles are single crystalline after

salt-matrix annealing. The $L1_0$ FePt nanoparticles are very stable at temperature up to 1100 ℃ even after removing the salt matrix. The grain (or particle) size only increases to 3.4 ± 0.1 and 8.9 ± 0.2 nm for the 3 nm and 8 nm nanoparticles after they have been heated at 1100 ℃ for 1 hour, respectively. The XRD analysis agrees with the TEM results that the salt-matrix annealed $L1_0$ FePt particles are very stable at high temperatures.

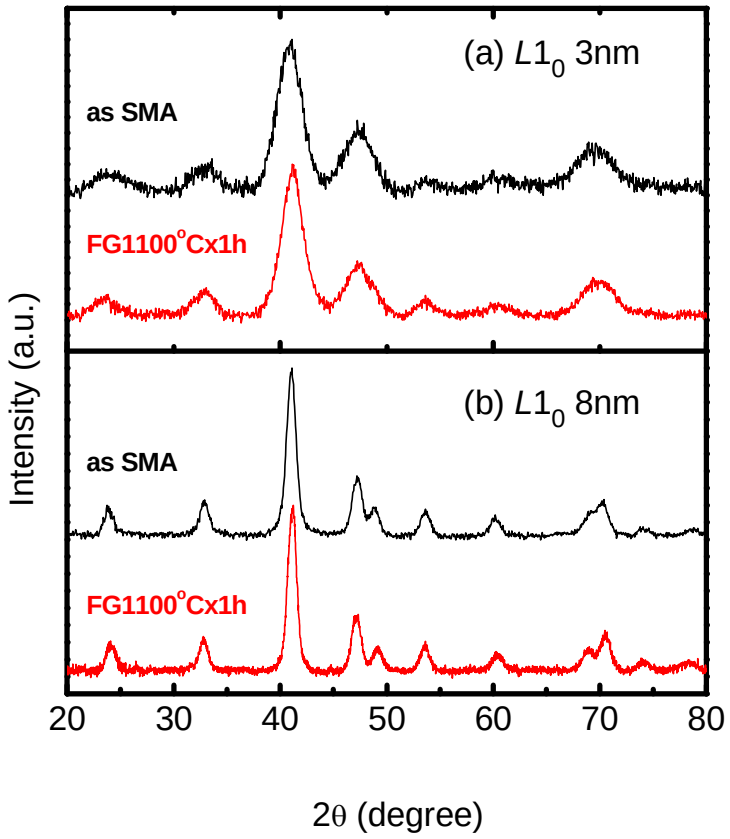

Figure 6.26 XRD patterns of the $L1_0$ nanoparticles made by using salt-matrix annealing method before and after annealing at 1100 °C for 1 hour for (a) 3 nm; and (b) 8 nm.

Figures 6.27 shows a high-resolution TEM image of the salt-matrix annealed 8 nm particles at 700 ℃ for 4 hours. A lattice-fringe distance of ab out 0.22 nm, which is typical for an interplanar distance of (111) in $L1_0$ FePt phase, was observed for the FePt particles. The structural lattice parameters of the $L1_0$ FePt nanoparticles are about a = 0.3855 nm and c = 0.3757 nm both before and after annealing at

1100 ℃ for 1 hour. Around the surface of the parti cles, a lattice fringe distance of 0.35 nm was observed due to a light elemental coating, which appears to be the result of graphitic carbon. This carbon shell can act as the diffusion barrier layer during annealing, thereby impeding sintering of the FePt nanoparticles. The carbon shells form around the FePt particles as a result of the pyrolysis of the surfactants during salt-matrix annealing at 700 ℃, since a large amount of oleylamine was used for ball milling of the salt powder.

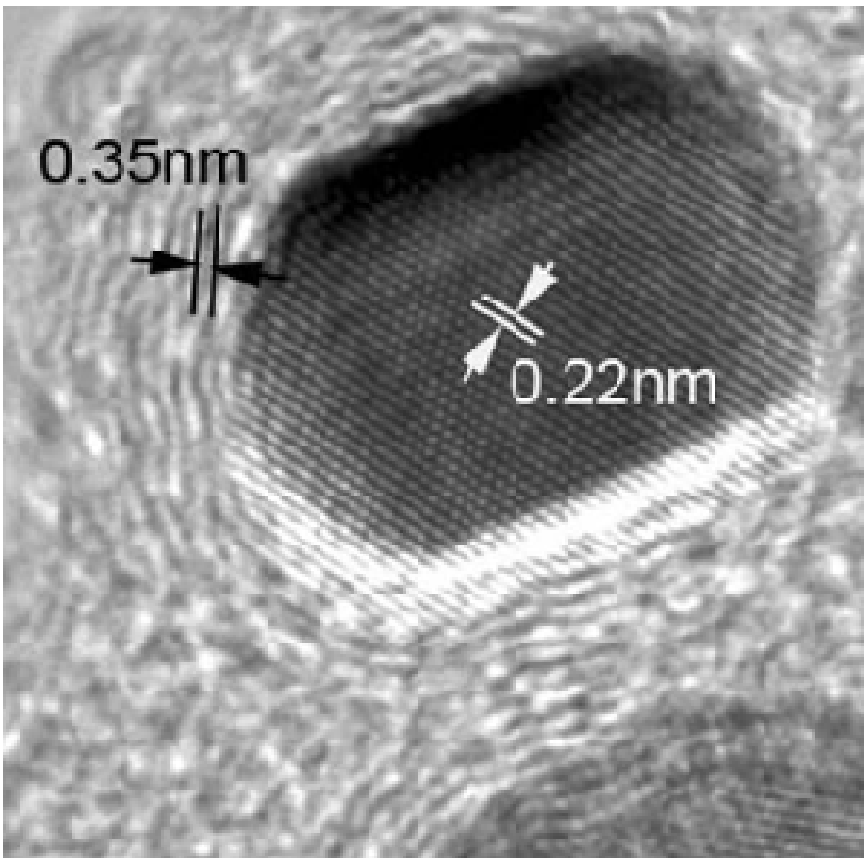

Figure 6.27 HRTEM image of the 8 nm salt-matrix annealed $L1_0$ FePt nanoparticles.

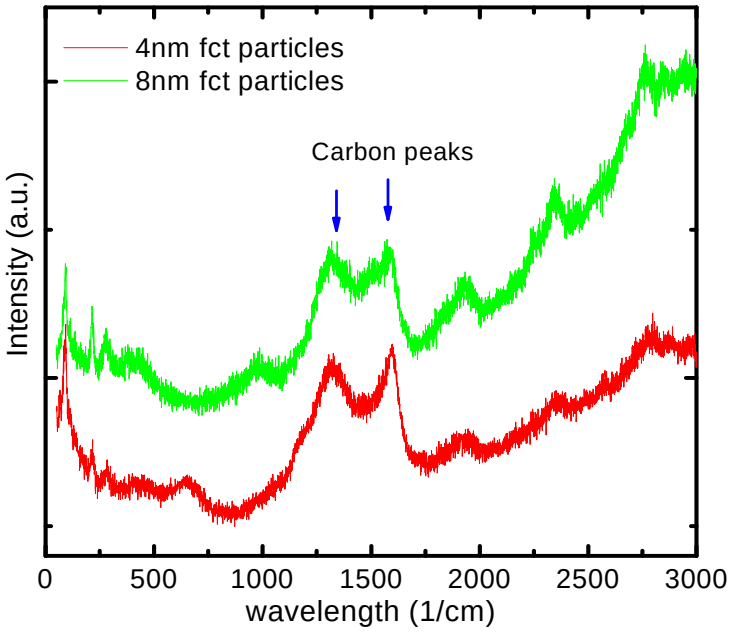

Figure 6.28 Raman spectra of the salt-matrix annealed 4 nm, and 8 nm FePt nanoparticles.

To further prove that the carbon layer is on the surface of the particles, Raman spectra were measured. Figure 6.28 shows the Raman spectra of the salt-matrix annealed 4 nm and 8 nm FePt nanoparticles. It was found that both samples had similar patterns. There are two major peaks around 1320 and 1580 cm^{-1} which are attributed to amorphous carbon and graphite, respectively.[152]

Table 6.1 weight ratio of carbon in salt-matrix annealed $L1_0$ FePt nanoparticles[153]

Particles Size	3 nm	4 nm	6 nm	8 nm
Carbon weight %	27	22	18	15

EDX was used to determine a rough estimation of the carbon content in the salt-matrix annealed particles with different sizes, as shown in Table I. EDX also confirms the existence of carbon in the salt-matrix annealed samples. It should be noted that the carbon content can be controlled by the amount of surfactants that are added to the salt-matrix. It was noted that the demagnetization loops of the $L1_0$ FePt

nanoparticles were smoother after annealing at 1100 ℃ for 1 hour, but the improvement is not signific ant. This is most likely due to an increase in the phase transition for partially ordered nanoparticles after the salt-matrix annealing. The chemical ordering parameters of the 8 nm $L1_0$ FePt nanoparticles was found to increase from 0.88 to 0.92 as a result of high-temperature annealing.

6.3 Conclusion

In conclusion, monodisperse $L1_0$ FePt nanoparticles of 3, 4, 5, 6, 7, 8, 9 and 15 nm have been successfully prepared by salt-matrix annealing technique developed in our lab, which marks the first time availability of the smallest ferromagnetic nanoparticles at room temperature. The processing method is simple and economic, and can be used for producing in large quantities the ferromagnetic nanoparticles free of nonmagnetic impurities. The effect of size of the FePt nanoparticles on the phase transition, chemical ordering and magnetic properties have been systematically studied. It has been found that fcc FePt particles with a diameter of about 2 nm cannot be transferred to the ordered fct structure. Under the same annealing conditions, the degree of chemical ordering increases with the particle size. The structural and magnetic analyses of 3 nm showed that after the annealing, the majority of the particles had ordered fct structure, while a small portion of the particles remained disordered. It was also revealed that magnetic properties, including magnetization and coercivity are strongly dependent on both particle size and chemical ordering and that they increases with particle diameter. The 8 nm $L1_0$ FePt nnoparticles with faceted shape give the highest coercivity (up to 35 kOe). Magnetic hardening is decreased in the 15 nm fct particles possibly because of their polycrystalline feature. The monodisperse $L1_0$-FePt nanoparticles with 3 nm to 8 nm particle size prepared by the salt-matrix method are highly thermally extremely stable even at 1100 ℃. High-re solution transmission electron microscopy, Raman spectra, energy dispersive spectra, and magnetic measurements suggest that the $L1_0$ FePt nanoparticles were coated by a carbon shell after salt-matrix annealing. $L1_0$ FePt nanoparticles with very high magnetic anisotropy can be used as building blocks for high-density recording media and high-energy product permanent magnets and can also be directly applied in biomedical technology. Finding a possible way to align $L1_0$ FePt nanoparticles in a magnetic field so that they have the enhanced amagnetic properties in aligned assemblies is a subject for future reseacrh.

CHAPTER 7

$CoFe_2O_4$, $NiFe_2O_4$ AND FeCo NANOPARTICLES

7.1 Monodisperse $CoFe_2O_4$ and $NiFe_2O_4$ Nanoparticles

There has been renewed research interest in ferrite nanoparticles in recent years because of their broad potential applications in several advanced technological fields, including permanent magnets, ultra-high-density recording media, magnetic fluids, magnetic drug delivery, MRI contrast enhancement, hyperthermia treatment, biosensors, and other nanodevices.[12, 25, 46, 38] The cubic MFe_2O_4 or $MO.Fe_2O_3$ (M = Fe, Co and Ni), is a common magnetic ferrite that has a cubic inverse spinel structure, with oxygen forming a fcc closed packing and M^{+2} and Fe^{+3} occuping either tetrahedral or octahedral sites. Magnetic configuration of MFe_2O_4 material can be engineered by adjusting the chemical identity of M^{+2} to provide a wide range of magnetic properties.[15, 153] For many applications the synthesis of uniform-size nanoparticles is of key importance because the magnetic properties depend strongly on their dimensions.

Recently, great efforts have been made by various groups to achieve fine-tuning of the size of ferrite nanoparticles by employing different synthesis techniques and by varying the experimental parameters such as the rate of heating, and the quantity of surfactants. Kim *et al*. prepared cobalt ferrite nanoparticles ranging from 2 nm to 14 nm by controlling co-precipitation temperature of Co^{+2} and Fe^{+2} ions in alkaline solution although the size distribution was pretty wide.[50] Chinnasamy *et al*.[51] employed a modified oxidation process to synthesize cobalt ferrite particles with diameters ranging from a few micrometers to about 15 nm. Rajendrain *et al*. demonstrated 6 nm to 20 nm sized cobalt ferrites prepared in aqueous solution at room temperature by the oxidative co-precipitation of Fe^{2+} and Co^{2+}.[61] Morais et al. showed the size-controlled synthesis of nanoparticles of 10 nm to15 nm in aqueous solution at 95^{o}C by controlling stirring speed.[60] Moumen *et al*. used oil-in-water micelle to prepare size-controlled Co-ferrite in the range of 2 to 5 nm.[64] Liu *et al*.[67] also reported the nanoparticles of 2 nm to 35 nm in diameter which that prepared in normal micelle using method similar to those used by Moumen *et al*.

Pillai *et al*.[66] Recently, Sun *et al.*[58, 59] synthesized ferrite nanoparticles with sizes variable from 3 nm to 20 nm in diameter by combining nonhydrolytic reaction with seed-mediated growth method.

As can be seen, ferrite nanoparticles have been synthesized by a wide variety of. Although these methods are able to produce nano-sized ferrite particles, the quality of the nanoparticles is often poor. In many cases, a large size distribution is reported and size control is arbitrary. It is desirable to have nanoparticles with a specific size and specific properties for particular application. e.g., magnetic nanoparticles must be superparamagnetic at room temperatures in order to avoid agglomeration to use as ferrofluids and in biomedical applications such as MRI contrast agents.[38] However, the superparamagnetic state must be avoided in high-density information storage, since the superparamagnetic relaxation of the data bits will cause the magnetic moment of each bit to fluctuate and consequently all the stored information will be lost. Compared with other methods used for preparing ferrite nanoparticles, the chemical solution method [58, 59] has unique advantages because it produces small particle size (down to 3 nm) with very narrow size distribution as well as good crystallinity and stability.

7.*1.1 $CoFe_2O_4$ Nanoparticles*

7.1.1.1 Size and Composition Control

$CoFe_2O_4$ nanoparticles were synthesized by the simultaneous chemical reduction of iron (III) acetylacetonate, Fe $(acac)_3$, and cobalt (II) acetylacetoneate, $Co(acac)_2$, by 1,2-hexadecanediol at high temperature in solution phase in the presence of the surfactants oleic acid and olyle amine as described in Chapter 3 (Section 3.10 and 3.10.1). The reaction of $Fe(acac)_3$ and $Co(acac)_2$ with surfactants at high temperature leads to the formation of monodisperse $CoFe_2O_4$ nanoparticles, which were separated from the reaction by a series of centrifugations of the end products. Using phenyl ether as solvent, 3 nm $CoFe_2O_4$ nanoparticles were obtained. 6 nm particles could be obtained following a similar process to that used for the synthesis of 6 nm Fe_3O_4 nanoparticles by replacing phenyl ether with benzyl ether and increasing the refluxing time by 30 minutes.

In the case of 3 nm particles, the final particle composition was controlled by varying the mole ratios of the precursors $Fe(acac)_3$ and $Co(acac)_2$. $Fe(acac)_3$ (1 to 3 mmol), $Co(acac)_2$ (1 mmol), 1,2-

hexadecanediol (10 mmol), oleic acid (5 mmol), oleyl amine (5 mmol), and phenyl ether (20 ml) were tested. The magnetization of annealed nanoparticles was found to increase rapidly with increasing mole ratio of precursors up to 1:1.5 and then to decrease as the ratios were increased further to 1:3. It was observed that a 1.5:1 mole ratio of $Fe(acac)_3$: $Co(acac)_2$ resulted in the highest magnetization value of 223 emu/g after the reduction process at 700 $^{\circ}$C for 30 minutes in forming gas (93% Ar + 7% H_2). At the optimized composition (1.5:1 precursor-mole ratio), larger $CoFe_2O_4$ particles were also made by using seed-mediated growth method. $CoFe_2O_4$ nanoparticle sizes ranging from 3 to 20 nm were successfully produced by seeding techniques by varying size, and quantity of seeds and surfactants in the initial scheme of synthesis of 4 nm particles as discribed in Chapter 3 (Section 3.10.2). The nanoparticles obtained were characterized by EDX, TEM, HRTEM, XRD, SAXS, AGM. and SQUID.

7.1.1.2 Structure and Morphology

Figure 7.1 shows XRD patterns of as-synthesized 3, 6, 8, 12, 15 and 20 nm $CoFe_2O_4$ nanoparticles. It can be seen from XRD that the as-synthesized $CoFe_2O_4$ nanoparticles are highly crystalline in nature, and the position and relative intensity of the peaks match well with the standard $CoFe_2O_4$ pattern. Sharpening of peaks can be seen with increasing in particle size due to the formation of large crystals.

The morphology of the as-synthesized $CoFe_2O_4$ nanoparticles was closely monitored by TEM observations. TEM analysis showed that $CoFe_2O_4$ nanoparticles as-synthesized in the first step as seeds and prepared by seed-mediated method are monodisperse. Figure 7.2 (A-F) shows typical TEM images of 3, 6, 8, 12, 15, and 20 nm $CoFe_2O_4$ nanoparticle monolayer assemblies deposited on TEM grid from their octane dispersion and dried at room temperature. It can be seen from the TEM images that the particles have a narrow size distribution (standard deviation < 10%). The grain sizes of the $CoFe_2O_4$ particles were calculated using the Scherrer equation:

$$L = \frac{0.94\lambda}{B(2\theta)\cos\theta}, \tag{7.1}$$

where L is the crystal dimension, λ = 0.154056 nm is the wavelength of the X-ray, and $B(2\theta)$ is the full width in radians subtended by the half-maximum intensity width of the peak at angle θ. The (311) peaks

were chosen to calculate the grain sizes in Figure 7.1. These grain sizes also represent the particle sizes because all of the particles are single crystals. The particle size directly observed from TEM micrograph images are in good agreement with the average size estimated from XRD patterns using the Scherrer equation.

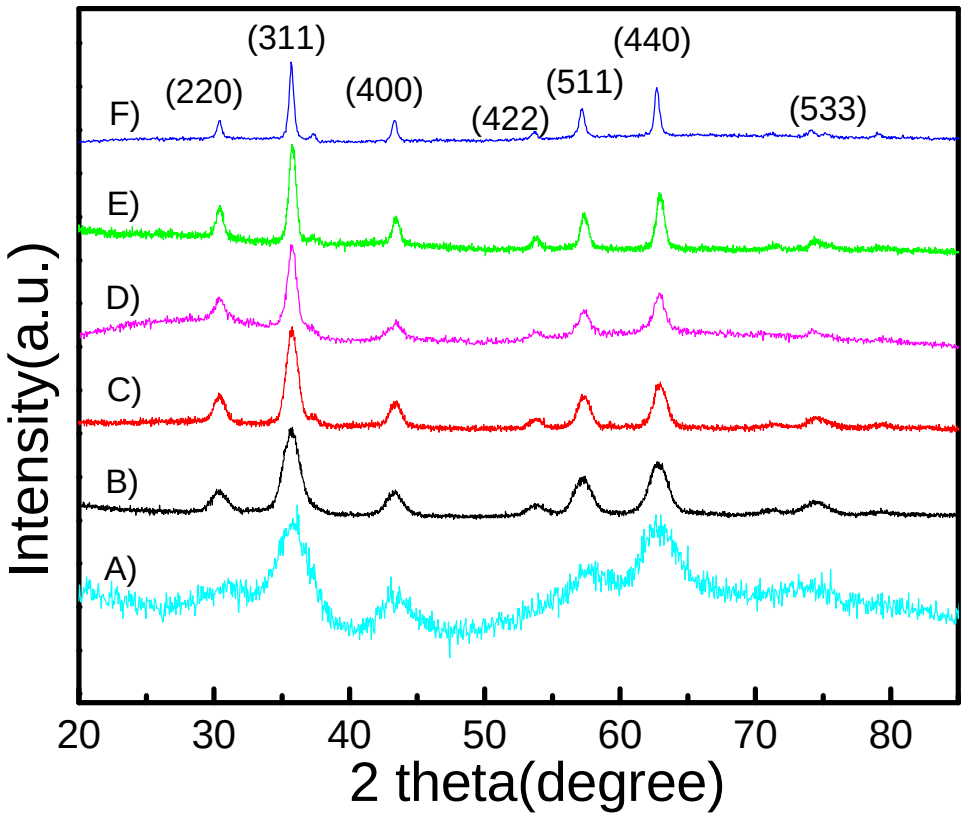

Figure 7.1 XRD patterns of the as-synthesized $CoFe_2O_4$ nanoparticles A) 3 nm, B) 6 nm, C) 8 nm, D) 12 nm, E) 15 nm, and F) 20 nm.

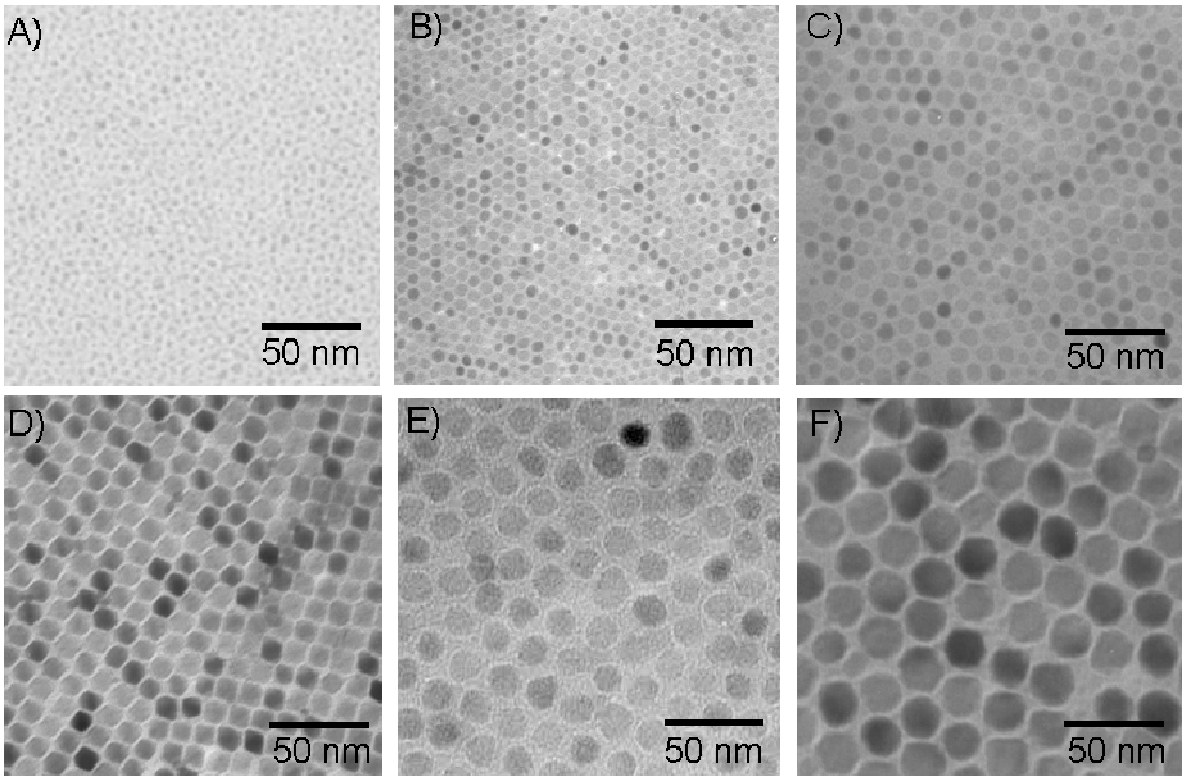

Figure 7.2 TEM images of the as-synthesized $CoFe_2O_4$ nanoparticles: sizes are A) 3 nm, B) 6 nm, C) 8 nm, D) 12 nm, E) 15 nm, and F) 20 nm.

Analysis of particles size and size distribution of some of the selected samples of as-synthesized $CoFe_2O_4$ nanoparticles was carried out using SAXS in the transmission geometry as described in Chapter 4 (Section 4.1.4). The experimental scattering curves were measured by SAXS and size was determined by the direct fitting of model curves to experimental scattering curves. All the samples were fitted with spherical a model for experimentally measured scattering curves. Figures 7.3 and 7.4 show the experimentally measured scattering curves and particle size and size distribution obtained by fitting scattering curves for 3 nm and 20 nm nanoparticles. Figures 7.3 (left), and 7.4 (left) show the typical SAXS patterns (scattering curves) measured in red-colored lines for 3 and 20 nm particles. The blue-colored lines represent the simulated data. The size distributions of the particles were obtained by fitting the scattering profiles as seen Figure 7.3(right) and 7.4(right). It can be seen that the particles have a narrow size distribution. The average particle diameter calculated from SAXS measurement is consistent

with that observed by TEM micrograph images and estimated from XRD patterns using the Scherrer equation. The average diameters were estimated to be 3.3 nm for 4 nm and 20.9 nm for 20 nm, which is in good agreement with the TEM images.

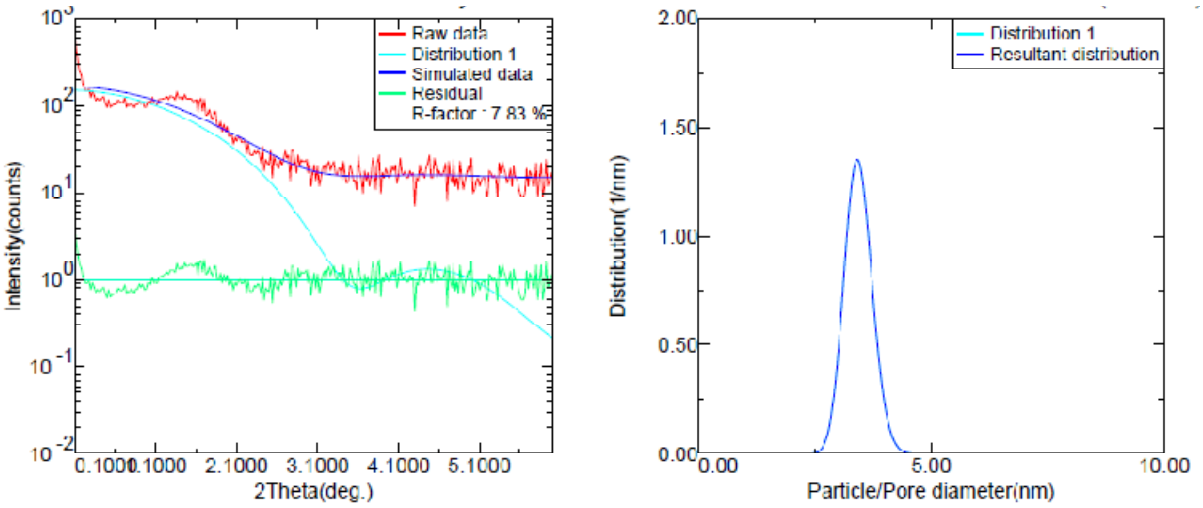

Figure 7.3 SAXS patterns (left), and size distribution of (right) 3 nm $CoFe_2O_4$ nanoparticles.

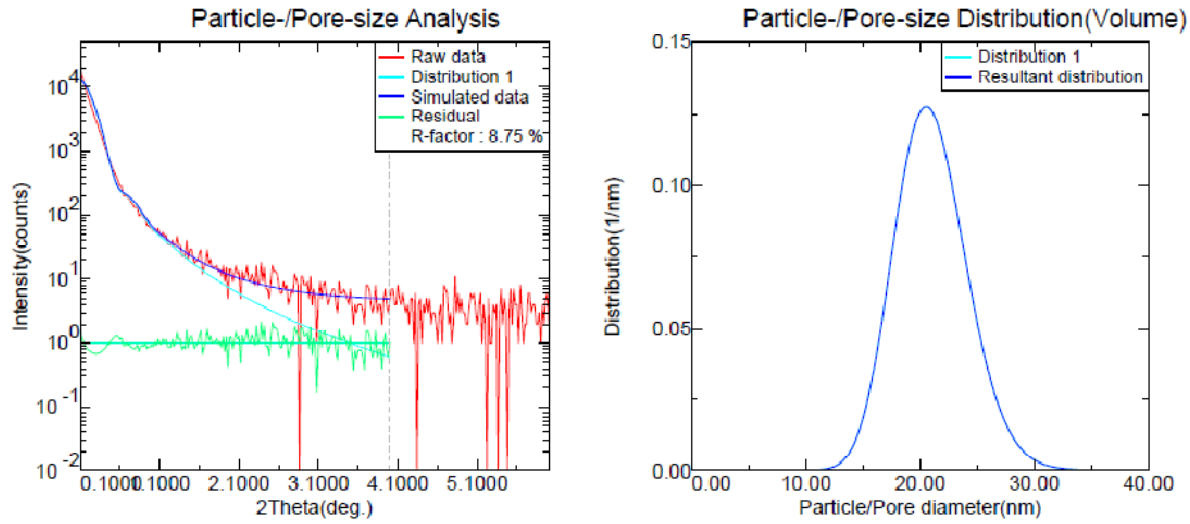

Figure 7.4 SAXS patterns (left), and size distribution of (right) 20 nm $CoFe_2O_4$ nanoparticles.

The composition of as-synthesized $CoFe_2O_4$ nanoparticles was determined by using EDX detector in HRTEM. The EDX spectra were acquired from 11 different areas in the sample. The EDX analysis software gave the average composition of Fe = 68.78 ± 3.5 atomic percentage. Figure 7.5 shows the typical EDX spectrum of $CoFe_2O_4$ nanoparticles deposited on the Cu grid.

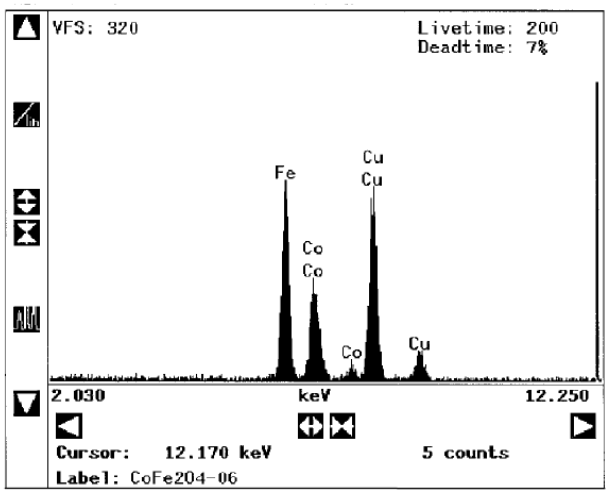

Figure 7.5 HRTEM-EDX of 3 nm $CoFe_2O_4$ nanoparticles.

7.1.1.3 Magnetic Properties

Magnetic properties of $CoFe_2O_4$nanoparticles at room temperature were measured by AGM. Figure 7.6 shows the in-plane hysteresis loops of 3, 8, 15 and 20 nm $CoFe_2O_4$ nanoparticle synthesized using a precursor mole ratio of $Fe(acac)_3$:$Co(acac)_2$ of 1:1.5. It has been found that particle sizes less than 12 nm are superparamagnetic at room temperature. This indicates that the thermal energy can overcome the anisotropy energy barrier of individual particles, and the net magnetization of particles assemblies is zero in the absence of an external field. Particles whose size is greater than 12 nm are ferromagnetic at room temperature. Figure 7.6 shows that the coercivity of particles size is greater than 12 nm increases with increasing in particle diameter and 20 nm particles show coercivity up to 1 kOe at room temperature. Magnetic properties of as-synthesized $CoFe_2O_4$ nanoparticles were measured by

SQUID at low temperature. Figure 7.7 shows the hysteresis loops of 3, 6, 8, 15 and 20 nm $CoFe_2O_4$ particles at 10 K. All the particles were ferromagnetic at this temperature. It was observed that the coercivity and the saturation magnetization of particles at low temperature are also size dependent and increase with particle diameters up to 20 nm (as shown in figure 7.8) The 20 nm particles showed a coercivity of 21.5 kOe at 10 K.

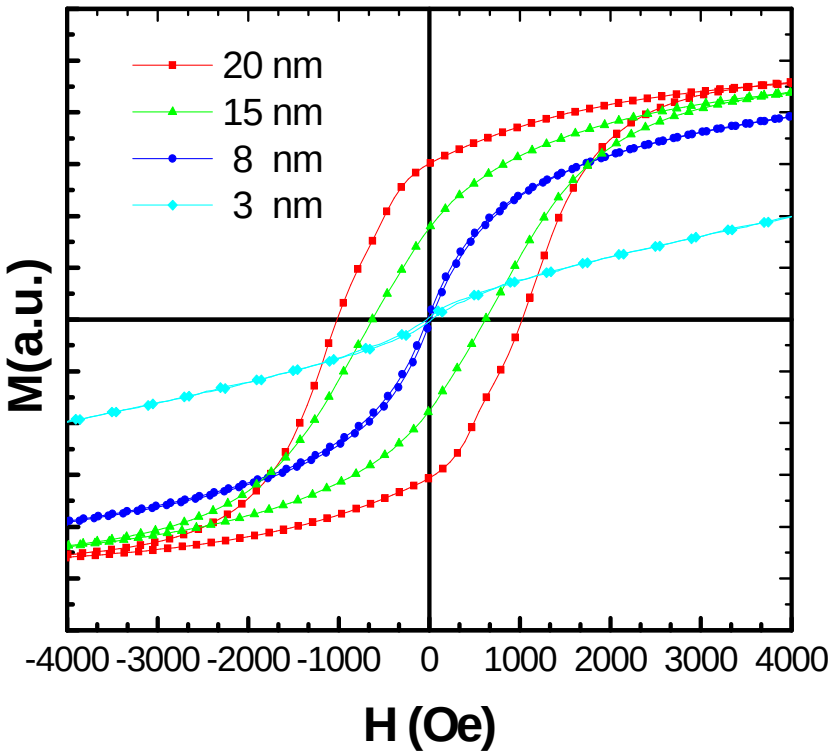

Figure 7.6 Hysteresis loops of the 3, 8, 15 and 20 nm $CoFe_2O_4$ nanoparticle assemblies measured at room temperature.

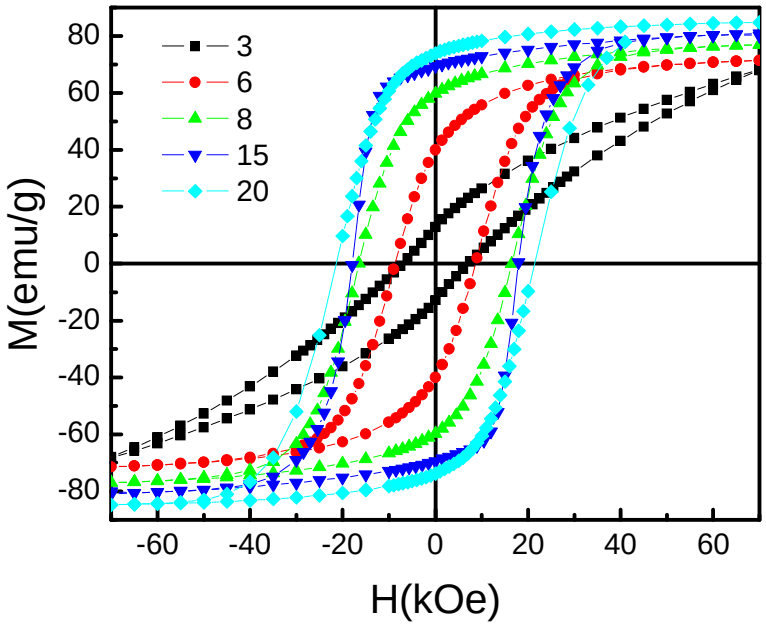

Figure 7.7 Hysteresis loops of the 3, 6, 8 15 and 20 nm $CoFe_2O_4$ nanoparticle assemblies measured at 10 K.

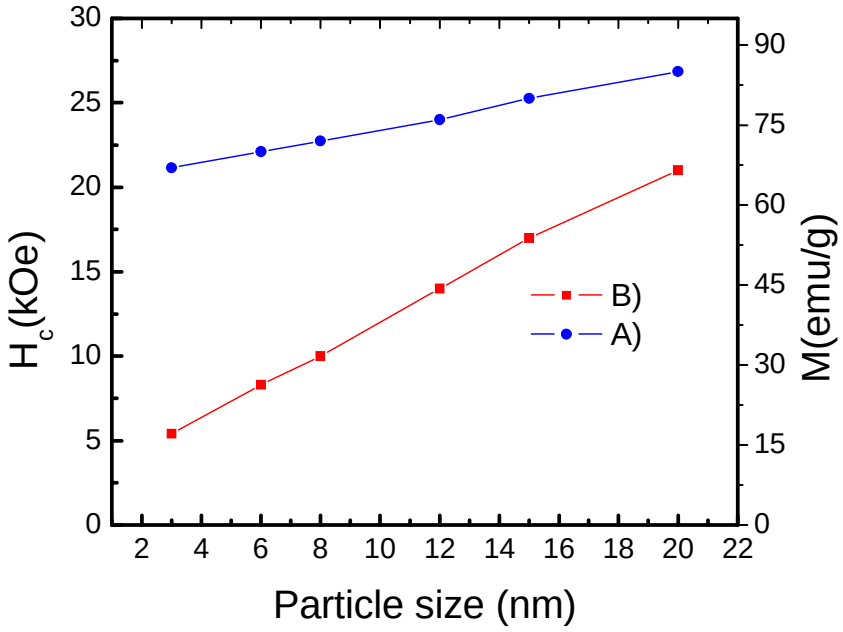

Figure 7.8 Coercivity and saturation magnetization of 3, 6, 8, 15 and 20 nm $CoFe_2O_4$ nanoparticle assemblies measured at 10 K.

The temperature-dependent magnetizations of different sized particles were measured with zero-field cooling (ZFC) and field cooling (FC) procedures. Figure 7.9 shows the plot of temperature versus normalized magnetization for 3, 6, and 10 nm $CoFe_2O_4$ nanoparticles measured with ZFC in an applied magnetic field of 100 Oe between 5K and 330K. The *M* vs *T* curves show peaks that are characteristic of superparamagnetic particles. The peak temperature in the *M* vs *T* curve (blocking temperature T_B), rises with increasing particle size. The T_B values are 30, 210, and 250 K for 3, 6, and 10 nm particles respectively.

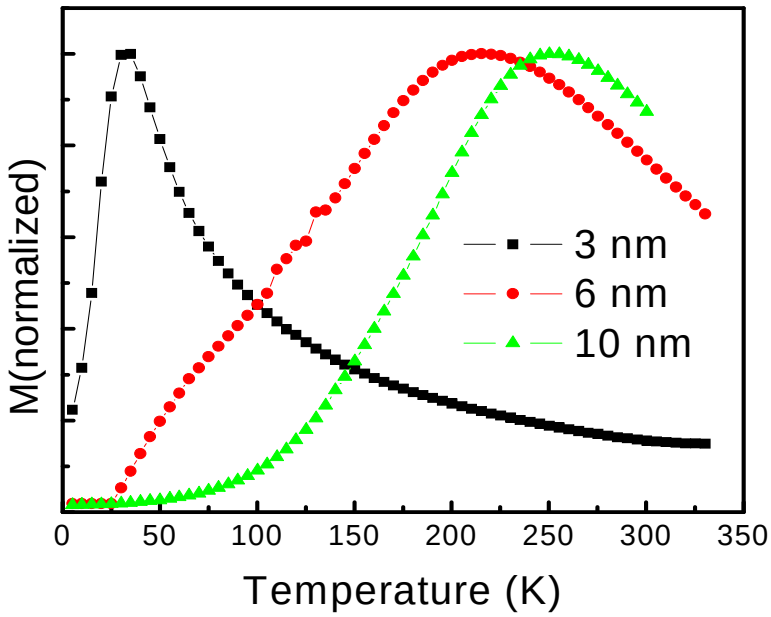

Figure 7.9 Magnetization verses temperature for 3, 6 ,and 10 nm $CoFe_2O_4$ nanoparticles measured with zero-field cooling at 100 Oe.

Magnetic viscosity means that the external field *H* is kept constant and the magnetization is monitored as a function of time. Viscocity is normally caused by the thermal activation of magnetization reversals over activation energy barriers ΔE. The theoretical and experimental work on magnetic viscosity behaviors of ferromagnetic materials has been extensively studied during the last decades.[37, 154, 164] For

an ensemble of magnetizations in metastable states with identical ΔE, the relaxation time τ is related to an absolute temperature T by the Arrhenius-Neel law:[166]

$$\tau = \tau_o e^{\Delta E/K_B T}, \quad (7.2)$$

where τ_0 is a characteristic time constant, which is of the order of 10^{-10} ~10^{-12}. However, for most materials with a broad and slowly varying distribution of ΔE, the time dependence of magnetization is well described by the relation:[37]

$$M(H; t) = M_0(H) - S(H) \ln(t + t_0), \quad (7.3)$$

where S is the magnetic viscosity coefficient, while M_0 and t_0 are fitting constants. According to Equation (7.3), the magnetic viscosity coefficients $S(H)$ can be obtained by fitting the time dependence of magnetization. Figure 7.10 (A-C) shows the field dependence of magnetic viscosity coefficients $S(H)$ at different temperatures for 6, 8 and 12 nm $CoFe_2O_4$ nanoparticles. Since the field dependent energy barrier can be described as:[165 -167]

$$\Delta E(H) = \Delta E_0 [1 - H/Hs]^{\alpha} \quad (7.4)$$

Here, α varies between 0.86 and 2, depending on the particle assembly and magnetization reversal behaviors. When the applied field is zero, the energy barrier is as high as $\Delta E_0 = KuV$ and thus S is small. Increasing the applied field decreases ΔE resulting in the increase of S. When H is around Hs, ΔE is around zero and S reach the maximum ($Smax$). Further increase of H will increase the energy barrier again, S will approach zero. This is the reason that all $S(H)$ curves show a bell shape and why the maximum S value was obtained around the switching field of $CoFe_2O_4$ nanoparticles. As discussed above, $Smax$ is related to $KuV = kBT$ according to Equations (7.2) and (7.3). The increase of either Ku or V will increase the energy barrier and as reduce $Smax$. On the other hand, the raising the temperature increases the thermal agitation energy and leads to the increase of $Smax$. Figure 7.11 shows the temperature dependence of $Smax/Ms$. One can see that $Smax/Ms$ increases with increasing temperature for the 6 to 12 nm particles. Moreover, it was found that the slope of temperature dependent $Smax/Ms$ curves increases with decreasing particle size. This is attributed to the faster decrease of $KuV = kBT$ with rising temperatures for smaller particles.

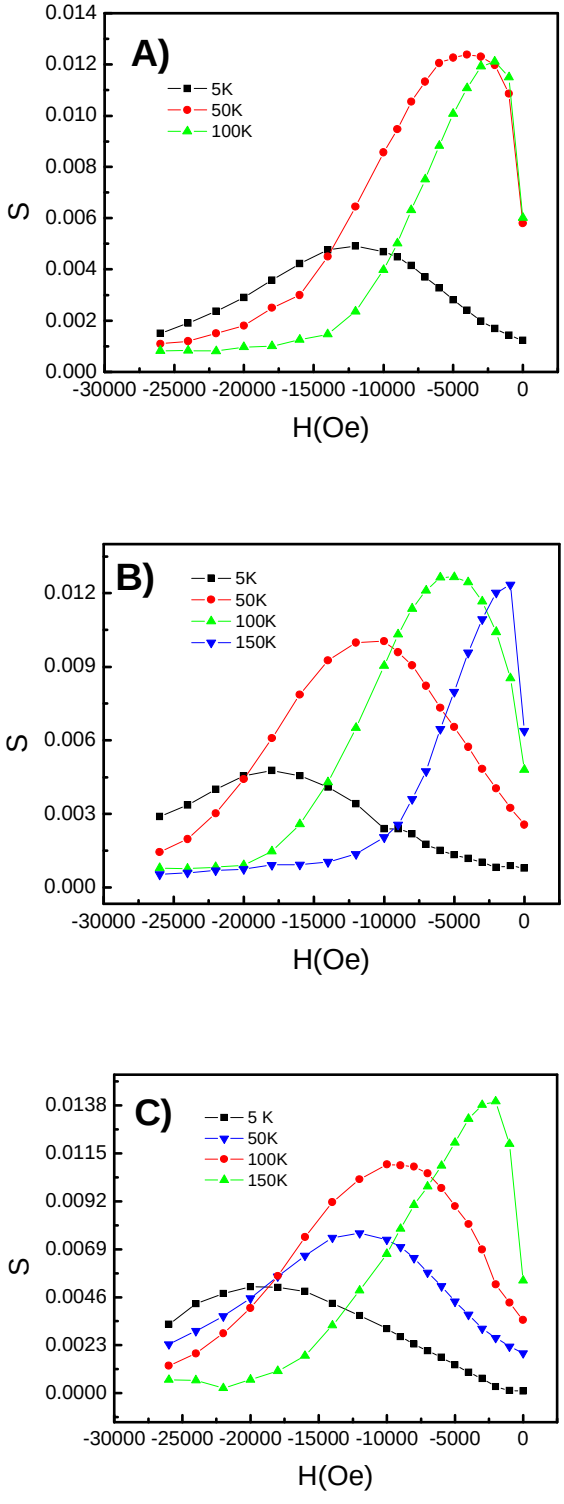

Figure 7.10 Magnetic viscosities of A) 6 nm, B) 8 nm, and C) 12 nm as-synthesized $CoFe_2O_4$ nanoparticles.

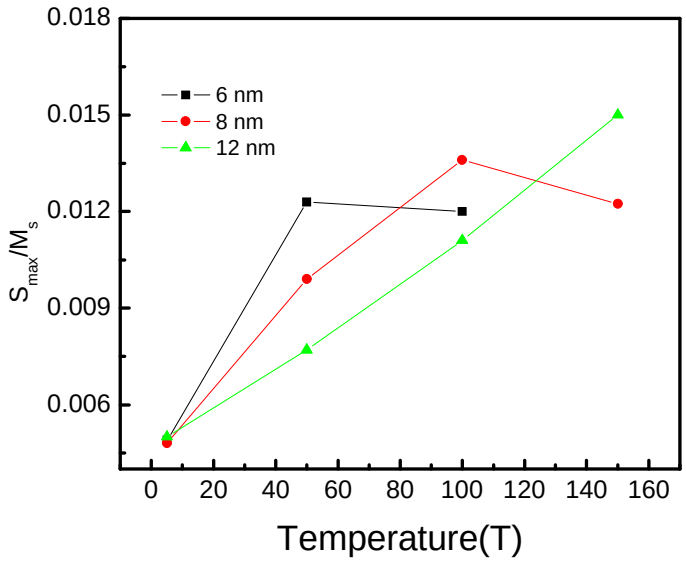

Figure 7.11 Temperature dependence of maximum viscosity coefficients of $CoFe_2O_4$ nanoparticles of different size.

Mössbauer spectroscopy was also used to characterize the magnetic properties of $CoFe_2O_4$ nanoparticles. Figure 7.12 and 7.13 show typical Mössbauer spectra for 3 and 11 nm $CoFe_2O_4$ nanoparticles recorded at various temperatures. In the case of 3 nm $CoFe_2O_4$, the spectrum shows typical superparamagnetic behavior with a complete collapse of magnetism and with only a quadrupole doublet at room temperature, as opposed to bulk materials of ferrite or magnetite, which show well resolved magnetic components on the two sites (octahedral coordination and tetrahedral coordination). Due to the absence of a magnetic signature, these two sites are indistinguishable in this sample, and a single doublet fits well with the spectrum. For all the temperatures measured here, the spectra show broadening, as expected for nano-sized particles. The spectra at 80 K and 50 K were fitted with a magnetic hyperfine field distribution and a quadrupole doublet. The magnetic signature indicates that fluctuation of some of the particles was slow; hence some particles were well below their blocking temperatures (magnetic field) at these temperatures. The additional quadrupole doublet in the spectra at these temperatures shows that there are some particles that fluctuate fast compared to the Mössbauer sensing time scale (10^{-7} – 10^{-9} s), implying that the blocking temperatures for these particles are below

the corresponding measuring temperatures here (50 K and 80 K). The spectrum at 7 K is fitted with only a hyperfine field distribution where all particles are well below the blocking temperature, and hence ordered magnetically. This confirms that the blocking temperature of 3 nm $CoFe_2O_4$ nanoparticles lies between 7 K to 50 K. Results from Mössbauer spectra measurement are consistent with ZFC measurements as observed in Figure 7.9 the T_B of 3 nm particles is 30 K. As the particle size increases, we expect a well oriented magnetic signature in magnetic materials. This is the case here, as compared to the 3 nm as seen in Figure 7.13 for 11 nm $CoFe_2O_4$ nanoparticles.

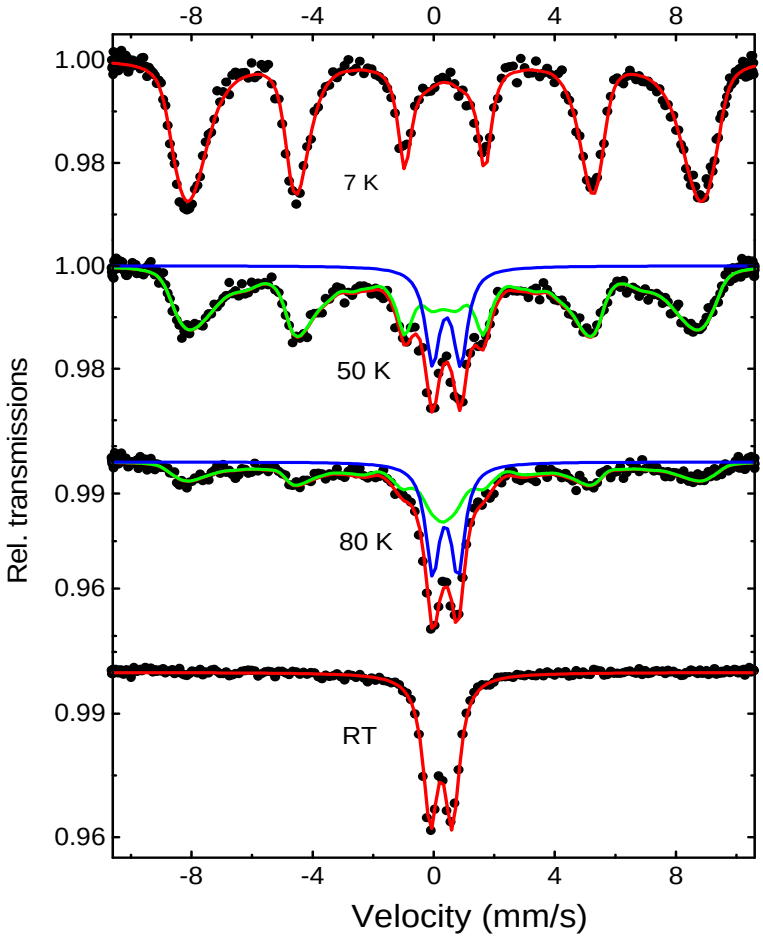

Figure 7.12 Mössbauer spectra of 3 nm $CoFe_2O_4$ nanoparticles at four different temperatures a) 7 K, b) 50 K, c) 80 K, and d) room temperature (300K).

Table 7.1 Hyperfine interaction parameters for 3 nm $CoFe_2O_4$ nanoparticles

Temperature	*Isomer shift*	*Quadrupole splitting*	*Hyperfine field*
RT	0.358(2)	0.716(4)	--------
80 K	0.42(2) 0.50(1)	0.01(3) 0.82(2)	29.5(8)* ---------
50 K	0.450(8) 0.526(6)	0.003(15) 0.91(3)	41.7(8)* ----------
7 K	0.466(5)	-0.004(9)	49.1(3)*

The spectrum at 8 K shows two well resolved sites for ferrites, with the hyperfine interaction parameters given in the Table 7.2 for 11 nm $CoFe_2O_4$ nanoparticles. As the temperature increases, the spectrum starts to broaden, but the two sites are still well resolved at 50 K. At room temperature, the two sites merge together, and the spectrum is fitted with a hyperfine field distribution and a quadrupole doublet. The doublet again indicates that some particles at this temperature are well above their blocking temperature and hence fluctuate fast. This result matches well with the result obtained from AGM and SQUID at room temperature and low temperature as mentioned above 12 nm $CoFe_2O_4$ particles are ferromagnetic at room temperature. Tables 7.1 and 7.2 show the hyperfine interaction parameters for 3 and 11 nm $CoFe_2O_4$ nanoparticles.

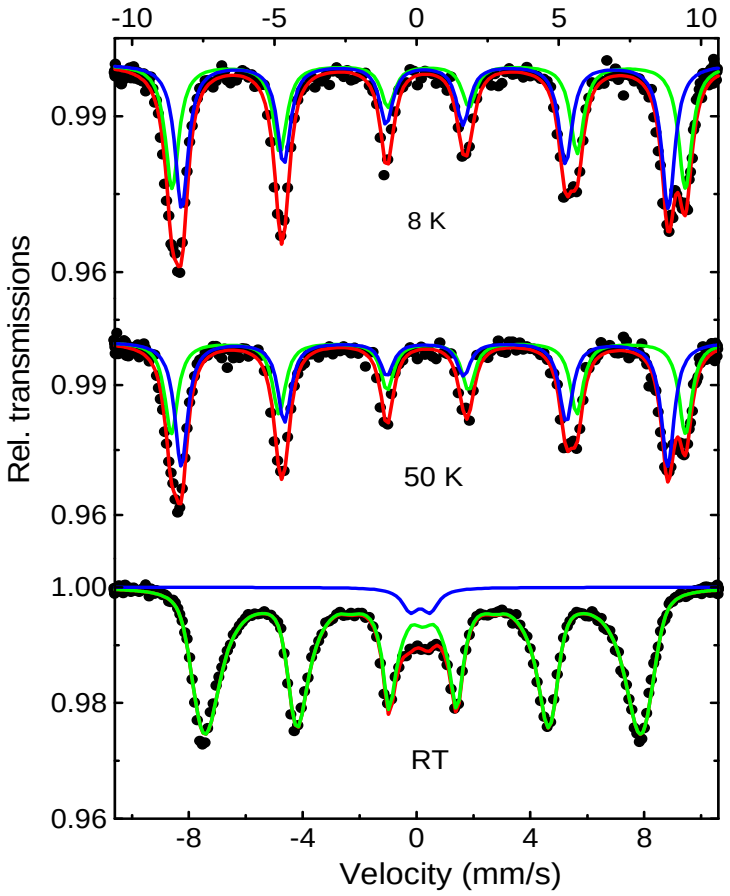

Figure 7.13 Mössbauer spectra of 11 nm $CoFe_2O_4$ nanoparticles at three different temperatures a) 8 K, b) 50 K, c) 80 K, and c) room temperature (300K).

Table 7.2 Hyperfine interaction parameters for 11 nm $CoFe_2O_4$ nanoparticles.

Temperature	*Isomer shift*	*Quadrupole splitting*	*Hyperfine field*
RT	0.331(2) 0.24(3)	-0.006(4) 0.70(8)	41.4(4)* --------
50 K	0.515(6) 0.397(5)	0.02(1) -0.19(1)	55.72(5) 52.69(4)
8 K	0.522(5) 0.408(4)	-0.02(10) -0.017(8)	55.81(4) 52.78(3)

Note: (1) * indicates average hyperfine field fitted assuming continuous distribution of the internal magnetic field.

(2) The isomer shifts are quoted with respect to metallic iron at room temperature (i.e., the Mössbauer drive velocity is calibrated using metallic iron foil at room temperature).

(3) Numbers in parentheses are errors in the respective parameters as extracted from the theoretical fit to the experimental data.

7.1.1.4 Conclusion

Monodisperse $CoFe_2O_4$ nanoparticles with particle size from 3 nm to 20 nm have been synthesized by chemical solution methods. Particles larger than 6 nm were synthesized by a seed-mediated growth method. The composition was controlled by varying the mole ratios of the precursors $Fe(acac)_3$ and $Co(acac)_2$ in the solution. Low temperature (10 K) and room temperature (300 K) magnetic measurements on these particles showed a strong dependence of the magnetic properties on the particle size. Particle of whose size was greater than 12 nm showed ferromagnetic behavior at room temperature, particles whose sizes were less than 12 nm showed ferromagnetic behavior below room temperature. The blocking temperature T_B values are 30 K, 210 K and 250 K for 3, 6 and 10 nm particles respectively. A coercivity value of 21 kOe was obtained at 10 K for the 20.5 nm particles. The magnetic viscosity of $CoFe_2O_4$ is size dependent and increases with decreases in particles size.

7.1.2 $NiFe_2O_4$ Nanoparticles

7.1.2.1 Size Control

Synthesis was carried out by using standard airless chemical synthesis technique in a nitrogen atmosphere. The $NiFe_2O_4$ nanoparticles were synthesized as described in Chapter 3 (Section 3.11) by the simultaneous chemical reduction of $Ni(acac)_2$ and the thermal decomposition of $Fe(CO)_5$ at high temperature in solution phase. In a typical synthesis of 18 nm $NiFe_2O_4$ nanoparticles, a mixture of $Ni(acac)_2$, and of 1,2- hexadecanediol was added to a 125 mL European flask containing a magnetic stir bar. Benzyl ether was then transferred into the flask, and the contents were stirred while purging with N_2 for 20 minutes at room temperature. The flask was then heated to 120 ^oC and the temperature was held for 20 minutes. During this time of $Fe(CO)_5$ was injected into the flask while the N_2 purge continued. After

3 minutes, oleic acid and oleyl amine were injected, and the mixture was maintained under an N_2 blanket heated to 160 ^oC at a rate of 5 ^oC per minute and then held for 10 minutes. The flask was maintained at the refluxing temperature of 295 ^oC for 30 minutes before cooling down to room temperature under the N_2 blanket. Afterwards, all handling was performed in air.

The size of the $NiFe_2O_4$ nanoparticles was controlled well by varying types of solvent, amount of surfactants and heating rates. For example, when benzyl ether was replaced by phenyl ether, particle size was reduced from 18 nm to 6 nm (keeping other reaction parameters same). But when benzyl ether was used as solvent and the amount of both the surfactants were increased from 1 mL to 2 mL the size of the particles was increased from 18 nm to 22 nm.

7.1.2.2 Structure and Morphology

Figure 7.14 shows XRD patterns of as-synthesized 6, 18, and 22 nm $NiFe_2O_4$ nanoparticles. It is can be seen from XRD that as-synthesized $NiFe_2O_4$ nanoparticles are highly crystalline in nature, and the position and the relative intensity of peaks match well with the standard $NiFe_2O_4$ pattern.

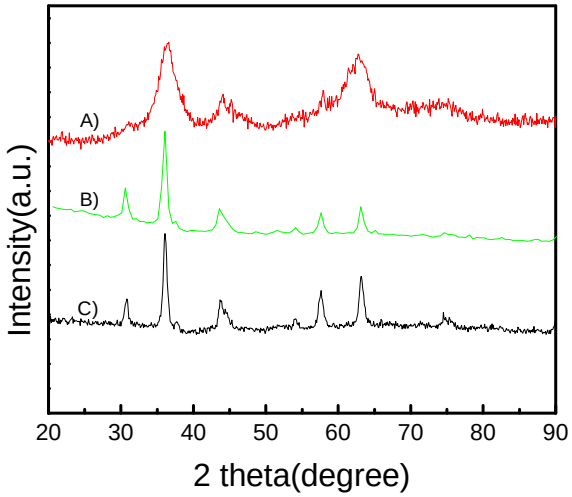

Figure 7.14 XRD patterns of $NiFe_2O_4$ nanoparticles A) 6 nm, B) 18 nm, and C) 22 nm.

Figure 7.15 shows TEM images of monolayer assemblies of 6, 18 and 22 nm as-synthesized $NiFe_2O_4$ nanoparticles, deposited on the TEM grid from their octane dispersion and dried at room temperature. TEM analysis shows that particles are monodisperse and have narrow size distribution

(standard deviation < 10 %). The grain sizes of the particles were calculated by the Scherrer equation (7.1). The (311) peaks were chosen to calculate the grain sizes (Figure 7.14). The average grain size of as-synthesized particles is good agreement with the direct observation of particle size from TEM micrograph images.

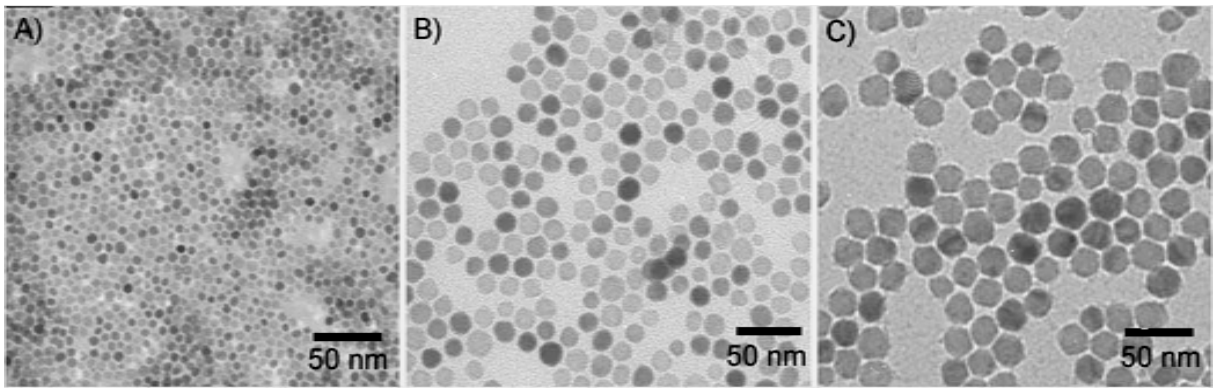

Figure 7.15 TEM images of $NiFe_2O_4$ nanoparticles A) 6 nm, B) 18 nm and C) 22 nm.

7.1.2.3 Magnetic Properties

Magnetic properties of $CoFe_2O_4$ nanoparticles at room temperature were measured by AGM. Figure 7.16 shows the typical in-plane hysteresis loops of 8, and 22 nm $CoFe_2O_4$ nanoparticle. $NiFe_2O_4$ nanoparticles have very low coercivity at room temperature. Hysteresis loops were measured at low temperature in SQUID. However, there was no noticeable change in the coercivity and the magnetization of the particles measured at room temperature and low temperature.

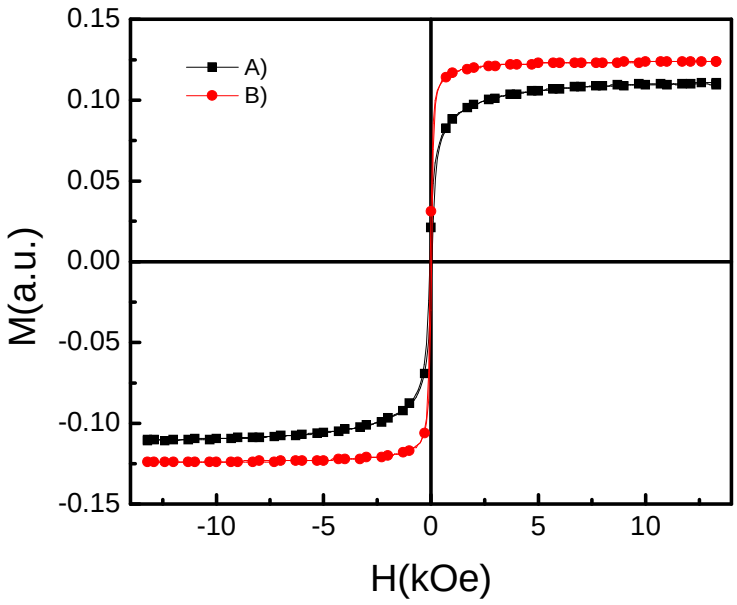

Figure 7.16 Hysteresis loops of $NiFe_2O_4$ nanoparticles A) 6 nm, and B) 22 nm.

7.1.2.4 Conclusion

Monodisperse $NiFe_2O_4$ nanoparticles were synthesized by the simultaneous chemical reduction of $Ni(acac)_2$ and the thermal decomposition of $Fe(CO)_5$ at high temperature in solution phase. Particle size of 6, 18 and 20 nm was obtained by controlling reaction parameter. The composition $NiFe_2O_4$ can be controlled by varying the mole ratios of the precursors $Fe(acac)_3$ and $Ni(acac)_2$ in the solution. Low temperature (10 K) and room temperature (300 K) hysteresis loop measurements of these particles showed no significant differences in magnetization and coercivity the particle size

7.2 FeCo Nanoparticles

7.2.1 Overview of the Issue

FeCo alloys are important soft magnetic materials because of their unique magnetic properties including large permeability and very high saturation magnetization. Recently, FeCo nanoparticles have attracted great interest because of their potential applications in microelectronic devices,[169] and biomedical technologies.[170] The particles can also be applied as building blocks of advanced

nanomagnets.[12.169 -171] Several chemical and physical methods of synthesis of FeCo nanoparticles have been reported recently.[172-179] However, preparation of monodisperse FeCo nanoparticles with controlled size (especially for sizes below 20 nm) and shape still remains a challenge due to the poor chemical stability of the nanoparticles. An important aspect of the application of any nanoparticles is their stability in the ambient conditions. Most chemically synthesized FeCo nanoparticles take on a disordered bcc structure and are not stable in air. Heat treatment is generally applied to make these particles air-stable. [44,46] However, heat treatment promotes the sintering of particles, leading to unwanted grain-growth that destroys the nanoscale morphology of the particles, which is undesirable for many applications. Thus, there is a need to develop a synthetic technique to control the morphology and stability of the particles. Here, we report a simple yet novel reductive annealing technique under salt-matrix[54, 84] to fabricate monodisperse air-stable FeCo nanoparticles with tunable size.

7.2.2 Morphology and Structure

FeCo nanoparticles were prepared as described in Chapter 3 (Section 3.12) by the reductive salt-matrix annealing of $CoFe_2O_4$ nanoparticles. Figure 7.16 shows TEM images of the as-synthesized $CoFe_2O_4$ nanoparticles and the reduced FeCo nanoparticles of different sizes. Figure 7.17 (A-C) shows the TEM images of 8, 12 and 20 nm as-synthesized $CoFe_2O_4$ nanoparticles and figure 7.17 (D-F) shows the TEM images of 8, 12 and 20 nm FeCo nanoparticles obtained by reductive salt-matrix annealing of the corresponding size $CoFe_2O_4$ nanoparticles. It can be seen clearly in Figure 7.16 that salt-matrix has successfully prevented the particles from sintering and growing at 450℃, which is the high enough temperature for a complete phase transformation from the $CoFe_2O_4$ phase to the FeCo alloy. Both the as-synthesized $CoFe_2O_4$ and the reduced FeCo alloy nanoparticles are monodisperse with a standard deviation of less than 12% in diameter. Our earlier studies of FePt nanoparticles of different sizes particles have also proved that this technique of salt-matrix annealing can be applied to heat-treatments of the FePt nanoparticles up to 700^{o} C for more than 4 hours without particle agglomeration and sintering, provided a suitable salt to particle ratio and proper annealing conditions are chosen.[54, 84]

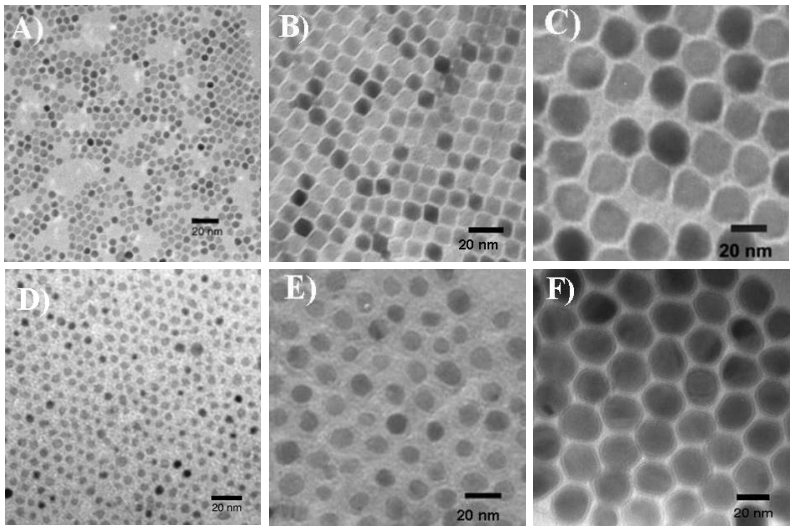

Figure 7.17 TEM images of A) 8 nm, B) 12 nm and C) 20 nm as-synthesized $CoFe_2O_4$ and D) 8 nm, E) 12 nm and F) 20 nm FeCo nanoparticles obtained after the reductive salt-matrix annealing of $CoFe_2O_4$ nanoparticles in forming gas (Ar 93% + H_2 7%) at 450 ^oC for 1 hour.

Figure 7.18(A) shows the XRD patterns of the 8, 12, and 20 nm as-synthesized $CoFe_2O_4$ nanoparticles. Figure 7.18 (B) shows the XRD patterns of 8, 12 and 20 nm FeCo nanoparticles obtained after the reductive salt-matrix annealing of the $CoFe_2O_4$ nanoparticles of the same sizes. Both the peak position and the intensities of the FeCo nanoparticles after reductive salt-matrix annealing match perfectly with FeCo structure, indicating that the $CoFe_2O_4$ nanoparticles were reduced to FeCo nanoparticles after the annealing. The grain size calculated using the Scherrer formula of as-synthesized $CoFe_2O_4$ nanoparticles (in Figure 7.18 A (a-c)) were around 8.0 ± 0.2 nm, 12 ± 0.2 nm, and 20 ± 0.6 nm, respectively. The grain size of FeCo nanoparticles (Figure 7.18 B (a-c)) were 8.4 ± 0.1 nm, and 12.7 ± 0.6 nm, and 20.9 ± 0.8 nm, respectively after the heat treatment at 450 ℃ for 1 hour, all these value s are very close to the values before annealing. It should be noted that the grain size significantly increased to 30 nm when the 8 nm as-synthesized $CoFe_2O_4$ nanoparticles were annealed without salt-matrix at the same temperatures for the time, suggesting that the salt-matrix prevented the particles from sintering.

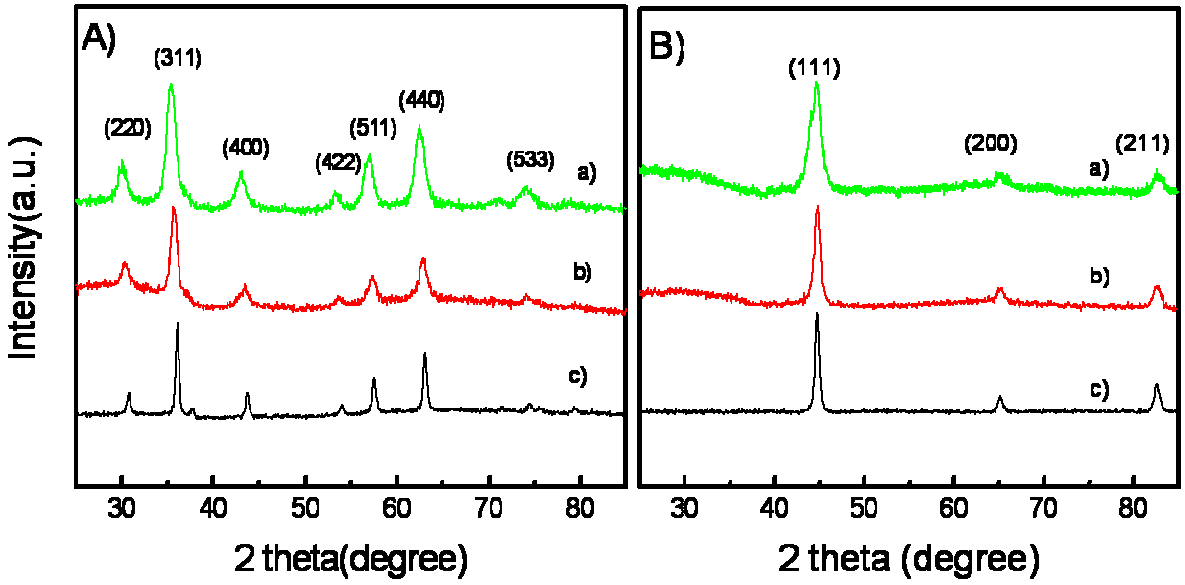

Figure 7.18 (A) X-Ray diffraction patterns of (a) 8 nm, (b) 12 nm and (c) 20 nm as-synthesized $CoFe_2O_4$ nanoparticles, (B) X-Ray diffraction patterns of ,(a) 8 nm, (b) 12 nm, and (c) 20 nm FeCo nanoparticles obtained by salt-matrix annealing of $CoFe_2O_4$ at 450^o C for 1 hour under forming gas (Ar 93 % + H_2 7%).

As discussed above, both the XRD and the TEM analyses have confirmed that monodisperse FeCo nanoparticles can be successfully obtained by reductive salt-matrix annealing of $CoFe_2O_4$ nanoparticles. It was also found that the FeCo nanoparticles were stable in the ambient conditions. Our previous studies of a high-resolution TEM image of FePt nanoparticles after salt-matrix annealing showed that a carbon shell forms around the particle as a result of pyrolysis of the surfactant during salt-matrix annealing at high temperatures.[86] It is believed that the FeCo nanoparticles were surrounded by a carbon layer due to the decomposition of the surfactant, which was confirmed by Raman spectra. Figure 7.19 shows the Raman spectra of 8 nm FeCo nanoparticles obtained by salt-matrix annealing. There are two major peaks around 1320 and 1580 cm^{-1} which are attributed to the amorphous carbon and graphite, respectively.[86, 131] It has also been reported that the annealing process leads to a homogeneous atomic distribution of iron and cobalt within individual nanoparticles that transform from disordered bcc structure to ordered bcc structure and thereby becom more stalble.[169 -171]

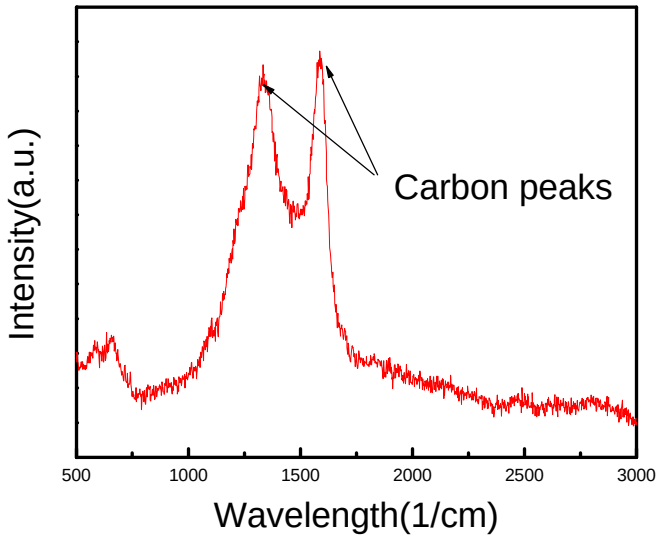

Figure 7.19 Raman spectra of 8 nm FeCo nanoparticles obtained by salt-matrix annealing of $CoFe_2O_4$ at 450^o C.

The presence of carbon on the surface of nanoparticles causes difficulty in determining actual magnetization value. AAS was used to determine quantitatively the content of Fe/Co metals in the samples. The AAS result showed that the presence of carbon on the surface of nanoparticles counted 30%, 27%, and 24 % at the weight of the 8, 12 and 20 nm FeCo nanoparticle samples, respectively. The amount of carbon content can be reduced by washing the as-synthesized $CoFe_2O_4$ nanoparticles several times with a mixture of hexane (10 mL) and ethanol (40 mL) before salt-matrix annealing. We used these results to calibrate the magnetization values measured directly from the samples.

7.2.3 Magnetic properties

Figure 7.20 shows the hysteresis loops of 8, 12 and 20 nm FeCo nanoparticles obtained by salt-matrix annealing at 450 ^{o}C for 1 hr in forming gas. All the particles are ferromagnetic at room temperature and have a coercivity of less than 300 Oe. The saturation magnetization of FeCo nanoparticles is size dependent and increases with particle size. Saturation magnetizations of 104, 135 and 168 emu/g were obtained for 8, 12 and 20 nm FeCo nanoparticles, respectively. The size-dependent Ms may be explained by the finite-size-scaling theory and surface effects.[84] The magnetic properties of the FeCo nanoparticles

are also composition dependent. The final composition of FeCo nanoparticles can be tuned by adjusting the initial molar ratio of the Fe and Co precursors in the synthesis of $CoFe_2O_4$ nanoparticles. Figure 7.19 (inset) shows the variation of saturation magnetization of 20 nm FeCo nanoparticles with the initial Fe/Co molar ratio. The highest magnetization was obtained for FeCo nanoparticles with atomic composition close to $Fe_{65}Co_{35}$, which is consistent with that for bulk FeCo alloys.[180, 181] EDX analysis of 8, 12 and 20 nm FeCo nanoparticles showed an average composition of $Fe_{63.6}Co_{36.4}$, $Fe_{66.8}Co_{33.2}$ and $Fe_{65.2}Co_{34.8}$, respectively.

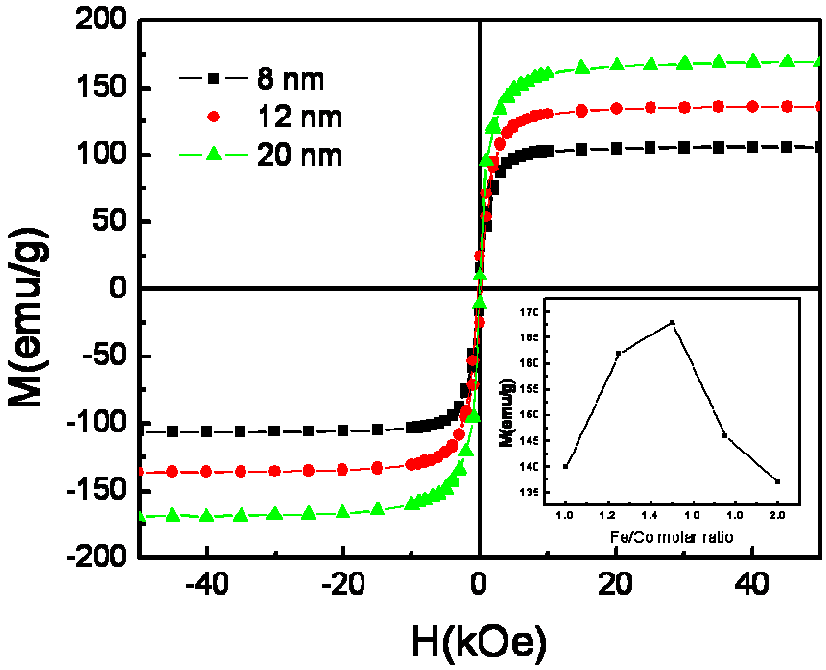

Figure 7.20 Hysteresis loops of 8, 12 and 20 nm FeCo nanoparticles obtained by salt-matrix annealing of $CoFe_2O_4$ at 450 ^oC for 1 hour under forming gas(Ar 93 % + H_2 7%), and (inset) saturation magnetization of 20 nm FeCo nanoparticles versus precursor mole ratios of Fe/Co used for the synthesis of $CoFe_2O_4$ nanoparticles.

7.2.4 Conclusion

We have developed a novel technique of preparing of monodisperse FeCo nanoparticles with controllable particle size and narrow size distribution through the reductive salt-matrix annealing of $CoFe_2O_4$ nanoparticles. The size and shape of FeCo nanoparticles can be well controlled by changing the size and shape of $CoFe_2O_4$ nanoparticles. Heat treated FeCo nanoparticles are air-stable owing to the formation of the ordered bcc structure as well as owing to the carbon shells formed on the surface of FeCo nanoparticles during heat treatments. The saturation magnetization of the particles is dependent on particle size and increases with particle diameter. These air-stable FeCo nanoparticles can be ideal building blocks for high-performance nanocomposite permanent magnets and nanostructured magnetic devices and they can also be suitable for biomedical applications.

CHAPTER 8

Sm-Co AND Nd-Fe-B BASED NANOPARTICLES

8.1 Sm-Co and Nd-Fe-B Based Nanoparticles by Surfactant-Assisted Ball Milling

8.1.1 Introduction

The fabrication of hard magnetic Sm-Co and Nd-Fe-B based nanoparticles has drawn a great deal of attention owing to the potential applications of these nanoparticles as building blocks in high-performance nanocomposite permanent magnets, ultra-high-density data recording media, and biomedical applications.[12, 78, 53, 184 -189] Rare-earth transition-metal (RE-TM) compounds based on the Sm-Co and Nd-Fe-B systems have a very high magnetocrystalline anisotropy (Sm-Co ~ (6 - 20) × 10^7 erg/cm^3 and Nd-Fe-B ~ 4.6× 10^7 erg/cm^3) among all the known materials and are ferromagnetic even when particle size is smaller than 4 nm.[25] Therefore they are very attractive for many advanced technological applications. In the RE-TM intermetallic compounds, the RE (Sm or Nd) unpaired 4*f* electrons provide the magnetocrystalline anisotropy, which is potentially much stronger than the shape anisotropy, whereas the TM (Co or Fe) 3*d* electrons provide most of the magnetization and determine the Curie temperature.[209] However, the fabrication of monodisperse Sm-Co and Nd-Fe-B nanoparticles, containing the RE metal has proven to be very challenging due to their high chemical instability and their being prone to oxidation. Recently, significant efforts have been made in the synthesis of Sm-Co and Nd-Fe-B based nanoparticles, using physical and chemical methods.[190-194] Physical methods such as dry ball-milling and melt-spinning have been used for the fabrication of nanostructured Sm-Co and Nd-Fe-B magnets but those methods provide limited control of particle size and grain.[194-204] Aproches using solution-phase chemical synthesis have been applied to the synthesis of $SmCo_5$ nanoparticles by polyol reduction of samarium acetylacetonate, $Sm(acac)_3$, with the thermal decomposition of $Co_2(CO)_8$.[204 - 207] However, most of the reported methods produced nanoparticles that had no coercivity at room temperature, indicating that the hard magnetic phases with high magnetocrystalline anisotropy may have not been formed. Hou

et al. adopted a procedure to make hard-magnetic nanocrystalline $SmCo_5$ (or Sm_2Co_{17}) particles from core/shell-structured Co/Sm_2O_3 nanoparticles by using high temperature reductive annealing at temperatures between 900 and 1100 ℃ under an inert atmosphere in the presence of metallic Ca and KCl. Although this method produced nanocrystalline particles with a well-controlled crystal morphology and coercivity up to 8 kOe at room temperature, high-temperature reductive annealing also caused significant coalescence and sintering between the particles and thus nanoscale morphology could not be retained in the final product.[208] Recently, Chinnasamy et al. reported room temperature coercivity in SmCo blade like morphology prepared by direct chemical method with particle size over 100 nm.[209] However, many particle-based applications demand hard magnetic nanoparticles with controlled morphology, including size and shape below 20 nm. Fabricating Sm-Co and Nb-Fe-B based nanoparticles that exhibit hard magnetic properties and controlling the particles size below 20 nm are still great challenges. Recently, our group (Wang et al. and Chakka et. al) has reported magnetic nanoparticles of Sm-Co, Nd-Fe-B, FeCo, Fe, and Co prepared by surfactants-assisted ball-milling method.[88, 90, 210] By controlling the settling-down time of the nanoparticle dispersion in solutions and selecting the optimal speed and the period of centrifugal separation for size selection, Sm_2Co_{17} nanoparticles with narrow size distribution and room temperature coercivity above 3 kOe have been successfully produced. However, the strains and amorphorization induced during the high energy ball milling causes the degradation of the magnetic properties of the particles. Therefore, heat treatment is still necessary for developing better hardening of the particles in order to improve the properties for potential applications.

In this work, the size dependent structural and magnetic properties of $Sm_2Co_{17,}$ $SmCo_5$ and $Nd_2Fe_{14}B$ nanoparticles prepared by surfactant-assisted ball milling process will be discussed. Our recent efforts on post annealing of ball milled particles in order to improve the hardening of ball milled particles will also be discussed.

8.1.2 Function of Surfactants in Ball Milling

Preparation of Sm-Co and Nd-Fe-B based nanoparticles by surfactant-assisted ball milling has been described in Chapter 3 (Section 3.6) in detail. Systematic investigations of the process variables such as the amounts of the solvent, and surfactants, the milling time, the effect of size of ball on grinding, and the weight ratio of ball to powder which have direct effects the on milled products have been reported by our group in previous studies.[88, 90, 210] After the raw materials (Sm-Co and Nd-Fe-B powders) were ball-milled with surfactants (oleic acid and oleyl amine) in heptane solvent for 20 hours, a colored liquid as shown in Figure 8.1 was obtained, along with coarse particles (referred from now onward as "slurry") that later sedimented at the bottom of the milling vial. However, when surfactants were not added to that the heptane, the solvent remained clear after milling because there were no nanoparticles dispersed in the liquid (as shown in Figure 8.1).

Figure 8.1 Particles in heptane solvent after milling.

Oleic acid ($C_{18}H_{34}O_2$) and oleylamine ($C_{19}H_{38}N$) have (COOH)- , (NH_2)- polar groups, respectively, as their head-part and a short hydro-carbon chain (R) as their tail-part as shown in Figure 8.2. When ball milling of raw powder is carried out in the presence of surfactants, as soon as fresh surfaces or nanoparticles are formed, during the milling process, these polar groups are absorbed on to the surface of the nanoparticles by the formation of chemical bonds (Figure 8.2). The tail portions (R) of the surfactants repel each other, which prevents agglomeration of the nanoparticles. This greatly reduces

cold welding and re-welding of crushed particles and thus finally leads to finer particle sizes. The tail portions of the surfactant are hydrophobic in nature and are soluble in heptane (C_7H_{16}) which helps nanoparticles to disperse into the heptane. This particle size (less < 15 nm) can disperse in heptane for long periods of time. As soon as the heptane dispersion of particles (after the ball milling) is transferred to a storage container, larger size particles sediment quickly at the bottom of the container because of gravity.

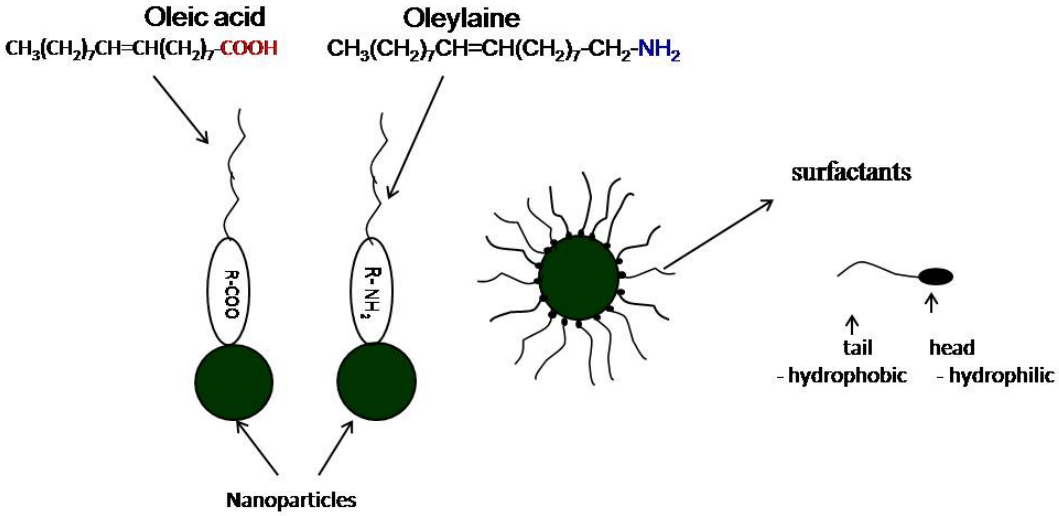

Figure 8.2 Schematic showing the structure of surfactants and the coating on a particle.[210]

The function of surfactants is multifold and can be summarized as follows:[88, 90, 210]

- The surfactant-induced surface modification can greatly enhance dispersion of nanoparticles in a solvent.
- The oil-like surfactants coated on the surfaces also act as lubricants on the particle surfaces, which reduces Fe contamination from the balls and the wall of the vial.
- The surfactants prevent the cold welding and re-welding of crushed- particles during the ball milling; thus, fine particle size can be obtained.

8.1.3 Sm_2O_{17} Nanoparticles

As discussed above, the surfactants absorbed by particles during milling greatly enhance the dispersion of Sm_2Co_{17}, $SmCo_5$, and Nd-Fe-B nanoparticles in a solvent. It was found that the suspension time of these particles milled without surfactants in heptane was less than 1 minute, while particles milled with surfactants remained floating in heptane for several seconds or even many days, depending on particle size. Based on the above observations, different sizes of the nanoparticles were separated by using centrifugal separation and controlling the settling-down time of the nanoparticle solutions. Figure 8.3 (A) shows a SEM image of the Sm_2Co_{17} slurry particles settled down in 5 minutes at bottom of vial from heptane dispersion after the 20 hour ball milling. The as-milled slurry particles have an irregular shape and have a wide size distribution from several nanometers to larger than 7 μm. Figure 8.3 (B) shows a typical TEM image of a mixture of different sizes Sm_2Co_{17} nanoparticles which range from 3 to 50 nm collected before size selection suspended for 3 hours in heptane solvent after milling. Figure 8.3 (C) and 8.3 (D) show TEM images of 20 and 5 nm Sm_2Co_{17} nanoparticles obtained after the size selection process. It was found that the small size nanoparticles (15 nm <) floated in the heptane solvent even after a centrifugation of 3000 rotations per minute (rpm) (relative centrifugal force: 1600*g*) for 30 minutes. Therefore, the small nanoparticles can be separated simply by applying a centrifugation procedure to remove the larger particles from the solution. Figure 8.3 (D) shows the morphology of the nanoparticles with an average size of 5 nm obtained from centrifugation of mixture of different size particles. To obtain larger nanoparticles, the slurry was dispersed once in heptane and was allowed to settle down on vial to remove the smallest floating nanoparticles. The top layer of liquid was discarded, and then the remaining part was transferred into a plastic bottle and redispersed in heptane again by ultrasonic vibration. The dispersed solution was then settled down statically for 30 minutes and 4 hours. A low-speed centrifugal separation of 500 rpm (45 *g* relative centrifugal force) was carried out to remove the largest particles from the particles collected by using different settling-down times to narrow the size distribution. The morphology of the nanoparticles that obtained after the settling-down process of 3 hours is shown in figure 8.3 (C), where nanoparticles with an average size of 20 nm were obtained. Compared with the as-milled particles before size selection (Figure 8.3 (B)), the nanoparticles after the size selection

have much more narrow size distributions (Figure 8.3 (C) and 8.3 (D)). Using a similar size selection process, but a shorter settling-down time, larger size nanoparticles can be obtained.

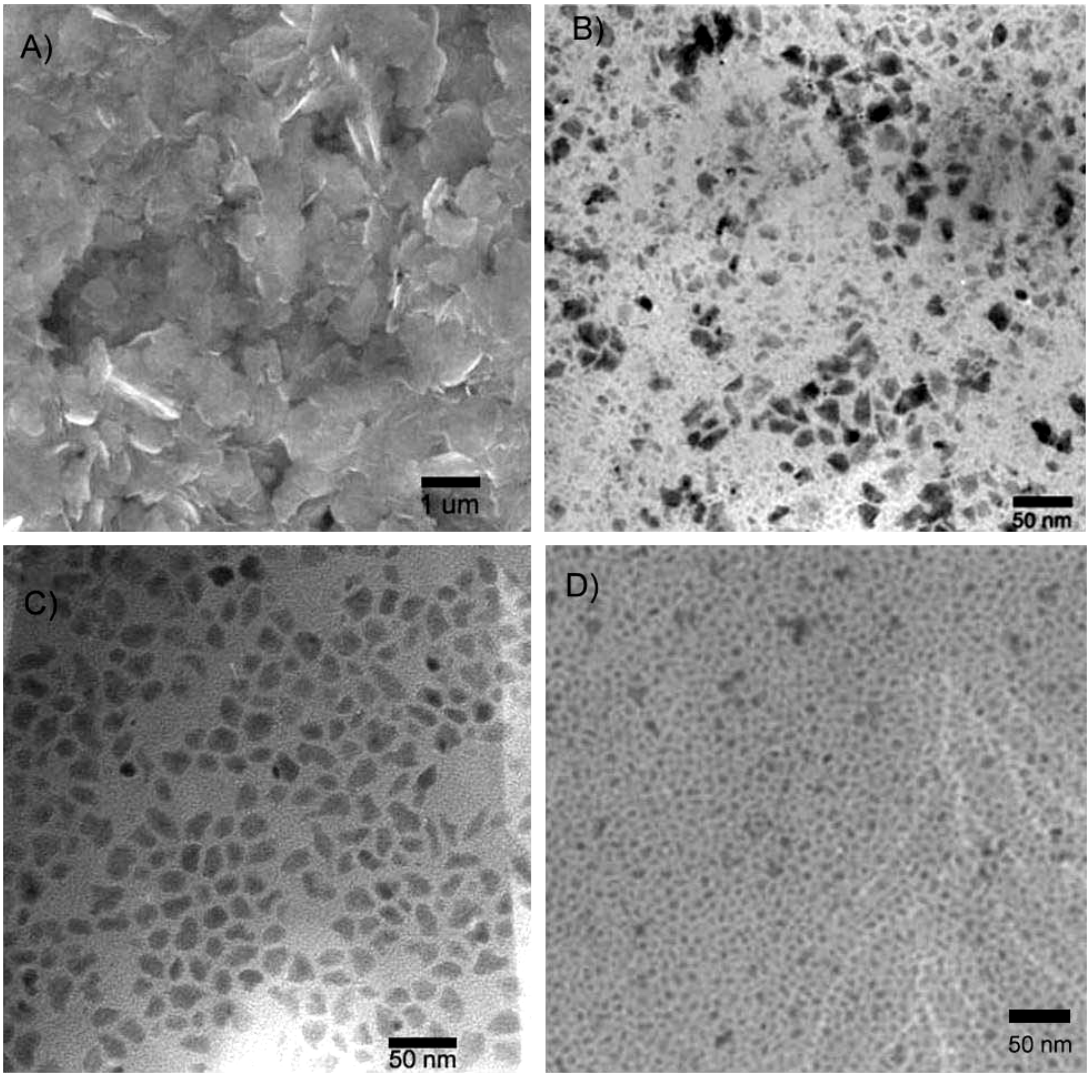

Figure 8.3 SEM and TEM images of Sm_2Co_{17} nanoparticles ground for 20 hours in heptane with surfactants: A) as-milled slurry particles with sizes of about 3 –7 μm, B) nanoparticles with sizes of about 3–30 nm, C) nanoparticles with sizes ~ 20 nm separated by 3 hours of settling-down time and D) ~ 5 nm nanoparticles separated by centrifugation.

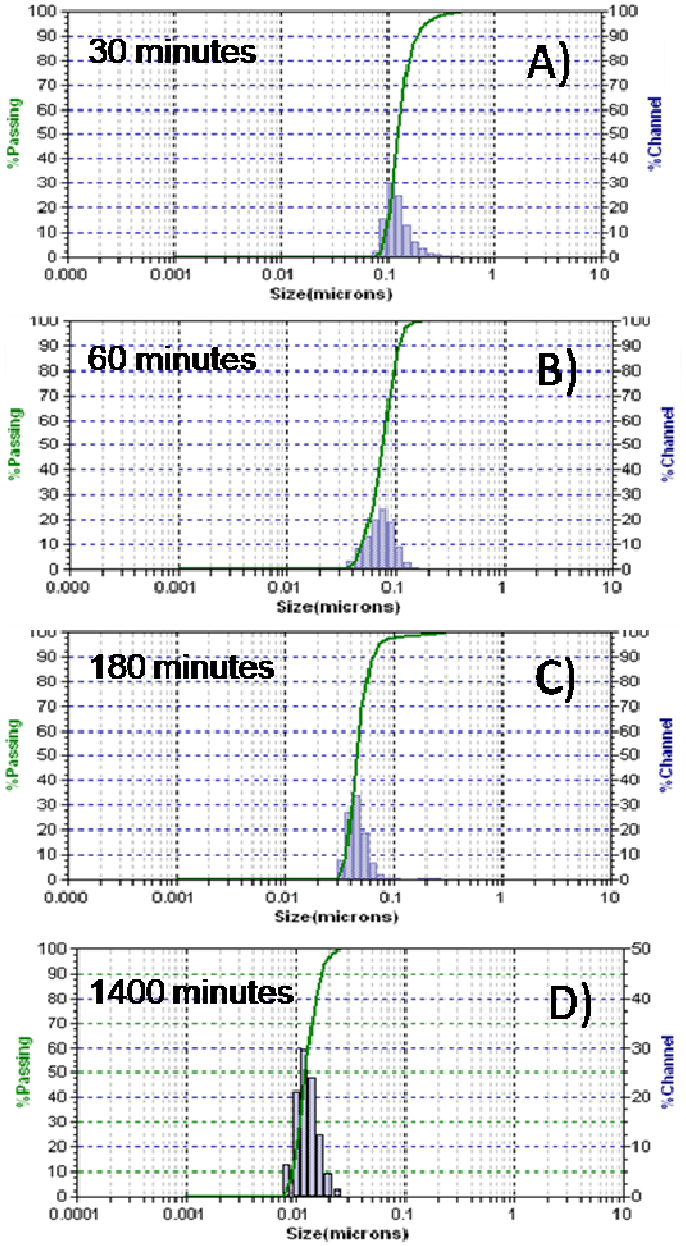

Figure 8.4 Particle size distribution (as measured by the laser particle size analyzer) of the Sm_2Co_{17} particles collected using different settling down time.

Figure 8.4 (A-D) gives the statistical size distributions of the nanoparticles measured by a laser particle-size analyzer (LPSA) after the size-selection process and using different settling-down times. It ca be observed from the histogram obtained by the LPSA that the size distribution of ball-milled nanoparticles obtained by using the size-selection process is reasonable and that the size of the

nanoparticles decreases with increasing settling-down time. Figure 8.5 gives the statistical distribution of the LPSA –measured Sm_2Co_{17} slurry particles that were ball-milled for 20 hours in heptane in presence of surfactants.

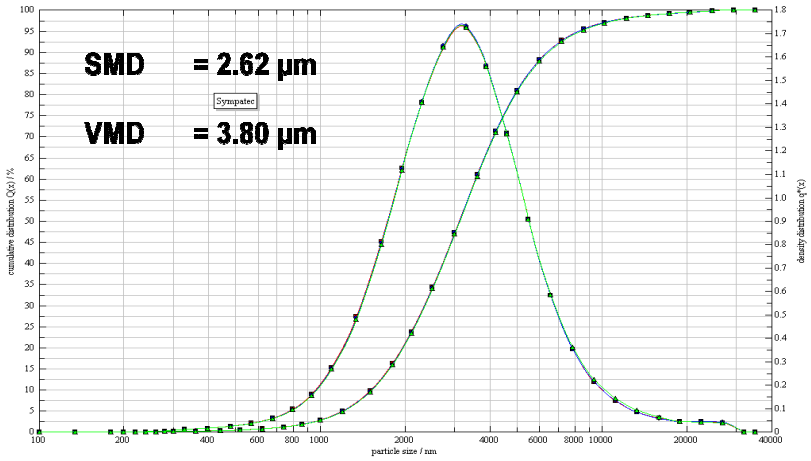

Figure 8.5 Particle size (as measured by Laser particle size analyzer) for Sm_2Co_{17} slurry particles ball-milled for 20 hours in heptane in the presence of surfactants (in Sympatech).

For comparision, Figure 8.6 shows the XRD patterns of Sm_2Co_{17} particles of different sizes obtained by the size-selection process and the starting powder. It can be seen that no peaks from oxides, pure iron and cobalt, are present in the diffraction patterns, indicating that the prepared nanoparticles have been effectively protected from oxidation by handling the solution in the glove box and embedding the particles in epoxy. The diffraction patterns also confirm that no detectable contamination or decomposition in the particles has occurred during the milling process. The EDX measurements showed that the compositions of the nanoparticle samples were close to the compositions of the starting Sm_2Co_{17} powder. As expected the results also show that the diffraction peaks broaden with decreasing particle size. The strains and amorphorization induced by high-energy ball milling may also have contributed to the broadening of the diffraction peaks, so it is difficult to calculate quantitatively the particle size from the width of the diffraction peaks.

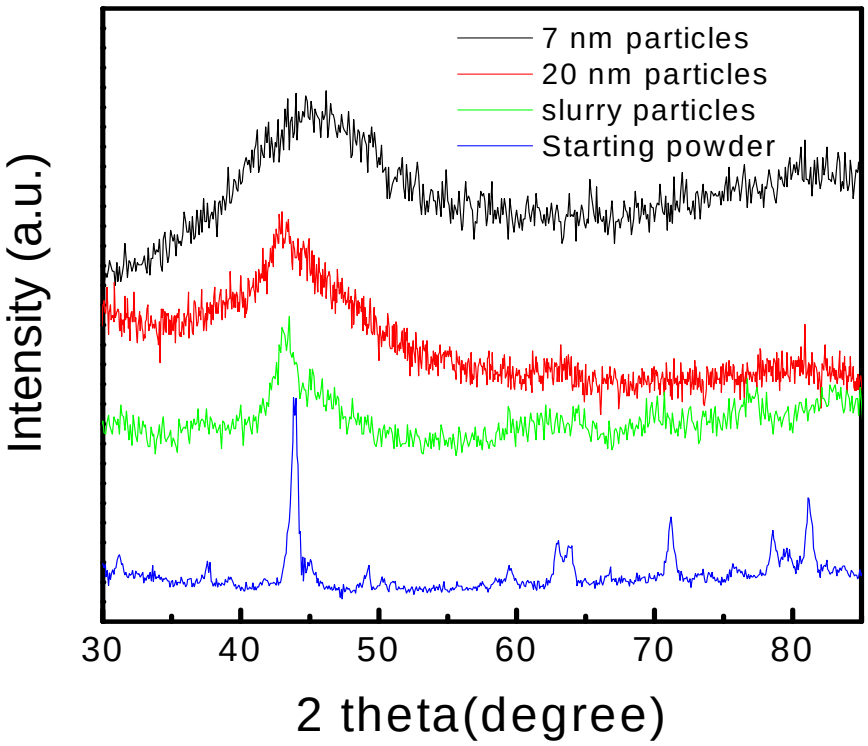

Figure 8.6 XRD patterns of A) Sm_2Co_{17} starting raw powder, B) slurry particles ball-milled for 20 hours C) ~ 20 nm Sm_2Co_{17} nanoparticles separated from 20 hours ball-milled powder and D) ~5 nm Sm_2Co_{17} separated from 20 hours ball-milled powder.

As mentioned above, it is hard to estimate the grain size of ball-milled particles because of the broadening of XRD peaks due to the strains and amorphorization induced by high-energy ball-milling. Analysis of particle size and size distribution of ball-milled Sm_2Co_{17} particles were carried out using SAXS in the transmission geometry (as described in Chapter 4 (Section 4.1.4)). The experimental scattering curves were measured by SAXS, and the size was determined by the direct fitting of model curves to experimental scattering curves. All the samples were fitted with a spherical model for experimentally measured scattering curves. Figure 8.7 shows the experimentally measured scattering curves and particle size and size distribution obtained by fitting scattering curves for permanently suspended nanoparticles and nanoparticles collected using 3 hours of settling-down time. Figures 8.7 (A) and 8.7 (C) shows the typical SAXS patterns (scattering curves) measured in red colored lines for permanently

suspended nanoparticles and nanoparticles collected using 3 hours settling down time. The blue-colored lines represent the simulated data. The size distributions of the particles were obtained by fitting the scattering profiles (as seen figure 8.7(B) and 8.7(D)). The average particle diameter calculated from SAXS measurement is close to that observed on the TEM micrograph images. The average diameters were estimated to be 4 nm for ~ 5 nm particles and 22 nm for ~ 20 nm particles, which is in close agreement with the TEM images.

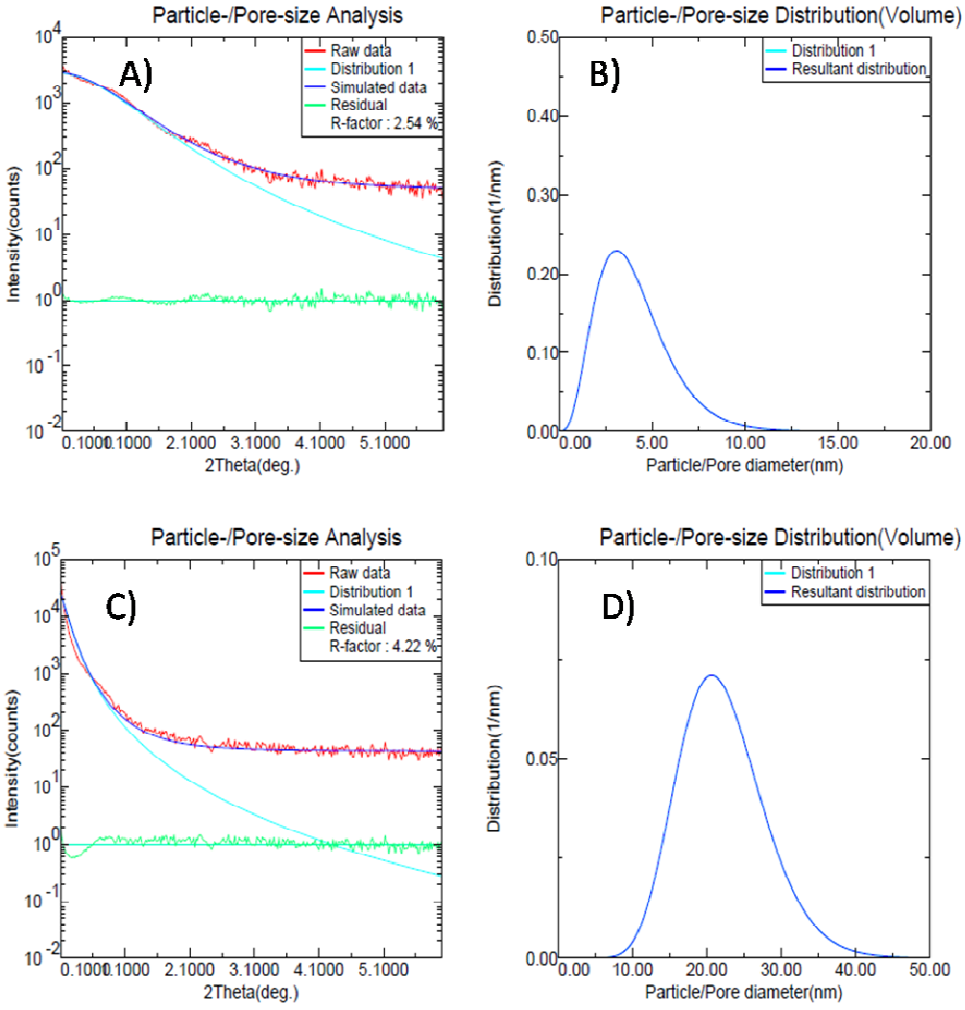

Figure 8.7 A) SAXS scattering profile of permanently suspended Sm_2Co_{17} nanoparticles nanoparticles and B) their size distribution, C) SAXS scattering profile of Sm_2Co_{17} nanoparticles collected using 3 hours of settling-down time and D) their size distribution.

Figure 8.8 shows room-temperature magnetization loops of the Sm_2Co_{17} nanoparticles collected from different settling-down times (30 minutes, 2 hours, 3 hours, and 12 hours and more than 7 days) after 20 hours ball-milling time. All the loops show a single-phase-like magnetization behavior (no kinks on the demagnetization curves), indicating no second phases in the particles. Figure 8.9 shows the dependence of particle size and coercivity on settling-down time. It can be observed that with increasing settling-down time, particle size decreases and thus the coercivity of particles also decease.

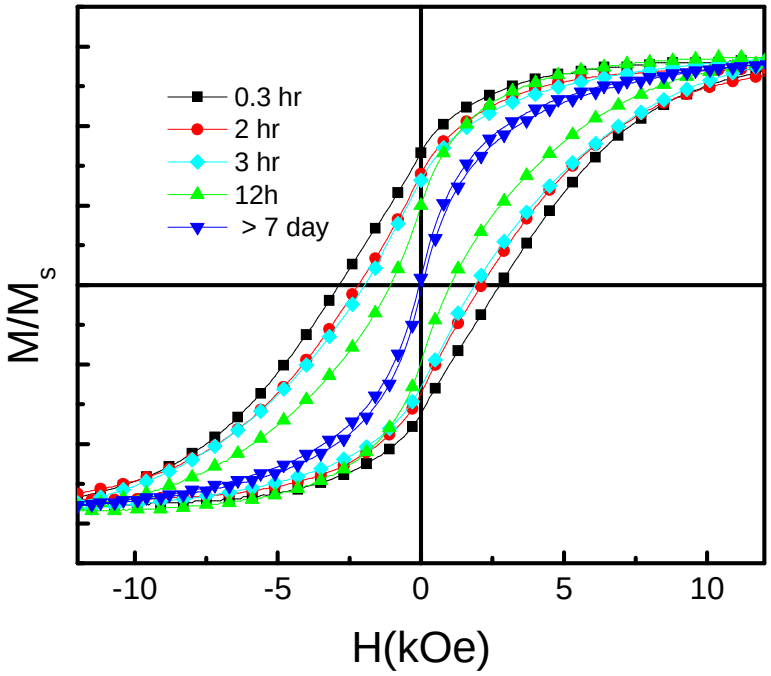

Figure 8.8 Hysteresis loops of Sm_2Co_{17} nanoparticles collected after different settling-down time.

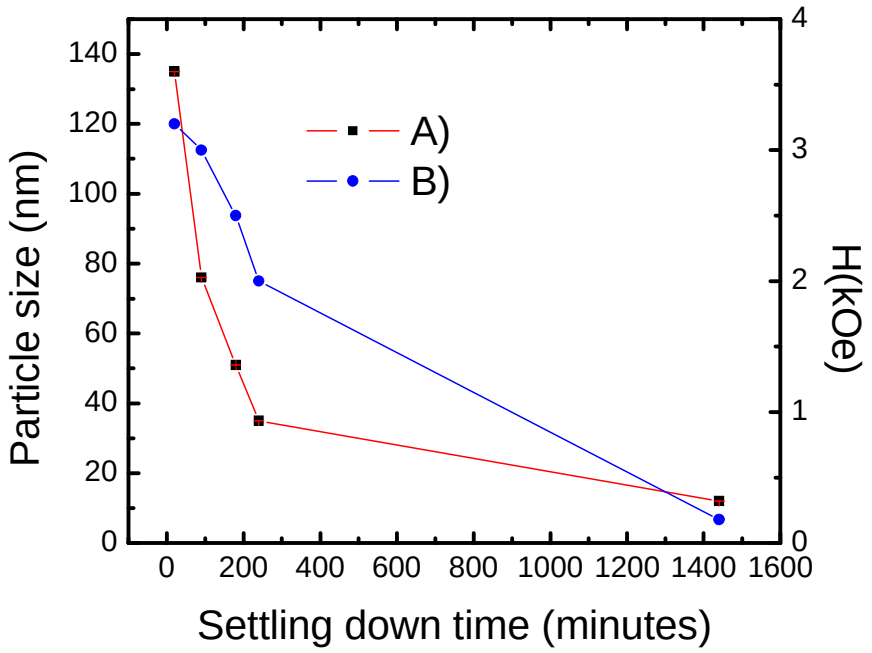

Figure 8.9 Dependence of A) particle size, and B) coercivity on settling-down time

The coercivity at room temperature of nanoparticles prepared by our methodology is significantly higher compared to the reported values of Sm–Co nanoparticles synthesized by other methods for these ranges of particle sizes. There is still much to be understood about the size-dependent coercivity of these nanoparticles. One possible explanation is that increased defects in the smaller particles lower the magnetocrystalline anisotropy.[94] In addition, local strains can also cause low-energy nucleation sites.[195,196] It is also possible that ball-milling has led to partial amorphorization in the nanoparticles and that the smaller particles have a more amorphous structure that leads to reduced coercivity. It should be mentioned that the quantitative determination of the magnetization of the particles is difficult due to the effects of the epoxy and the surfactants that cover the particles. The magnetization of nanoparticles that had settling-down time of 3 hours was 52 emu/g. The mass of the nanoparticles was determined using by microbalance after drying the particles inside the glove box in an inert medium and sealing them in an air tight plastic capsule. Once the mass was calculated the plastic capsule was taken inside the glove box

and epoxy was put on it to prevent the nanoparticles from oxidizing and moving while they were being measured by SQUID.

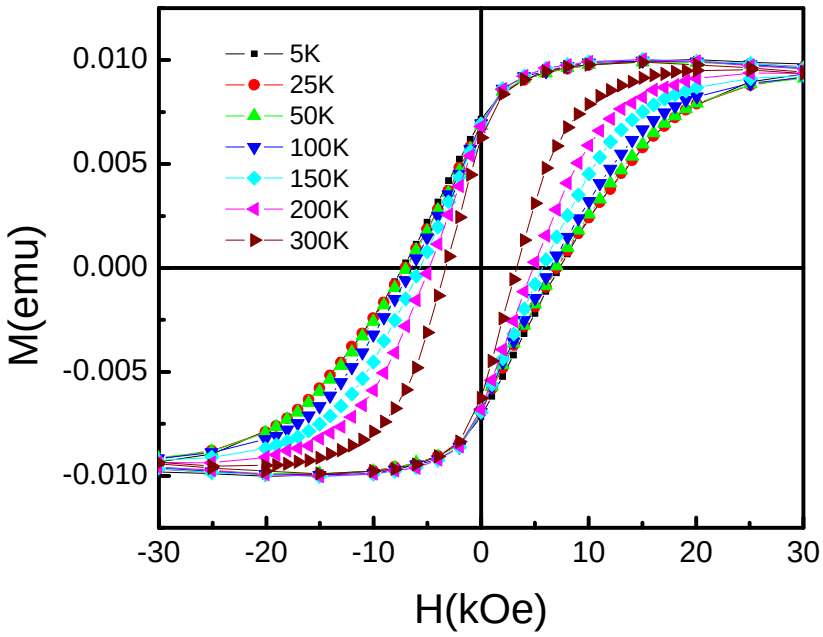

Figure 8.10 Low-temperature hysteresis loops of 20 nm Sm_2Co_{17} nanoparticles at different temperatures.

Low-temperature magnetic properties of different size particles were also studied by SQUID. Figure 8.10 shows the hysteresis loops of 20 nm nanoparticles measured at different temperatures. Figure 8.11 shows the variation of coercivity with temperature for 20 nm particles and slurry particles. It was found that with decreasing temperature the coercivity of particles increased. Furthermore, it was also found that the coercive force of the particles increased by more than 50% as the measuring temperature went down to 200 K because of the enhancement of the magnetocrystalline anisotropy of the Sm-Co phase in the particles. However, a similar increase was not observed in the 5 nm nanoparticles, indicating that the small particles are more prone to amorphorization and oxidation, which might also have resulted in a loss of magnetocrystalline anisotropy compared to the larger particles (Figure 8.12).

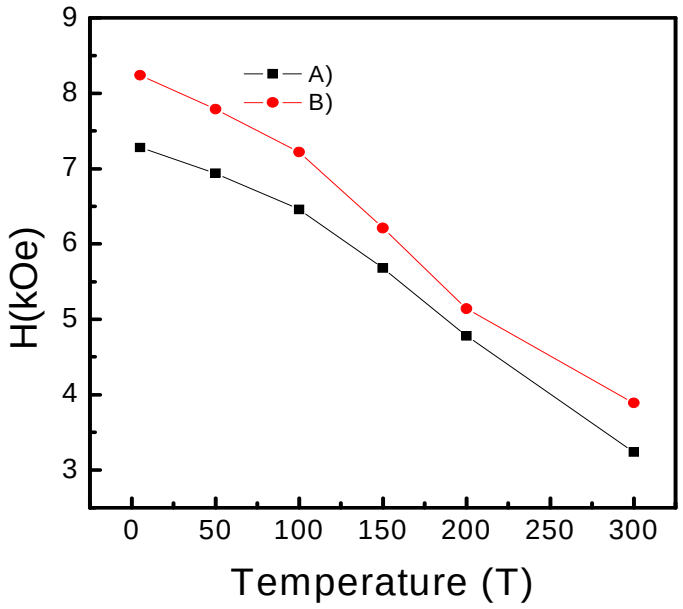

Figure 8.11 Temperature dependent coercivity of ball milled Sm_2Co_{17} A) slurry particles, and B) 20 nm nanoparticles.

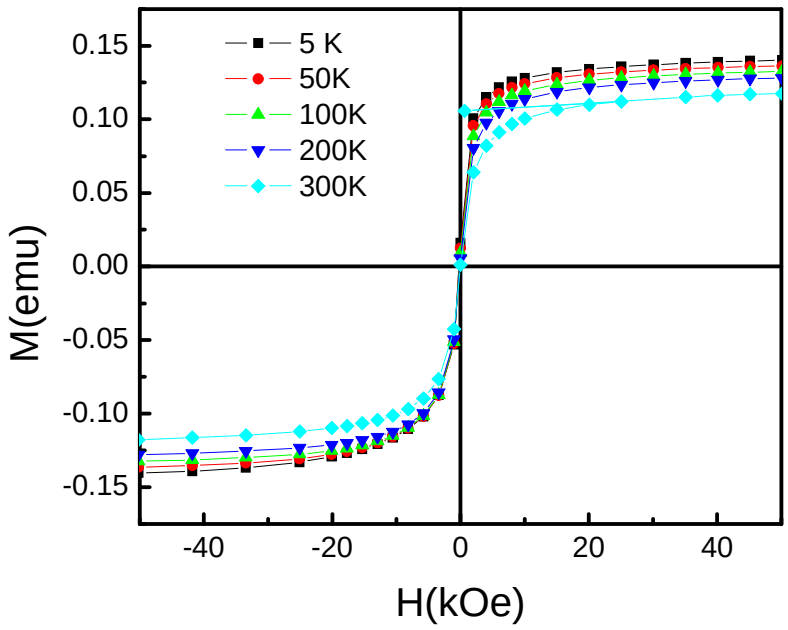

Figure 8.12 Low-temperature coercivity of ~5 nm Sm_2Co_{17}nanoparticles. Sm_2Co_{17} nanoparticles were obtained by size selection process after 20 hours ball-milling in the presence of surfactants.

Figure 8.13 shows the room- temperature magnetic viscosity of Sm_2Co_{17} slurry particles (3-7 μm) and Sm_2Co_{17} 20 nm particles are different for the two sizes of particle. It has been observed that the magnetization of the 20 nm nanoparticles is more susceptible to thermal fluctuations, which is to be expected for smaller volumes.

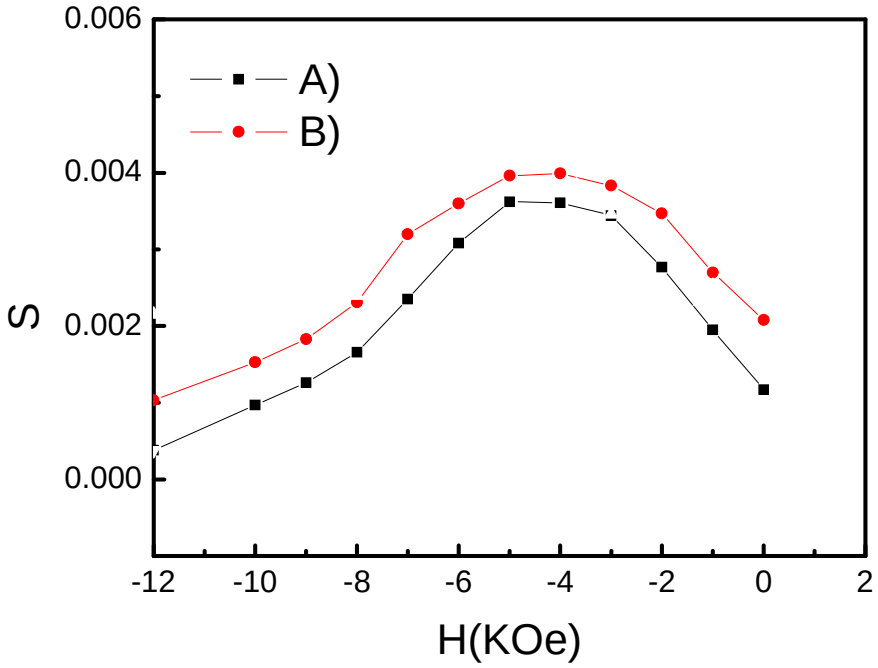

Figure 8.13 Room-temperature magnetic viscosity of ball-milled Sm_2Co_{17} A) slurry particles, and B) 20 nm particles.

8.1.4 $SmCo_5$ Nanoparticles

The $SmCo_5$ compound has the highest magnetocrystalline anisotropy (6 - 20) × 10^7 erg/cm^3) among all the known hard magnetic materials and also has a high Curie temperature (T_c =1020 K), suggesting that the nanoparticles of this compound are promising for many technological applications. Typically, the $SmCo_5$ phase a has higher coercivity compared to Sm_2Co_{17}, therefore, nanoparticles of $SmCo_5$ that were prepared using surfactant-assisted ball-milling technique were expected to have a higher coercivity compared to Sm_2Co_{17}. Figure 8.14 shows the SEM image of $SmCo_5$ slurry particles ball-

milled for 20 hours in heptanes with the surfactants oleic acid and oleyl amine. It can be seen from Figure 8.13 that the particles exhibit irregular shape and large size distribution and have an average particles size of about 3 µm.

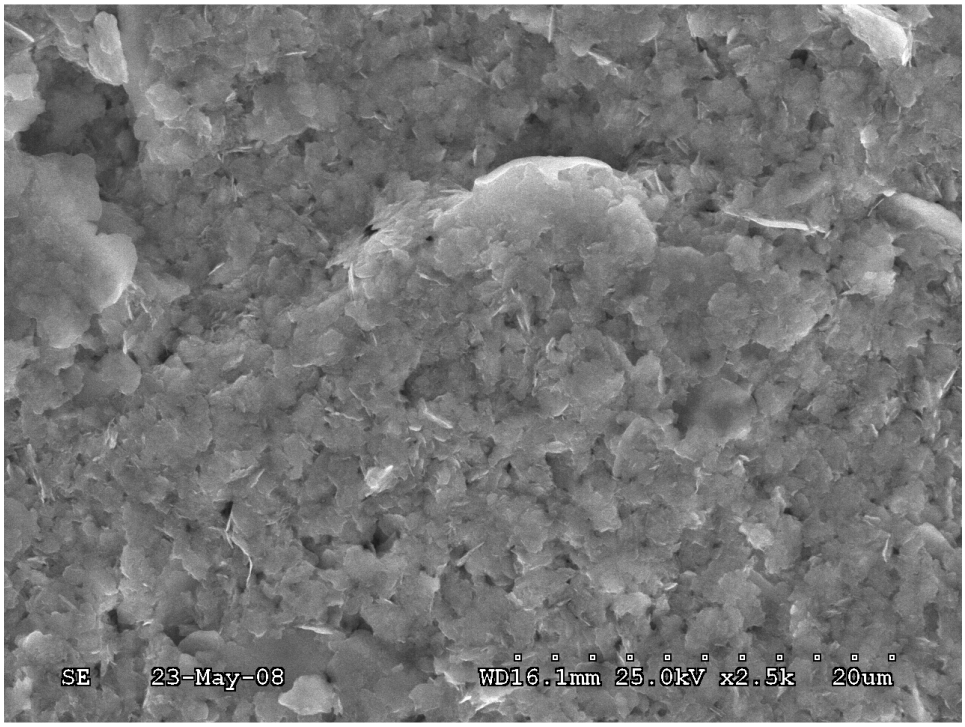

Figure 8.14 SEM images of $SmCo_5$ slurry particles ball-milled for 20 hours in heptanes with surfactants oleic acid and oleylamine.

Figure 8.15 A) and B) show TEM images of ~ 6 nm and ~ 20 nm $SmCo_5$ nanoparticles, respectively. To collect the small-size nanoparticles, the as-milled $SmCo_5$ slurry was vibrated ultrasonically with heptane solvent and settled down for 20 hours, during which time large particles settled down gradually, while smaller particles were still floating in the solution. To obtain the larger nanoparticles, the slurry was washed once in heptane to remove the smallest floating nanoparticles. Then, the remaining part was transferred into a centrifugal tube and dispersed in heptane again by using similar ultrasonic vibration process; the dispersed solution was then settled down for 3 hours. After this

settling-down time, a low-speed centrifugal separation of 500 rpm was carried out to remove the largest particles. It can be seen from Figure. 8.15 that both the sizes of nanoparticle exhibit irregular shape and nanoparticles possess a narrow size distribution.

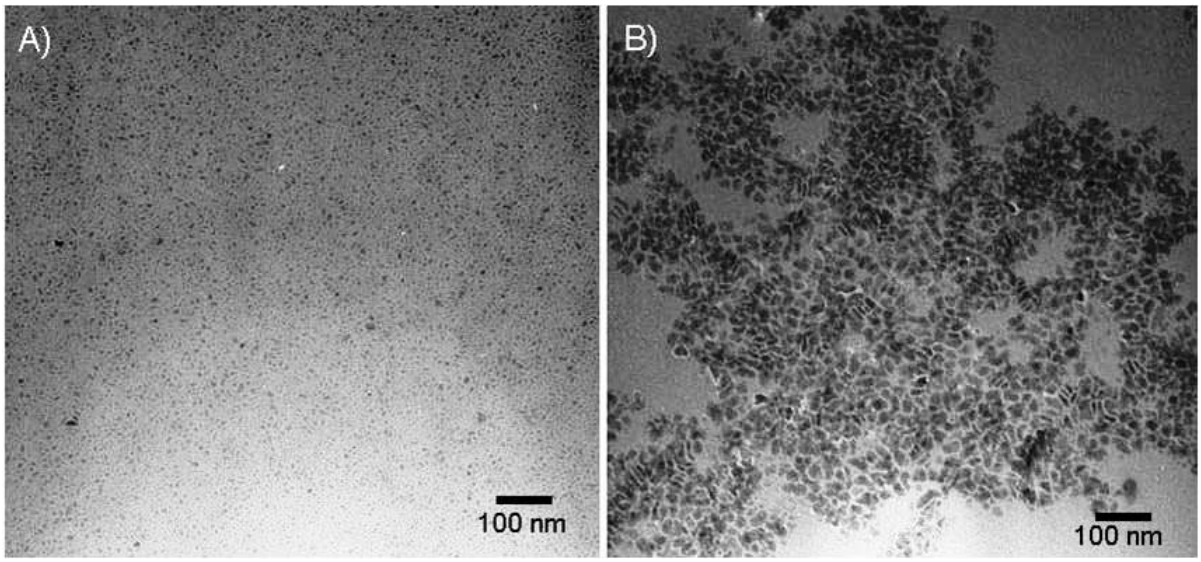

Figure 8.15 TEM images of $SmCo_5$ nanoparticles: A) ~ 6 nm, and B) ~ 20 nm obtained by size selection process from $SmCo_5$ powder that was milled for 20 hours.

Figure 8.16 (A) shows the XRD patterns of the 20 nm $SmCo_5$ nanoparticles obtained by the size selection process using 4 hours of settling-down time from ball-milled powder for 10, 15, and 20 hours of milling time. For comparison, the pattern of the starting raw powders is also shown in Figure. 8.16 A (a). It can be seen that diffraction the peaks of all the 20 nm nanoparticles are very broad and there is no noticeable difference in the XRD patterns of nanoparticles collected using same settling-down time but from different ball-milling periods. However, the XRD patterns of the slurry particles show changes in diffraction patterns with increasing milling times (as shown in Figure 8.16 (B)). The Peaks in the XRD patterns broaden with increasing milling time because of the decrease in particles size. Apart from the decrease in particle size, the strains and amorphorization induced during the ball-milling process may also contribute to the broadening of the diffraction peaks. It is, therefore, difficult to calculate quantitatively

the particle size from the width of the diffraction peaks. As in the case of Sm_2Co_{17}, no diffraction peaks from rare earth oxides and Fe contamination were observed in the XRD patterns. This indicates that the prepared particles have been well-protected from oxidation during the fabrication and examination process.

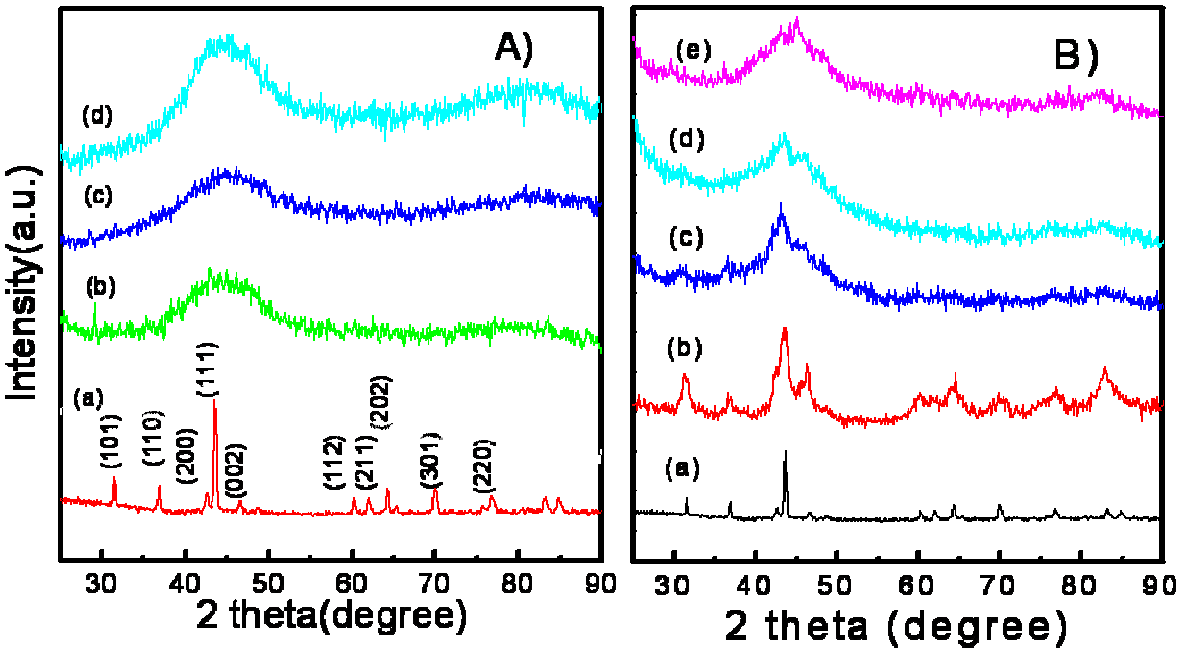

Figure 8.16 XRD patterns of A) (a) starting $SmCo_5$ powder and the $SmCo_5$ nanoparticles collected using 4 hour settling-down time from milled for (b) 10 hours (c) 15 hours (d) 20 hours and (B) as-milled $SmCo_5$ slurries with different milling time (a) starting powder, and milled for (b) 5 hours (c) 10 hours (d) 15 hours and 20 hours.

Figure 8.17 shows the typical hysteresis loop of both the small (20 nm) and the large $SmCo_5$ particles (~3 µm) obtained after 20 hours of ball-milling at 300 K. The intrinsic coercive force of the small and big nanoparticles is 2 and 11 kOe, respectively. The significant reduction of the coercive force for nanoparticles may be due to the amorphous structure of the nanoparticles. However, the coercivity of the $SmCo_5$ nanoparticles dropped much more compared to the Sm_2Co_{17} phase nanoparticles after 20 hours of ball-milling, this indicates that $SmCo_5$ is more prone to amorphorization, which may result in more structural change of the $SmCo_5$ phase during the preparation process as compared with the large particles.

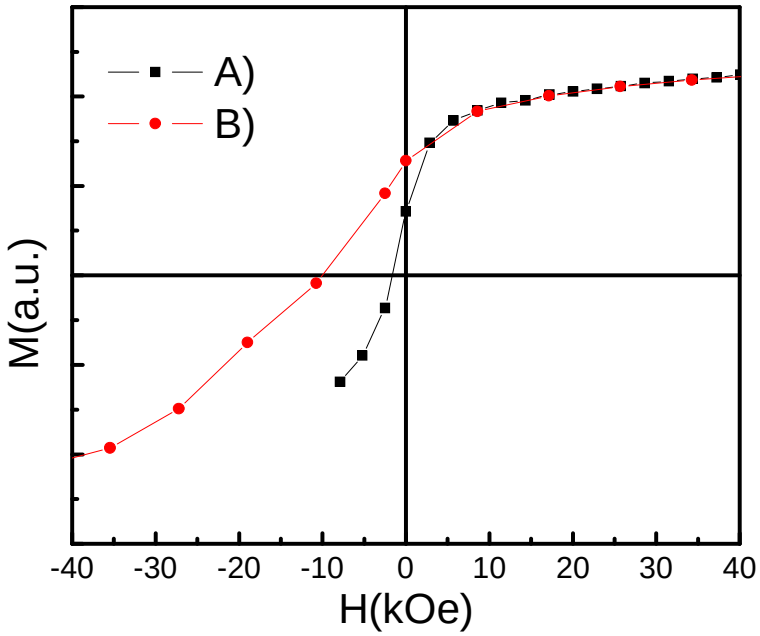

Figure 8.17 Room-temperature hysteresis loops of: A) 20 nm $SmCo_5$ nanoparticles, and B) slurry particles for 20 hours ball-milled.

8.1.5 $Nd_2Fe_{14}B$ Nanoparticles

In previous sections of this chapter, the preparation of $SmCo_5$ and Sm_2Co_{17} nanoparticles with different sizes and narrow size distribution via surfactant-assisted high-energy ball-milling and subsequent size-selection has been discussed. A high coercive force of 3.1 kOe for Sm_2Co_{17} nanoparticles at room temperature was obtained. The technique was also applied to prepare Nd-Fe-B nanoparticles of different sizes and the results of structural characterization and magnetic properties will be discussed below.

$Nd_2Fe_{14}B$ raw powder was ball-milled for 10 hours in the presence of both the surfactants (as described in Chapter 3 (Section 3.16)) Figure 8.18 A) and B) show TEM images of ~7 nm and ~20 nm Nd-Fe-B nanoparticles, respectively. To collect the small-size nanoparticles, the as-milled Nd-Fe-B slurry was vibrated ultrasonically with heptane solvent and settled down for 20 hours, during which time large particles settled down gradually, while smaller particles were still floating in the solution. To obtain the larger nanoparticles, the slurry was washed once in heptane to remove the smallest floating

nanoparticles. Then, the remaining part was transferred into a surfactant-coated centrifugal tube and dispersed in heptane again by using a similar ultrasonic vibration process; the dispersed solution was then settled down for 3 hours. After this settling-down time, a low-speed centrifugal separation of 500 rpm was carried out to remove the largest particles. It can be seen from Figure 8.18 that both sizes of nanoparticles exhibit irregular shape and that the nanoparticles possess narrow size distribution.

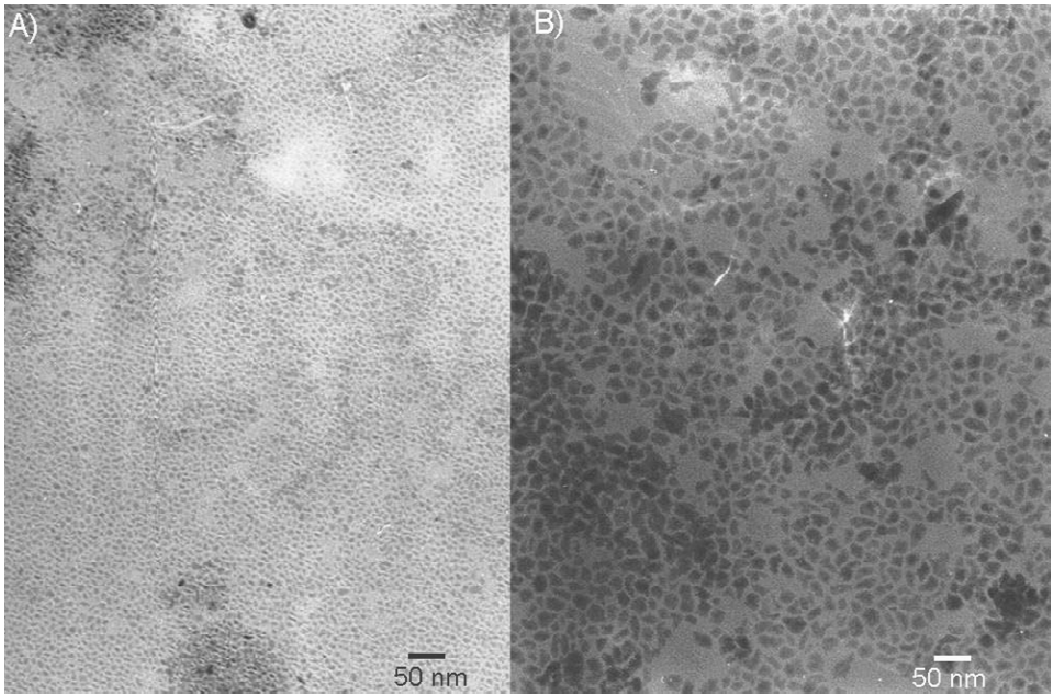

Figure 8.18 TEM images of $Nd_2Fe_{14}B$ nanoparticles: A) ~7 nm B) ~ 20 nm obtained by size selection process from $Nd_2Fe_{14}B$ powder that was milled for 10 hours.

Figure 8.19 shows the XRD patterns of the Nd-Fe-B nanoparticles with different sizes obtained by the size-selection process. For comparison, the pattern of the starting raw powders is also shown in Figure 8.19. It can be seen that the diffraction peaks of the ~7 nm and ~20 nm nanoparticles are very broad. Apart from the decrease in particle size, the strains and amorphorization induced during the ball-milling process may also contribute to the broadening of the diffraction peaks. It is therefore difficult to calculate calculate quantitatively the particle size from the width of the diffraction peaks. In addition, no

diffraction peaks from rare earth oxides, which always exist in the XRD patterns of oxidized Nd-Fe-B nanoparticles in our experiments, has been found either of the patterns for the small and the large nanoparticles, indicating that the prepared nanoparticles have been effectively protected from oxidation during the fabrication and examination process.

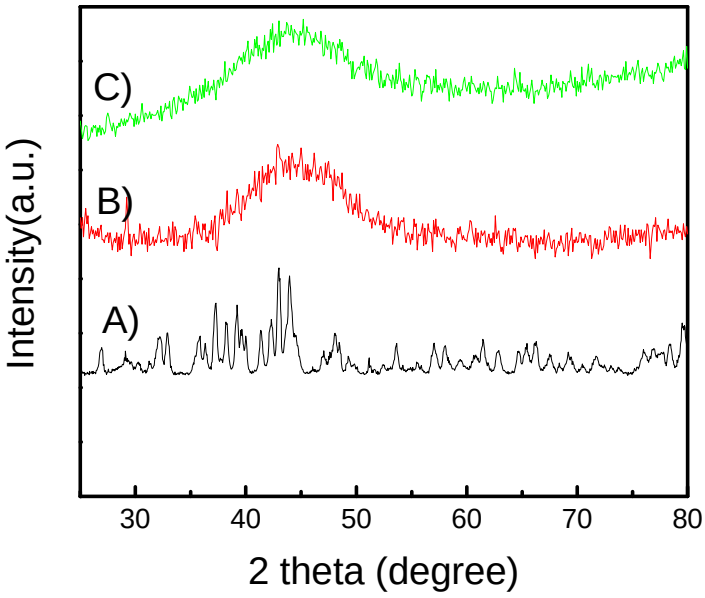

Figure 8.19 XRD patterns of Nd-Fe-B:A) starting raw powder and B) ~20 nm and C) ~ 7 nm nanoparticles collected by size selection process $Nd_2Fe_{14}B$ powder that was milled for 10 hours.

Figure 8.20 shows the magnetization hysteresis loops of Nd-Fe-B permanently suspended nanoparticles (~7 nm), nanoparticles collected using 3 hours of settling down time (~20 nm), and as-milled slurry particles (~7 μm) collected after 10 hours of ball milling at 300 K. The coercivity of the permanently suspended nanoparticles (~7 nm), nanoparticles collected using 3 hours settling-down time (~20 nm), and as-milled slurry particles (~7 μm) is 0.1, 0.5, and 3.2 kOe, respectively. The low coercivity of the particles may be due to the amorphous structure of the nanoparticles and to some possible contamination during the preparation process (as discussed earlier).

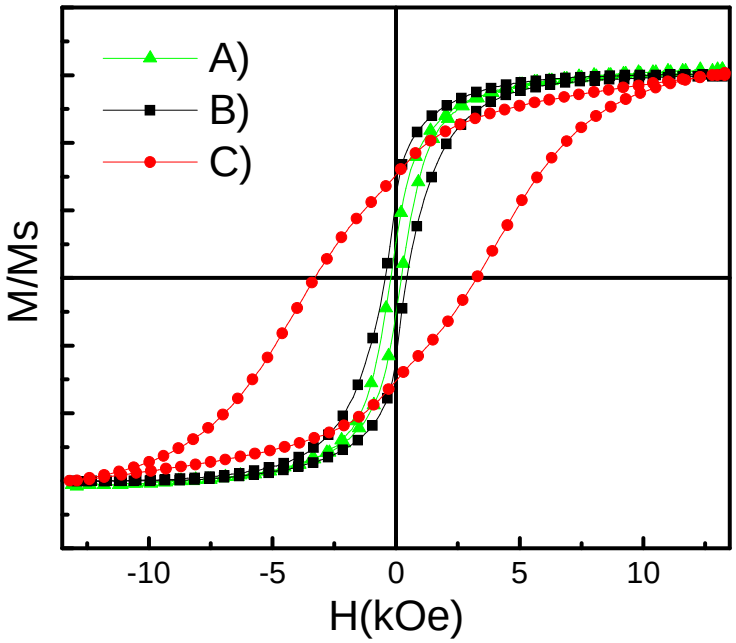

Figure 8.20 The room temperature hysteresis loops of Nd-Fe-B: A) permanently suspended nanoparticles (~ 7 nm), B) nanoparticles collected using 3 hours of settling-down time (~20 nm), and C) as-milled slurryparticles (~7 µm).

8.1.6 High Vacuum Annealing

By controlling the size-selection process, such as settling-down time and centrifugal separation, Sm-Co nanoparticles with narrow size distribution and room-temperature coercivity of ~ 3 kOe have been produced. The high-impact energy of ball milling destroys regular crystal structure and induces the amorphous phase, which may be the reason for the low coercivity of ball milled particles. The coercivity of ball-milling particles can be improved if the amorphous phase can be transferred to the crystalline phase by post-annealing. In this section, we discuss our recent efforts to post-annealing of ball milled particles in order to improve their coercivity.It is known that RE-TE nanoparticles are very active and therefore they are prone to the oxidation that causes the decomposition of Sm-Co particles decreases their coercivity due to the formation of the magnetically soft phase. Higher-temperature, oxidation of RE-TE nanoparticles is very severe. The Sm_2Co_{17} particles that were ball-milled were annealed in a high vacuum (6×10^{-5} torr) furnace to avoid oxidation. As-milled Sm_2Co_{17} slurry particles and nanoparticles dry

powder were annealed on copper foils at different temperatures at vacuum furnace for 30 minutes. Figure 8.21 shows the annealing-temperature dependence of the coercivity for different milling times of Sm_2Co_{17} slurry particles. It can be seen that the coercivity continuously decreases from 3.6 kOe to 300 Oe with increasing annealing temperature from 250 ^{o}Cto 500 ^{o}C for 30 minutes annealing time. Figure 8.22 shows the XRD patterns of slurry particles annealed between 250 ^{o}C to 500 ^{o}C for 30 minutes in a high vacuum (6×10^{-5} torr) furnace. It was observed that the decomposition of Sm_2Co_{17} started at 250 ^{o}C and increased with annealing temperature, which caused a decrease in coercivity due to formation of soft phase (FeCo or Co). The coercivity of the nanoparticles (~ 20 nm) decreased remarkably from ~3 kOe to less than 100 Oe when annealed at 300 ^{o}C for 30 minutes in high-vacuum furnace (as shown in Figure 8.23), indicating that the decomposition is more severe for 20 nm nanoparticles. It is believed that the decomposition of Sm-Co phase is the key to decreasing the coercivity of both the slurry and the nanoparticles after annealing. However, it is not known clearly what causes the decomposition of the Sm-Co phase during annealing with particles ball-milled in the presence of surfactants. It could be the result of the high-oxidation affinity of the rere-earth containing particles. Therefore we tried several different combinations of surfactants and solvent to investigate these issues, which will be discussed in the next section.

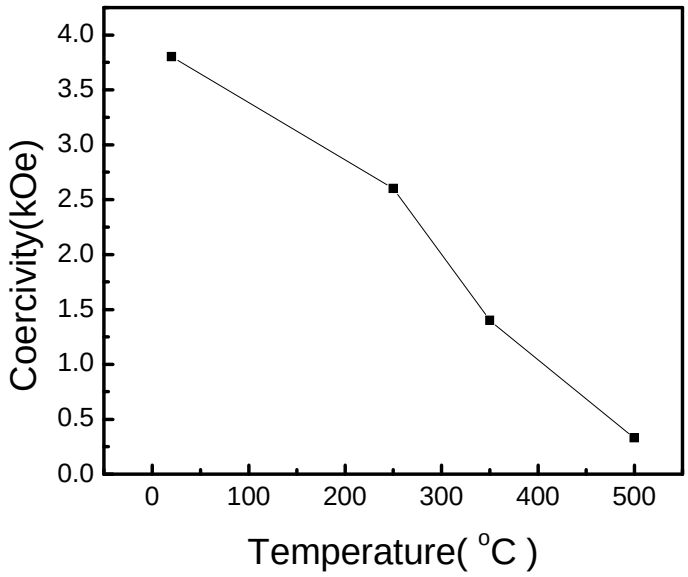

Figure 8.21 Room-temperature coercivity of Sm_2Co_{17} slurry particles ball-milled for 20 hours and annealed in different temperatures for 30 minutes in high-vacuum (5.6×10^{-5} Torr) furnace.

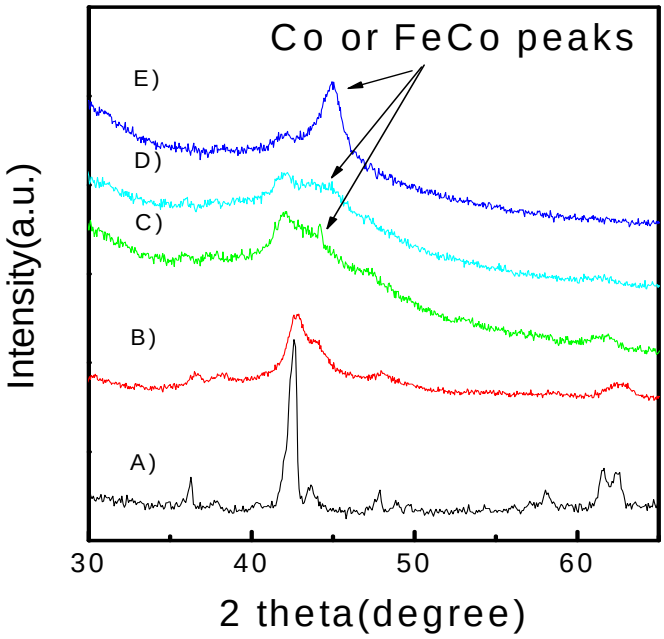

Figure 8.22 XRD patterns of Sm_2Co_{17}: A) starting powder, B) slurry particles milled for 20 hours, C) slurry particles annealed at 250 ^{o}C, D) slurry particles annealed at 350 ^{o}C and E) slurryparticles annealed at 500 ^{o}C for 30 minutes in a high vacuum (5.6 × 10 $^{-5}$ Torr) furnace.

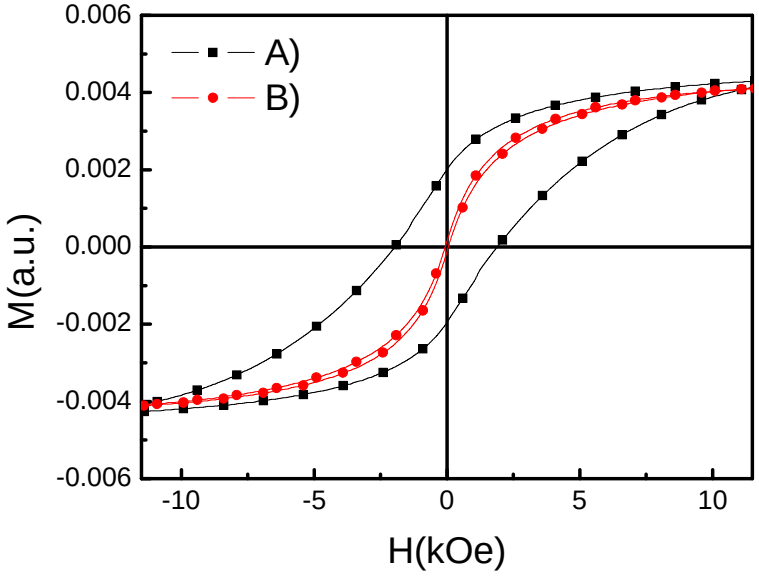

Figure 8.23 Room temperature hysteresis loops of 20 nm Sm_2Co_{17} nanoparticles: A) as ball-milled, and B) after the heat treatment at 300 ^{o}C for 30 minutes in a high vacuum (5.6 × 10 $^{-5}$ Torr) furnace.

8.1.7 Variation of Milling Conditions

In the earlier discussion of results in this chapter, all the ball-milling experiments were carried out using both surfactants oleic acid and oleylamine with heptane solvent. As discussed above, the heat treatment of Sm-Co (both the nanoparticles and slurry particles) always resulted in decreases in the coercivity because of decomposition. Therefore, we tried several different combinations of surfactants and solvents to investigate these problems. We also investigated the dispersion of particles and tried annealing slurry particles by changing the combination of surfactants and solvents. Figure 8.24 (A-C), shows XRD patterns of Sm_2Co_{17} starting powder and slurry particles annealed at 500 ^oC for 30 minutes in a high-vacuum furnace that was collected after 20 hours of milling using only oleic acid with heptane and only oleyl amine with heptane. It was interesting to see that the FeCo phase starts forming at an annealing temperature fo more than 250 ºC. The XRD intensity of the FeCo peaks increased, suggesting significant grain growth with increasing annealing temperature (Figure 8.24 (B) and 8.24 (C)) when surfactants were used during milling. The coercivity decreased with the formation of magnetically soft FeCo phase, while the magnetization increased. It is possible that the presence of surfactants promote oxidation even when annealing in a high-vacuum furnace connected with inert atmosphered glove box. The oxidation leads to the decomposition of Sm_2Co_{17} particles, and then the FeCo phase forms, since Sm_2Co_{17} starting powder contains Fe, Cu and Zr as dopants. Typical hysteresis loops of slurry particles before and after annealing at 500 ^oC for 30 minutes are shown in Figure 8.25. Several different combinations of surfactants and solvents were also tested for the dispersion of particles after 20 hours of milling and heat treatments were carried out in the high vacuum furnace at 500 ^oC for 30 minutes. Results of Sm_2Co_{17} particles produced under the different milling conditions have been summarized in Table 8.1 below. It can be seen in the Table 8.1 that dispersion of particles was not good when other combinations of surfactants and solvent were tried as when oleic acid, oleyl amine and heptane solvent were used.

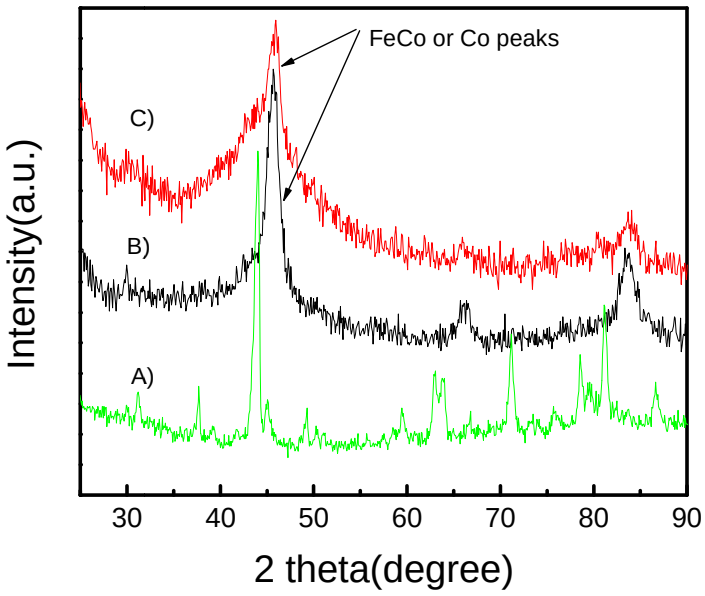

Figure 8.24 XRD patterns of Sm_2Co_{17}:A) starting powder, B) slurry ball -milled for 20 hours in heptane with oleic acid only as surfactant and annealed in the glove-box furnace in vacuum at 500 ^{o}C for 30 minutes, and C) slurry ball-milled for 20 hours in heptane with oleyl amine only as surfactant and annealed in the glove-box furnace in vacuum at 500 ^{o}C for 30 minutes.

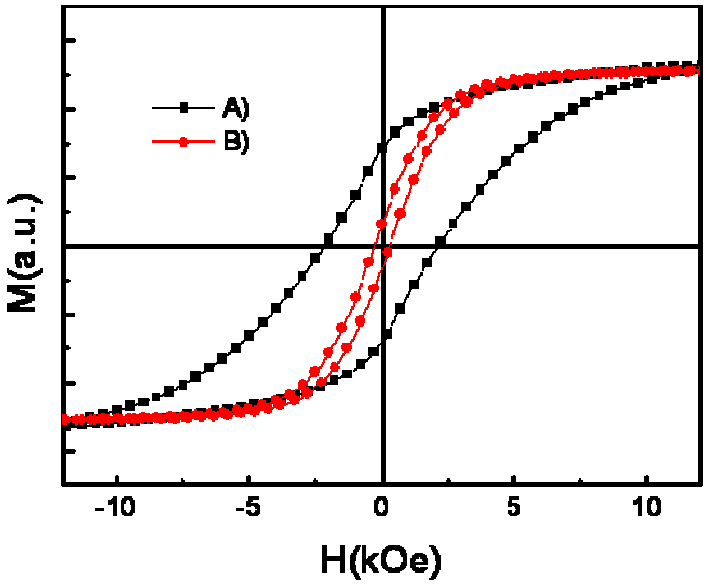

8.25 Hysteresis loops of Sm_2Co_{17} A) slurry ball milled for 20 hours in heptane with oleic acid only as surfactant, B) slurry powder annealed in the glove-box in vacuum- furnace at 500 ^{o}C for 30 minutes.

Table 8.1 Summary of the different milling conditions used for ball-milling of Sm_2Co_{17} powder and the coercivity of as-milled slurry particles for 20 hours and after post annealing at 500 ^oC for 30 minutes in a high vacuum furnace

#	Surfactants	Solvent	Particles Dispersion	Hc (kOe) Slurry	Hc (kOe) Annealed slurry
1	Oleic acid &Oleylamine	Haptane	very good	4.5	0.3
2	HDD + Oleylamine	Dicloro- benzene	not good	3.1	0.32
3	Ethylene glycol	-	good	1.3	0.13
4	Oleic acid	Heptane	good	3.5	0.75
5	Pentanedione	Heptane	not good	1.8	0.44
6	Tetraethelenpentamine	Heptane	not good	2.7	0.2
7	Trioctlyphosphine (TOP)	Heptane	very bad	0.7	0.12
8	Igepal	Heptane	not good	0.6	0.13
9	Tween 21	Heptane	good	2.8	0.23
10	Polyvinylpyrrolidone	1,2-propanediol	good (ethanol)	2.5	0.3
11	-	1,2-propanediol	good (ethanol)	2.1	0.32
12	1-methyl-2 pyrrolidone	-	good (ethanol)	2.3	0.13
13	Oleylamine	Heptane	good	1.8	0.25
14	Tetra -ethylene glycol	-	not good	2.1	0.40

8.1.8 Conclusion

Nanoparticles of rare-earth transition-metals including Sm_2Co_{17}, $SmCo_5$, and $Nd_2Fe_{14}B$ were successfully prepared by surfactant-assisted ball-milling techniques. The surfactants play key roles in preventing the cold welding and re-welding of crushed particles, enhancing the dispersion of the nanoparticles, and reducing the contamination during milling. Different-size particles with narrow size distribution can be obtained using a size selection process by controlling the settling-down time and by choosing the optimal speeds and periods for the centrifugal separation of the nanoparticles in solution. Both the particle size and the coercivity of Sm-Co and NdFeB nanoparticles are dependent on settling-down time and decrease with the increasing settling down time. Room temperature coercivity of as-milled Sm_2Co_{17}, $SmCo_5$, and $Nd_2Fe_{14}B$ nanoparticles of size ~ 20 nm obtained after 3 hours of setting-down time was 3.2, 2.0, and 0.5 kOe, respectively. The coercivity of ~20 nm particles increased more than 50% as the measuring temperature went down to 200 K because of the enhancement of the magnetocrystalline anisotropy of the Sm-Co phase in the particles, the coercivity of small particles ~ 5 nm is not temperature dependent, however, indicating that the small particles are more prone to amorphorization and oxidation,

which might also have resulted in a loss of magnetocrystalline anisotropy as compared to the larger particles. The XRD diffraction patterns of nanoparticles were broadened with decreasing particle size. Amorphorization and the strain induced by high-energy ball-milling may also contribute to the broadening of the diffraction peaks. Post-annealing of ball-milled particles in the presence of surfactants did not retain the properties but lost the phase of the starting raw powder when annealed at a high-vacuum temperature above 300 ^{o}C. Decomposition of the phase could be because of the high oxidation affinity of rare-earth containing particles. The optimization of ball-milling conditions and the surface coating of nanoparticles may improve the oxidation resistance of nanoparticles.

8.2 Magnetic Field Ball-Milling of Nd-Fe-B and Sm-Co Particles

8.2.1 Overview of the Issue

Nanocomposite hard magnetic materials have drawn considerable attention for their potential for very high energy products. [11,12, 211] However, this potential can be realized only if the nanosized grains of the hard magnetic phases can be aligned to form desired textures in the materials. It turns out to be a significant challenge to fabricate nanostructured bulk magnets with texture. The difficulties in achieving the alignment originate from the strong inter-particle reactions and reduced anisotropy of the particles as well as from the low thermal stability of the nanoparticles. Very fine ferromagnetic nanoparticles may have a superparamagnetic behavior. They also agglomerate easily and can be contaminated by oxygen and other reactive elements. As a consequence of these difficulties, hard magnetic nanoparticles can hardly be aligned using an electromagnet as for examples, in the situation for sintered bulk magnets of microsized hard magnetic powder particles. Other techniques for producing anisotropic bulk magnets, such as hot pressing, are associated with long thermal exposure and can cause excessive grain growth. For these reasons, assemblies of magnetic nanoparticles and nanostructured bulk magnets are generally magnetically isotropic. One of the possible approaches to producing anisotropic bulk nanocomposites magnets is to fabricate anisotropic micrometer sized or submicrometer sized particles containing aligned nanosized grains in the particles, so that anisotropic bulk magnets can be made from the particles. In this section, our recent experiments in preparing anisotropic hard magnetic particles with nanosized grain structures by ball milling in a magnetic field will be discussed. Ball-milling is an effective technique for

producing mechanically alloyed materials and powder particles.[75, 212] In recent years ball-milling has been widely applied to preparing nanostructured hard magnetic powder particles because with this technique one can produce powder particles with very fine particle size and grain size.[213, 214] Combined with subsequent heat treatments, a controlled nanostructure can be obtained in the particles. However, as mentioned above, the nanostructured powder particles produced in ordinary ball-milling are generally magnetically isotropic. The motivation of this investigation was based on the possible alignment effects of an external magnetic field on field-ball milled particles.

8.2.2 Magnetic Properties

$Nd_2Fe_{14}B$ and Sm_2Co_{17} based coarse powders (~ mesh 325) were obtained by pulverizing ingots. The grain size in the ingot is of the order of tens of micrometres. The powders were then ball-milled in a magnetic field (>3 kOe) as described in Chapter 3 (Section 3.17). For comparison, the powders were also milled under the same conditions without a magnetic field. On comparing the magnetic hysteresis loops of the $Nd_2Fe_{14}B$ powders milled in a magnetic field with those milled without a magnetic field, it is striking to observe that the remanent magnetization to saturation magnetization ratio (*M*r /*M*s*)* for the field-milled samples is remarkably higher than for those milled without the field. The increase in the *M*r /*M*s ratio upon field milling is in the range from 15% to 24% (measured in the easy magnetization direction). The increased *M*r /*M*s ratio indicates an enhanced anisotropy of the particles. To understand this point better, we also measured the hysteresis loops in the hard magnetization direction (perpendicular to the alignment direction). Figure 8.26 shows the loops measured in both the easy and the hard directions of the samples (only loops for samples prepared for 25 and 100 hours were plotted here). It can be clearly seen that samples milled in the field have higher anisotropy than those milled without an applied magnetic field. It is evident that the powders milled in a magnetic field have enhanced magnetic anisotropy.

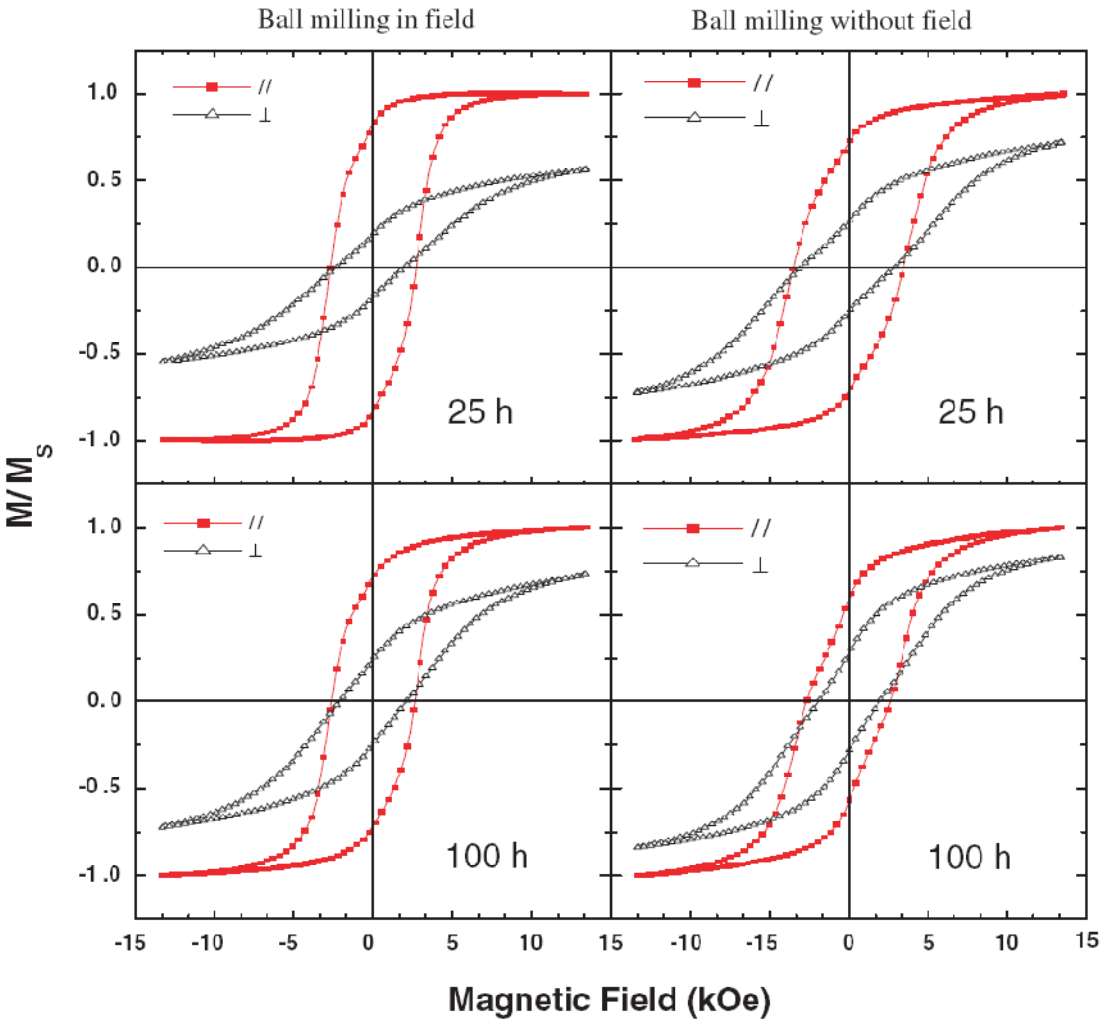

Figure 8.26 Magnetic hysteresis loops measured in both the alignment direction (easy magnetization direction) and the direction perpendicular to the easy direction of $Nd_2Fe_{14}B$ powder samples aligned in solidified epoxy. The left column has loops of the powders milled in a magnetic field and the right column has loops of thepowders milled without a magnetic field.

8.2.3 Morphology and Structure

SEM and TEM observations were made along with the magnetic characterization of the particles. It was found that the particle size reduces rapidly in the early hours of the milling, in both the field-ball milling and non-field-ball milling. The average size reaches its minimum after about 25 hours and remains unchanged with further milling. In our experiments, the minimum average size was about 100 nm. It is important to note that the particles size is not equal to the grain size. The grain size, starting with the

original particle size of tens of micrometres, reduces to nanometric order with milling. Figure 8.27 is a TEM image of a $Nd_2Fe_{14}B$ submicrometre particle milled for 25 hours in a magnetic field in Vertrel solvent.

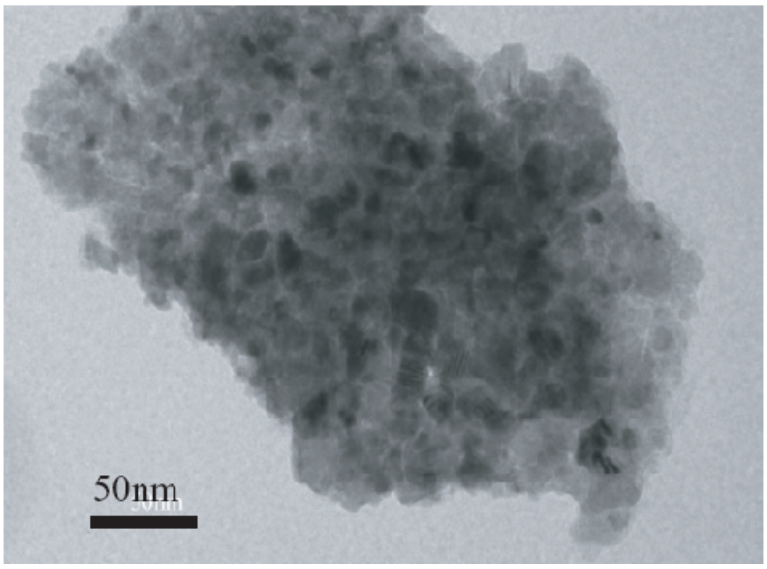

Figure 8.27 TEM image of an $Nd_2Fe_{14}B$ particle field-milled for 25 hours in Vertrel XF solvent. It can be clearly seen from this figure that the particles contain many grains smaller than 50 nm.

Samples milled without an applied field show a similar morphology. The average grain size is about 20 nm. The small grains inside a particle were formed either from plastic deformation of the particles during milling or from joining (welding) of the small nanoparticles. The joining (welding) of small first-degree nanoparticles into larger second-degree particles is an important process in ball-milling. Our laser analyser measurements revealed that there were a considerable number of nanosized particles in the liquid after the ball milling even though the average size never reached the nanometric order. After milling for a certain time the crushing and the welding reached equilibrium, and the average particle size remained unchanged with further milling. Eventually an amorphous structure will be created with further milling of the particles due to the severe plastic deformation. The reduced particle size and grain size resulting from severe plastic deformation lead to the monotonic reduction of the *M*r /*M*s ratio with milling time because of the reduced magnetic anisotropy. It should be noted from Figure 8.26 that samples

milled without a magnetic field still possess some magnetic anisotropy. This is not strange because some large particles in the powders can still be aligned in epoxy with a magnetic field, while small particles can only be aligned when they are joined together to form larger anisotropic second degree particles. When the milling time was longer than 100 hours, the anisotropy was dramatically reduced or essentially vanished, depending on the amorphization of the particles observed through the XRD and TEM measurements. Field-induced anisotropy during ball milling has also been observed in Sm_2Co_{17} powder samples. Figure 8.28 shows the milling time dependence of the *M*r /*M*s ratio of $Nd_2Fe_{14}B$ and Sm_2Co_{17} samples milled with and without a magnetic field. It is interesting to note that the difference between the *M*r /*M*s ratios of field-milled samples and non-field-milled samples tends to be larger with increasing milling time in the case of $Nd_2Fe_{14}B$, while in the case of Sm_2Co_{17} the difference becomes smaller (it vanishes at 100 hours). This is attributed to the difference between these two materials in their amorphization that leads to a reduction in magnetic anisotropy, and our XRD results are consistent with the magnetic measurements.

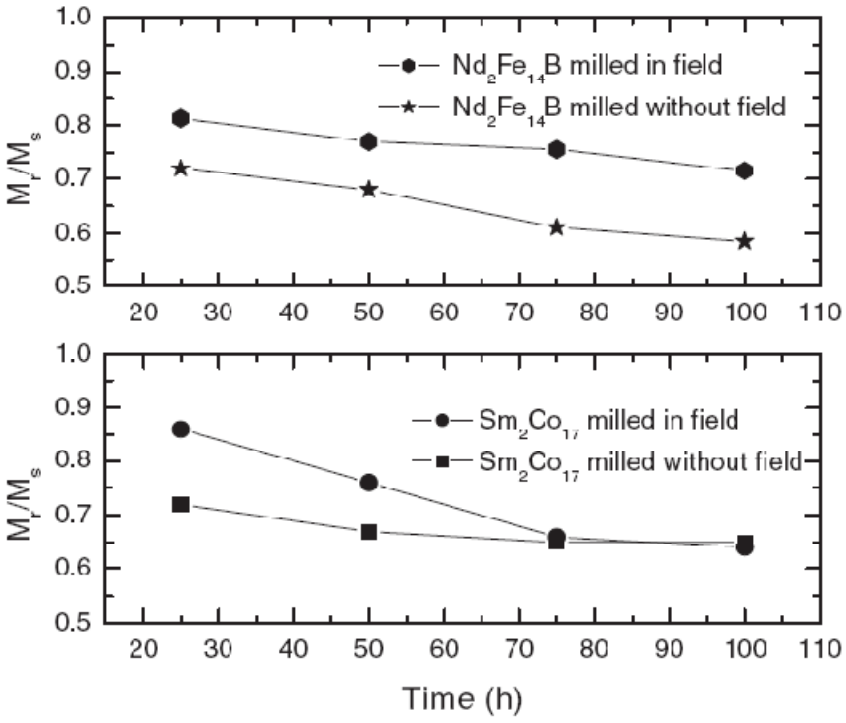

Figure 8.28 Values of *M*r /*M*s of $Nd_2Fe_{14}B$ samples and Sm_2Co_{17} samples plotted versus milling time.

We made careful observations and analyses by SEM, XRD and TEM of the field-ball milled and non-field-ball milled particles and found no considerable difference in the particle size and grain size, which excludes the possibility that the difference in the magnetic anisotropy was caused by a difference in the particle size or grain size. From Figure 8.27 we have seen that each particle contains hundreds of grains which normally align randomly in the particles in order to reduce the static magnetic energy. To understand the mechanism of the field-induced anisotropy in the powder particles, we used a transparent vial to observe the powder and ball motion behavior during milling. It was interesting to see that in the presence of a magnetic field the powder particles form chains along the field direction. The dimensions of the chains were a few centimeters in length and a few millimeters in diameter. The particles inside the chains were aligned. While the chains were colliding with the balls, re-joined small particles preferentially aligned themselves along the chain's long axis direction, which is normally parallel to the magnetic field direction. Without a magnetic field, the smaller particles naturally join the larger particles with their easy magnetization directions in a random way to reduce the magnetic static energy. In the presence of a magnetic field, in an ideal situation, each final 'second-degree particle' will be a short 'chain' of many nanosized particles. This will result in anisotropic micrometre or submicrometre particles.

To verify whether the nanosized grains are aligned in the powder particles milled in a magnetic field, we carried out XRD measurements of aligned powder samples of the $Nd_2Fe_{14}B$ materials milled with and without a magnetic field for 100 hours (Figure 8.29). The patterns (a) and (b) were from samples hardened in epoxy without an applied magnetic field and so we did not see any alignment. On comparing the patterns (c) and (d), it is evident that the field-milled samples (even their grain sizes are very fine after being milled for 100 hours) have a very good *c*-axis (the easy magnetization direction) alignment. Pattern (c) shows a much stronger reflection intensity of the *c*-axis planes (the x-ray patterns (c) and (d) were measured under the same conditions).

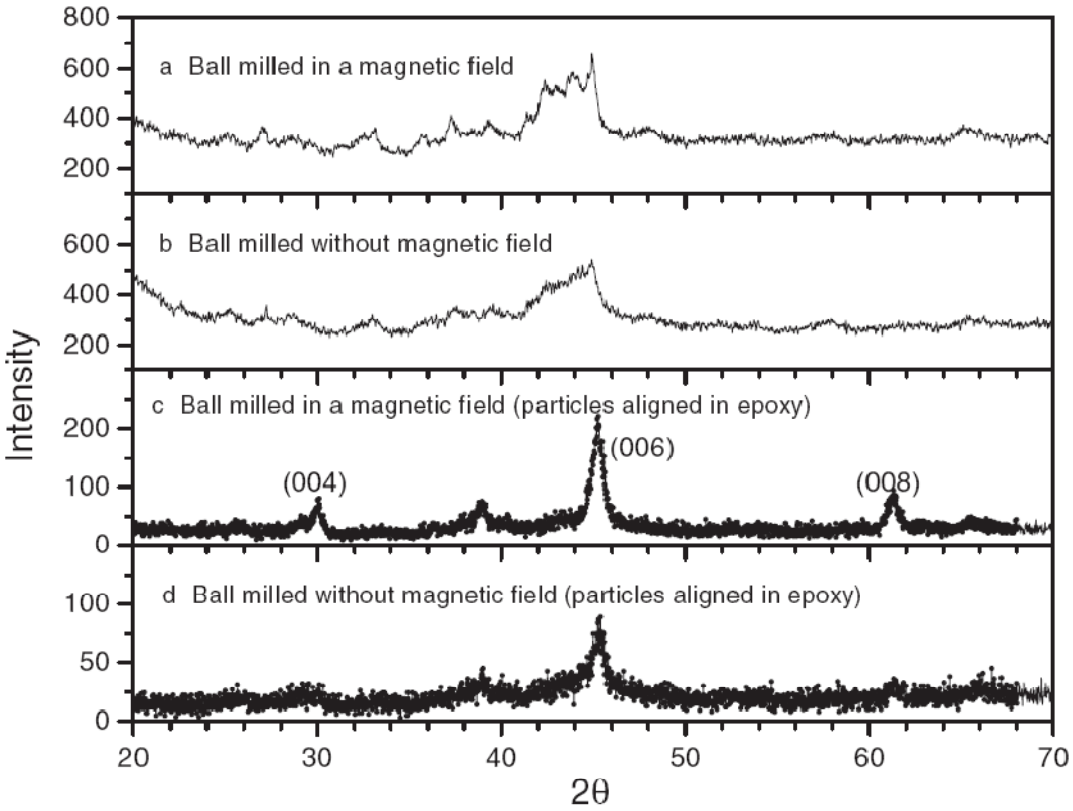

Figure 8.29 XRD patterns of $Nd_2Fe_{14}B$ powder samples milled for 100 hours.

The non-field-milled powders had a low-degree alignment due to the existence of some largesize grains and particles in the powders; however, the intensity of the (006) peak is substantially weaker than that in pattern (c), and other peaks in the *c*-axis are not recognizable. Considering the possible misalignment in the epoxy bonded magnetic particle specimens, pattern (c) shows a strong texture in the fieldmilled particles. A simple estimation of the anisotropic field by extrapolation of the loops in Figure 1 for the 100 hours fieldmilled samples gives a value of 4.5 T at room temperature (with error bar ~20–30%), which is of the same order of the value of 7.3 T for $Nd_2Fe_{14}B$ single crystals. [215, 216] If we include the reduced anisotropy due to the reduced particle size and grain size, this value of 4.5 T is a sign that most nanosized grains and particles are quite well aligned and therefore the submicrometer particles are strongly anisotropic. This is consistent with the texture observed from the XRD results. There may be other mechanisms causing this fieldmilling-induced anisotropy in the hard magnetic particles. For

instance, the enhanced *M*r /*M*s ratio in the field-milled samples may also originate from the improved inter-grain exchange coupling. The details need to be investigated further.

8.2.4 Conclusion

In summary, $Nd_2Fe_{14}B$ and Sm_2Co_{17} particles of submicrometer sizes were prepared by ball-milling in a magnetic field. Structural and magnetic characterization revealed that these submicrometer particles milled in a magnetic field, consisting of nanosize grains, exhibit strong magnetic anisotropy compared with the particles milled without a magnetic field. Magnetic field milling shows promise for producing nanostructured anisotropic hard magnetic particles. These nanostructured anisotropic submicrometer particles can be used for fabricating anisotropic bulk nanocomposite magnets. We have noticed that magnetic field milling was adopted to improve the energy product of bonded single-phase $Nd_2Fe_{14}B$ magnets.[217] We are currently working to extend this technique in order to produce nanocomposite anisotropic powder particles and bulk magnets.

CHAPTER 9

SUMMARY AND CONCLUSION

In this study, the fabrication and characterization of superparamagnetic and ferromagnetic nanoparticles of hard magnetic materials (FePt, $SmCo_5$, Sm_2Co_{17}, and $Nd_2Fe_{14}B$) and soft magnetic materials ($CoFe_2O_4$, $NiFe_2O_4$, and FeCo) have been reported.

FePt nanoparticles of different sizes ranging from 2 to 15 nm with narrow size distribution have been prepared in a predictable and reproducible manner via chemical solution methods. The size of these particles can be controlled in a systematic manner. FePt nanoparticle size increases with the increasing concentration of the surfactants (oleic acid and oleyl amine) used during the synthesis. This effect is attributed to the slow rate of nucleation at a high concentration of the stabilizer. The average size of nanoparticles changes also when the heating rate changes.

A facile procedure has been developed for the preparation of FePt nanorods and nanowires with uniform diameter of 3 nm and a controllable length ranging from 15 to 150 nm by the simultaneous reduction of $Pt(acac)_2$ and $Fe(CO)_5$ in the presence of 1, 2-hexadecanediol, oleyl amine and oleic acid in ether solvent. Further experiments indicated that the shape of the FePt nanocystals, including nanowires, nanorods, oval-shaped nanoparticles, spherical nanoparticles, nanocubes and nanosized mult-pods can be conveniently controlled through one-pot reactions without any solvent but with just surfactants. The molar ratio of surfactants and the sequence of the injection of the surfactants is the key to controlling the reaction kinetics and anisotropic growth of the nanocrystals. The diameter of the FePt nanorods was controlled from 3 to 5 nm by changing the molar ratio of oley amine to oleic acid. The as-synthesized FePt nanocrystals have a chemically disordered fcc structure and are superparamagnetic at room temperature. Their blocking temperature is size dependent, which increases with particle size. After the heat treatment at 700 ^{o}C the fcc structured FePt nanocrystals were transformed into $L1_0$ ordered phase with a continuous thin film morphology, and coercivity values up to 25 kOe were obtained.

The shape control techniques adopted for FePt nanocrystals in this study can be extended for the synthesis of other nanostructured materials.

Monodisperse $L1_0$ FePt nanoparticles of 3, 4, 5, 6, 7, 8, 9, and 15 nm were successfully prepared by the salt-matrix annealing technique developed in our lab, which marks the availability of the smallest ferromagnetic nanoparticles at room temperature. The processing method is simple and economic, and can be used for producing in large quantities of the ferromagnetic nanoparticles free of nonmagnetic impurities. The effect of size of the FePt nanoparticles on the phase transition, chemical ordering and magnetic properties have been systematically studied. It has been found that fcc FePt particles with a diameter of about 2 nm cannot be transformed to the ordered fct structure. Under the same annealing conditions, the degree of chemical ordering increases with particle size. The structural and magnetic analyses of 3 nm FePt particles showed that after annealing the majority of the particles had ordered $L1_0$ phase, while a small portion of the particles remained disordered. The magnetic properties of $L1_0$ FePt nanoparticles including magnetization and coercivity are strongly dependent on both particle size and chemical ordering which in turn increases with particle diameter. The 8 nm $L1_0$ nanoparticles with faceted shape give the highest coercivity up to 35 kOe. Magnetic hardening is decreased in the 15 nm fct particles possibly due to their polycrystalline feature. $L1_0$ FePt nanoparticles were coated with carbon shell during salt-matrix annealing and they showed high thermal stability even at 1100 ℃ after the complete removal of the salt matrix. Preparation of $L1_0$ phase FePt nanocrystals of different morphologies by salt-matrix annealing and discovery of a possible way to align $L1_0$ FePt nanocrystals in magnetic field to attain enhanced magnetic properties in aligned assemblies are subjects of future work.

Monodisperse $CoFe_2O_4$ nanoparticles with particle sizes from 3 nm to 20 nm were synthesized by the chemical reduction of Fe $(acac)_3$, and $Co(acac)_2$ at high temperature in solution phase and followed by seed-mediated growth method. The composition was controlled by varying the mole ratio of the precursors $Fe(acac)_3$ and $Co(acac)_2$ in the solution. Low temperature and room temperature magnetic measurements of these particles showed strong dependence of the magnetic properties on the particle size. Particle size greater than 12 nm showed ferromagnetic behavior at room temperature, whereas

particles less than 12 nm showed ferromagnetic behavior below room temperature. The blocking temperature T_B values are 30 K, 210 K and 250 K for 3, 6 and 10 nm particles respectively. A coercivity value of 21 kOe was obtained at 10 K for the 20.5 nm particles. Magnetic viscosity of $CoFe_2O_4$ is size dependent and increases with decreasing particles size.

Monodisperse $NiFe_2O_4$ nanoparticles were synthesized by the simultaneous chemical reduction of $Ni(acac)_2$ and the thermal decomposition of $Fe(CO)_5$ at high temperature in solution phase. Particles of 6, 18 and 20 nm with narrow size distribution were obtained by controlling the reaction parameters. Low temperature and room temperature hysteresis loop measurements on these particles showed no significant differences in magnetization and coercivity.

FeCo nanoparticles with controllable particle size and narrow size distribution were prepared by the reductive salt-matrix annealing of $CoFe_2O_4$ nanoparticles. The size and shape of FeCo nanoparticles can be well controlled by changing the size and shape of $CoFe_2O_4$ nanoparticles. Heat treated FeCo nanoparticles are air-stable owing to the formation of the ordered bcc structure as well as the carbon shells formed on the surface of FeCo nanoparticles during heat treatments. The saturation magnetization of the particles is dependent on particle size and increases with particle diameter.

Nanoparticles of rare-earth transition-metals including Sm_2Co_{17}, $SmCo_5$, and $Nd_2Fe_{14}B$ were successfully prepared by surfactant-assisted ball-milling technique. The surfactants play key roles in preventing cold welding of the crushed particles, leading to the formation of disperse nanoparticles. Different size particles with narrow size distribution were obtained using a size selection process by controlling the settling-down time and choosing optimal speeds and periods for the centrifugal separation process of the nanoparticles in solution. Both particle size and coercivity of Sm-Co and Nd-Fe-B nanoparticles are dependent on settling down time and decrease with increasing settling down time. Room-temperature coercivity of the as-milled Sm_2Co_{17}, $SmCo_5$ and $Nd_2Fe_{14}B$ nanoparticles of size ~ 20 nm obtained after 3 hours of settling-down time was 3.2, 2.0, and 0.5 kOe respectively. The coercivity of ~20 nm particles increased more than 50% as the measuring temperature went down to 200 K due to the enhancement of the magnetocrystalline anisotropy of the Sm-Co phase in the particles, the coercivity value of small particles of ~ 5 nm was not temperature dependent, however, indicating that the small

particles are more prone to amorphorization and oxidation, which might also have resulted in a loss of magnetocrystalline anisotropy as compared to the larger particles. XRD diffraction patterns of nanoparticles broadened with decreasing particle size. Amorphorization and strain induced by high-energy ball milling may also contribute to the broadening of the diffraction peaks. Post-annealing of ball-milled particles in the presence of surfactants did not retain properties but led to a loss of the phase of starting raw powder when annealed at high- vacuum temperature above 300 ^{o}C. The decomposition could be caused by the high oxidation affinity of rare-earth containing particles. The optimization of ball milling conditions and coating of surface of the nanoparticles may improve the oxidation resistance of nanoparticles. Surfactant-assisted ball milling technique is also a step towards defining a technique for obtaining nanostructures of composed of any metallic alloys and compounds.

$Nd_2Fe_{14}B$ and Sm_2Co_{17} particles of submicrometer were prepared by ball milling in a magnetic field. Structural and magnetic characterization revealed that the submicrometer particles milled in a magnetic field, consisting of nanosize grains, exhibit strong magnetic anisotropy compared to the particles milled without a magnetic field. Magnetic field-milling shows promise for producing nanostructured anisotropic hard magnetic Sm-Co and Nd-Fe-B based particles. These nanostructured anisotropic submicrometer particles can be used for fabricating anisotropic bulk nanocomposite magnets. Extending this technique to produce nanocomposite anisotropic powder particles and bulk magnets will be an interesting subject for future work.

The fabrication techniques presented in this study for the preparation of magnetic nanoparticles with controllable size and shape may also be extended to the preparation of nanoparticles and nanostructures composed of other materials. The magnetic nanoparticles studied in this work which exhibit a variety of unique magnetic phenomena may serve as promising building blocks for the fabrication of ultra- high-density magnetic recording media, exchange-coupled nanocomposite permanent magnets and various other nanodevices. These superparamagnetic and ferromagnetic nanoparticles can also be used for a wide variety of biomedical applications, including in MRI as contrast agents, for targeted drug delivery, for destroying of cancer cells via hyperthermia treatment, for cell separation and as biosensors.

APPENDIX A

UNITS FOR MAGNETIC PROPERTIES

Table A.1 Units of magnetic properties[45]

Quantity	Symbol	Gaussian & cgs emu [a]	Conversion factor, C [b]	SI & rationalized mks [c]
Magnetic flux density, magnetic induction	B	gauss (G) [d]	10^{-4}	tesla (T), Wb/m^2
Magnetic flux	Φ	maxwell (Mx), $G \cdot cm^2$	10^{-8}	weber (Wb), volt second (V·s)
Magnetic potential difference, magnetomotive force	U, F	gilbert (Gb)	$10/4\pi$	ampere (A)
Magnetic field strength, magnetizing force	H	oersted (Oe),[e] Gb/cm	$10^3/4\pi$	A/m [f]
(Volume) magnetization [g]	M	emu/cm^3 [h]	10^3	A/m
(Volume) magnetization	$4\pi M$	G	$10^3/4\pi$	A/m
Magnetic polarization, intensity of magnetization	J, I	emu/cm^3	$4\pi \times 10^{-4}$	T, Wb/m^2 [i]
(Mass) magnetization	σ, M	emu/g	1 $4\pi \times 10^{-7}$	$A \cdot m^2/kg$ Wb·m/kg
Magnetic moment	m	emu, erg/G	10^{-3}	$A \cdot m^2$, joule per tesla (J/T)
Magnetic dipole moment	j	emu, erg/G	$4\pi \times 10^{-10}$	Wb·m [i]
(Volume) susceptibility	χ, κ	dimensionless, emu/cm^3	4π $(4\pi)^2 \times 10^{-7}$	dimensionless henry per meter (H/m), Wb/(A·m)
(Mass) susceptibility	χ_ρ, κ_ρ	cm^3/g, emu/g	$4\pi \times 10^{-3}$ $(4\pi)^2 \times 10^{-10}$	m^3/kg $H \cdot m^2/kg$
(Molar) susceptibility	χ_{mol}, κ_{mol}	cm^3/mol, emu/mol	$4\pi \times 10^{-6}$ $(4\pi)^2 \times 10^{-13}$	m^3/mol $H \cdot m^2/mol$
Permeability	μ	dimensionless	$4\pi \times 10^{-7}$	H/m, Wb/(A·m)
Relative permeability [j]	μ_r	not defined		dimensionless
(Volume) energy density, energy product [k]	W	erg/cm^3	10^{-1}	J/m^3
Demagnetization factor	D, N	dimensionless	$1/4\pi$	dimensionless

a. Gaussian units and cgs emu are the same for magnetic properties. The defining relation is $B = H + 4\pi M$.
b. Multiply a number in Gaussian units by C to convert it to SI (e.g., $1\ G \times 10^{-4}\ T/G = 10^{-4}\ T$).
c. SI (*Système International d'Unités*) has been adopted by the National Bureau of Standards. Where two conversion factors are given, the upper one is recognized under, or consistent with, SI and is based on the definition $B = \mu_0(H + M)$, where $\mu_0 = 4\pi \times 10^{-7}$ H/m. The lower one is not recognized under SI and is based on the definition $B = \mu_0 H + J$, where the symbol I is often used in place of J.
d. 1 gauss $= 10^5$ gamma (γ).
e. Both oersted and gauss are expressed as $cm^{-1/2} \cdot g^{1/2} \cdot s^{-1}$ in terms of base units.
f. A/m was often expressed as "ampere-turn per meter" when used for magnetic field strength.
g. Magnetic moment per unit volume.
h. The designation "emu" is not a unit.
i. Recognized under SI, even though based on the definition $B = \mu_0 H + J$. See footnote *c*.
j. $\mu_r = \mu/\mu_0 = 1 + \chi$, all in SI. μ_r is equal to Gaussian μ.
k. $B \cdot H$ and $\mu_0 M \cdot H$ have SI units J/m^3; $M \cdot H$ and $B \cdot H/4\pi$ have Gaussian units erg/cm^3.

R. B. Goldfarb and F. R. Fickett, U.S. Department of Commerce, National Bureau of Standards, Boulder, Colorado 80303, March 1985
NBS Special Publication 696 For sale by the Superintendent of Documents, U.S. Government Printing Office, Washington, DC 20402

APPENDIX B

CRYSTRAL STRUCTURE OF FERRITE

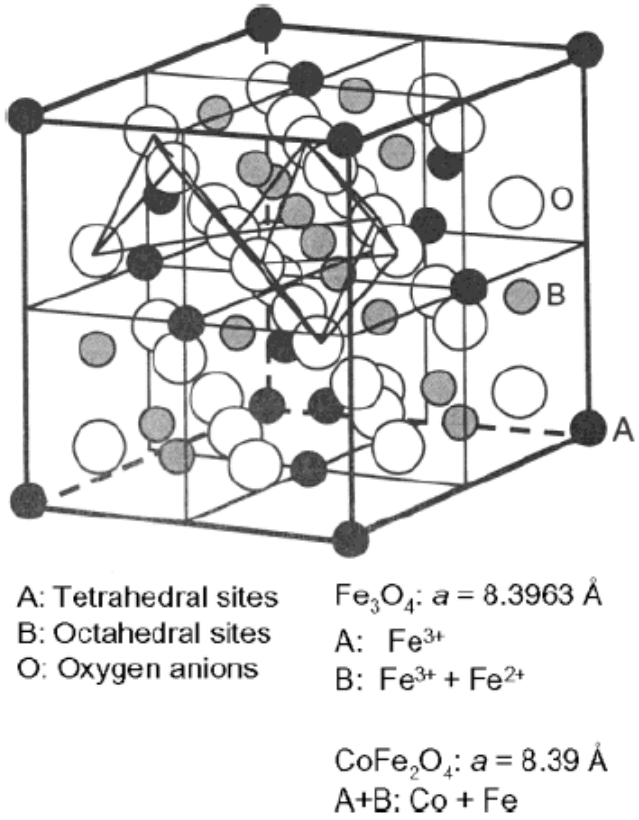

Figure B.1 Schematic model of the Spinel unite cell structure.[155]

The Spinel structure has two cation sites: the tetrahedrally coordinated A sites and the octahedrally coordinated B sites. For Fe_3O_4, the A and B positions are occupied by $Fe^{3+}$and Fe^{2+} cations, respectively. For $CoFe_2O_4$, the A and B positions are equally occupied by Co and Fe cations. Fe_3O_4 and $CoFe_2O_4$ have almost the same lattice parameters: a = 8.3963 Å for Fe_3O_4, a = 8.39 Å for $CoFe_2O_4$. The mass densities for Fe_3O_4 and $CoFe_2O_4$ are almost identical.

APPENDIX C

PHASE DIAGRAM OF FePt

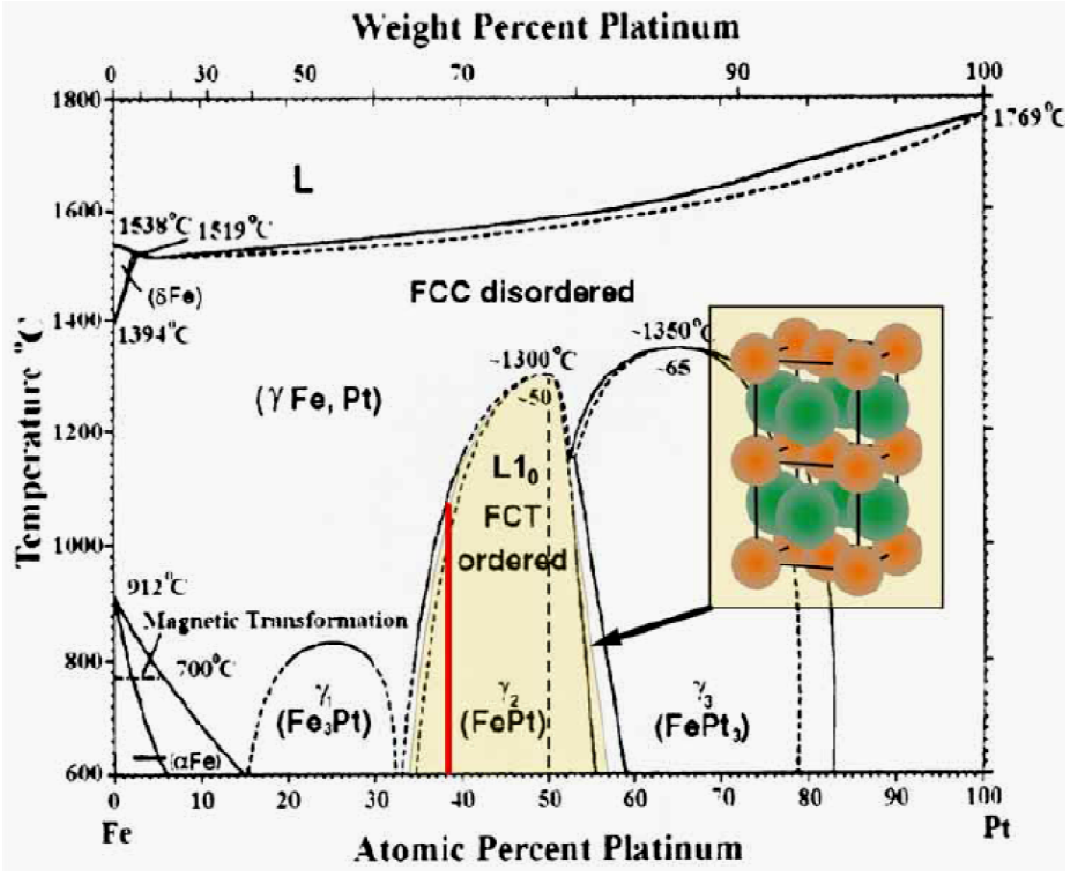

Figure C.1 FePt phase diagram and schematic representation of structure transformation between fcc and fct FePt. Orange circles represent Fe atoms and green circles represent Pt atoms in unit cells.[218]

APPENDIX D

PHASE DIAGRAM AND CRYSTAL STRUCTURE OF $SmCo_5$

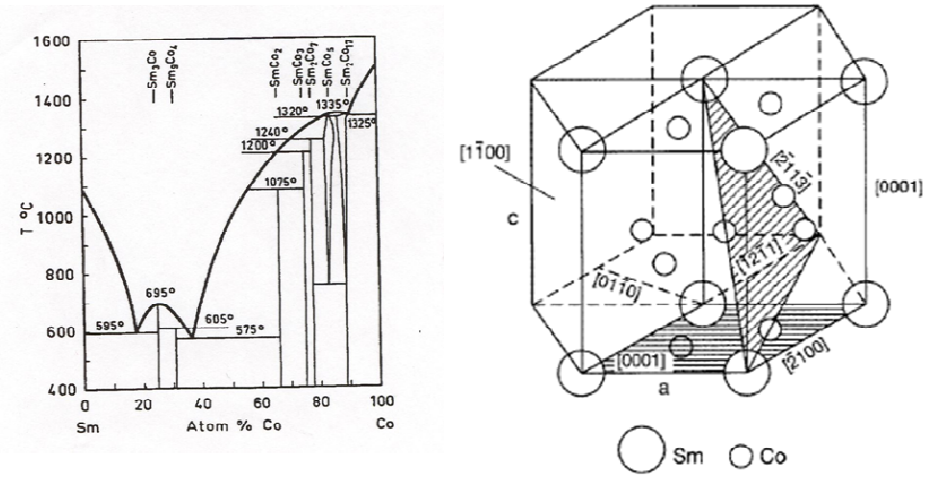

Figure D.1 Phase diagram of SmCo and crystal structure of $SmCo_5$.[219]

APPENDIX E

PHASE DIAGRAM AND CRYSTAL STRUCTURE OF $Nd_2Fe_{14}B$

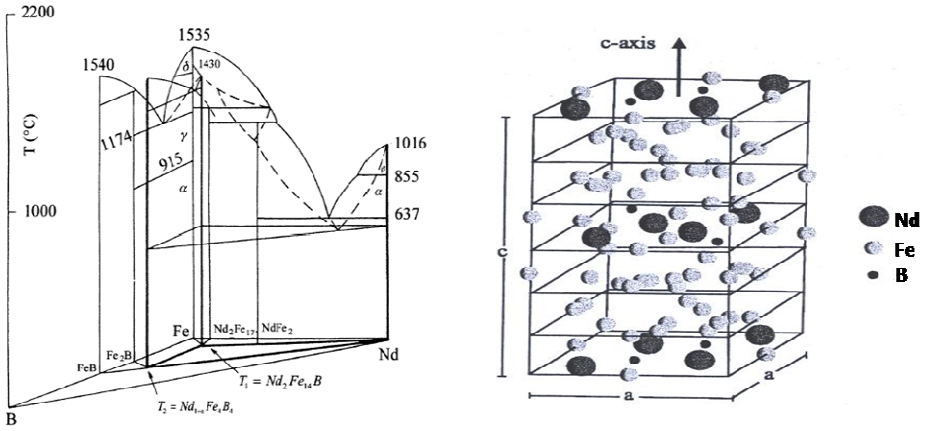

Figure E.1 Phase diagram of Nd-Fe-B and crystal structure of $Nd_2Fe_{14}B$.[219]

APPENDIX F

PROPERTIES OF HARD MAGNETIC MATERIALS

Table F.1 Properties of hard magnetic materials[25]

- anisotropy field: $H_K = 2K_u/M_S$;
- domain wall width: $\delta_W = \pi (A/K_u)^{1/2}$
- domain wall energy: $\gamma_W \cong 4 (A \cdot K_u)^{1/2}$
- single particle domain size: $D_C = 1.4 \gamma_W / M_S^2$
- exchange coupling constant $A=10^{-6}$ erg/cm
- minimal stable grain size: $D_p = (60 k_B T/K_u)^{1/3}$ (τ=10 years)

alloy system	material	K_u (10^7erg/cm^3)	M_S (emu/cm^3)	H_K (kOe)	T_C(K)	δ_W (Å)	γ (erg/cm^3)	D_C (μm)	D_p (nm)
	CoPtCr	0.20	298	13.7	--	222	5.7	.89	10.4
Co-alloys	Co	0.45	1400	6.4	1404	148	8.5	.06	8.0
	Co_3Pt	2.0	1100	36	--	70	18	.21	4.8
	FePd	1.8	1100	33	760	75	17	.20	5.0
$L1_0$	FePt	6.6-10	1140	116	750	39	32	.34	3.3-2.8
phases	CoPt	4.9	800	123	840	45	28	.61	3.6
	MnAl	1.7	560	69	650	77	16	.71	5.1
rare-earth	$Fe_{14}Nd_2B$	4.6	1270	73	585	46	27	.23	3.7
transition metals	$SmCo_5$	11-20	910	240-400	1000	22-30	42-57	.71-.96	2.7-2.2

APPENDIX G

RESEARCH ACCOMPLISHMENTS

Awards

- Awarded "Scharff Award Scholarship" on March 22, 2005 by University of Texas at Arlington, Department of Physics for research achievements.

News Published for Research Involved

- Magnets warm up to get stronger, published in *nanotechweb.org* ,August 29, 2007
- Just Add Salt titled news articles published in Physics Web in August 4, 2005.

  Link to the articles: *http://physicsweb.org/articles/news/9/8/3/1*
- For nanoparticles, just add salt titled news articles published in Nanotechweb.org

  Link to the articles: http://www.nanotechweb.org/articles/news/4/8/6/1
- Physicists Discover Table Salt is Solution to Creating the Smallest Magnets titled news articles published in UTA Today in August 15, 2005.

List of Publications

1. Narayan Poudyal, Girija S Chaubey, Vikas Nandwana, Chuan-bing Rong, Kazuaki Yano and J Ping Liu, Synthesis of FePt nanorods and nanowires by a facile method, Nanotechnology 19 (2008) 355601
2. Narayan Poudyal, Baki Altuncevahir, Vamsi Chakka, Kanghua Chen, Truman D Black, J. P. Liu, Yong Ding, and Zhong Lin Wang, Field-ball milling induced anisotropy in mangetic particles, J. Phys. D: Appl. Phys. 37 (2004) L45-L48.
3. Narayan Poudyal, Girija S. Chaubey, Chuan-bing Rong, and J. Ping Liu, Shape Control of FePt Nanocrystals, J. Applied Physics,(2008) (submitted).
4. M.Yue, Y.Wang, N. Poudyal, C. Rong and *J. Liu,* Preparation, structural and magnetic properties of Nd-Fe-Bbased nano-particles. J. Applied Physics (2008) (in press).
5. C. Westman, S. Jang, C. Kim, S. He, G. Harmon, N. Miller, B. Graves, N. Poudyal, R. Sabirianov, H. Zeng, M. DeMarco, and J. P. Liu, " Surface induced suppression of magnetization in nanoparticles", J. Phys. D: Appl. Phys. 41 (2008) 225003

6. X. Hu, L. Xie , N. Poudyal , and .J.Ping Liu and *J. Yuan*, Observation of L10-like chemical ordered decahedral FePt nanoparticles by Cs-corrected HRTEM. J. Applied Physics,(2008) (in press).
7. Kazuaki Yano, Vikas Nandwana, Narayan Poudyal, Chuan-bing Rong and J. Ping Liu, Rapid thermal annealing of FePt nanoparticles, J. Applied Physics, 104 (2008), 013918.
8. Chuan-Bing Rong, Narayan Poudyal, Girija S. Chaubey, Vikas Nandwana, Yuzi Liu, Y. Q. Wu, M. J. Kramer, M. E. Kozlov, R. H. Baughman, and J. Ping Liu, High thermal stability of carbon-coated $L1_0$- FePt nanoparticles prepared by salt-matrix annealing, J. Appl. Phys. 103, 07E131 (2008)
9. Girija S. Chaubey, Vikas Nandwana, Narayan Poudyal, Chuan-bing Rong, and J. Ping Liu, Synthesis and Characterization of Bimagnetic Bricklike Nanoparticles, Chem. Mater., 20 (2), 475–478, 2008
10. Chuan-bing Rong, Narayan Poudyal, Girija S Chaubey, and Vikas Nandwana, R. Skomski, Y. Q. Wu and M. J. Kramer, J. Ping Liu, Structural phase transition and ferromagnetism in monodisperse 3 nm FePt particles, J. Applied Physics, 102 (2007), 043913
11. Chuan-Bing Rong, Vikas Nandwana, Narayan Poudyal, and J. Ping Liu, Mikhail E. Kozlov and Ray H. Baughman, Yong Ding and Zhong Lin Wang, Bulk FePt-based nanocomposite magnets with enhanced exchange coupling , J. Applied Physics, 101 (2007), 023908.
12. Girija S. Chaubey, Carlos Barcena, Narayan Poudyal, Chuanbing Rong, Jinming Gao, Shouheng Sun, and J. Ping. Liu, Synthesis and Stabilization of FeCo Nanoparticles, J. Am. Chem. Soc., 129 (2007), 7214-7215.
13. Shishou Kang,Shifan Shi, Zhiyong Jia, G. B. Thompson, David E. Nikles, J. W. Harrell, Daren Li, Narayan Poudyal, Vikas Nandwana, and J. P. Liu Microstructures and magnetic alignment of L10 FePt nanoparticles, J. Applied Physics, 101 (2007), 09J113.
14. Chuan-bing Rong, Vikas Nandwana, Narayan Poudyal, J.P. Liu, Tetsuji Saito, Yaqiao Wu, and Matthew J. Kramer , Bulk FePt/Fe3Pt nanocomposite magnets prepared by spark plasma sintering, J. Applied Physics, 101 (2007), 101 (2007), 09K515.

15. Vikas Nandwana, Kevin E. Elkins, Narayan Poudyal, Girija S. Chaubey, Kazuaki Yano, and J. P. Liu,Size and Shape Control of Monodisperse FePt nanoparticles,J. Phys. Chem. C, 111(2007), 4185-4189.
16. Chuan-bing Rong, Vikas Nandwana, Narayan Poudyal, Yang Li, J Ping Liu, Yong Ding and Zhong Lin Wang Formation of Fe3Pt phase in FePt-based nanocomposite magnets, J. Phys. D: Appl. Phys. 40 (2007), 712–716.
17. Chuanbing Rong, Daren Li, Vikas Nandwana, Narayan Poudyal, Yong Ding, Zhonglin Wang, Hao Zeng and J.Ping Liu, Size-dependent chemical and magnetic ordering in L10 FePt nanoparticles, Advanced Materials (2006), 18, 2984–2988.
18. B. A. Jones, J. D. Dutson1, K. O'Grady, B. J. Hickey, Daren Li, Narayan Poudyal, and J. Ping Liu, Magnetic Properties of FePt Nanoparticles Annealed With NaCl, IEEE Trans on Magn., 42 (2006), 3066-3068.
19. J. P. Liu, K. Elkins, D. Li, V. Nandwana, N. Poudyal, Phase Transformation of FePt Nanoparticles, IEEE Trans on Magn., 42 (2006), 3036-3041
20. Daren Li, Narayan Poudyal, Vikas Nandwana, Zhiqiang Jin, Kevin Elkins, J. Ping Liu, Hard Magnetic FePt Nanoparticles by Salt-Matrix Annealing, J. Applied Physics, 99 (2006), 08E911.
21. Kevin Elkins, Daren Li, Narayan Poudyal, Vikas Nandwana, Zhiqiang Jin, Kanghua Chen and J Ping Liu, Monodisperse face-centred tetragonal FePt nanoparticles with giant coercivity, J. of Applied Physics 38 (2005), 2306–2309.
22. Rashed A. Islam , Vishwas Bedekar, Narayan Poudyal, J. Ping Liu, and Shashank Priya Magnetoelectric properties of core-shell particulate nanocomposites (submitted to APL)
23. Vishwas Bedekar, Narayan Poudyal, Chuan-bing Rong and J. Ping Liu Choong-un Kim, Shashank Priya, Magnetoelectric Properties of Piezoelectric – Magnetostrictive Nanocomposites Synthesized Using High Pressure Compaction Technique (to be submitted to APL)
24. Narayan Poudyal, Girija S. Chaubey, Chuan-bing Rong and J. Ping Liu, Synthesis of Monodisperse FeCo Nanoparticles by Reductive Salt-matrix Annealing, Applied Physics Litter (2008) (to be submitted to APL).

25. Paul Trevenot, Aswhin Nair, Narayan Poudyal, J. Ping Liu, and Liping Tang, Magnetic Nanoparticles to Enhance Cell Seeding and Distribution in Tissue Engineering Scaffolds. Nanotechnolog,IEEE Nano Conference, August 19 - 21, 2008.

Conference Presentations

1. Narayan Poudyal, Girija S. Chaubey, Chuan-bing Rong, and J. Ping Liu, Shape Control of FePt Nanocrystals, 53rd MMM Conference, November 10-14, 2008, Austin, Texas, USA.
2. Narayan Poudyal, Girija S. Chaubey, Chuan-bing Rong and J. Ping Liu, Synthesis of Monodisperse FeCo Nanoparticles by Reductive Salt-matrix Annealing, 53rd MMM Conference, November 10-14 , 2008, Austin, Texas, USA.
3. Girija S. Chaubey, Narayan Poudyal, Yuzi Liu, Chaunbing Rong, and J. Ping Liu, Large-scale Synthesis of Hard Magnetic Nanocomposite Particles by a Facile Method 53rd MMM Conference, November 10-14 , 2008, Austin, Texas, USA.
4. M.Yue, Y.Wang, N. Poudyal, C. Rong and *J. Liu,* Preparation, structural and magnetic properties of Nd-Fe-Bbased nano-particles. 53rd MMM Conference, November 10-14 , 2008, Austin, Texas, USA.
5. X. Hu, L. Xie , N. Poudyal , and .J.Ping Liu and *J. Yuan*, Observation of L10-like chemical ordered decahedral FePt nanoparticles by Cs-corrected HRTEM. 53rd MMM Conference, November 10-14, 2008, Austin, Texas, USA.
6. Chuanbing Rong, Vikas Nandwana, Narayan Poudyal,; Girija S Chaubey, Magnetic hardening in isolated FePt nanoparticles, The 8th International Conference on Nanotechnology,IEEE Nano Conference, August 19 - 21, 2008 Arlington, Texas USA.
7. Paul Trevenot, Aswhin Nair, Narayan Poudyal, J. Ping Liu, and Liping Tang, Magnetic Nanoparticles to Enhance Cell Seeding and Distribution in Tissue Engineering Scaffolds. The 8th International Conference on Nanotechnology, IEEE Nano Conference, August 19 - 21, 2008 Arlington, Texas USA.

8. Narayan Poudyal, Girija.S. Chaubey, Vikas Nandwana and J.Ping Liu, Synthesis and Characterization of FePt Nanorods and Nanowires, 52nd MMM Conference, November 5-9 , 2007, Tampa, Florida, USA.
9. C. Rong, N. Poudyal, G. Chaubey, V. Nandwana, Y. Liu, Y.Wu, M. Kramer, M. Kozlov, R. Baughman and J.P. Liu, High thermal stability of carbon-coated L10-FePt nanoparticles prepared by salt-matrix annealing, 52nd MMM Conference, November 5-9, 2007,Tampa, Florida, USA.
10. K. Yano, V. Nandwana, N. Poudyal, G. S. Chaubey and J.P. Liu, Chemical synthesis of FePt@Au core/shell nanoparticles, 52nd MMM Conference, November 5-9, 2007,Tampa, Florida, USA.
11. Girija Shankar Chaubey, Yiping Wang, Chaung-bin Rong, Narayan Poudyal, Vikas Nandwana, Kevin E. Elkin and J. Ping Liu, Silica Encapsulation and Magnetic Properties of Hard Magnetic Sm_2Co_{17} Nanoparticles Obtained by Mechanical Ball-milling Process , MRS Fall 2007 , (SESSION I10: Poster Session) November 28, 2007 8:00 PM , Boston, USA.
12. Kazuaki Yano, Vikas Nandwana, Narayan Poudyal, Chuan-bing Rong and J. Ping Liu, Rapid Thermal Annealing of Monodisperse FePt Nanoparticles ,MRS Fall 2007 , (SESSION I6) 8:45 AM - 11:45AM, November 25 - 30, Boston ,USA.
13. Narayan Poudyal , Girija S. Chaubey , Chuan-bing Rong , J. Ping Liu, FeCo Nanoparticles by Salt-Matrix Annealing, 2007 Amecial Physical Society March Meeting, March 5-9, Denver, Colorado, USA.
14. Chuanbing Rong, Vikas Nandwana, Naranyan Poudyal, Yang Li, J.Ping Liu, Mikhail E Kozlov, Anvar Zakhidov and Ray Baughman, Inter-particle Magnetic Interactions in Nanoparticle Compacts, MRS Fall 2006 , (session P4) 4.45 PM - 5;00PM, Boston, USA.
15. G.S. Chaubey, N. Poudyal, C. Rong and J.P. Liu, Novel synthesis of air-stable FeCo nanoparticles, The 233rd American Chemical Society National meeting March 26, 2007 Chicago, IL, USA.
16. Chuan-bing Rong, V. Nandwana, N. Poudyal, J. Ping Liu, Bulk FePt/Fe3Pt nanocomposite magnets prepared by spark plasma sintering, 10th joint MMM/InterMag Conference, Jan 7-11, 2007, Baltimore, Maryland, USA.

17. D. Li, N. Poudyal, V. Nandwana, Z. Jin, K. E. Elkins and J. P. Liu, Hard Magnetic FePt Nanoparticles by salt matrix annealing, 50th Conference on Magnetism and Magnetic Materials, San Jose, California, October 30-November 3, 2006, Baltimore, Maryland, USA.
18. D. Li, N. Poudyal, V. Nandwana, J.P. Liu, Size effect on chemical ordering in face-centered tetragonal FePt nanoparticles, APS March Meeting 2006, March 17, Baltimore, Maryland, USA.
19. Narayan Poudyal, Girija S. Chaubey, Chaubing Rong, J. Ping Liu, Novel Approaches for the Synthesis of FeCo Nanoparticles, 2006 Texas Section of the American Physical Scociety joint fall meeting,Thursday–Saturday, October 5–7, 2006; Arlington, Texas, USA.
20. Narayan Poudyal, Tejaswi Vedantam, Baki Altuncevahir, J. Ping Liu, Tailoring Magnetic Properties of Co-ferrite Nanoparticles, American Physical Society (APS) March Meeting 2005, Los Angles, California, USA.
21. Narayan Poudyal, Baki Altuncevahir, Truman D. Black, and J. Ping Liu, Effect of Ball Milling on Magnetic Hysteresis of SmCo Particles, International Conference on Photonic, Excitonic, Spintronic Processes In Nanostructures, University of Texas at Dallas, USA, Jan 2004.
22. Narayan Poudyal, Tejaswi Vedantam, Baki Altuncevahir, Vamsi Chakka, J. Ping Liu, Tailoring the Magnetic Properties of $Co_xFe_{3-x}O_4$ Nanoparticles, Poster presentation at the DARPA MetaMaterials PI Review, Washington DC, August 2004.
23. Narayan Poudyal, Tejaswi Vedantam, Baki Altuncevahir, Vamsi Chakka, J. Ping Liu, Tailoring Magnetic Properties of Co-ferrite Nanoparticles, Poster presentation at the SPRING 04 Conference on research in nanotechnology,University of Texas at Dallas, USA in Nov 2004.
24. Narayan Poudyal, Baki Altuncevahir, Vamsi Chakka1, Kanghua Chen, Truman D Black1, J.P. Liu, Yong Ding and Zhong Lin Wang, Field-induced magnetic anisotropy in ball-milled powder particles, MRS Fall Meeting 2004, p145, Boston, USA.

REFERENCES

1. Soshin Chikasumi, “Physics of Magnetism” John Wiley and Sons, (1964).
2. B. D. Cullity, “Introduction to Magnetic Materials”, Addison-Wesley Publishing, (1972).
3. Nicola A. Spaldn, “Magnetic Materials: Fundamentals and Device Applications”, Cambridge University Press, (2003).
4. William D. Callister, Jr., “Material Science and Engineering: An Introduction”, John Wiley & Sons, (2000).
5. Robert C. O’ Handley, “Modern Magnetic Materials: Principles and Applications”, Wiley & Sons, (2000).
6. J.C. Anderson, “Magnetism and Magnetic Materials”, Chapman and Hall Ltd. (1968).
7. J. M. D. Coey, “Magnetic Materials”, Journal of Alloys and Compounds, 326, 2 (2000).
8. Narayan Poudyal, Synthesis and Characterization of Magnetic Nanoparticles, M.S. Thesis, The University of Texas at Arlington, AAT 1430791 (2005).
9. J. M. D. Coey, “Permanent Magnetism”, Solid State Communications, 102, 101 (1997).
10. E. F. Kneller, and R. Hawing “The exchange-spring magnet: new material for permagnet magnets”, IEEE Transactions on Magnetics, 27, 3588 (1991).
11. R. Skomski, J.M.D. Coey, “Giant energy product in nanostructured two-phase magnets”. Physical. Review B, 48, 15812(1993).
12. Hao Zeng, Jing Li, J.P. Liu, Zhoung L. Wang, and Shouheng Sun, “Exchange-coupled nanocomposite magnets by nanoparticles self-assembly” Nature, 420,395 (2002).
13. J. P. Liu, “Novel approaches to the synthesis and processing of nanocomposite magnets”, 18th International workshop on high performance magnets and their applications, Annecy (France) (2004).

14. R. Coehoorn, D. B. de Mooij and C. de Waard “Meltspun permanent magnet materials containing Fe_3B as the main phase”, Journal of Magnetism and Magnetic Material, Volume 80, 10 (1989).
15. J. Sort, S. Surmach, J. S. Munoz, and M. D. Baro, “Improving the energy product of hard magnetic materials”, Physical Review B, 65, 174420 (2002).
16. D.C. Jiles, “Recent advances and future directions in magnetic materials”, Acta Meterialia, 15, 5907 (2003).
17. Eric E. Fullerton, J. S. Jiang, S. D. Bader, “Hard/Soft magnetic heterostructures: model exchange-spring magnets”, Journal of Magnetism and Magnetic Materials, 200, 392 (1999).
18. R. Skomski and J.M.D Coey, “Exchange Coupling and Energy Product in Random Two phase Aligned Magnets”, IEEE Transactions on Magnetics, 30, 607(1994).
19. J. P. Liu, “Nanosturctured Soft and Hard Magnetic Materials”, Chapter-6 of Handbook of nanophase and nanostructured materials, ed. by Z.L. Wang, Y. Liu and Z. Zhang, Kluwer Academic/Plenum Publishers and Tsinghua University Presss, 3, 244-268 (2003).
20. http://www.azom.com/details.asp?ArticleID=637
21. http://www.magnets.bham.ac.uk/magnetic_materials/
22. H. N. Bertram, H. Zhou, and R. Gustafson, “Signal to noise ratio scaling and density limit estimates in longitudinal magnetic recording”, IEEE Transactions on Magnetics, 34, 1845 (1998).
23. S. H. Charap, P. L. Lu, and Y. He, “Thermal stability of recorded information at high densities”, IEEE Transactions on Magnetics, 33, 978 (1997).
24. D. Weller and A. Moser, “Thermal effect limits in ultrahigh density magnetic recording”, IEEE Transactions on Magnetics, 35, 4423 (1999).
25. D. Weller, A. Moser, L. Folks, M. E. Best, W. Lee, M. F. Toney, M. Schwckert, J. U. Thiele and M. F. Doerner, “High K_μ Materials Approach to 100 Gbits/in^2”, IEEE Transactions on Magnetics, 36, 10 (2000).

26. M. Watanabe, T. Nakayama, K. Watanabe, T. Hirayama, and A. Tonomura, “Microstructure and Magnetic Properties of High-Coercive Fe-Pt Alloy Thin Films”, Materials Transactions, JIM, 37, 489 (1996).
27. Y. H. Wang, Y. Zhang, G. C. Hadjipanayis and D. Weller, “Fabrication and Characterization of Ordered FePt Nanoparticles”, Journal of Applied Physics, 93, 7172 (2003).
28. Y. K. Takahashi, T. Koyama, M. Ohnuma, T. Ohkubo and K. Hono, “Size Dependence of Ordering in FePt Nanoparticles”, Journal of Applied Physics, 95, 2690 (2004).
29. Y. K. Takahashi, T. Ohkubo, M. Ohnuma and K. Hono, “Size Effect on the Ordering of FePt Granular Films”, Journal Applied Physics, 93, 7166 (2003).
30. T. Miyazaki, O. Kitakami, S. Okamoto, Y. Shimada, Z. Akase, Y. Murakami, D. Shindo, Y. K. Takahashi and K. Hono, “Size Effect on the Ordering of L10 FePt Nanoparticles”, Physical Review Letters B, 72, 144419 (2005).
31. R. V. Chepulskii and W. H. Butler, “Temperature and Particle-Size Dependence of the Equilibrium Order Parameter of FePt Alloys”, Physical Review Letters B, 72, 134205 (2005).
32. Young-Wook Jun, Jung-Wook Seo, And Jinwoo Cheon, “Nanoscaling Laws of Magnetic Nanoparticles and Their Applicabilities in Biomedical Sciences”, Account, 41,179 (2008).
33. Jales, D. Introduction to Magnetism and Magnetic Materials; CRC Press, Boca Raton, FL, (1998).
34. Morales, M. P.; Veintemillas-Verdaguer, S.; Montero, M. I.; Serna, C. J. Surface and internal spin canting in γ-Fe2O3 nanoparticles. Chem. Mater. 11, 3058–3064 (1999).
35. Morales, M. P.; Serna, C. J.; Bødker, F.; Mørup, S. Spin canting due to structural disorder in maghemite. J. Phys.: Condens. Matter 9, 5461–5467(1997).
36. J. H. Gao, D.L. Sun, Q.F. Zhan, W. He, and Z.H. Cheng, Phys. Rev. B, 75, 064421 (2007).
37. R. Street and J.C. Woolley, Proc. Phys. Soc., London, Sect. A 62, 562 (1949).
38. M. A. Willard, L.K. Kulrihara, E.E. Carpenter, S. Calvin and V.G. Harris, “Chemically prepared magnetic nanoparticles”, International Material Reviews, 49, 3 (2004).

39. Taeghwan Hyeon, “Chemical synthesis of magnetic nanoparticles”, Chemical communication, 927 (2003).

40. Catherine C. Berry and Adam S. G. Curtis, “Fictionalization of magnetic nanoparticles for application in biomedicine”, Journal of Physics. D: Applied Physics, 36, R198 (2003).

41. Adam Curtis, “Biomedical aspects of magnetic nanoparticles”, Euro physics News, 34, 6 (2003).

42. M. Chastellain, A. Petri, M. Hofmann and H. Hofmann, “Synthesis and patterning of magnetic nanostructures”, European Cells and Materials, 3, 1, 11 (2002).

43. D. K. Kim W. Voit, W. Zapka, B. Bjelke, M. Muhammed, and K. V. Rao, “Material Research Society Symp. Proc.” 676, (2001).

44. L. Fu, V.P. Dravid, K. Klug, X. Liu and C.A. Mirkin, “ Synthesis and patterning of magnetic nanostructures”, European Cell and Materials, 3 Suppl. 2, 156 (2002).

45. R. B. Goldfarb and F. R., U. S. Department of Commerce, National Bureau of Standards, Boulder, Colorado 80303,. NBS Special Publication 696. For sale by the Superintendent of Documents, U.S. Government Printing Office, Washington, DC 200402, March (1985).

46. C.A. Ross, “Patterned Magnetic Recording Media”, Annual Review of Material Research, 31, 203(2001).

47. S. Okamoto, O. Kitkami, N. Kickuchi, T. Miyazaki, and Y. Shimada, “Size dependences of magnetic properties and switching behavior in FePt $L1_0$ nanoparticles”, Physical Review B, 67, 094422 (2003).

48. D. Weller, M. F. Doerner, “Extremely high-density longitudinal magnetic recording media” Annual review of materials science, 30, 611 (2000).

49. Y. Shi, J. Ding and H. Yin, “$CoFe_2O_4$ nanoparticles by the mechanochemical method”, Journal of Alloys and Compounds, 303, 290 (2002).

50. Yeong II Kim, Don Kim, and Choong Sub Lee, “Synthesis and characterization of $CoFe_2O_4$ magnetic nanoparticles prepared by temperature-controlled co-precipitation method”, Physica B, 337, 42 (2003).

51. C.N. Chinnasamy, M. Senoue, B. Jeyadevan, Oscar Perales-Perez, K. Shinoda, and K. Tohji, " Synthesis of size-controlled cobalt ferrite particles with high coercivity and squareness ratio", Journal of colloid and interface science , 263, 80 (2003).

52. Q. A. Pankhurst, J. Connolly J, S. K. Jones and J. Dobson J, "Applications of magnetic nanoparticles in biomedicine", Journal of Physics D: Applied Physics, 36, R167 (2003).

53. S. Sun, Eric E. Fullerton, D. Weller and C. B. Murray, "Compositionally controlled FePt nanoparticle Materials", IEEE Transactions on magnetics, 37,1239 (2001).

54. Kevin Elkins, Daren Li, Narayan Poudyal, Vikas Nandwana, Zhiqiang Jin, Kanghua Chen and J.Ping Liu, " Monodisperse face-centered tetragonal FePt nanoparticles with giant coercivity", Journal of Physics D: Applied Physics, 38, 2306 (2005).

55. Hao Zeng, Shouheng Sun, J. Li and Z. L. Wang, and J. P. Liu, "Tailoring magnetic properties of core/shell nanoparticles", Applied Physics Letters, 85, 792 (2004).

56. http://www.carolina.com/physics/aboutferro.asp

57. http://www.zarm.uni-bremen.de/2forschung/ferro/basic_info/applic/index.htm

58. Shouheng Sun, Hao Zeng, David B. Robinson, Simone Raoux, Philip M. Rice, Shan X. Wang, and Guanxiong Li, "Monodisperse MFe_2O_4 (M = Fe, Co, Mn) Nanoparticles", J. Am. Chem. Soc, 126, 273 (2004).

59. Shouheng Sun, and Hao Zeng, "Size-Controlled Synthesis of Magnetite Nanoparticles", J. Am. Chem. Soc., 124, 8204 (2002).

60. Christy R, Vestal and Z. John Zhang, "Magnetic spinel ferrite nanoparticles from microemulsions" International Journal of Nanotechnology", 1 ½ (2004).

61. M. Rajendran, R. C. Pullar, A. K. Bhattacharya, D. Das, S. N. Chintalapudi and C. K. Majumdar, "Magnetic properties of nanocrystalline $CoFe_2O_4$ powders prepared at room temperature: variation with crystallite size", Journal of Magnetism and Magnetic Materials, 232,71 (2001).

62. P.C. Morais, V.K. Garg, A.C. Oliveira, L.P. Silva, R.B. Azevedo, A.M.L. Silva, E.C.D. Lima, " Synthesis and characterization of size-controlled cobalt-ferrite-based ionic ferrofluids", Journal of Magnetism and Magnetic Materials, 225 , 37 (2001).

63. T. Pannaparayil and S.Komarneni, “Synthesis and characterization of ultra fine cobalt ferrites”, IEEE Transactions on magnetics, 25, 5 (1989).

64. N. Moumen, P. Veillet M. P. Pileni, “Controlled preparation of nanosize cobalt ferrite magnetic particles”, Journal of Magnetism and Magnetic Materials, 149, 67(1995).

65. Yangkyu Ahn , Eun Jung Choi , Sehun Kim , Hang Nam Ok , “Magnetization and Mössbauer study of cobalt ferrite particles from nanophase cobalt iron carbonate”, Materials Letters, 50 , 47 (2001).

66. V. Pillai, and D.O. Shah, “ Synthesis of high-coercivity cobalt ferrite particles using water-in-oil microemulsions”, Journal of Magnetism and Magnetic Materials, 163, 243 (1996).

67. Chao Liu, Bingsuo Zou, Adam J. Rondinone, and Z. John Zhang “Chemical Control of Superparamagnetic Properties of Magnesium and Cobalt Spinel Ferrite Nanoparticles through Atomic Level Magnetic Couplings”, Journal of American Chemical Society, 122, 6263 (2000).

68. R. Vijayakumar, Yu Koltypin, I. Felner, A. Gedanken, “Sonochemical synthesis and characterization of pure nanometer-sized Fe_3O_4 particles”, Material Science and Engineering A, 286, 101 (2000).

69. V. V. Yakovlev, V. Lazarov, J. Reynolds, and M. Gajdardziska-Josifovska, “Laser-induced phase transformations in semiconductor quantum dots”, Applied Physics Letters, 76, 2050 (2000).

70. W. D. Ristenpart, I. A. Aksay, and D. A. Saville, “Assembly of colloidal aggregates by electro-hydrodynamic flow: Kinetic experiments”, Physical Review E, 69, 021405 (2004).

71. Gerardo F. Goya, “Handling the particles size and distribution of Fe_3O_4 nanoparticles through ball milling”, Solid state communications, 130,783 (2004).

72. Bid, A. Banerjee, S. Kumar, S. K. Pradhan, Udaya De, D. Banerjee, “ Nanophase iron oxides by ball-mill grinding and their Mössbauer characterization”, Journal of Alloys and Compounds, 326, 292 (2001).

73. Kurikka V.P.M. Shafi, Aharon Gedanken, Ruslan Prozorov, Judit Balohgh, “Sonochemical Preparation and Size-Dependent Properties of Nanostructured $CoFe_2O_4$ Particles”, Chemical Material, 10, 3445 (1998).

74. G. B. Ji, S.L. Tang, S.K. Ren, F.M. Zhang, B.X. Gu, Y.W. Du, “Simplified synthesis of single-crystalline magnetic $CoFe_2O_4$ nanorods by a surfactant-assisted hydrothermal process”, Journal of Crystal Growth, 270,156 (2004).

75. C. Suryanarayana “ Mechanical alloying and milling, Progess in Material Science 46,1 (2001)

76. Kevin E. Elkins , Tejaswi S. Vedantam, J. P. Liu, Hao Zeng, Shouheng Sun, Y Ding, and Z. L. Wang, Nano Letter, 3, 1647(2003).

77. V. Nandwana, K. E. Elkins, N. Poudyal, G.S. Chaubey, K. Yano, J. P .Liu, J. Phys. Chem. C 111 4185 (2007).

78. S. Sun S, C. B. Murray, D. Weller, L. Folks and A. Moser, “Monodisperse FePt Nanoparticles and Ferromagnetic FePt Nanocrystal Superlattices”, Science, 287 1989 (2000).

79. M. Chen, J.P. Liu, and S. Sun, “One-Step Synthesis of FePt Nanoparticles with Tunable Size”, Journal of American Chimerical Society, 126, 8394 (2004).

80. X. Teng and H. Yang “Synthesis of Face-Centered Tetragonal FePt Nanoparticles and Granular Films from $Pt@Fe_2O_3$ Core-Shell Nanoparticles”, Journal of American Chemical Society, 125, 14559 (2003).

81. N. Poudyal, G. S. Chaubey, V. Nandwana, C. B. Rong, K. Yano and J Ping Liu, Nanotechnology 19 ,355601 (2008).

82. N. Poudyal, G. S. Chaubey, C. B. Rong, and J Ping Liu, Shape Control of FePt Nanocrystals, (submitted to J. App. Phys.) (2008).

83. K. Elkins, D. Li, N. Poudyal, V. Nandwana, Z. Q. Jin, K. H. Chen, and J.P. Liu, J. Phys. D: Appl. Phys. 38, 2306 (2005).

84. C. B. Rong, D. R. Li, V. Nandwana, N. Poudyal, Y. Ding, Z. L. Wang, H. Zeng, and J. P. Liu, Adv. Mater. 18, 2984 (2006).

85. D. Li, N. Poudyal, V. Nandwana, Z. Jin, K. Elkins, J. P. Liu J. Applied Phys. 99 , 08E911(2006).

86. C.B. Rong, N. Poudyal, G. S. Chaubey, V. Nandwana, Y. Liu, Y. Q. Wu, M. J. Kramer, M. E. Kozlov, R. H. Baughman, J. P. Liu, J. Appl. Phys. 103, 07E131 (2008).
87. M.Yue, Y.Wang, N. Poudyal, C. Rong and *J. Liu,* Preparation, structural and magnetic properties of Nd-Fe-Bbased nano-particles. J. Applied Physics (2008) (in press).
88. V. M. Chakka, B. Altuncevahir, Z. Q. Jin, Y. Li, and J. P. Liu, J. Appl. Phys. 99, 08E912 (2006).
89. Yiping Wang, Yang Li, Chuanbing Rong and J. Ping Liu, Sm-Co hard magnetic nanoparticles prepared by surfactant-assisted ball milling. Nanotechnology, 18, 465701 (2007).
90. Narayan Poudyal, Baki Altuncevahir, Vamsi Chakka, Kanghua Chen, Truman D Black, J. P. Liu, Yong Ding, and Zhong Lin Wang, Field-ball milling induced anisotropy in mangetic particles, J. Phys. D: Appl. Phys. 37, L45-L48 (2004).
91. Brent Fultz and Jame M Howe, Transmission Electron Microscopy and Diffractometry of Materials, third edition, Springer Berlin Heilberg (2008).
92. http://www.microscopy.ethz.ch
93. http://www.microtrac.com/downloads/2006/Nano(US)Web.pdf
94. http://upload.wikimedia.org/wikipedia/commons/0/0a/Bragg_diffraction.png
95. S. Sun, Adv. Mater. 18, 393 (2006).
96. M. Chen, J.P. Liu, S. Sun, J. Am. Chem. Soc.126, 8394 (2004).
97. B. D. Cullity and S. R. Stock, X-ray diffraction third edition, Prentice Hall, 170.
98. Chuan-Bing Rong, Vikas Nandwana, Narayan Poudyal, and J. Ping Liu, Mikhail E. Kozlov and Ray H. Baughman, Yong Ding and Zhong Lin Wang, Bulk FePt-based nanocomposite magnets with enhanced exchange coupling , J. Applied Physics, 101, 023908 (2007).
99. J. Lyubina, O. Gutfleisch, R. Skomski, K.-H. Muller, L. Schultz, Scripta Materialia ,469–474 (2005).
100. B. Rellinghaus, S. Stappert, M. Acet, E. F. Wassermann J. Magnetism and Magnetic Materials 266 142–154 (2003).
101. S. Sun, S. Anders, T. Thomson, J.E.E.E Baglin, M. F. Tney, H. F. Hamann, C. B. Murray, B. D. Terris, J. Chem. B 107, 5419 (2003).
102. Hao Zeng, Jing Li, Z. L. Wang, J. P. Liu, and Shouheng Sun NanoLetters, 4, 187-190 (2004).

103. Girija S. Chaubey, Vikas Nandwana, Narayan Poudyal, Chuan-bing Rong, and J. Ping Liu Chem. Mater., 20 475–478 (2008).

104. A. I. Hochbaum, R.Chen , R. D .Delgado, W. Liang , E. C.Garnett , M. Najarian, A. Majumdar, P.Yang , Nature 451 163 (2008).

105. C. K. Chan, H. Peng , G. Liu , K. McIlwrath, X. F. Zhang, R. A Huggins, Y. Cui , Nature Nanotechnology 3 31(2008)

106. S. D. Bader, Rev.Mod.Phys.78 1 (2006).

107. Y. Wang, H. J. Yang , Am. Chem. Soc. 127 5316 (2005).

108. X. Peng, L. Manna , W. Yang, J. Wickham , E. Scher, A. Kadavanich , A. P.Alivisatos, Nature 404 59 (2000).

109. S. Kan, T. Mokari, E. Rothenberg , U. Banin, Nature Materials 2 155 (2003).

110. L. Thomas, M. Hayashi, X. Jiang , R. Moriya , C. Rettner ,S. S. P Parkin , Nature 443 197 (2006)

111. R. P.Cowburn, Nature 448 544 (2006).

112. K. Yong, Y. Sahoo, M. T. Swihart, P. N.Prasad , J. Phys. Chem. C 111 2447 (2007).

113. V. F. Puntes, K. M. Krishnan , A. P. Alivisatos, Science 291 2115 (2001).

114. L. Gou and C.J. Murphy, Chem. Mater. 17 3668 (2001).

115. J. Wu, Y.Lee, H. Chiang, D. K. Wong, J. Phys. Chem. B 110 37(2006).

116. S. Zeng, K.Tang, T. Li, J. of Colloid and Interface Science 312 513 (2007).

117. C. B. Rong, H. W. Zhang, X. B. Du, J. Zhang, S.Y. Zhang, B. G .Shen, J. Appl. Phys. 96 3921 (2004).

118. M.Chen, J. Kim, J.P.Liu, H. Fan, S. Sun, J. Am. Chem. Soc 128 7132 (2006).

119. Y. Dahmane, L. Cagnon, J. Voiron, S. Pairis, M. Bacia, L. Ortega, N. Benbrahim, A. Kadri ,J. Phys. D: Appl. Phys. 39 4523 (2006).

120. G. R.Trichy, D. Chakraborti, J. Narayan, H. Zhou, J. Appl. Phys. 102, 033901(2007).

121. R. C. Che, M.Takeguchi, M.Shimojo, W. Zhang, K. Furuya. Appl. Phys. Lett. 87 223109 (2005).

122. R.Tsukamoto, M.Muraoka, M.Seki, H.Tabata, I. Yamashita, Chem. Mater. 19 2389 (2007).

123. M.Chen, T. Pica, Y. Jiang, P. Li, K. Yano, J. P. Liu , A. K Datye , H. Fan, J Am. Chem. Soc.129 6348 (2007).

124. Y.Hou, H. Kondoh, R. Che, M. Takeguchi, T. Ohta, small 2 235 (2006).

125. C. Wang, Y. Hou, J. Kim, Sun S, Angew. Chem. Int. Ed.46 1(2007).

126. Z. R. Dai, Z. L. Wang, S. Sun, Nano Lett. 1 443(2001).

127. T.Klemmer, D. Hoydick, H. Okamura, B. Zhang, W. A. Soffa, Scripta Metal Mater. 33 1793(1995

128. Boukai,Y. Bunimovich, J.Tahir-Kheli, J.K. Yu, W. A. Goddard III, J. R. Heath, Nature 451, 10 (2008).

129. E. V. Shevchenko, D. V. Talapin, N. A. Kotov, S. O'Brien, C. B. Murray, Nature 439, 55(2006).

130. C.T. Black, C.B. Murray, R.L. Sandstrom, S. Sun, Science 290, 1131, (2000).

131. Chuan-Bing Rong, Narayan Poudyal, Girija S. Chaubey, Vikas Nandwana, Yuzi Liu, Y. Q. Wu, M. J. Kramer, M. E. Kozlov, R. H. Baughman, and J. Ping Liu J. Appl. Phys. 103, 07E131 (2008).

132. Ivanov, L. V. Solina, V. A. Demshima, et al., Phys. Met. Metal. 35, 81 (1973).

133. S. Sun, S. Anders, T. Thomson, J.E.E.E Baglin, M. F. Tney, H. F. Hamann, C. B. Murray, B. D. Terris, J. Chem. B 107,5419 (2003).

134. S. S. Kang, J. W. Harrell, and D. E. Nikles, Nano Lett. 2, 1033 (2002).

135. Q. Y. Yan, T. Kim, A. Purkayastha, P. G. Ganesan, M. Shima, and G.Ramanath, Adv. Mater. (Weinheim, Ger.) 17, 2233 (2005).

136. J. W. Harrell, D. E. Nikles, S. S. Kang, X. C. Sun, Z. Jia, S. Shi, J. Lawson, G. B. Thompson, C. Srivastava and N. V. Seetala., Scr. Mater. 53, 411 (2005).

137. S. S. Kang, Z.Y. Jia, S.F. Shi, D. E. Nikles, and J. W. Harrell, J. Appl. Phys., 97, 10J318 (2005).

138. B. Jeyadevan, A. Hobo, K. Urakawa, C. N. Chinnasamy, K. Shinoda, and K. Tohji, J. Appl. Phys., 93, 7574 (2003).

139. S. Yamamoto, Y. Morimoto, T. Ono, and M. Takano, Appl. Phys. Lett., 87, 032503 (2005).

140. Kazuaki Yano, Vikas Nandwana, Narayan Poudyal, Chuan-bing Rong and J. Ping Liu, J. Applied Physics, 104, 013918((2008).

141. H. Zeng, S. Sun, R. L. Sandstrom, C.B. Murray, J. Magn. Magn. Mater. 266,277 (2003).

142. S. Saita, S.J. Maenosonos, J. Phys: Condens. Matter 16, 6385 (2004).

143. Y. K. Takahashi, T. Ohkubo, M. Ohnuma, and K. Hono, “Size effect on the ordering of FePt granular films,” J. Appl. Phys., vol. 93, pp.7166–7168, (2003).

144. Y. K. Takahashi, T. Koyama, M. Ohnuma, T. Ohkubo, and K. Hono, “Size dependence of ordering in FePt nanoparticles,” J. Appl. Phys., vol. 95, pp. 2690–2696, (2004).

145. T. Miyazaki, O. Kitakami, S. Okamoto, Y. Shimada, Z. Akase, Y. Murakami, D. Shindo, Y. K. Takahashi, and K. Hono, “Size effect on the ordering of L1 FePt nanoparticles,” Phys. Rev. B, 72, 144419 (2005).

146. J. A. Christodoulides, P. Farber, M. Daniil, H. Okaumura, G. C. Hadjipanayis,V. Skymryev, A. Simopoulos, and D.Weller, “Magnetic, structural and microstructural properties of FePt/M (M = C; BN) granular films,” IEEE Trans. Magn., vol. 37, no. 4, pp. 1292–1294, Jul. (2001).

147. J. P. Liu, K. Elkins, D. Li, V. Nandwana, N. Poudyal, IEEE Trans on Magn., 42, 3036-3041(2006).

148. Advanced Magnetic Nanostructures, edited by D. J. Sellmyer and R. Skomski (Springer, Berlin, 2006).

149. T. Miyazaki, O. Kitakami, S. Okamoto, Y. Shimada, Z. Akase, Y. Murakami, D. Shindo, Y. K. Takahashi, and K. Hono, Phys. Rev. B 72,144419 (2005).

150. B. E. Warren, X-Ray Diffraction _Dover, New York,, Chap. 12(1990).

151. C. Kufazvinei, R. W. Leahy, S. M. Lipson, W. J. Blau, F. C. Dillon, T. R. Spalding, M. A. Morris, J. D. Holmes, G. Allan, and J. Patterson, Proc.SPIE 5824, 149 (2005).

152. Chuan-bing Rong, Narayan Poudyal, Girija S Chaubey, and Vikas Nandwana, R. Skomski, Y. Q. Wu and M. J. Kramer, J. Ping Liu J. Applied Physics, 102, 043913. (2007).

153. Y. Shi, J. Ding and H. Yin, “$CoFe_2O_4$ nanoparticles by the mechanochemical method”, Journal of Alloys and Compounds, 303, 290(2002).

154. Jing Li, Hao Zeng, Shouheng Sun, J. Ping Liu, and Zhong Lin Wang, “Analyzing the Structure of CoFe-Fe_3O_4 Core-Shell Nanoparticles by Electron Imaging and Diffraction”, Journal of Physical Chemistry B, 108, 14005 (2004).

155. P. Gaunt, Philos. Mag. 34, 775 (1976).

156. E. P. Wohlfarth, J. Phys. F: Met. Phys. 14, L155 (1984).

157. R.W. Chantrell, A. Lyberatos and E. P. Wohlfartht, J. Phys. F: Met. Phys. 16, L145 (1986).

158. R. Street, R.K. Day, and J.B. Dunlop, J. Magn. Magn. Mater. 69, 106 (1987)

159. D. Givord, P. Tenaud, and T. Viadieu, IEEE Trans. Magn. 24, 1921 (1988).

160. J. F. Liu and H. L. Luo, J. Magn. Magn. Mater. 86, 153(1990).

161. J. F. Liu, S. M. Pan, H. L. Luo, D. L. Hou, and X. F. Nie, J. Phys. D 24, 384 (1991).

162. D.C. Crew, S.H. Farrant, P.G. McCormick, and R. Street, J. Magn. Magn. Mater. 163, 299 (1996).

163. D C Crew, P G McCormick and R Street, J. Phys. D: Appl. Phys. 29, 2313(1996).

164. R. Skomski, R.D. Kirby, and D.J. Sellmyer, J. Appl. Phys. 85, 5069 (1999).

165. H. W. Zhang, C. B. Rong, J. Zhang, S. Y. Zhang, and B .G. Shen, Phys. Rev. B, 66, 184436 (2002).

166. L. Neel, Adv. Phys. 4, 191 (1955).

167. E.C. Stoner, E.P. Wohlfarth, Philos. Trans. Roy. Soc. London A, 240, 599 (1948).

168. H. Pfei®er, Phys. Stat. Sol. A 118, 295 (1990).

169. M. El-Hilo, K. O'Grady, R.W. Chantrell, J. Magn. Magn. Mater., 248, 360 (2002).

170. C. Desvaux, C. Amiens, P. Fejes, P. Renaud, M. Respaud, P. Lecante, E. Snoeck, B. Chaudret Nature Mater. 4, 750 (2005).

171. G. Reiss, A. Hütten, Nature Mater. 4, 725 (2005).

172. G. S. Chaubey, C. Barcena, N. Poudyal, C.B. Rong, J. Gao, S. Sun, J. P. Liu J. Am. Chem. Soc. 129, 7214 (2007).

173. G. Viau, F. Fievet-Vicent, F. Fievet J. Mater. Chem. 6, 1047(1996).

174. X. Su, H. Zheng, Z. Yang, Y. Zhu, A. Pan J. Mater. Sci. 38, 4581(2003).

175. H. Bo¨nnemann, R.A. Brand, W. Brijoux, H. W. Hofstadt, M. Frerichs, V. Kempter, W. Maus-Freidrichs, N. Matoussevitch, K.S. Nagabhushana, V. Voights, V. Caps, Appl. Organomet. Chem. 19, 790 (2005).

176. D. Kodama, K. Shinoda, K. Sato, Y. Konno, R. J. Joseyphus, K. Motomiya, H. Takahashi, T. Matsumoto, Y. Sato, K. Tohji, B Jayadevan, Adv. Mater. 18, 3154 (2006).

177. D. Kodama, K. Shinoda, K. Sato, Y Sato, B. Jeyadevan, K Tohji, K. IEEE Trans. Magn. 42, 2796 (2006).

178. J. Bai, Y. H. Xu, J. P. Wang, IEEE Trans. Magn. 43, 3340 (2007).

179. S. W. Seo, J. H. Lee, Z. Sun, Y. Suzuki, D. Mann, Z. Liu, M. Terashima, P. Yang, M. V. Mcconnell, D.G. Nishimura, H. Dai, Nature Mater. 5, 971(2006).

180. T. Zhang, K. S. Tomas Gan, P. Lee, R. V. Ramanujan, R. S. Rawat J. Phys. D: Appl. Phys. 39, 2212 (2006).

181. C. Kufazvinei, R. W. Leahy, S. M. Lipson, W. J. Blau, F. C. Dillon, T. R. Spalding, M. A. Morris, J. D. Holmes, G. Allan, J. Patterson, Proc. SPIE 5824, 149 (2005).

182. R. M. Bozorth, Ferromagnetism; Van Nostrand: New York, (1951).

183. R. S. Sunder, S.C. Deevi Int. Mater. Rev. 50, 157(2005).

184. M. Hasegawa, K. Uchida, Y. Nozawa, M. Endoh, S. Tanigawa, S. G. Sankar, M. Tokunaga, J. Magn. Magn. Mater. 124, 325 (1993).

185. T. Budde, H. H. Gatzen, J. Magn. Magn. Mater., 2027,272–276 (2004).

186. E. Pina, F. J. Palomares, M. A. Garcia, F. Cebollada, A. de Hoyos, J. J. Romero, A. Hernando, J. M. Gonzalez, J. Magn. Magn. Mater., 290, 1234 (2005).

187. J. Sayama, K. Mizutani, Y. Yamashita, T. Asahi, T. Osaka, IEEE Trans. Magn. 41, 3133 (2005).

188. H. Raisigel, O. Cugat, J. Delamare, Sens. Actuators A 130, 438 (2006).

189. T. Budde, H. H. Gatzen, J. Appl. Phys. 99, 08N304 (2006).

190. Ono K, Kakefuda Y, Okuda R, Ishii Y, Kamimura S, Kitamura A and Oshima M J. Appl. Phys. 91 8480 (2002).

191. H. Gu, B. Xu, J. Rao, R. K. Zheng, X. X. Zhang, K. K. Fung and C. Y. C. Wong, J. Appl. Phys. 93 7589 (2003).

192. S. Stoyanov, V. Skumryev, Y. Zhang, Y. Huang Y, G. Hadjipanayis and J. Nogues, J. Appl. Phys. 93 7592 (2003).

193. X. Teng and H. Yang J. Nanosci. Nanotechnol. 7 3569(2007).

194. J. H. Hong, W. S. Kim, J. I. Li and N. H.Hur , Solid State Commun. 141 541 (2007).

195. J. Ding, P. G. McCormick, R. Street, J. Alloys Compd., 228, 102(1995).

196. S. K. Chen, J. L. Tsai, T. S. Chin, J. Appl. Phys. 79, 5964 (1996).

197. E. M. Kirkpatrick, D. L. Leslie-Pelecky, J. Appl. Phys., 87, 6734 (2000).

198. K. Gallagher, M. Venkatesan, J. M. D. Coey, IEEE Trans. Magn, 37, 2528 (2001).

199. L. Li, W. Y. Zhang, Y. Q. Zhou, J. Q. Li, B. G. Shen, J. Zhang, Appl. Phys. Lett., 80, 2660 (2002).

200. J. Zhou, R. Skomski, D. J. Sellmyer, J. Appl. Phys, 93, 6495.(2003).

201. Hsiao, S. Aich, L. H. Lewis, J. E. Shield, IEEE Trans. Magn, 40, 2913 (2004).

202. J. Sort, J. Nogue´s, S. Surin˜ach, J. S. Mun˜oz, and M. D. Baro´ , E. Chappel, F. Dupont, and G. Chouteau, Appl. Phys. Lett., 79, 1142, (2001)

203. V. Pop, O. Isnard, I. Chicinas, D. Givord, J. M. Le Breton, J. Optoelectron. Adv. Mater., 8, 494 (2006).

204. K. Ono, Y. Kakefuda, R. Okuda, Y. Ishii, S. Kamimura, A. Kitamura,M. Oshima, J. Appl. Phys. 91, 8480 (2002).

205. H. W. Gu, B. Xu, J. C. Rao, R. K. Zheng, X. X. Zhang, K. K. Fung, C. Y. C. Wong, J. Appl. Phys. 93, 7589 (2003).

206. X. Teng, H. Yang, J. Nanosci. Nanotechnol. 7, 356 (1997).

207. J. H. Hong, W. S. Kim, J. I. Lee, N. H. Hur, Solid State Commun., 141, 541 (2007).

208. Y. Hou, Z. Xu, S. Peng, C. Rong, J. P. Liu and S. Sun Adv. Mater., 19, 3349–3352 (2007).

209. C. N. Chinnasamy, J. Y. Huang, L. H. Lewis, B. Latha, C. Vittoria, and V. G. Harris, Appl Phys. Lett. 93, 032505 (2008).

210. V. M. Chakka, Master thesis,“ Study of magnetic nanoparticles produced by surfactant assisted ball milling (2005).

211. R. Coehoorn, D. B. de Mooij and C. de Waard, J. Magn.Magn. Mater. 80 101(1989).

212. L. Lu and M. O. Lai, Mechanical Alloying (Boston, MA: Kluwer) (1998).

213. McCormick P G, Handbook on the Physics and Chemistry of Rare Earths ed K A Gschneidner Jr and L Eyring (BV, amsterdam: Elsevier) pp 47–81 (1997).

214. Venkatesan M, Jiang C and Coey J M D, J. Magn. Magn.Mater. 242–245 1350 (2002).

215. Givord D, Li H S and Perrier del a Bathie R, Solid State Commun. 51 857(1984).

216. Sagawa M, Fujimura S, Yamamoto H, Matsuura Y and Hyrosawa S, J. Appl. Phys. 57 4094(1985).

217. Akira M, Osamu Y and Tetsuji S, Japanese patent—195712 (2000).

218. T. B. Massalski, J. L. Murray, L. H. Bernet and H. Baker, “Binary Phase Diagrams”, ASM International, Materials Park, Ohio, 1096 (1986).

219. H.R. Kichmayr, “Premanet Magnets and Hard Magnetic Matrials” Journal of Physics D: AppliedPhysics 29, 2763-2778(1996).

BIOGRAPHICAL INFORMATION

After completing high school in his native country of Nepal, Narayan Poudyal pursued his college education in Pane, India. He then received his Bachelor's Degree in Science, and Master's Degree in Physics from Tribhuvan University, Kathmandu in Nepal. He then worked as a lecturer at Tribhuvan University for two years. Mr. Poudyal was also involved in the Occidental Public School (OPS) in Kathmandu since its inception as one of the schools's founding members. He served on the Executive Board and as Head of the Department of Science and Mathematics at OPS for four years. After a certain period of time, he felt the need for better understand and broader knowledge of physics, which motivated him to continue his studies in Physics. Subsequently, in 2002, Mr. Poudyal joined the Department of Physics at The University of Texas at Arlington (UTA) in the US. He was awarded a Master's Degree in Physics in August 2005.

He then decided to pursue Ph D in Applied Physics under the supervison of Professor J. Ping Liu. The opportunity to work on the fabrication of magnetic nanoparticles and to study their unique magnetic properties has enriched his knowledge and experience in the area of nano-scale magnetism and nanotechnology, an area that has attracted great attention around the world. His and his group research dealing with the development of advanced nanomaterials including magnetic nanoparticles and nanocomposites were reported in the *PhysicsWorld* and *NanotecWeb* for its significant contributions to the relevant research fields. He wants to explore and contribute more in this area while pursuing his career in a related field.